SKBdoc id 1416908

Future evolution of groundwater composition at Forsmark during an extended temperate period

Steven Joyce, Hannah Woollard

AMEC

Niko Marsic, Magnus Sidborn

Kemakta Konsult AB

December 2013

Title Future evolution of groundwater composition at Forsmark during an extended temperate period

Prepared for SKB

Your Reference

Our Reference

Contact Details

AMEC
Building 150
Harwell Oxford
Didcot
Oxfordshire
OX11 0QB
United Kingdom

Tel +44 (0) 1635 280300
Fax +44 (0) 1635 280301

amec.com

	Name	Job Title	Signature	Date
Main author	Steven Joyce	Principal Consultant		
Reviewed by				
Approved by				

Abstract

As part of the SR-Site safety assessment to support the license application for a spent nuclear fuel repository at Forsmark, groundwater flow and transport calculations were carried out to model the evolution of groundwater composition with time over the temperate climate period from 8,000 BC to 12,000 AD. Geochemical calculations were carried out based on the groundwater compositions exported from the groundwater flow and transport models at selected times and locations. The results of these calculations were used to assess the impact on safety functions related to the geochemical conditions, particularly salinity, pH and redox conditions.

Additional climate cases were also considered for SR-Site, but not used for the hydrogeological modelling. One of these is the global warming case, which considers the effects of a temperate climate period that extends to around 60,000 AD. One implication of this case is that the repository site would be exposed to an extended period of meteoric water infiltration. The consequence of this is that the more dilute and more oxidising meteoric water could potentially penetrate to repository depth during the temperate climate period.

The work reported here carries out groundwater flow, transport and geochemical calculations for the global warming case to assess the impact on groundwater composition within the repository site. The methodology used is similar to SR-Site, but uses a new capability to couple the geochemical calculations with the groundwater flow and transport calculations. Additional cases are also considered with different geochemical reactions that represent either an updated understanding of the site geochemistry or the implications of a more dilute composition for the infiltrating meteoric water.

The results of this work show that there is only a minor change in the geochemical environment of the site beyond the climate period considered for SR-Site and very little change beyond 20,000 AD. The groundwater composition is primarily determined by flow and transport, with only minor changes resulting from the geochemical reactions considered.

Contents

1 Introduction

1.1 Background

The license application submitted by SKB for a spent nuclear fuel repository at Forsmark is supported by the SR-Site safety assessment to demonstrate the long-term safety of the proposed repository (SKB 2011). One part of SR-Site was groundwater flow and transport modelling of the repository site during the operational phase (Svensson and Follin 2010) and during the post-closure phase. Modelling of the post-closure phase was divided into a temperate climate period (Joyce et al. 2010) and a periglacial and glacial climate period (Vidstrand et al. 2010).

One aspect of the temperate climate period modelling was to calculate the evolution of groundwater composition for the time span 8,000 BC to 12,000 AD. This corresponds to the current Holocene period that started at the end of the Weichselian glaciation, but is also taken to represent future inter-glacial periods. The interval from 8,000 BC to around 1,000 AD corresponds to a time when the Forsmark site was submerged. The subsequent interval up to 12,000 AD corresponds to a period when the site is above sea level and the shoreline is retreating due to post-glacial land rise. The reference glacial cycle (SKB 2010) predicts that the Holocene period will continue to 9,000 AD, corresponding to the first occurrence of permafrost. The reference glacial cycle corresponds to the SR-Site base case. A simplified reference glacial cycle (SKB 2010) was also defined for groundwater modelling purposes which defined the end of the temperate climate period as 10,000 AD.

The groundwater composition at selected times was exported from the flow and transport models and used to carry out geochemical calculations (Salas et al. 2010). These calculations determined the concentrations of chemical species, the pH and the redox potential from equilibration with one of two sets of minerals at selected locations. There was no feedback from the geochemical calculations to the flow and transport calculations, i.e. it was a one-way decoupled approach.

Additional climate cases were also considered for SR-Site (SKB 2010), but not included in the groundwater modelling. One such case is the global warming case, which describes a future climate development influenced by both natural climate variability and the possibility of global warming attributed directly or indirectly to human activity. The global warming case predicts that temperate conditions will dominate until around 60,000 AD. This will expose the Forsmark site to an extended period of meteoric water infiltration, which will have implications for groundwater composition and the associated safety functions (particularly salinity, pH and redox conditions).

1.2 Scope

The work described here attempts to model the evolution of groundwater composition during the extended temperate period associated with the global warming climate case. The time span considered is from 8,000 BC to 60,000 AD. The modelling includes the effects of groundwater flow, transport and chemical reactions. The work is based on the regional-scale modelling methodology described in Joyce et al. (2010) and the geochemical calculations described in Salas et al. (2010). However, an approach is adopted which integrates the calculations of flow, transport and chemistry.

A number of cases will be simulated, each considering a different set of geochemical reactions, as follows:

1. No chemical reactions, i.e. the groundwater composition will be determined only by groundwater flow and transport.
2. Equilibration of groundwater with calcite, quartz and amorphous iron (II) sulphide. This is the “base case” from Salas et al. (2010) for the situation with significant activity of sulphate-reducing bacteria. However, the hydroxyapatite reactions are not included as they are not deemed relevant to this work.
3. Equilibration of groundwater with calcite, quartz and iron (III) oxyhydroxide. This is the “base case” from Salas et al. (2010) for the situation where the redox state is not affected by sulphate-reducing bacteria. Again, the hydroxyapatite reactions are not included.
4. Equilibration of groundwater with calcite, quartz, amorphous iron (II) sulphide, kaolinite, albite, and K-feldspar. This case represents an updated understanding of the site geochemistry relative to SR-Site.
5. As Case 2, but with a more dilute composition for meteoric water.

1.3 Report structure

This report is structured as follows:

- Section 1 provides background information to set the work into context.
- Section 2 describes the concepts and methodology used for this study.
- Section 3 describes the numerical modelling.
- Section 4 presents the results.
- Section 5 presents the conclusions.

2 Concepts and methodology

2.1 Conceptual model

The Forsmark site consists of fractured crystalline rock overlain with Quaternary deposits. Based on the characteristics of the geology, the rock was sub-divided into rock domains (SKB 2008), as shown in Figure 2-1. The repository itself is located in a so-called tectonic lens in which the bedrock is less affected by ductile deformation within surrounding belts of high ductile strain. The upper 200 m of the bedrock is characterised by an increased intensity of sub-horizontal to gently dipping fractures and sheet-joints forming a shallow bedrock aquifer. Below this is sparsely fracture bedrock of low permeability. The intensity of fractures generally decreases with increasing depth.

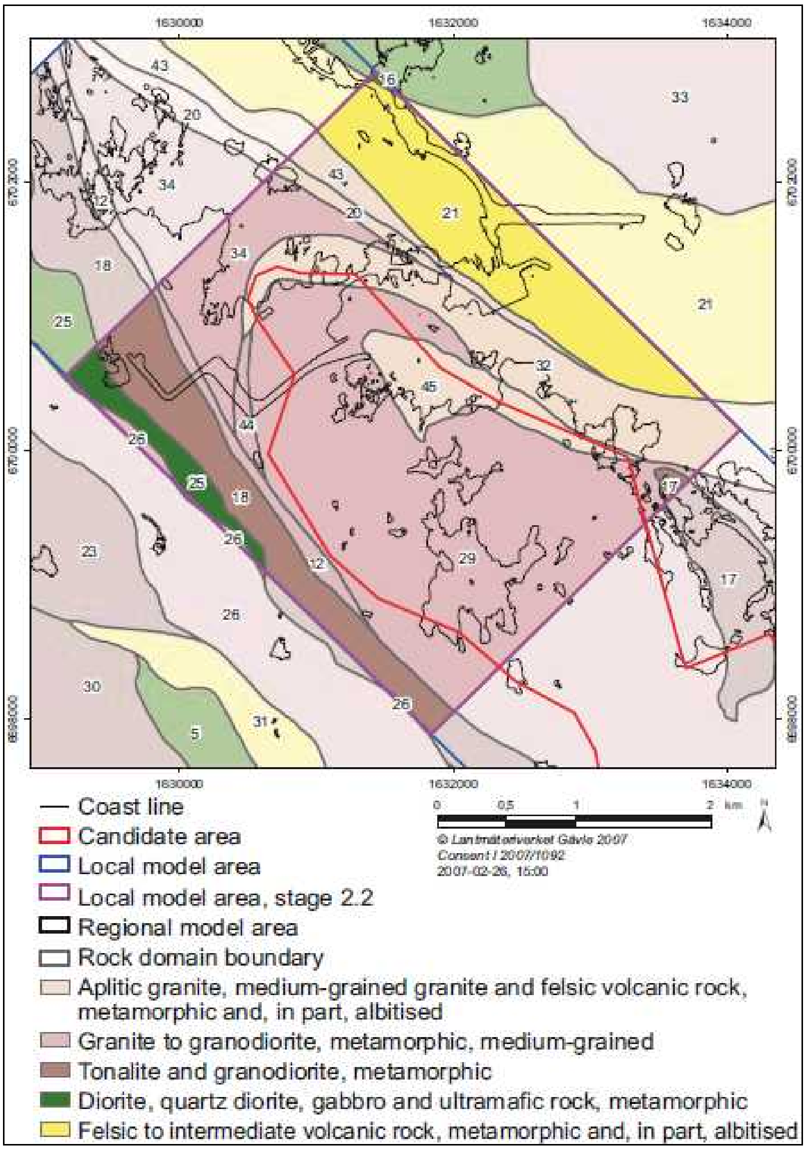

Figure 2-1. *Illustrations of the rock domains at the surface of the local model areas for Forsmark. (SKB 2008).*

A conceptual model of the site hydrogeology was developed during the site-descriptive modelling (SDM), culminating in SDM-Site (SKB 2008), serving as a basis for the SR-Site safety assessment (SKB 2011). The conceptual model describes three hydraulic domains:

- HCD (Hydraulic Conductor Domain) representing deformation zones;
- HRD (Hydraulic Rock mass Domain) representing the less fractured bedrock in between the deformation zones;
- HSD (Hydraulic Soil Domain) representing the regolith (Quaternary deposits).

These domains are illustrated in Figure 2-2.

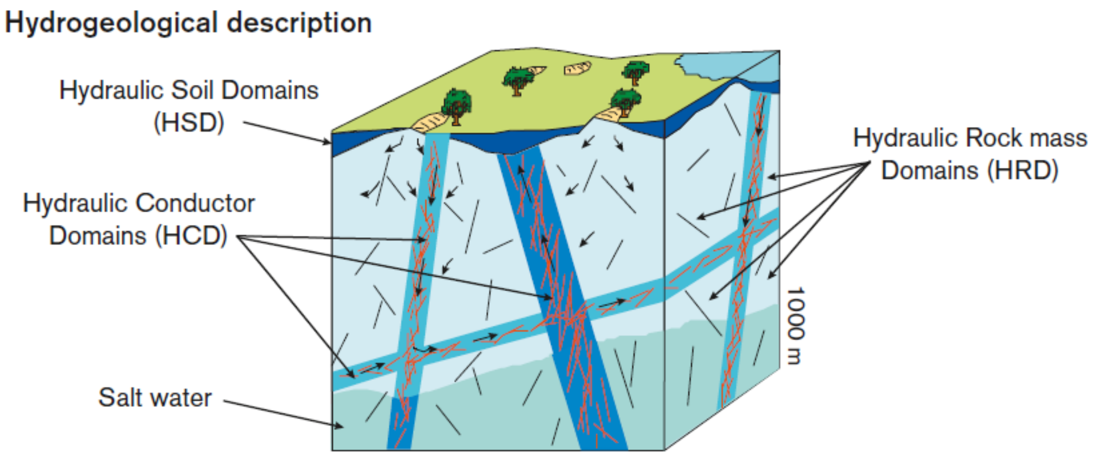

Figure 2-2. Schematic diagram showing the division of the crystalline bedrock and the regolith (Quaternary deposits) into three hydraulic domains, HCD, HRD and HSD. (Rhén et al. 2003, Figure 3-2).

2.1.1 Hydraulic Conductor Domain (HCD)

The deformation zones forming the HCD are defined as structures where there are a concentration of brittle, ductile or combined brittle and ductile deformation. They are envisaged as being composed of swarms of smaller fractures. Each deformation zone structure is characterised by a transmissivity and thickness. Analysis of the site data identified a depth trend for the deformation zone transmissivities, which decrease with increasing depth. An initial deterministic model of the HCD was devised with a uniform horizontal transmissivity (Figure 2-3: top). However, variants were also produced that introduced stochastic horizontal variability, conditioned on borehole measurements to provide both statistical properties (mean, standard deviation, depth trend) and deterministic values at the borehole intercepts with deformation zones (Figure 2-3: bottom).

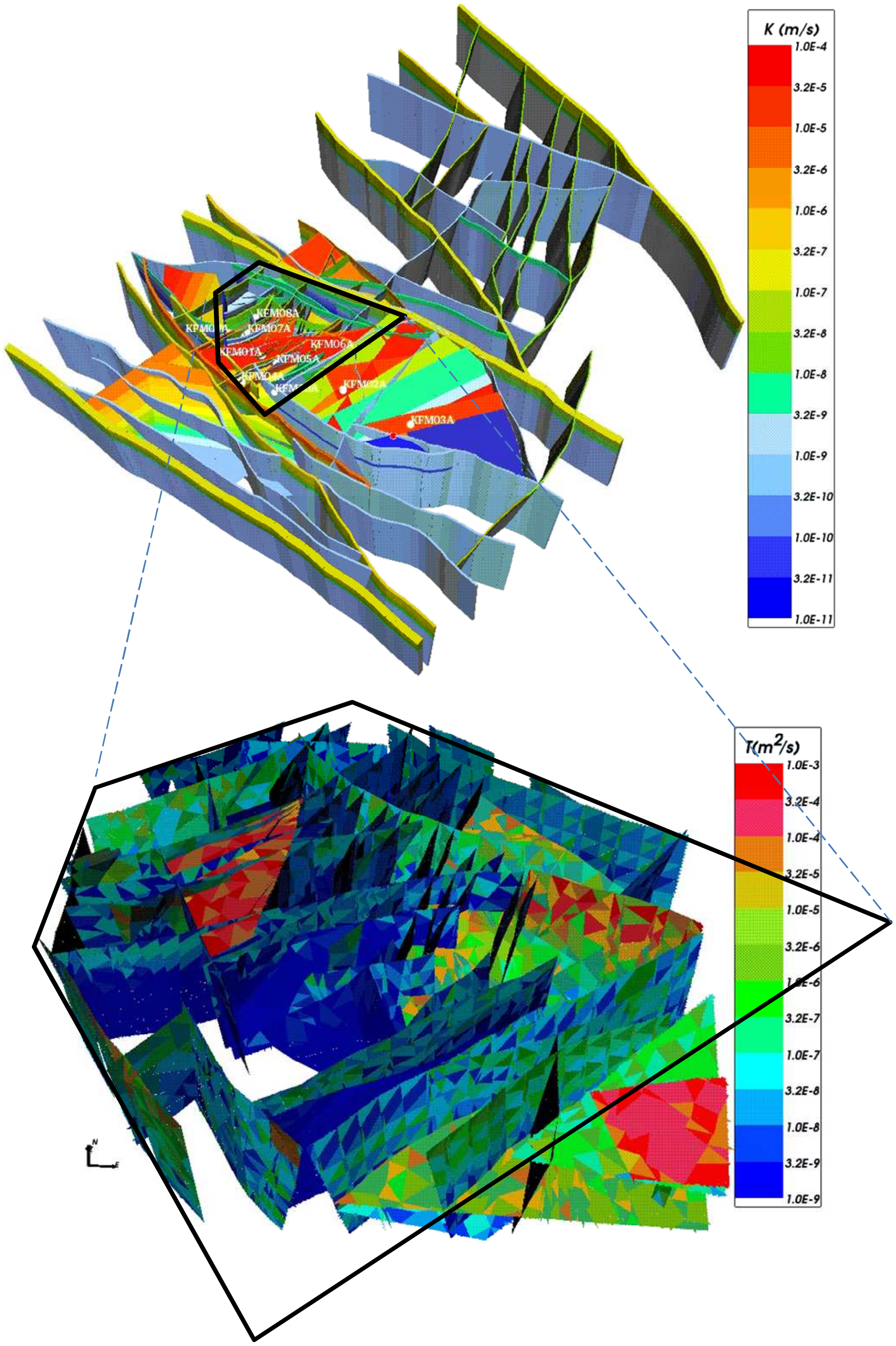

Figure 2-3. *Property model of the deformation zones. Top: Regional scale deformation zones with deterministic properties, represented as volumes to show their assigned width and coloured by hydraulic conductivity. Bottom: Visualisation of one stochastic realisation of the deformation zones that occur inside the local model domain, represented as surfaces and coloured by transmissivity. Adapted from Follin (2008).*

2.1.2 Hydraulic Rock mass Domain (HRD)

The fractured bedrock between the deformation zones was divided into a number of fracture domains, characterised by fracture properties and location. These fracture domains were denoted FFM01 to FFM06 and are shown schematically in Figure 2-4 to Figure 2-6. Fracture domain FFM06 has a similar structural context to FFM01 and so these two fracture domains were merged. There was insufficient data to fully describe FFM04 and FFM05 and so their properties were characterised by analogy to FFM03. Due to the depth trend in fracture intensity in Forsmark, the FFM01/06 domain was divided into three depth zones (above -200 m, -200 m to -400 m and below -400 m elevation). The FFM03, FFM04 and FFM05 domains were divided into two depth zones (above and below -400 m elevation). Additionally, fractures were divided by orientation into four sub-vertical fracture sets (NS, NE, NW, EW) and one sub-horizontal fracture set (HZ). A process of analysis and calibration allowed a parameterisation of a hydrogeological discrete fracture network (Hydro-DFN) to be produced. This assumed a power-law relationship between intensity and fracture size:

$$f(r) = \frac{k_r r_0^{k_r}}{r^{k_r+1}} \tag{2-1}$$

where r_0 and k_r are the location parameter and the shape parameter, respectively. Additionally, a semi-correlated relationship between fracture size and transmissivity was used for the hydrogeological base case:

$$\log(T) = \log\left(a\, r^b\right) + \sigma_{\log(T)}\, N[0,1] \tag{2-2}$$

where T is the fracture transmissivity, r is the fracture radius, a and b are constants and $N[0,1]$ denotes a normally distributed random deviate with a mean equal to zero and a standard deviation of 1. The parameters defining the Hydro-DFN for each fracture domain in the candidate area are given in Table 2-1. Outside the candidate area limited borehole data only allowed an approximate parameterisation of the bedrock properties, as shown in *Table 2-2*.

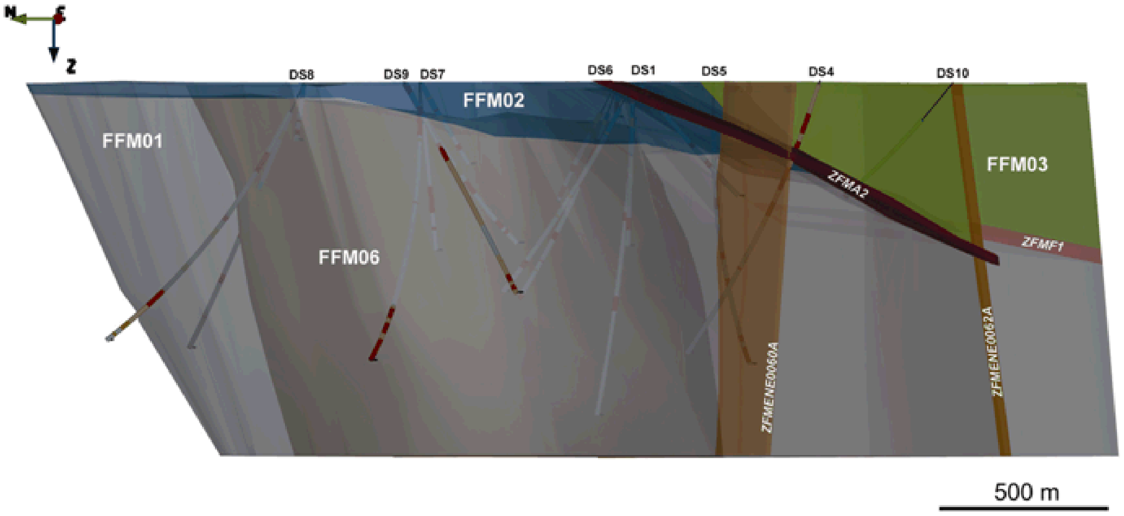

Figure 2-4. Three-dimensional representation of the fracture domain model, viewed towards ENE. Fracture domains FFM01, FFM02, FFM03 and FFM06 are coloured grey, dark grey, blue and green, respectively. The gently dipping and sub-horizontal zones A2 and F1 as well as the steeply dipping deformation zones ENE0060A and ENE0062A are also shown. (Follin 2008).

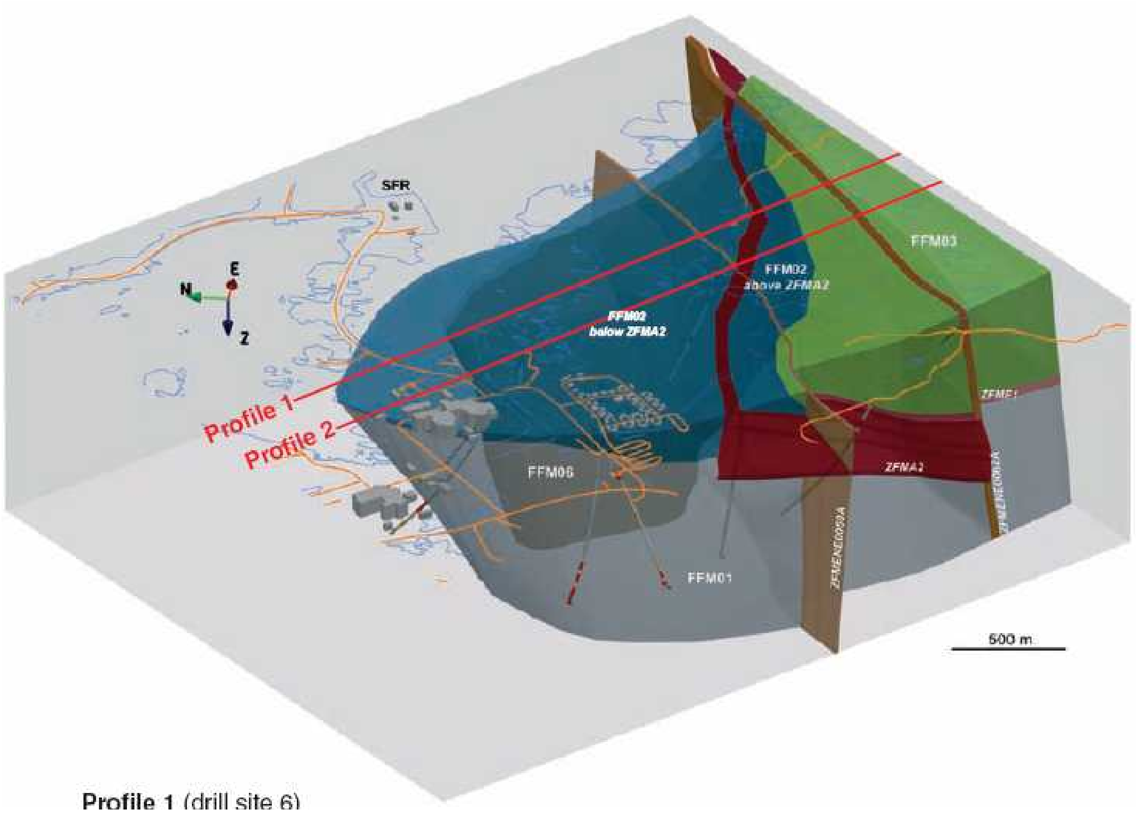

Figure 2-5. Three-dimensional view towards ENE showing the relationship between deformation zone A2 (red) and fracture domain FFM02 (blue). Profile 1 and 2 are shown as cross-sections in Figure 2-6. (Follin 2008).

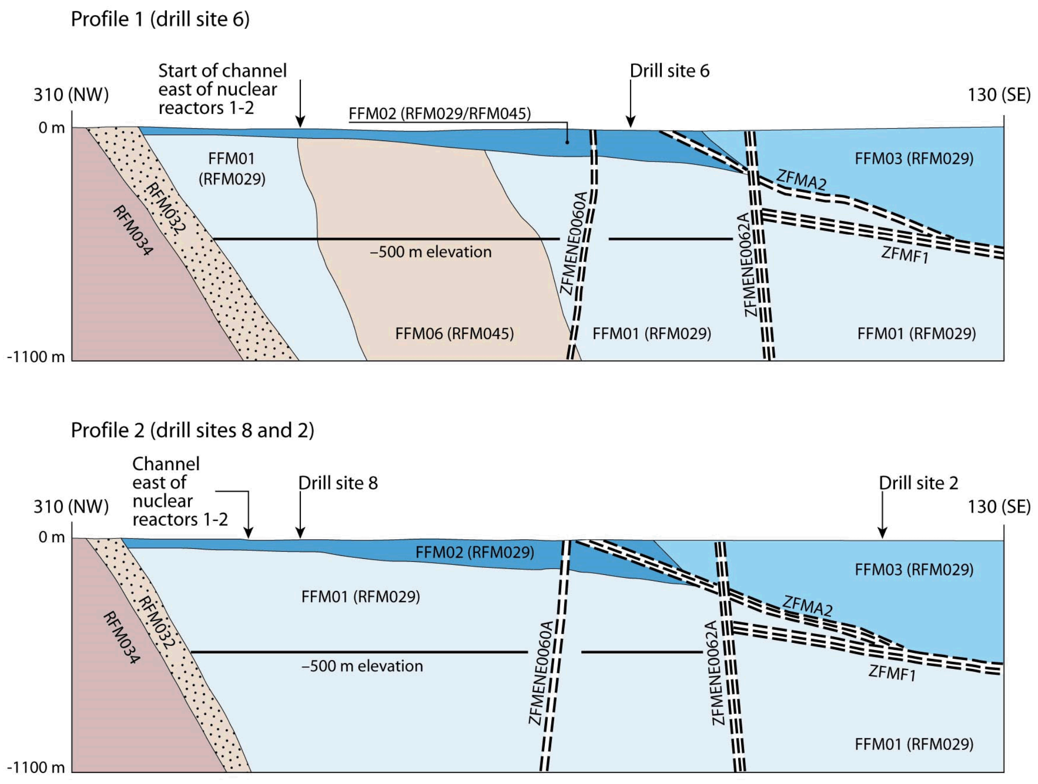

Figure 2-6. *Simplified profiles in a NW-SE direction that pass through the target volume. The locations of the profiles are shown in Figure 2-5. The key fracture domains, FFM01,- 02 and -06, for a final repository at Forsmark occur in the footwall of zones A2 (gently dipping) and F1 (sub-horizontal). The major steeply dipping zones ENE0060A and ENE0062A are also included in the profiles. (Olofsson et al. 2007, Figure 5-1).*

Table 2-1. Hydrogeological DFN parameters for the semi-correlated transmissivity model of each fracture domain with depth dependency. Combined from Tables C-1 to C-3 in Follin (2008).

Fracture domain	**Fracture set name**	**Orientation set pole: (trend, plunge), conc.**	**Size model, power-law (r_0, k_r)**	**Intensity, (P_{32}), valid size interval: (r_0, 564 m)**	**Parameter values for the transmissivity model shown in Eq. (2-2)**
(m RHB 70)			(m, -)	(m^2/m^3)	T (m^2s^{-1})
FFM01 FFM06 > –200	NS	(292, 1) 17.8	(0.038, 2.50)	0.073	$(a,b,\sigma) = (6.3 \cdot 10^{-9}, 1.3, 1.0)$
	NE	(326, 2) 14.3	(0.038, 2.70)	0.319	
	NW	(60, 6) 12.9	(0.038, 3.10)	0.107	
	EW	(15, 2) 14.0	(0.038, 3.10)	0.088	
	HZ	(5, 86) 15.2	(0.038, 2.38)	0.543	
FFM01 FFM06 –200 to –400	NS	As above	As above	0.142	$(a,b,\sigma) = (1.3 \cdot 10^{-9}, 0.5, 1.0)$
	NE	As above	As above	0.345	
	NW	As above	As above	0.133	
	EW	As above	As above	0.081	
	HZ	As above	As above	0.316	
FFM01 FFM06 < –400	NS	As above	As above	0.094	$(a,b,\sigma) = (5.3 \cdot 10^{-11}, 0.5, 1.0)$
	NE	As above	As above	0.163	
	NW	As above	As above	0.098	
	EW	As above	As above	0.039	
	HZ	As above	As above	0.141	
FFM02 > –200	NS	(83, 10) 16.9	(0.038, 2.75)	0.342	$(a,b,\sigma) = (9.0 \cdot 10^{-9}, 0.7, 1.0)$
	NE	(143, 9) 11.7	(0.038, 2.62)	0.752	
	NW	(51, 15) 12.1	(0.038, 3.20)	0.335	
	EW	(12, 0) 13.3	(0.038, 3.40)	0.156	
	HZ	(71, 87) 20.4	(0.038, 2.58)	1.582	
FFM03 FFM04 FFM05 > –400	NS	(292, 1) 17.8	(0.038, 2.60)	0.091	$(a,b,\sigma) = (1.3 \cdot 10^{-8}, 0.4, 0.8)$
	NE	(326, 2) 14.3	(0.038, 2.50)	0.253	
	NW	(60, 6) 12.9	(0.038, 2.55)	0.258	
	EW	(15, 2) 14.0	(0.038, 2.40)	0.097	
	HZ	(5, 86) 15.2	(0.038, 2.55)	0.397	
FFM03 FFM04 FFM05 < –400	NS	As above	As above	0.102	$(a,b,\sigma) = (1.8 \cdot 10^{-8}, 0.3, 0.5)$
	NE	As above	As above	0.247	
	NW	As above	As above	0.103	
	EW	As above	As above	0.068	
	HZ	As above	As above	0.250	

Table 2-2. Homogeneous and isotropic hydraulic properties used for the HRD outside the candidate area (Follin et al. 2007a).

Elevation (m RHB 70)	Hydraulic conductivity (m/s)	Kinematic porosity (-)
> –200	$1 \cdot 10^{-7}$	$1 \cdot 10^{-5}$
–200 to –400	$1 \cdot 10^{-8}$	$1 \cdot 10^{-5}$
< –400	$3 \cdot 10^{-9}$	$1 \cdot 10^{-5}$

2.1.3 Hydraulic Soil Domain

The regolith at Forsmark was deposited during the Quaternary period and so are generally known as Quaternary deposits. The conceptual model of the HSD consists of nine layers (L1-L3 and Z1-Z6) of varying extents and thicknesses as shown in Figure 2-7. A description of each layer is given in *Table 2-3*. Suggested hydraulic properties from the SDM for groundwater flow modelling are given in *Table 2-4* and *Table 2-5*.

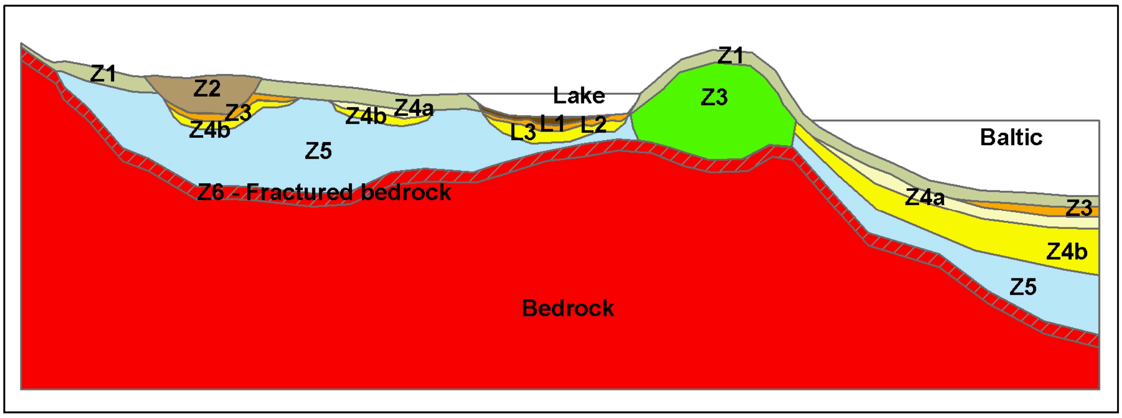

Figure 2-7. *Conceptual model for the layering of Quaternary deposits at Forsmark (Hedenström et al. 2008).*

Table 2-3. Names and definitions of Quaternary deposits (Hedenström et al. 2008).

Layer	Description and comments
L1	Layer consisting of different kinds of gyttja/mud/clay or peat. Interpolated from input data, thickness will therefore vary.
L2	Layer consisting of sand and gravel. Interpolated from input data, thickness will therefore vary.
L3	Layer consisting of different clays (glacial and postglacial). Interpolated from input data, thickness will therefore vary.
Z1	Surface affected layer present all over the model, except where peat is found and under lakes with lenses. Thickness is 0.10 m on bedrock outcrops, 0.60 m elsewhere. If total regolith thickness is less than 0.60 m, Z1 will have the same thickness as the total, i.e. in those areas only Z1 will exist.
Z2	Surface layer consisting of peat. Zero thickness in the sea. Always overlies by Z3.
Z3	Middle layer of sediments. Only found where surface layers are other than till, clay or peat.
Z4a	Middle layer consisting of postglacial clay. Always overlies by Z4b.
Z4b	Middle layer of glacial clay.
Z5	Corresponds to a layer of till. The bottom of layer Z5 corresponds to the bedrock surface.
Z6	Upper part of the bedrock. Fractured rock. Constant thickness of 0.5 m. Calculated as an offset from Z5.

Table 2-4. Values of the saturated hydraulic conductivity of the Quaternary deposits suggested for groundwater flow modelling in SDM stage 2.2 (Bosson et al. 2008).

Layer	*K* [m/s] of layers with several types of Quaternary deposits					
	Fine till	**Coarse till**	**Gyttja**	**Clay**	**Sand**	**Peat**
L1	–	–	$3 \cdot 10^{-7}$	–	–	< 0.6m depth: $1 \cdot 10^{-6}$
Z1	$3 \cdot 10^{-5}$	$3 \cdot 10^{-5}$	–	$1 \cdot 10^{-6}$	$1.5 \cdot 10^{-4}$	> 0.6m depth: $3 \cdot 10^{-7}$
Z5	$1 \cdot 10^{-7}$	$1.5 \cdot 10^{-6}$	–	–	–	–
	***K* [m/s] of layers with one type of Quaternary deposits**					
L2	$3 \cdot 10^{-4}$					
L3	< 0.6m depth: $1 \cdot 10^{-6}$; > 0.6m depth: $1.5 \cdot 10^{-8}$					
Z2	$3 \cdot 10^{-7}$					
Z3	$1.5 \cdot 10^{-4}$					
Z4	$1.5 \cdot 10^{-8}$					

Table 2-5. Values of the total porosity and the specific yield of the Quaternary deposits suggested for groundwater flow modelling in SDM stage 2.2 (Bosson et al. 2008).

Layer	Total porosity [–] and specific yield [–] of layers with several types of Quaternary deposits					
	Fine till	**Coarse till**	**Gyttja**	**Clay**	**Sand**	**Peat**
L1	–	–	0.50 / 0.03	–	–	0.60 / 0.20
Z1	0.35 / 0.15	0.35 / 0.15	–	0.55 / 0.05	0.35 / 0.20	0.40 / 0.05
Z5	0.25 / 0.03	0.25 / 0.05	–	–	–	–
	Total porosity [–] and specific yield [–] of layers with one type of Quaternary deposits					
L2	0.35 / 0.20					
L3	0.55 / 0.05					
Z2	0.40 / 0.05					
Z3	0.35 / 0.20					
Z4	0.45 / 0.03					

2.2 Methods and tools

The modelling was carried out using ConnectFlow version 10.5 (AMEC 2013a, b, c). ConnectFlow is a suite of groundwater flow and transport software that is able to represent rock using continuous porous medium (CPM), discrete fracture network (DFN), or combined CPM/DFN concepts. An equivalent continuous porous medium (ECPM) concept based on upscaled DFN properties is also available. The modelling carried out for this study uses CPM and ECPM representations. The main concepts and methods used for this work are summarised in the following sections. Further details can be found in Joyce et al. (2010), Hartley and Joyce (2013) and AMEC (2013a, b, c).

2.2.1 Discrete fracture network (DFN) representation

The DFN concept is very useful since it naturally reflects the individual flow conduits in fractured rock and the available field data. The properties of the network are usually characterised in terms of:

- Spatial distribution (e.g. Poisson, fractal, clustered around points or lineaments);
- Fracture intensity (and its spatial variation);
- Fracture sets distinguished by orientation;
- Fracture size (e.g. log-normal, power-law distributions);
- Transmissivity-size relationships.

The properties of each fracture are primarily:

- Size;
- Orientation (strike and dip);
- Transmissivity (and possibly spatial variability within the fracture);
- Transport aperture;
- Storativity.

In ConnectFlow, fractures are usually rectangular, but may be right-angled triangles where a complex surface has been triangulated into many pieces (e.g. for a deformation zone). For stochastic fractures, the properties are sampled from probability distribution functions (PDFs) specified for each fracture set. The properties may be sampled independently or correlated with other properties.

2.2.2 Continuous porous medium (CPM) representation

CPM models are considered appropriate for certain types of rock, in which flow is predominantly through an interconnected network of pores in the rock matrix, such as for many sandstones, or for soils and unconsolidated deposits. The model assumes continuity in three dimensions and hence a high degree of connectivity between points in the modelling domain. Connectivity is only reduced when very low conductivity layers or flow barriers are incorporated in the model. The flow through such domains is modelled by Darcy's law, which relates specific discharge (Darcy flux) to the driving force, i.e. the pressure gradient and/or buoyancy force.

The CPM representation is less useful for fractured rocks as it can only represent bulk properties over large volumes. However, it can be of use for regions of a model where there is limited data available on fracturing and it is appropriate to use generic rock properties, e.g. in rock mass volumes far away from the repository host rock.

2.2.3 Equivalent porous medium modelling representation

In order to assess the implications of a discrete fracture network for flow and transport on the regional-scale, it is often necessary for practical reasons to convert the DFN model to an ECPM model with appropriate properties. The resulting parameters are a directional hydraulic conductivity tensor, fracture kinematic porosity and other transport properties (such as the fracture surface area per unit volume). In ConnectFlow, a flux-based upscaling method is used that requires several flow calculations through a DFN model in different directions (Jackson et al. 2000, Hartley and Joyce 2013).

2.2.4 Implicit fracture zones (IFZ)

The properties of large deterministic structures, such as deformation zones, in CPM or ECPM models can be represented in ConnectFlow using the implicit fracture zone (IFZ) approach. This approach combines the properties of each cell in the model that is intersected by a structure with the corresponding properties of the intersecting structure, taking the volume of the cell occupied by the structure and its orientation into account (Hartley and Joyce 2013). The result of this process is to produce a spatial distribution of cell properties (hydraulic conductivity tensor, porosity and flow wetted surface) that represent the combined influence of both the deterministic structures and bedrock stochastic fractures.

2.2.5 Groundwater flow

Groundwater flow in a CPM or ECPM model in ConnectFlow is expressed in terms of Darcy's law

$$\mathbf{q} = -\frac{k}{\mu} \cdot (\nabla P - \rho \mathbf{g}) \qquad \textit{(2-3)}$$

and the equation for conservation of mass

$$\frac{\partial(\phi_f \rho)}{\partial t} + \nabla \cdot (\rho \mathbf{q}) = 0 \qquad \textit{(2-4)}$$

where

- $\mathbf{q}$ is the specific discharge (or Darcy flux) [m/s];
- k is the equivalent permeability tensor due to the fractures carrying the flow [m^2];
- μ is the groundwater viscosity [kg/m/s];
- P is the (total) pressure in the groundwater [N/m^2];
- ρ is the groundwater density [kg/m^3];
- $\mathbf{g}$ is the gravitational acceleration [m/s^2];
- t is the time [s];

- ϕ_f is the kinematic porosity due to the fractures carrying the flow [-];

In general, the density and viscosity of the water depend on temperature, pressure and total salinity. Temperature and salinity are in turn transported by the groundwater. When the variations in temperature or solute concentration are large enough to produce significant changes in density or viscosity, it is necessary to couple the solution of the groundwater flow problem to that of the heat or solute transport problem. For this study transport of heat is not included.

2.2.6 Solute transport

ConnectFlow calculates solute transport using the advection-dispersion equation

$$\frac{\partial(\phi_f \rho c)}{\partial t} + \nabla \cdot (\rho \mathbf{q} c) = \nabla \cdot (\phi_f \rho D \cdot \nabla c) \qquad \textit{(2-5)}$$

where

- c is the solute mass fraction in the groundwater flowing through the fractures [-];
- D is the (effective) dispersion tensor [m^2/s];

For a single transported component, Equations (2-3), (2-4) and (2-5) can be solved in ConnectFlow as a coupled set of equations. However, for the transport of many components it is not usually practicable to solve the full set of coupled equations. In this case, sequential iteration can be used as an operator splitting method to decouple the equations and solve each groundwater flow and transport equation separately. Multiple iterations of the sequence of equations can be carried out for increased accuracy at the expense of computational time, but normally a single iteration is sufficient for a system that is evolving slowly relative to the time step size.

2.2.7 Rock matrix diffusion (RMD)

Rock matrix diffusion (RMD) is the process of migration of solutes from fractured rock into the less mobile water within the rock matrix over long time periods. The rock matrix diffusion method used for the ConnectFlow modelling in SR-Site is not compatible with the calculation of chemical reactions, so a newer method based on a finite volume approach has been used for this study. This method divides the rock matrix into separate elements and calculates the transport of components from one element to the next at each time step before carrying out chemical reactions.

2.2.8 Geochemistry calculations

ConnectFlow is able to combine groundwater flow and transport calculations with geochemical calculations (reactive transport). At each time step, the mass fractions of components are updated based on the results of chemical reaction calculations carried out at equilibrium. The chemical reactions are calculated by the iPhreeqc software library (Charlton and Parkhurst 2011), which provides an interface to the widely used PHREEQC geochemical software (Parkhurst and Appelo 1999). The data produced by PHREEQC are used to calculate the mass fractions of components for the next time step in ConnectFlow. Figure 2-8 shows a flow diagram describing the reactive transport system in ConnectFlow. Chemical reactions are calculated for both the fractures and the rock matrix.

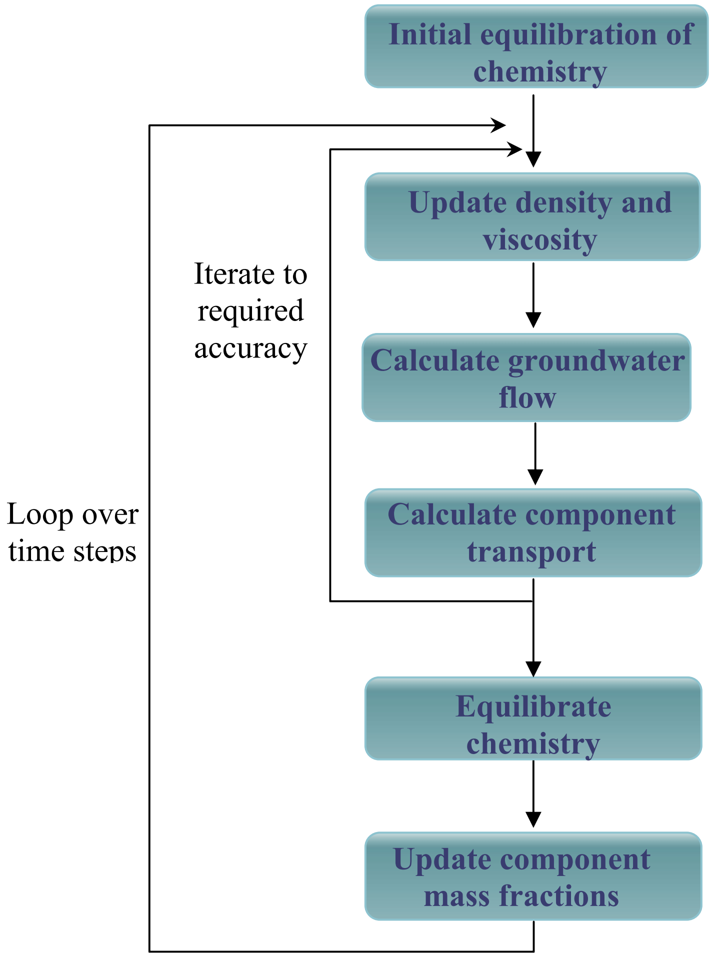

***Figure 2-8.** Flow diagram of reactive transport within ConnectFlow.*

The chemical calculations are based on a set of thermodynamic constraints defined in a separate database. The database used is basically the same as the one used in the SR-Site calculations performed by Salas et al. (2010). Some additional equilibrium constraints with mineral phases not included in the SR-Site calculations have been added to the database. The additional reaction formulas and their corresponding equilibrium constants are listed in the PhreeqC format in *Table 2-6*. See Parkhurst and Appelo (1999) for details on the input format.

Table 2-6. Additions to the thermodynamic database used in SR-Site (Salas et al. 2010). Reaction formulas and equilibrium constants are given in PhreeqC format (see Parkhurst and Appelo 1999 for details).

```
Albite
NaAlSi3O8 + 8H2O = Al(OH)4- + 3Si(OH)4 + Na+
log_k     -19.98
-analytic -5429.59545 -0.81939 293813.48663 1966.59164 -17577933.12184
```

```
K-feldspar
KAlSi3O8 + 8H2O = Al(OH)4- + 3Si(OH)4 + K+
log_k     -22.62
-analytic -5701.00975 -0.87173 304836.7864 2069.03705 -18119139.36096
```

```
Fe(OH)3(hematite_grenthe)
Fe(OH)3 + 3 H+ = Fe+3 + 3 H2O
log_k           -1.1
```

```
FeS(ppt)
FeS + H+ = Fe+2 + HS-
log_k           -3.00
```

```
Kaolinite_Grimaud
Al2Si2O5(OH)4 + 7H2O = 2Al(OH)4- + 2H+ + 2Si(OH)4
log_k     -37.3
```

3 Modelling

3.1 Model description

The models used in this study are based on the regional-scale model of the hydrogeological base case used for the SR-Site temperate climate period modelling (Joyce et al. 2010). The only changes have been to support reactive transport modelling and to extend the simulated period to 60,000 AD. The main features of the models are summarised in the following sections.

3.1.1 Model grid

The model grid is is approximately 15 km by 10 km in horizontal extent and extends from the ground surface to a depth of 1.2 km. The upstream boundaries of the model correspond to significant surface water divides and the downstream boundary represents the furthest shoreline position reached during the temperate period (Follin et al. 2007b). A local area is defined around the repository, approximately 3.3 km square. Within the local area the grid cells are 20 m square horizontally. Outside the local area the grid cells are 100 m square horizontally. Internal boundary conditions ensure continuity of pressure and flow where there are discontinuities in the grid at the boundaries of the local area. The cells are approximately cubes, except in the soil domain, where a 1 m vertical cell size is used. The upper layers of the model are also mapped to the surface topography which causes some adjustment of cell height.

3.1.2 Hydraulic properties

The model uses an equivalent porous medium (ECPM) representation, whose hydraulic properties are derived from the upscaling of a discrete fracture network (DFN) representing the Hydraulic Rock mass Domain (HRD), combined with the application of deformation zone and sheet joint properties using the implicit fracture zone method (IFZ), as described in Section 2.2. The Hydraulic Soil Domain (HSD) is represented by four 1 m deep layers. The vertical and horizontal components of the HSD hydraulic conductivity are different, i.e. the hydraulic conductivity is anisotropic. The horizontal component of the tensor is based on the arithmetic mean of the hydraulic properties of the original stratigraphy, whereas the vertical component is based on its harmonic mean.

The ECPM model used for this study is derived from the first realisation of the DFN for the HRD and the deterministic (with a depth trend) deformation zone model (referred to as r0 in Joyce et al. 2010).

3.1.3 Initial condition and boundary conditions

The initial condition and the boundary conditions are equivalent to those used for the SR-site temperate period regional-scale model (Joyce et al. 2010), which are the same as those used for the "Alternative Case" palaeohydrogeology model in Follin et al. (2007b). The groundwater composition is specified in terms of fractions of reference waters, which are then converted to an equivalent representation in terms of mass fractions of individual components within ConnectFlow. The composition of each reference water is shown in *Table 3-1*. The fraction of each reference water used in the initial condition varies according to depth and rock domain, as shown in Figure 3-1.

The boundary conditions for the sides of the model specify zero flux of water and zero flux of solute. The boundary condition on the bottom of the model specifies zero flux of water and the mass fractions of the solutes are held constant at their initial values. The top surface boundary condition leads to recharge or discharge of water depending on the calculated head relative to the ground surface elevation (taking land rise, the depth of the sea and the salinity of the sea into account). The composition of infiltrating water through the top boundary varies over time, consisting of Glacial water at early times, followed by Littorina Sea water for parts of the surface below the sea and then meteoric water for land areas above sea level.

Table 3-1. Reference water compositions.

	Deep Saline	Littorina	Altered Meteoric	Glacial	Old Meteoric	Dilute Meteoric
pH	8.000	7.951	7.314	9.300	8.500	7.030
pe	-4.449	-4.422	0.554	-5.260	-4.925	0.456
Component mass fractions (kg/kgs)						
Al	$1.854\cdot10^{-10}$	$8.662\cdot10^{-9}$	$2.081\cdot10^{-9}$	$1.404\cdot10^{-7}$	$2.465\cdot10^{-8}$	$4.000\cdot10^{-8}$
Br	$3.081\cdot10^{-4}$	$2.222\cdot10^{-5}$	$5.722\cdot10^{-7}$	0.000	$5.720\cdot10^{-7}$	0.000
C	$4.099\cdot10^{-7}$	$1.932\cdot10^{-5}$	$8.678\cdot10^{-5}$	$1.023\cdot10^{-6}$	$6.268\cdot10^{-6}$	$5.490\cdot10^{-5}$
Ca	$1.837\cdot10^{-2}$	$1.532\cdot10^{-4}$	$1.883\cdot10^{-5}$	$2.878\cdot10^{-6}$	$4.743\cdot10^{-5}$	$9.290\cdot10^{-5}$
Cl	$4.494\cdot10^{-2}$	$6.506\cdot10^{-3}$	$1.811\cdot10^{-4}$	$4.999\cdot10^{-7}$	$1.810\cdot10^{-4}$	$4.400\cdot10^{-6}$
F	$1.524\cdot10^{-6}$	$4.903\cdot10^{-7}$	$1.601\cdot10^{-6}$	0.000	$1.600\cdot10^{-6}$	0.000
Fe	$1.308\cdot10^{-8}$	$4.562\cdot10^{-7}$	$1.001\cdot10^{-7}$	$4.469\cdot10^{-8}$	$4.880\cdot10^{-10}$	$1.400\cdot10^{-7}$
K	$2.983\cdot10^{-5}$	$1.341\cdot10^{-4}$	$5.603\cdot10^{-6}$	$4.000\cdot10^{-7}$	$5.600\cdot10^{-6}$	$1.560\cdot10^{-6}$
Li	$4.419\cdot10^{-6}$	$7.007\cdot10^{-8}$	$1.401\cdot10^{-8}$	0.000	$1.400\cdot10^{-8}$	0.000
Mg	$2.019\cdot10^{-6}$	$4.482\cdot10^{-4}$	$7.503\cdot10^{-6}$	$9.999\cdot10^{-8}$	$7.501\cdot10^{-6}$	$4.200\cdot10^{-6}$
Na	$8.108\cdot10^{-3}$	$3.676\cdot10^{-3}$	$2.741\cdot10^{-4}$	$1.700\cdot10^{-7}$	$2.741\cdot10^{-4}$	$6.000\cdot10^{-6}$
S	$2.975\cdot10^{-6}$	$2.975\cdot10^{-4}$	$2.839\cdot10^{-5}$	$1.701\cdot10^{-7}$	$2.838\cdot10^{-5}$	$3.330\cdot10^{-6}$
Si	$2.295\cdot10^{-6}$	$3.560\cdot10^{-6}$	$3.767\cdot10^{-6}$	$4.676\cdot10^{-6}$	$3.919\cdot10^{-6}$	$4.350\cdot10^{-6}$
Sr	$3.209\cdot10^{-4}$	$2.682\cdot10^{-6}$	$3.801\cdot10^{-7}$	0.000	$3.801\cdot10^{-7}$	0.000

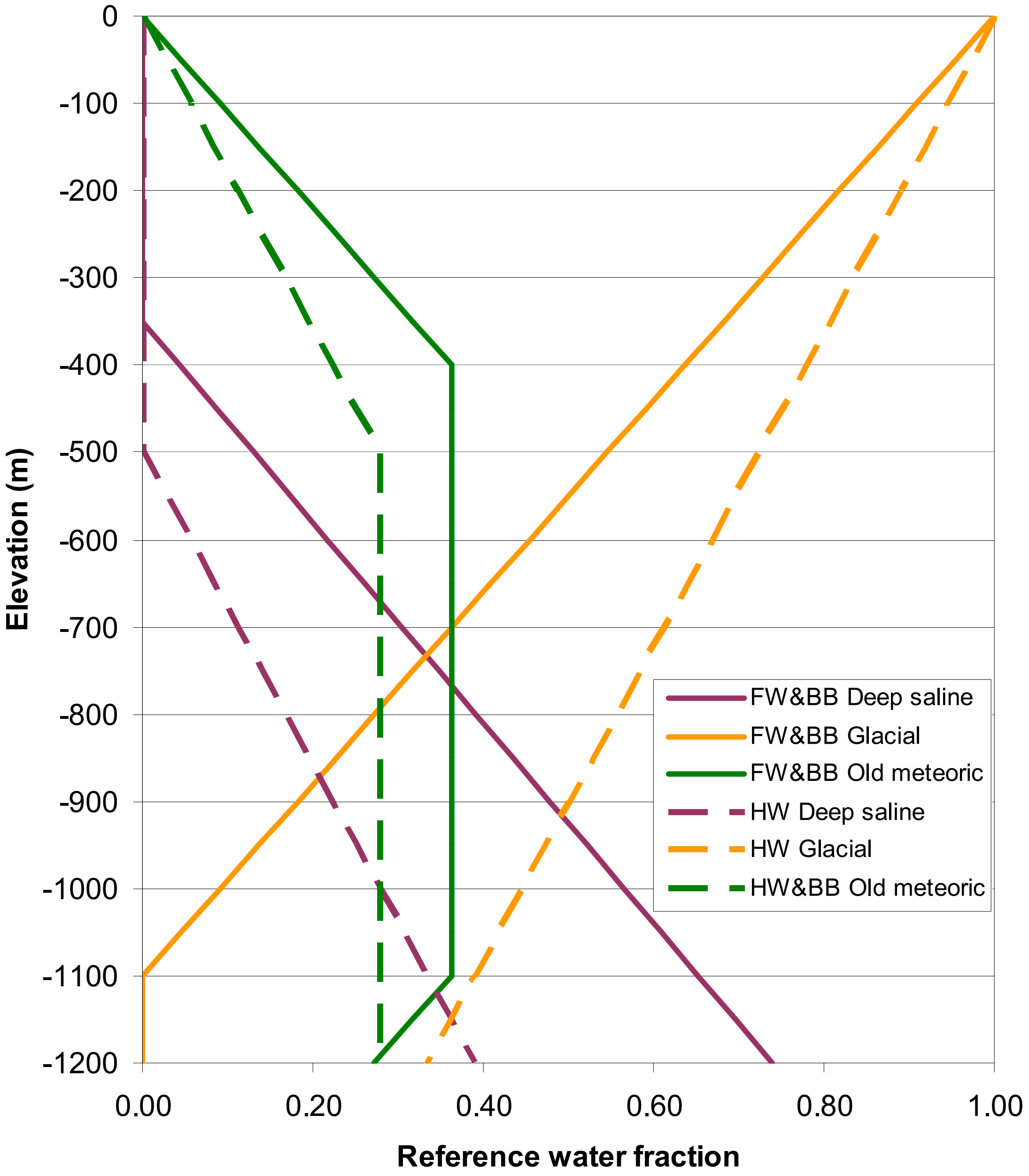

Figure 3-1.*The initial fraction of each reference water as a function of depth in the footwall and border borehole regions (FW&BB) of deformation zone A2 and the hanging wall (HW) bedrock of deformation zone A2. Figure 3-63 (Alternative Case) in Follin et al. (2007b).*

3.1.4 Solute transport

Calculations of variable density groundwater flow and solute transport are carried out for the simulation period of 8000 BC to 60,000 AD in 20 year time steps. An efficient multi-component sequential iteration method is used to transport each component individually and decouples the transport and flow calculations. For those cases involving chemical reactions, these are calculated at each time step. For reasons of efficiency, chemical reactions are only calculated at locations where the mass fraction of any component has changed by at least 2% since the last time chemical reactions were calculated at that location.

A finite volume implementation of rock matrix diffusion method is used for this study, which allows equilibration of chemical species to occur in the rock matrix. A finer discretisation of the rock matrix is used close to the fractures, becoming coarser further away.

3.2 Model cases

A number of cases are considered, as listed below. These cases explore some of the uncertainties in the geochemical reactions that may occur at the Forsmark site. Case 1 includes no chemical reactions and simply transports the chemical components. The other cases include chemical reactions with different mineral phases. Case 5 further includes a more dilute meteoric water (Dilute Meteoric water in *Table 3-1*) as compared to the other cases, infiltrating at the top boundary for land areas above sea level. Equilibrium conditions are assumed for all chemical reactions.

Case 1. No chemical reactions, i.e. the groundwater composition will be determined only by groundwater flow and transport.

Case 2. Equilibration of groundwater with calcite, quartz and amorphous iron (II) sulphide. This is the "base case" from Salas et al. (2010) for the situation with significant activity of sulphate-reducing bacteria. However, the hydroxyapatite reactions are not included as they are not deemed relevant to this work.

Case 3. Equilibration of groundwater with calcite, quartz and iron (III) oxyhydroxide. This is the "base case" from Salas et al. (2010) for the situation where the redox state is not affected by sulphate-reducing bacteria. Again, the hydroxyapatite reactions are not included.

Case 4. Equilibration of groundwater with calcite, quartz, amorphous iron (II) sulphide, kaolinite, albite, and K-feldspar. This case represents an updated understanding of the site geochemistry relative to SR-Site.

Case 5. As Case 2, but with a more dilute composition for meteoric water.

In each of the cases where chemical reactions are included the reference waters are initially equilibrated with the mineral phases and charge balanced. The equilibration reactions with these minerals are then repeated for each time step using the updated compositions from the transport calculations.

4 Results

4.1 Presentation of results

Results are presented to illustrate the evolution of the groundwater composition and chemical conditions within the proposed repository volume and in the wider regional context during an extended period of temperate climate conditions. The results are given at a number of times during the extended temperate climate period to illustrate the evolution over that period. The interval between selected times is smaller at earlier times when the site is evolving more quickly. The 2000 AD, 3000 AD, 5000 AD and 9000 AD times correspond to those selected for the SR-Site temperate period (Joyce et al. 2010). The 20,000 AD, 30,000 AD, 40,000 AD and 60,000 AD times correspond to the extended temperate climate period.

For each case, box and whisker plots show the statistical distribution of pH, Eh and total molalities (in moles per kilogram of water, mol/kg$_w$) of selected solution species sampled on a regular grid of points within the repository volume between elevations -490 m and -460 m. This grid consists of 65,237 points at a spacing of 10 m vertically. The points reside within a domain with the following corner coordinates (1630.62, 6701.17); (1633.37, 6701.17); (1633.37, 6698.9); (1630.62, 6698.9) (as used in Salas et al. 2010). The statistical measures are the median, the 25th and 75th percentiles, the mean and the 5th and 95th percentiles.

For each case, the pH, pe and mass fractions (in kilograms per kilogram of solution, kg/kg$_s$) of selected solution species at the deposition hole locations are presented visually on a representation of the repository layout by dots coloured by the magnitude of the quantity. Each dot corresponds to the centre of a deposition hole. These plots show the variation in each quantity across the repository for each selected time.

For each case, the regional evolution of the groundwater composition is visualised as a set of slices through the model coloured by pH, pe or the mass fractions (in kilograms per kilogram of solution, kg/kg$_s$) of selected solution species. Three slices are shown; a horizontal slice at repository depth and two vertical slices centred on the repository, one in the direction NW-SE and one in the direction SW-NE. In these plots the repository structures are shown to provide context, however they are not included in the model. For slices at 2000 AD, 3000 AD, 5000 AD and 9000 AD the shoreline is also included.

A consistent value range is used for each quantity presented to allow easy comparison between the cases and between the times considered.

4.2 Case 1 – No chemical reactions

Since this case involves no chemical reactions, the changes in groundwater composition over time are the result of the transport and mixing of reference waters, although this is done in terms of the individual components of the reference waters. For the temperate climate period at repository depth this is the gradual replacement of Littorina water with Altered Meteoric water. This leads to a reduction in salinity and an increase in the concentration of bicarbonate.

4.2.1 TDS and sum of cations

Figure 4-1 and Figure 4-2 show the statistical distribution of total dissolved solids (TDS) and the sum of cation charge molalities for Case 1. The plots are closely related, with the sum of cation charges plot mirroring the TDS plot. As expected, both TDS and the sum of cations decrease gradually over time, levelling out at around 20,000 AD. Below an elevation of -400 m, the rock in FFM01 is very sparsely fractured and the fracture network is poorly connected, leading to very low flows in the repository volume. Most of the flow in the repository area is above an elevation of -200 m, with horizontal flows dominating due to the presence of sub-horizontal sheet joints and gently dipping deformation zones. This depth dependence of fracture intensity and the anisotropy in the hydraulic properties of the host rock impede the penetration of groundwater from the surface to the repository. Penetration of dilute water is further hindered by buoyancy effects caused by the presence of water with higher salinity at or below repository depth. These effects limit the changes in groundwater composition caused by penetration of Altered Meteoric water beyond 20,000 AD.

At 9000 AD the 5th percentile for TDS within the repository volume is $9.86 \cdot 10^2$ mg/kg$_w$ and at 60,000 AD it is $7.01 \cdot 10^2$ mg/kg$_w$. This is consistent with the results for the simplified calculation of the penetration of dilute water presented in Figure 10-32 of SKB (2011), where 1% of deposition hole locations experience a salinity below 1 g/L at 10,000 AD and 2% of locations at 60,000 AD.

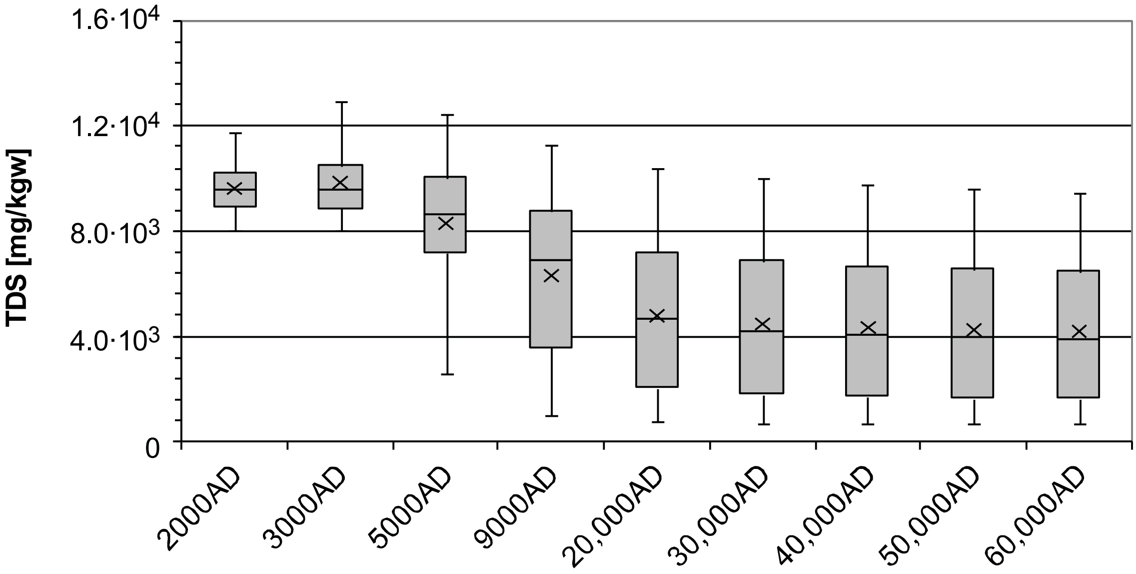

Figure 4-1. Box and whisker plot showing the statistical distribution of TDS for Case 1 on a regular grid of points within the repository volume between elevations -490 m and -460 m. The statistical measures are the median, the 25th and 75th percentiles (box), the mean (cross) and the 5th and 95th percentiles (whiskers).

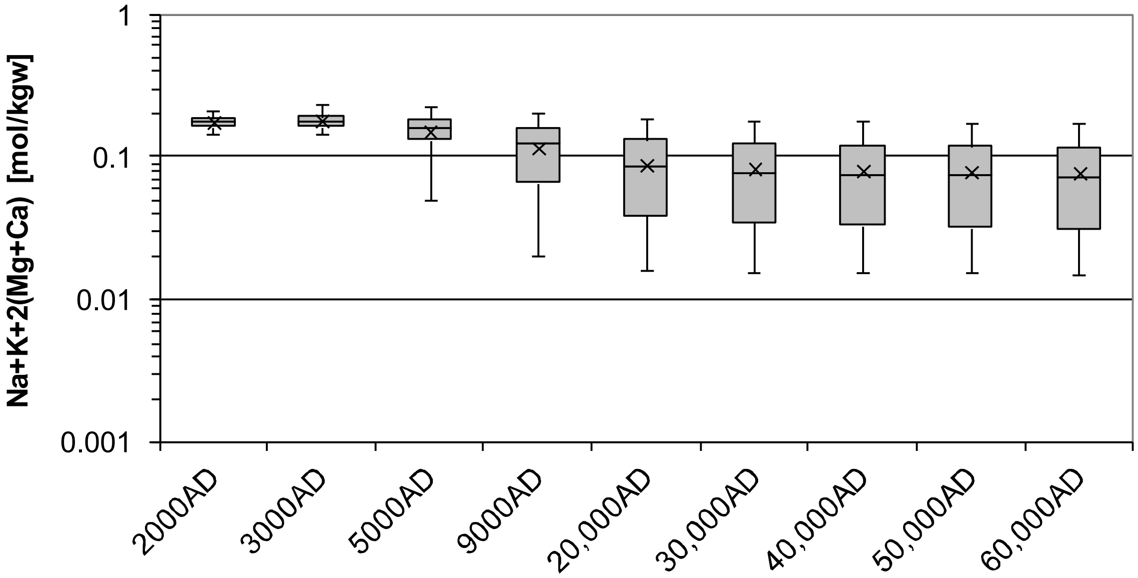

Figure 4-2. *Box and whisker plot showing the statistical distribution of the sum of cation charges (Na+K+2(Mg+Ca)) molalities for Case 1 on a regular grid of points within the repository volume between elevations -490 m and -460 m. The statistical measures are the median, the 25th and 75th percentiles (box), the mean (cross) and the 5th and 95th percentiles (whiskers).*

4.2.2 Carbon

Figure 4-3, Figure 4-4, Figure 4-5 and Figure 4-6 show the change in total inorganic carbon over time. The box and whisker plot (Figure 4-3) shows total inorganic carbon rising over time, but then levelling off. The images in Figure 4-4 and Figure 4-5 show that the infiltration of carbon varies spatially around the deposition holes due to the structural controls and heterogeneity imposed by the underlying fracture system and deformation zones. Again, there is little change after 20,000 AD. The increase in total inorganic carbon mass fractions is due to higher concentrations of bicarbonate present in the infiltrating Altered Meteoric water.

Figure 4-6 shows the evolution of total inorganic carbon over time across the model. On the horizontal slice at the level of the repository total inorganic carbon can be seen increasing in a north easterly direction over time, i.e. towards the retreating shoreline. As in the statistical and deposition hole plots the changes in the images after 20,000 AD are negligible compared to the changes seen at earlier times.

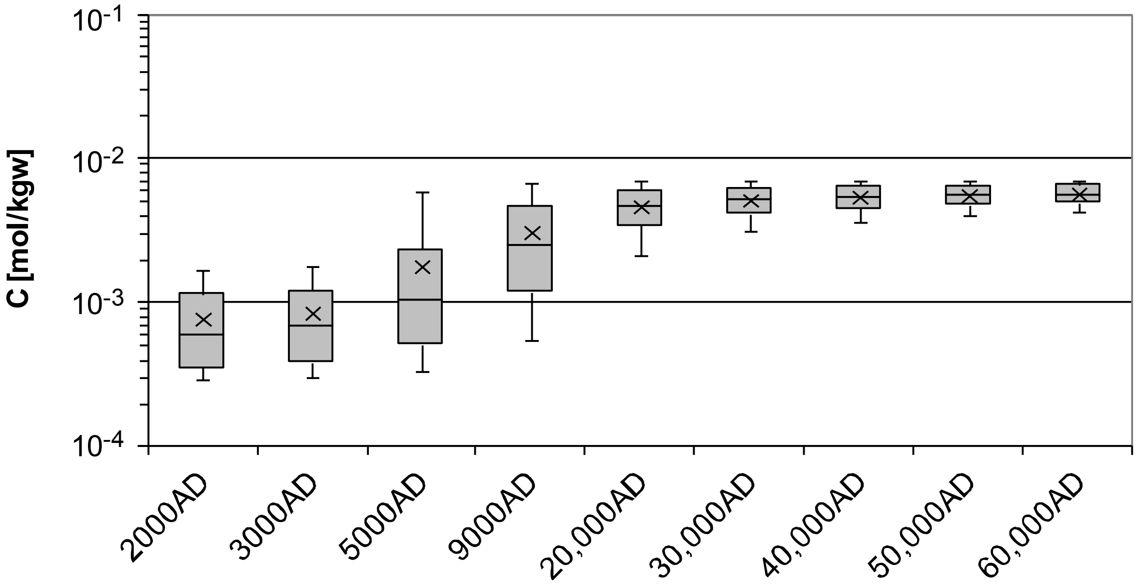

Figure 4-3. *Box and whisker plot showing the statistical distribution of total inorganic carbon molalities for Case 1 on a regular grid of points within the repository volume between elevations -490 m and -460 m. The statistical measures are the median, the 25th and 75th percentiles (box), the mean (cross) and the 5th and 95th percentiles (whiskers).*

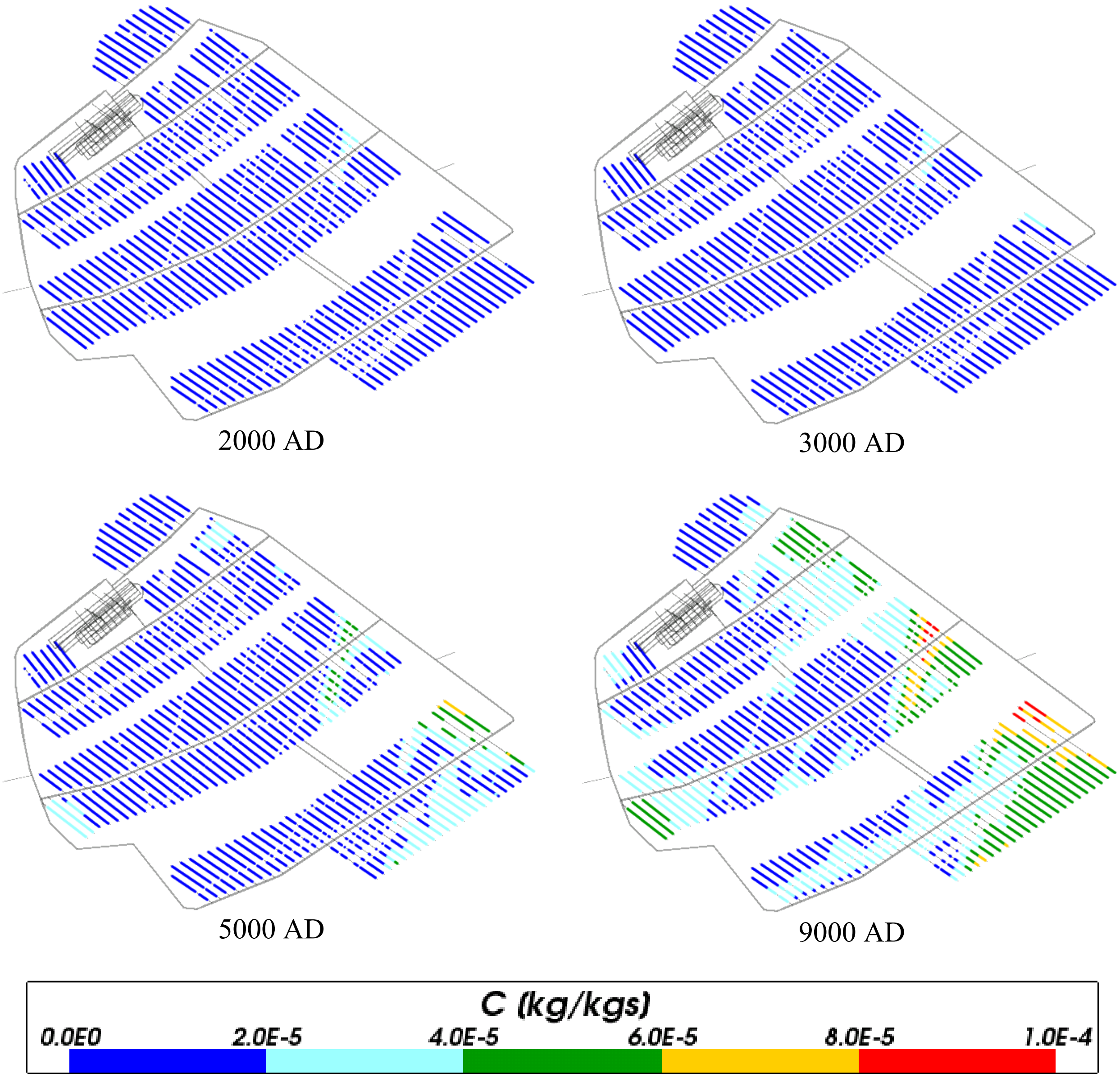

2000 AD

3000 AD

5000 AD

9000 AD

Figure 4-4. *Total inorganic carbon mass fractions for Case 1 at deposition hole locations for time periods 2000 AD to 9000 AD.*

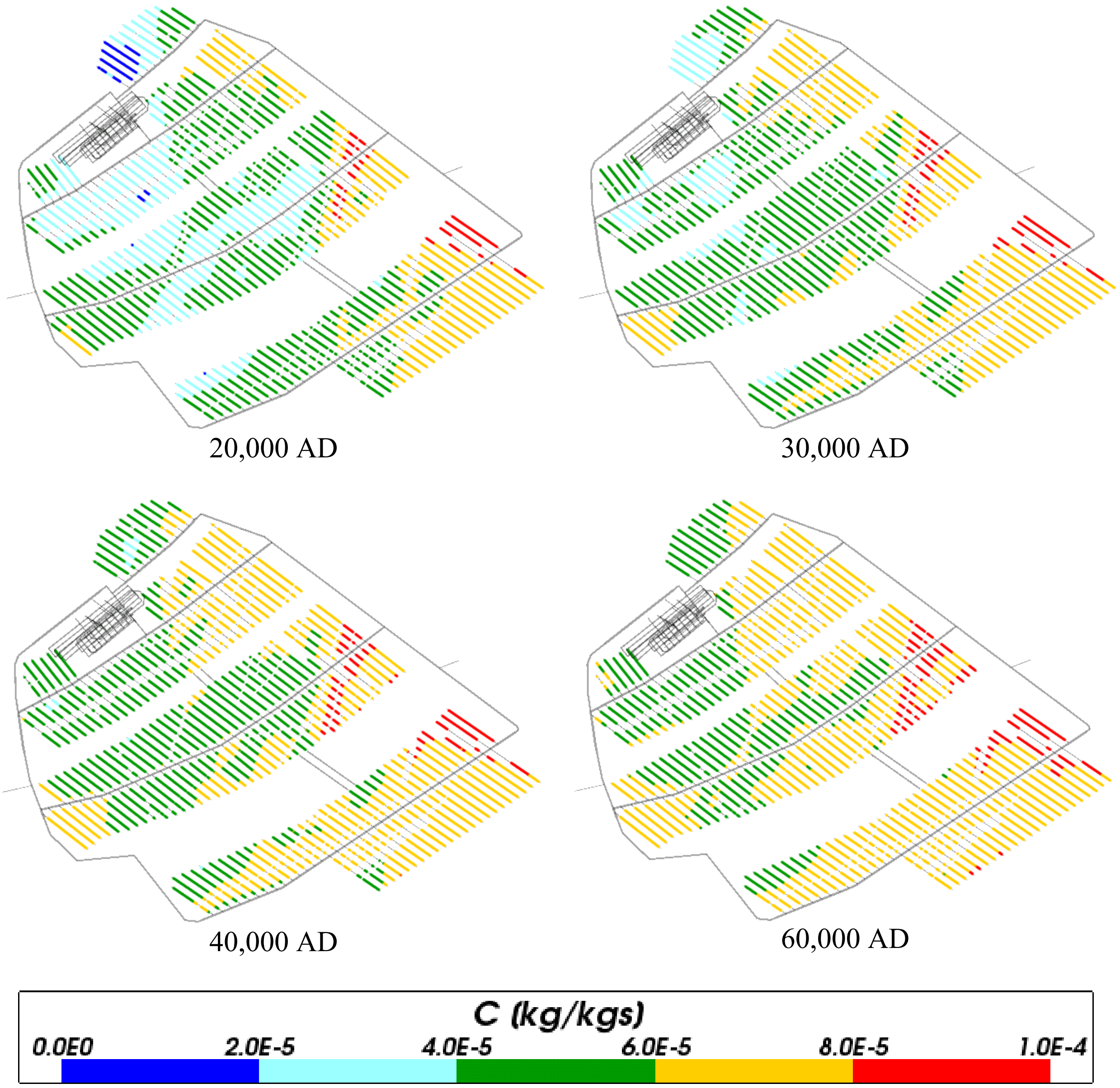

20,000 AD

30,000 AD

40,000 AD

60,000 AD

Figure 4-5. *Total inorganic carbon mass fractions for Case 1 at deposition hole locations for time periods 20,000 AD to 60,000 AD.*

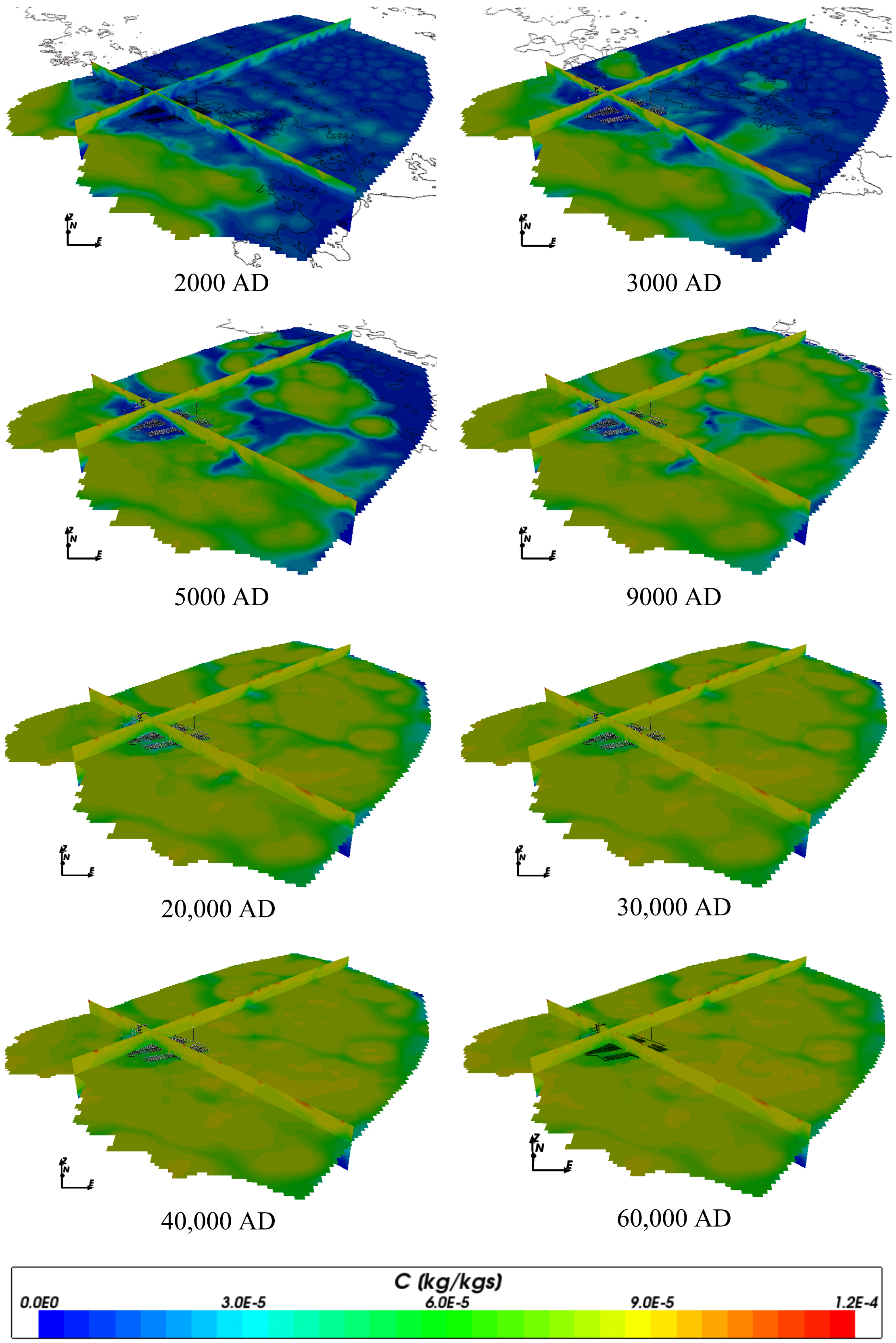

***Figure 4-6.** Total inorganic carbon mass fractions on regional scale slices through the repository volume for Case 1 for time periods 2000 AD to 60,000 AD.*

4.2.3 Calcium

Figure 4-7, Figure 4-8, Figure 4-9 and Figure 4-10 show the plots for total calcium. For this species the box and whisker plot (Figure 4-7) shows a slight decrease in calcium over time, however there is little change to the whiskers of the plot, showing that the spread of values stays reasonably constant over time. Figure 4-8 and Figure 4-9 show the change in the spatial distribution of calcium within the repository over time, with the calcium mass fractions generally decreasing, although there is a brief increase in one area at 3000 AD. There is little change in the spatial distribution of calcium with time at later times. The decrease in calcium mass fractions with time is due to the lower concentration of calcium in the infiltrating Altered Meteoric water compared to the Littorina water it is replacing.

The regional evolution of calcium is shown in Figure 4-10. As with carbon, there is evidence that a north easterly flow is influencing the amount of calcium at small times, with the amount of calcium decreasing with time. At times above 20,000 AD the majority of the regional area is low in calcium, with occasional high spots around the edges of the model. Higher values of calcium are also seen at depth (associated with Deep Saline water), as seen in the vertical slices.

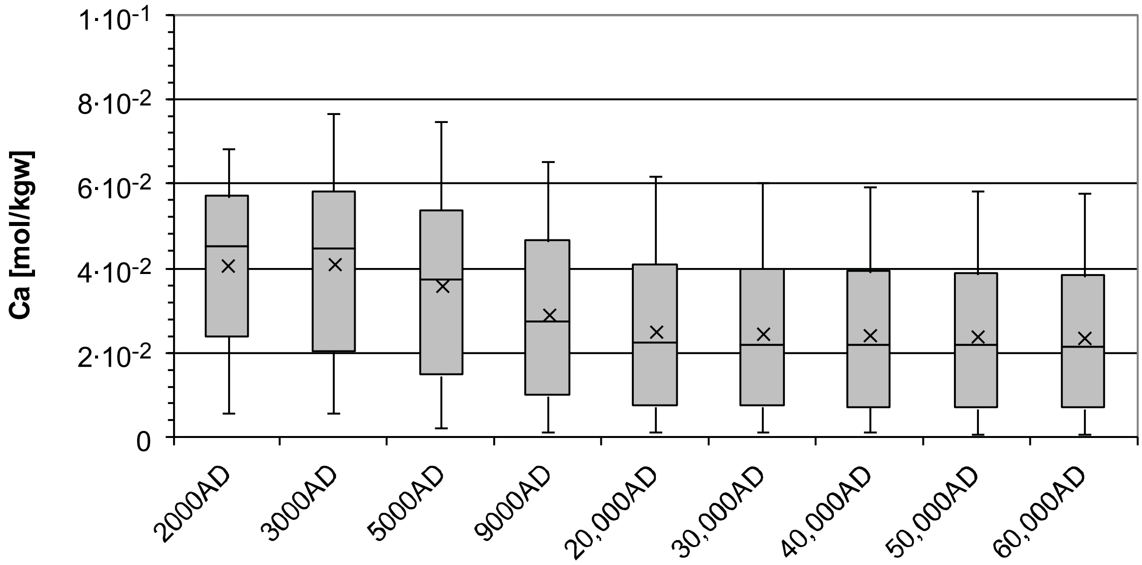

Figure 4-7. *Box and whisker plot showing the statistical distribution of total calcium molalities for Case 1 on a regular grid of points within the repository volume between elevations -490 m and -460 m. The statistical measures are the median, the 25th and 75th percentiles (box), the mean (cross) and the 5th and 95th percentiles (whiskers).*

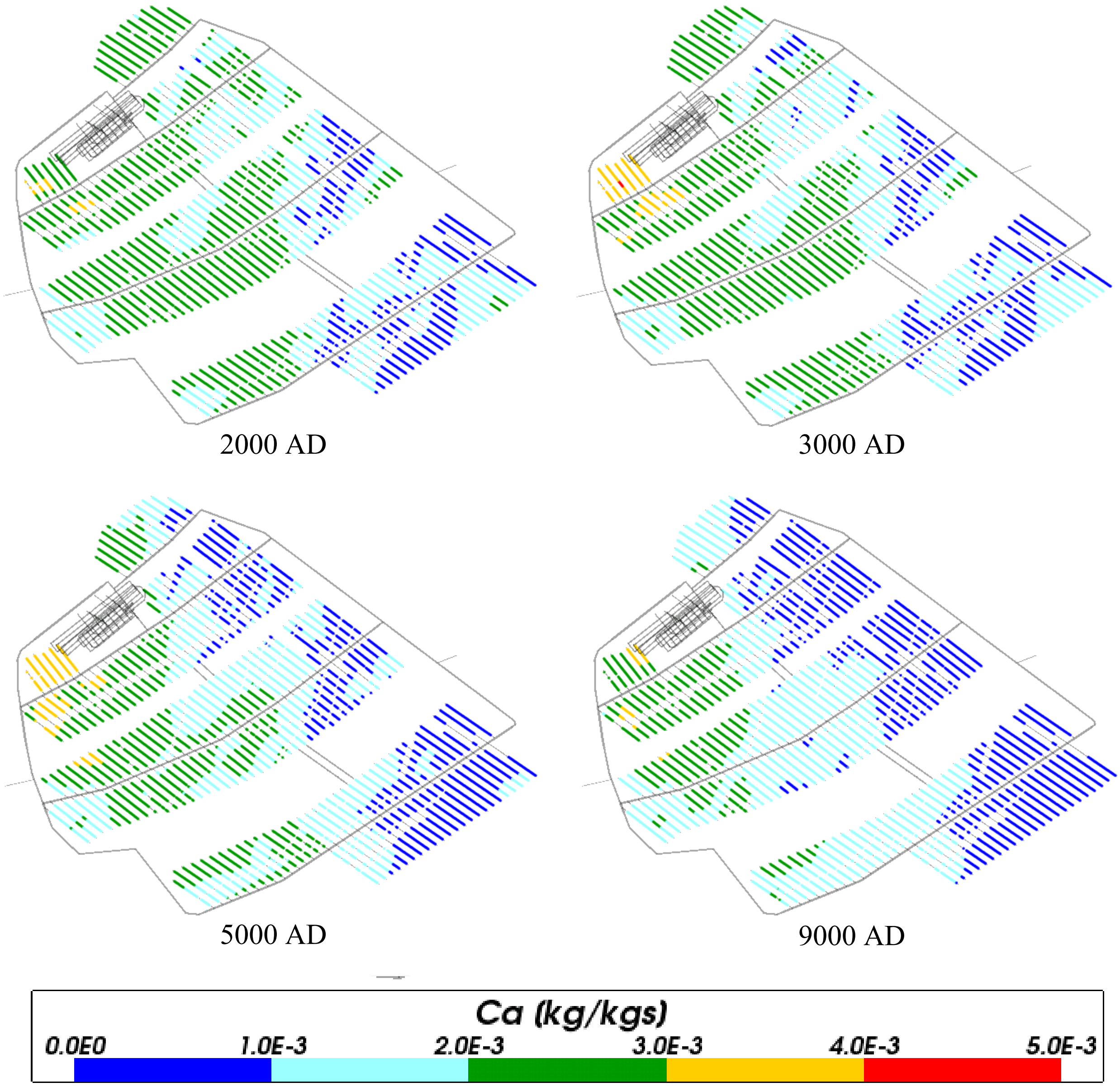

2000 AD

3000 AD

5000 AD

9000 AD

Figure 4-8. *Total calcium mass fractions for Case 1 at deposition hole locations for time periods 2000 AD to 9000 AD.*

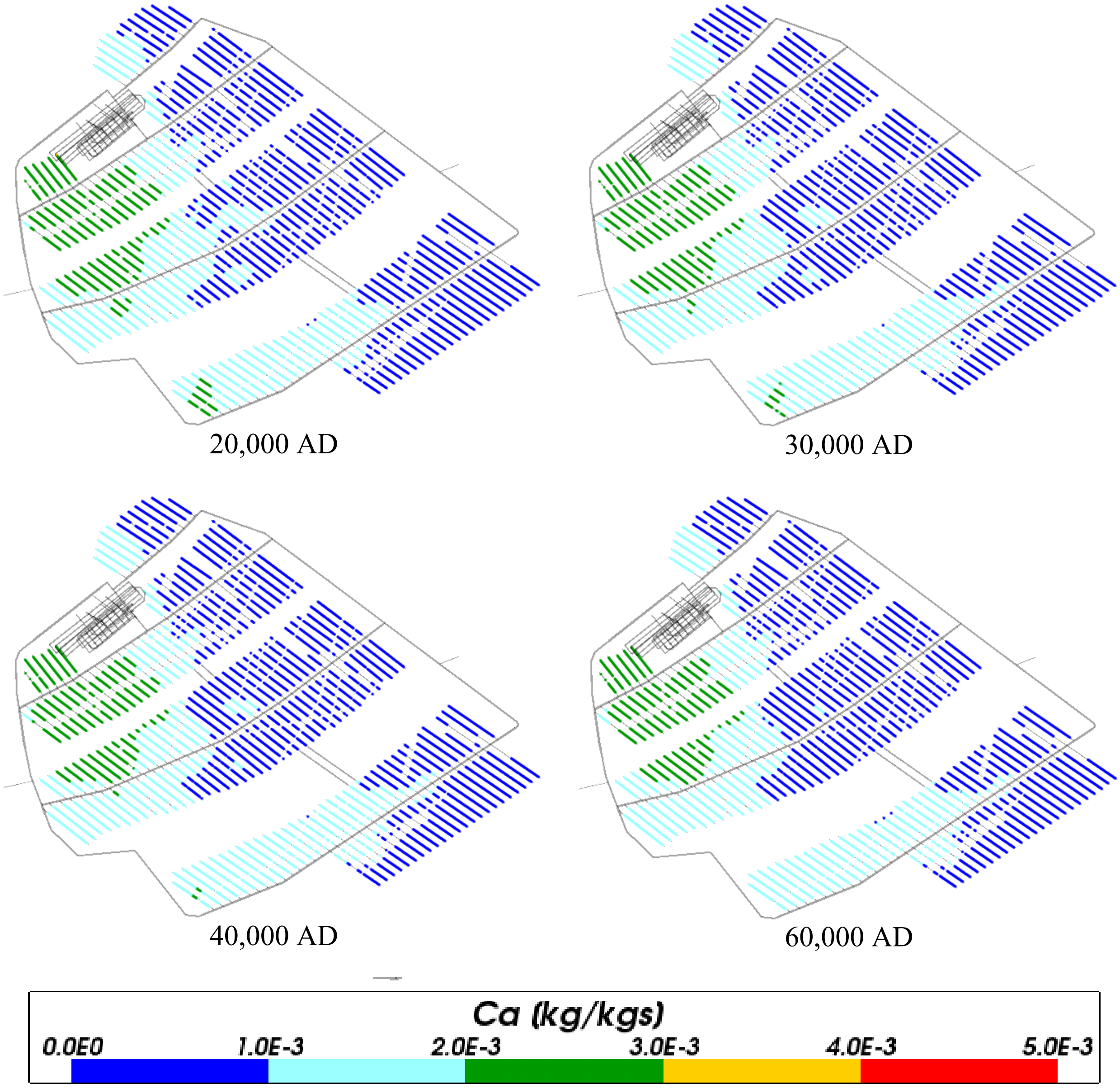

20,000 AD

30,000 AD

40,000 AD

60,000 AD

Figure 4-9. *Total calcium mass fractions for Case 1 at deposition hole locations for time periods 20,000 AD to 60,000 AD.*

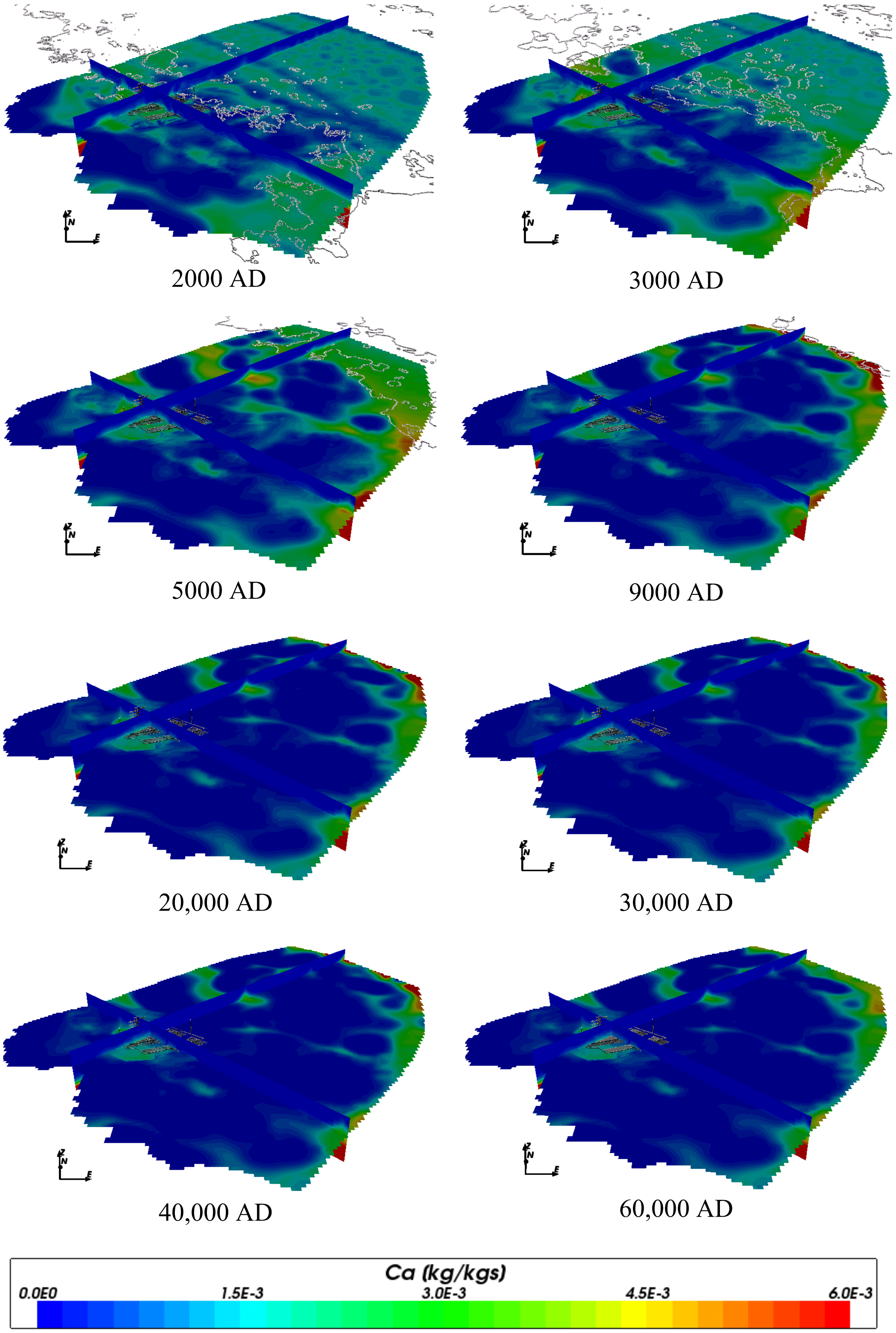

2000 AD

3000 AD

5000 AD

9000 AD

20,000 AD

30,000 AD

40,000 AD

60,000 AD

Figure 4-10. *Total calcium mass fractions on regional scale slices through the repository volume for Case 1 for time periods 20,000 AD to 60,000 AD.*

4.2.4 Chloride

The change in chloride levels over time is shown in Figure 4-11 to Figure 4-14. The box and whisker plot demonstrates that the amount of chloride decreases over time, again levelling off at approximately 20,000 AD. This is confirmed by the deposition hole colour changes seen in Figure 4-12 and Figure 4-13.

The regional evolution of chloride over the time period modelled (Figure 4-14) is similar to that of calcium, with the value of chloride decreasing over time and responding to a north easterly flow.

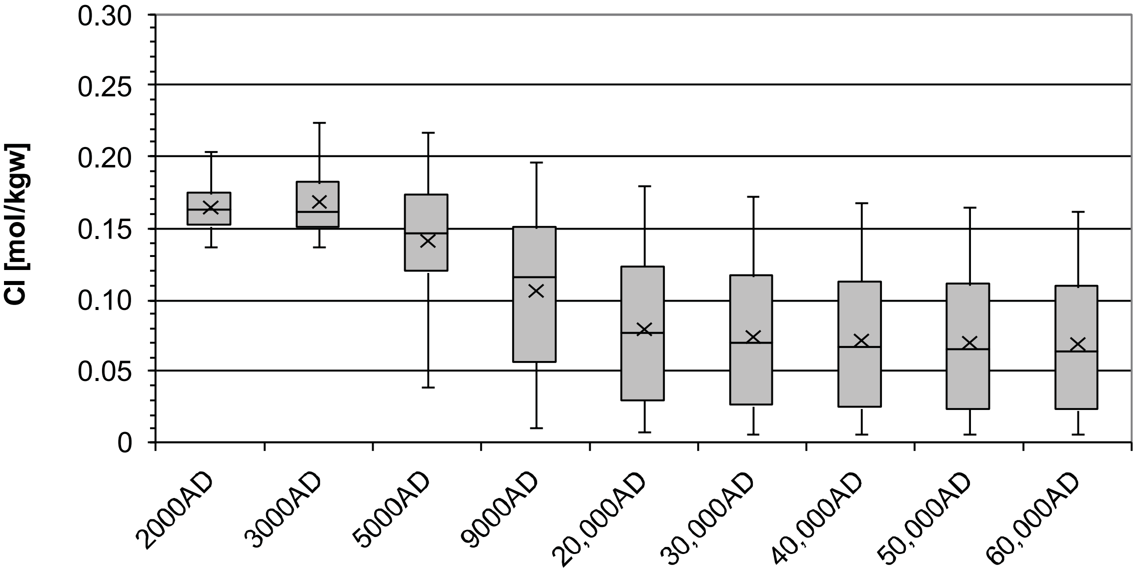

Figure 4-11. *Box and whisker plot showing the statistical distribution of total chloride molalities for Case 1 on a regular grid of points within the repository volume between elevations -490 m and -460 m. The statistical measures are the median, the 25th and 75th percentiles (box), the mean (cross) and the 5th and 95th percentiles (whiskers).*

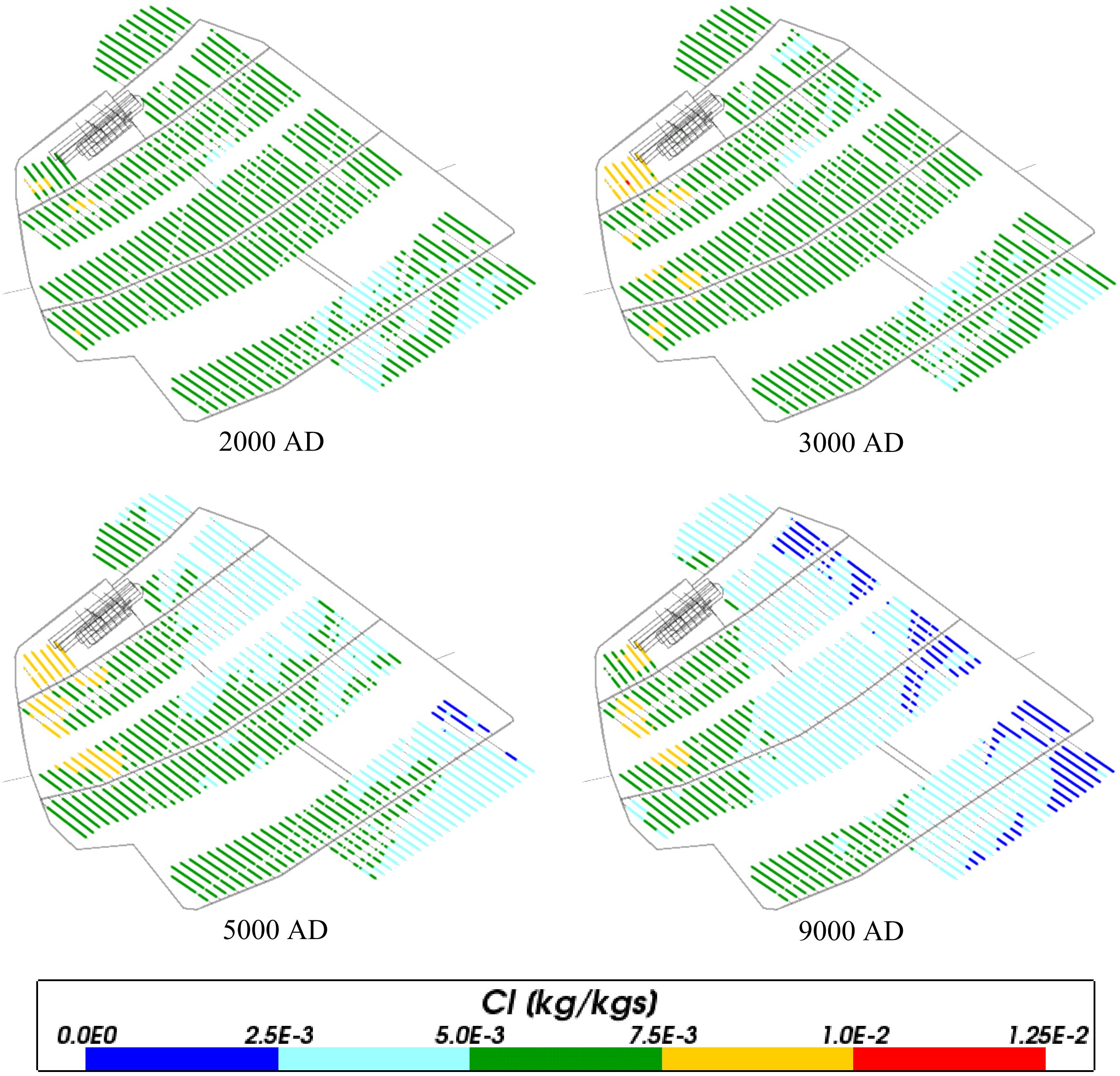
2000 AD
3000 AD
5000 AD
9000 AD

Figure 4-12. Total chloride mass fractions for Case 1 at deposition hole locations for time periods 2000 AD to 9000 AD.

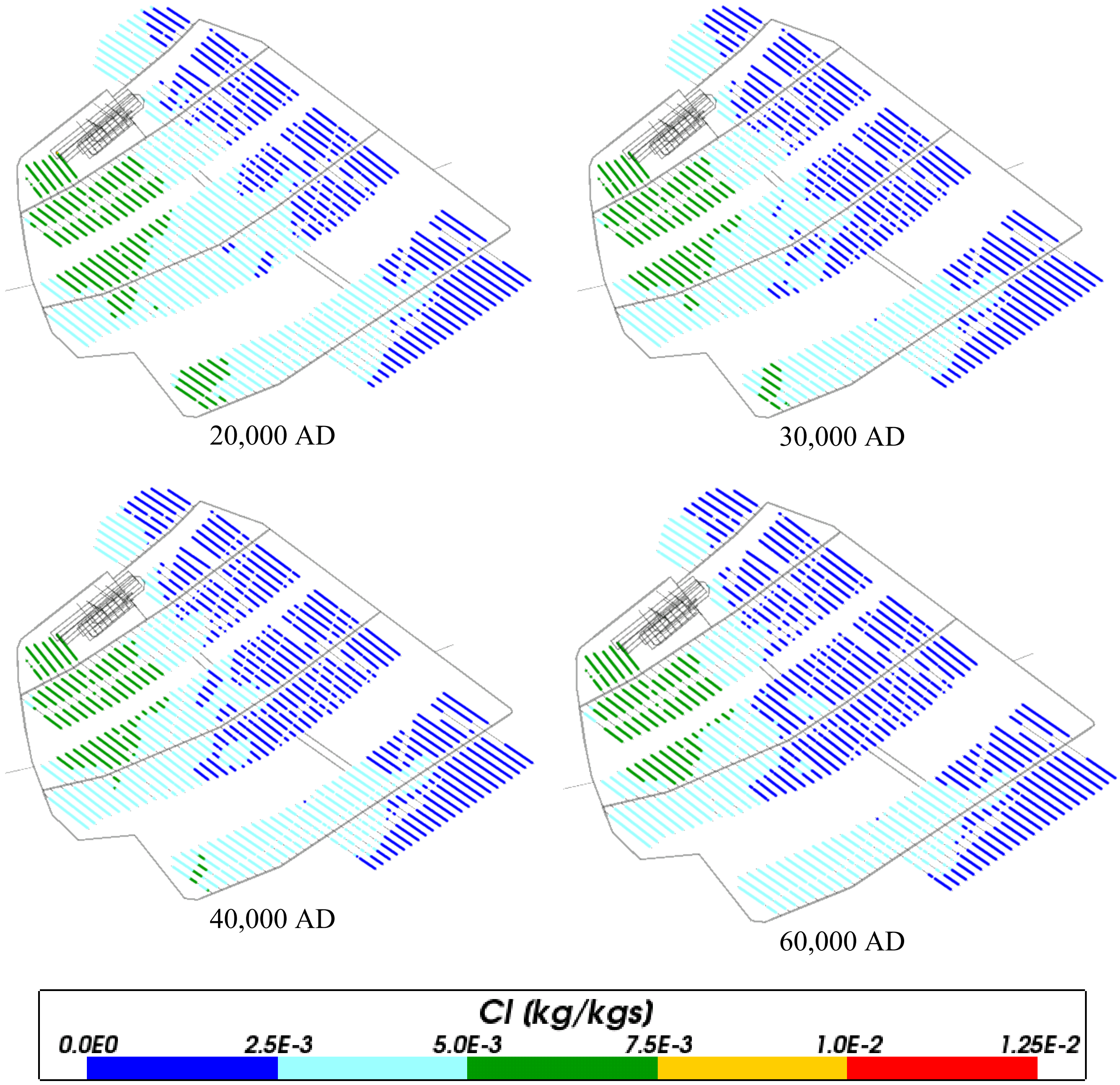

Figure 4-13. *Total chloride mass fractions for Case 1 at deposition hole locations for time periods 20,000 AD to 60,000 AD.*

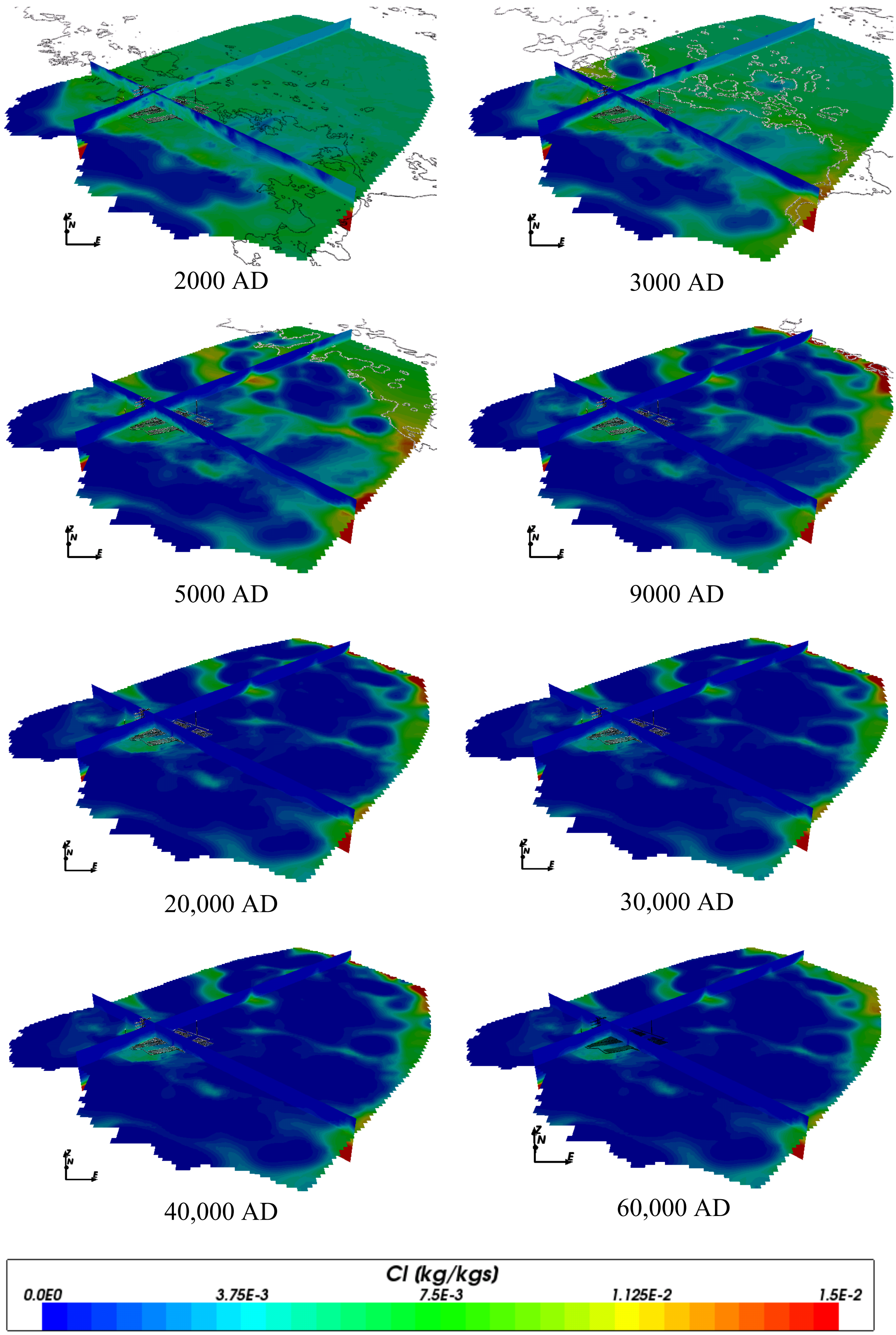

2000 AD

3000 AD

5000 AD

9000 AD

20,000 AD

30,000 AD

40,000 AD

60,000 AD

Figure 4-14. *Total chloride mass fractions on regional scale slices through the repository volume for Case 1 for time periods 2000 AD to 60,000 AD.*

4.2.5 Iron

The range for Figure 4-15, the box and whisker plot for the concentration of iron in the repository area, has been chosen to be consistent with the range used in the other cases. As iron remains comparatively low in Case 1, where no chemical calculations are completed, little change over time is seen. Similarly Figure 4-16 and Figure 4-17 show no variation in colouring around the deposition holes across the time periods, as any change in iron for Case 1 is insignificant compared to other cases.

As with the other plots, the concentration of iron across the model region (Figure 4-18) is low compared to the concentration of iron seen in other cases, so any change over time not apparent.

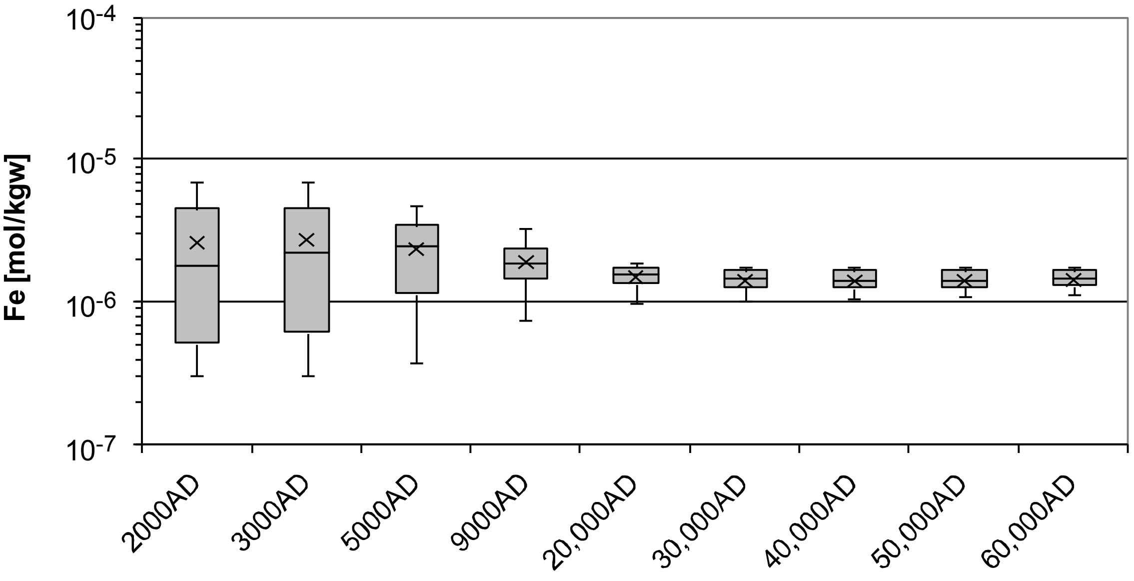

Figure 4-15. Box and whisker plot showing the statistical distribution of total iron molalities for Case 1 on a regular grid of points within the repository volume between elevations -490 m and -460 m. The statistical measures are the median, the 25th and 75th percentiles (box), the mean (cross) and the 5th and 95th percentiles (whiskers).

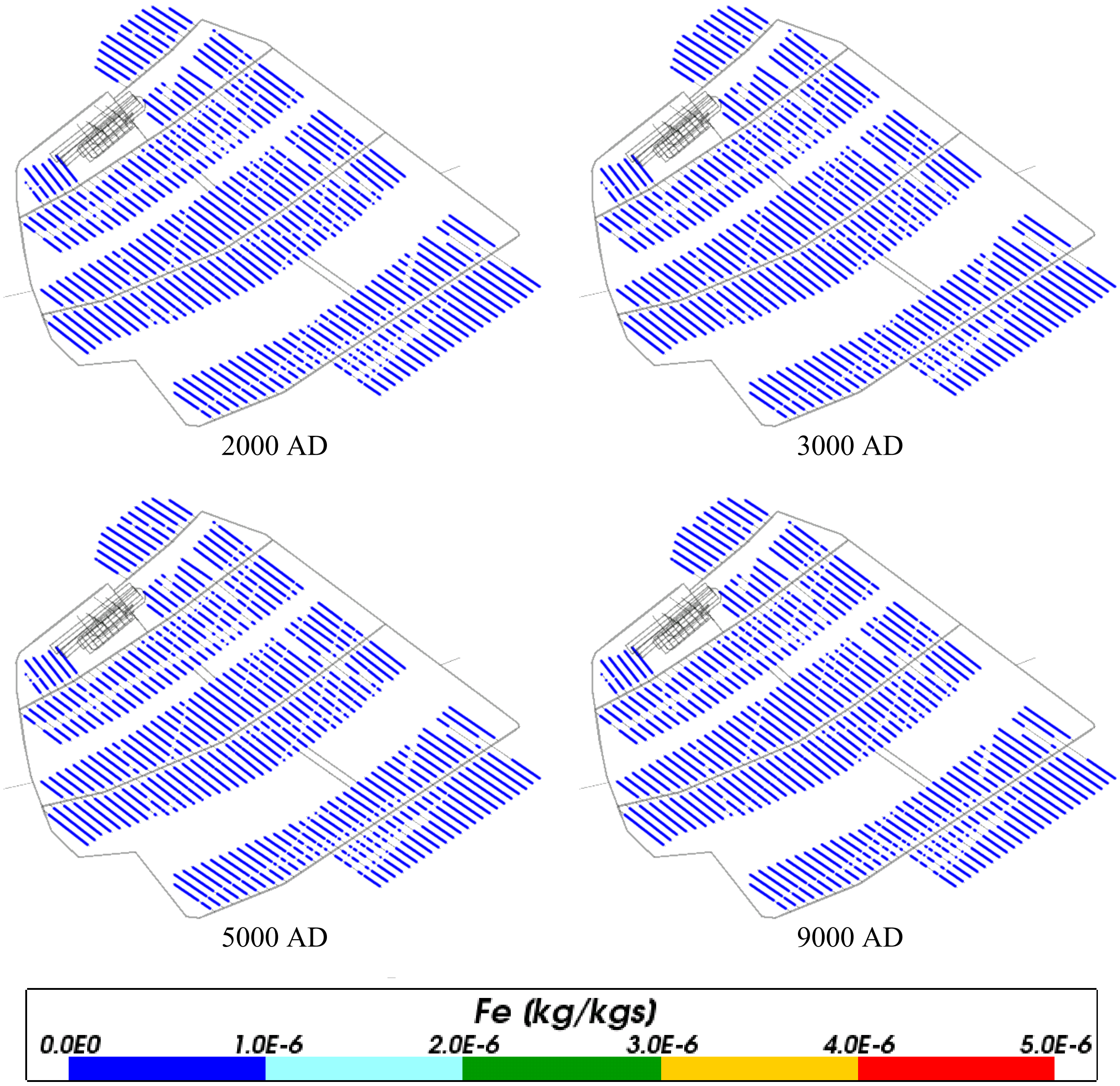

Figure 4-16. *Total iron mass fractions for Case 1 at deposition hole locations for time periods 2000 AD to 9000 AD.*

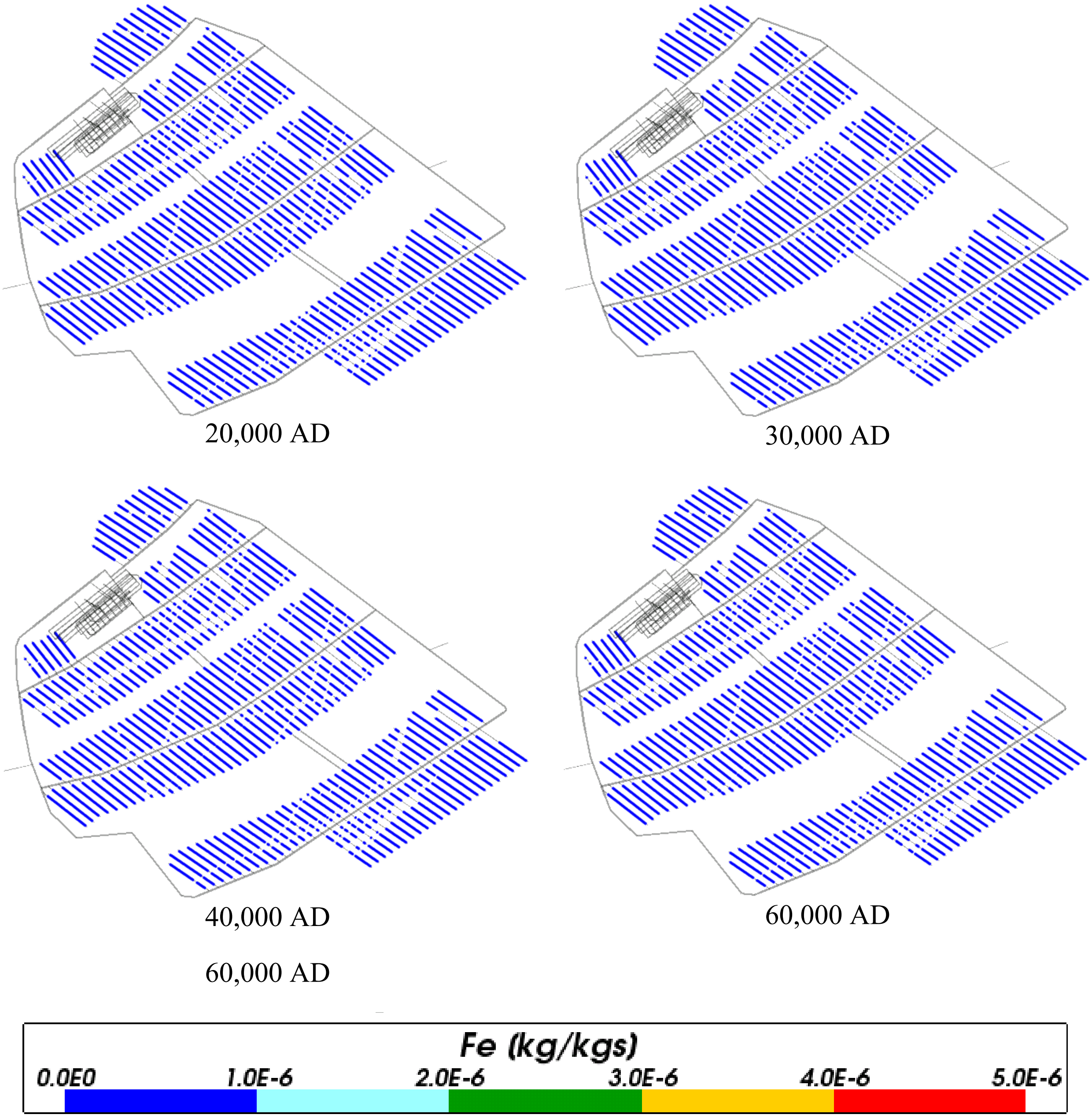

20,000 AD

30,000 AD

40,000 AD

60,000 AD

60,000 AD

Figure 4-17. *Total iron mass fractions for Case 1 at deposition hole locations for time periods 20,000 AD to 60,000 AD.*

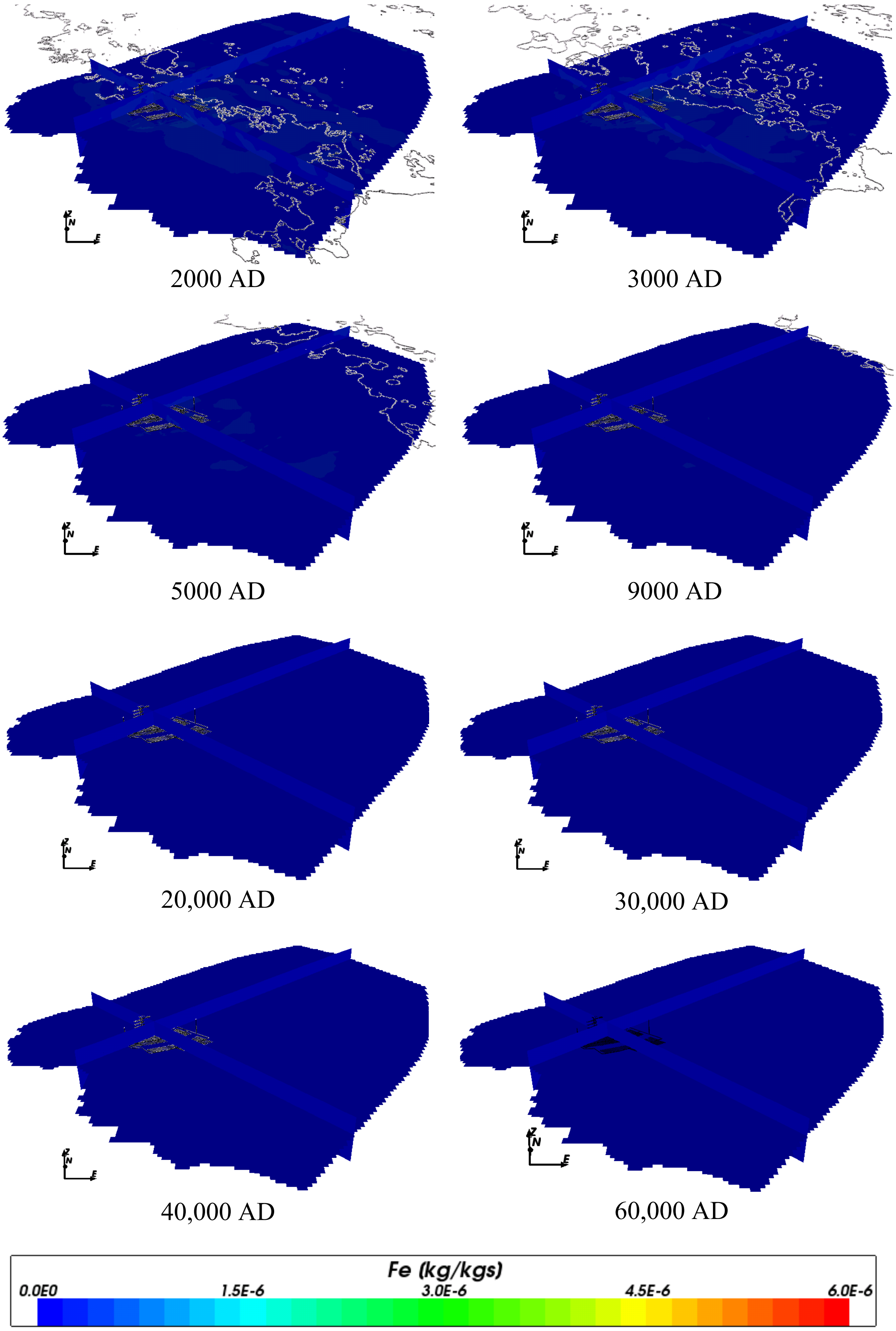

Figure 4-18. *Total iron mass fractions on regional scale slices through the repository volume for Case 1 for time periods 2000 AD to 60,000 AD.*

4.2.6 Sodium

The changes in sodium over time are shown in Figure 4-19 to Figure 4-22. The box and whisker plot shows the level of sodium decreasing over time, but levelling off at 20,000 AD with little change following. This trend is also followed in the deposition hole plots in Figure 4-20 and Figure 4-21.

At 2000 AD the concentration of sodium is relatively high across the model (Figure 4-22) due to the presence of Littorina water, but is gradually reduced due to the infiltration of less saline Altered Meteroic water, with the bulk of the area having low sodium values from 20,000 AD onwards.

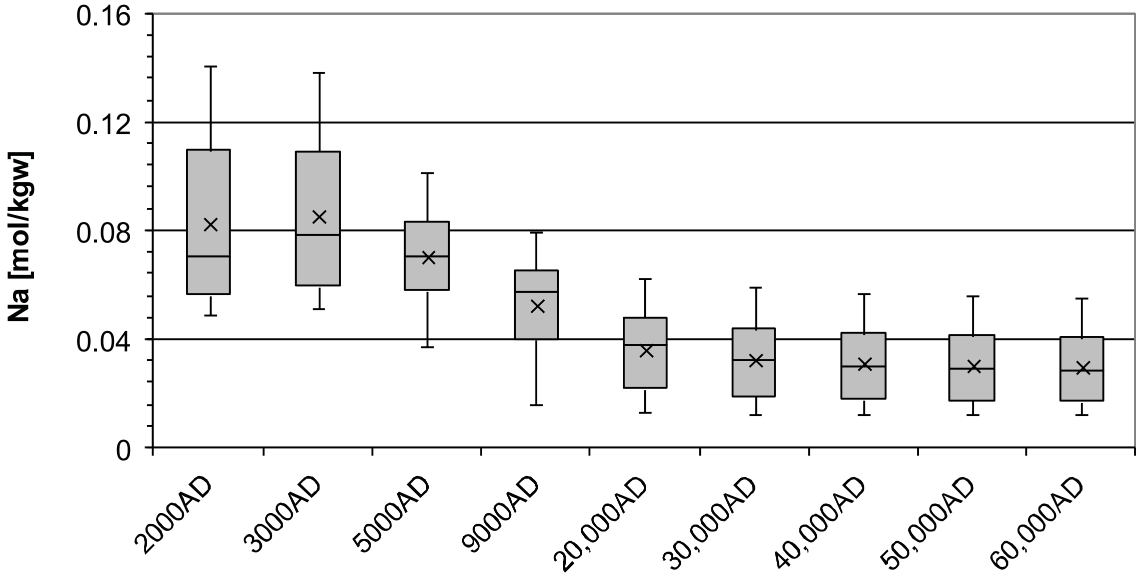

Figure 4-19. *Box and whisker plot showing the statistical distribution of total sodium molalities for Case 1 on a regular grid of points within the repository volume between elevations -490 m and -460 m. The statistical measures are the median, the 25th and 75th percentiles (box), the mean (cross) and the 5th and 95th percentiles (whiskers).*

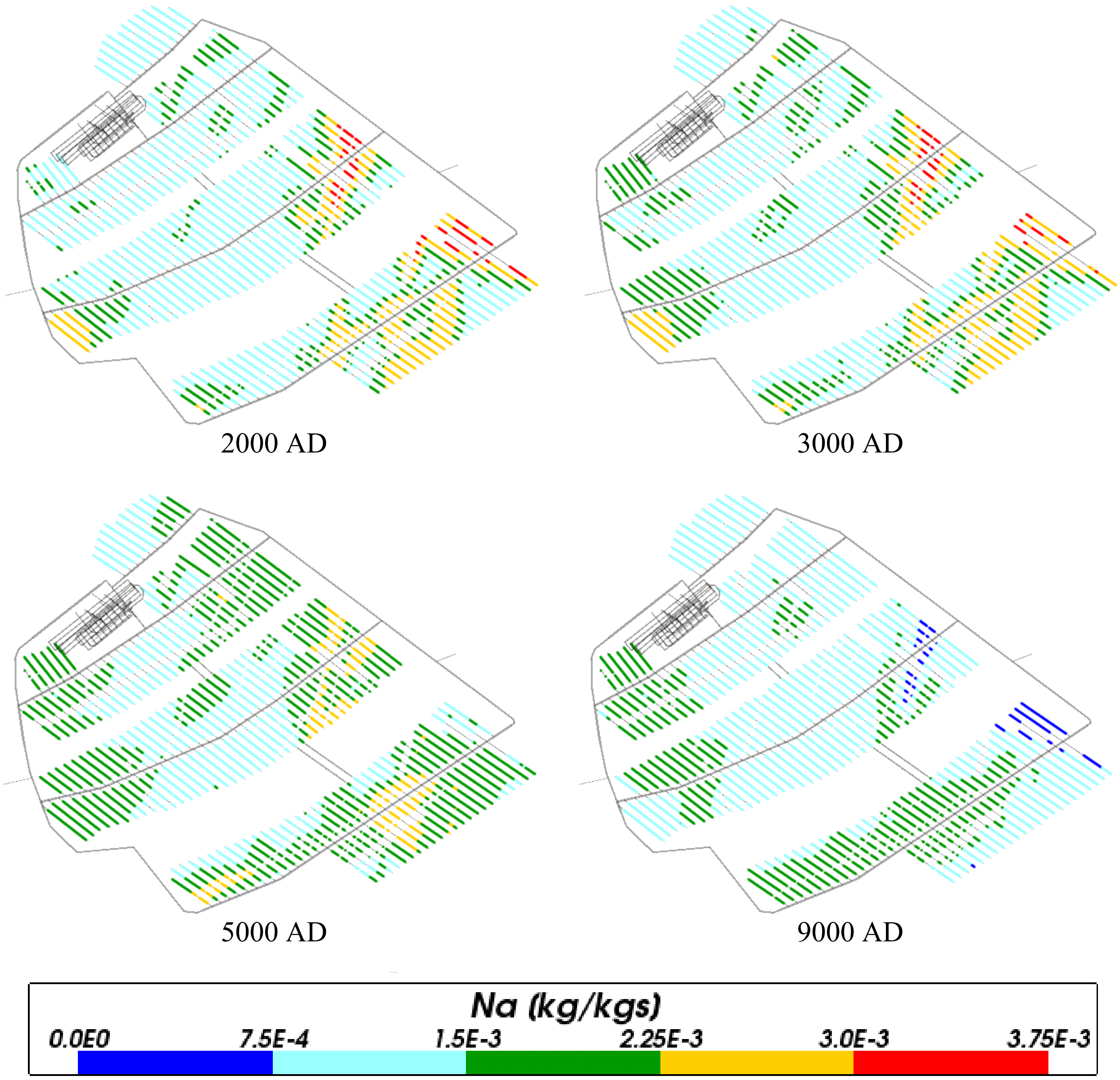
2000 AD
3000 AD
5000 AD
9000 AD

Figure 4-20. *Total sodium mass fractions for Case 1 at deposition hole locations for time periods 2000 AD to 9000 AD.*

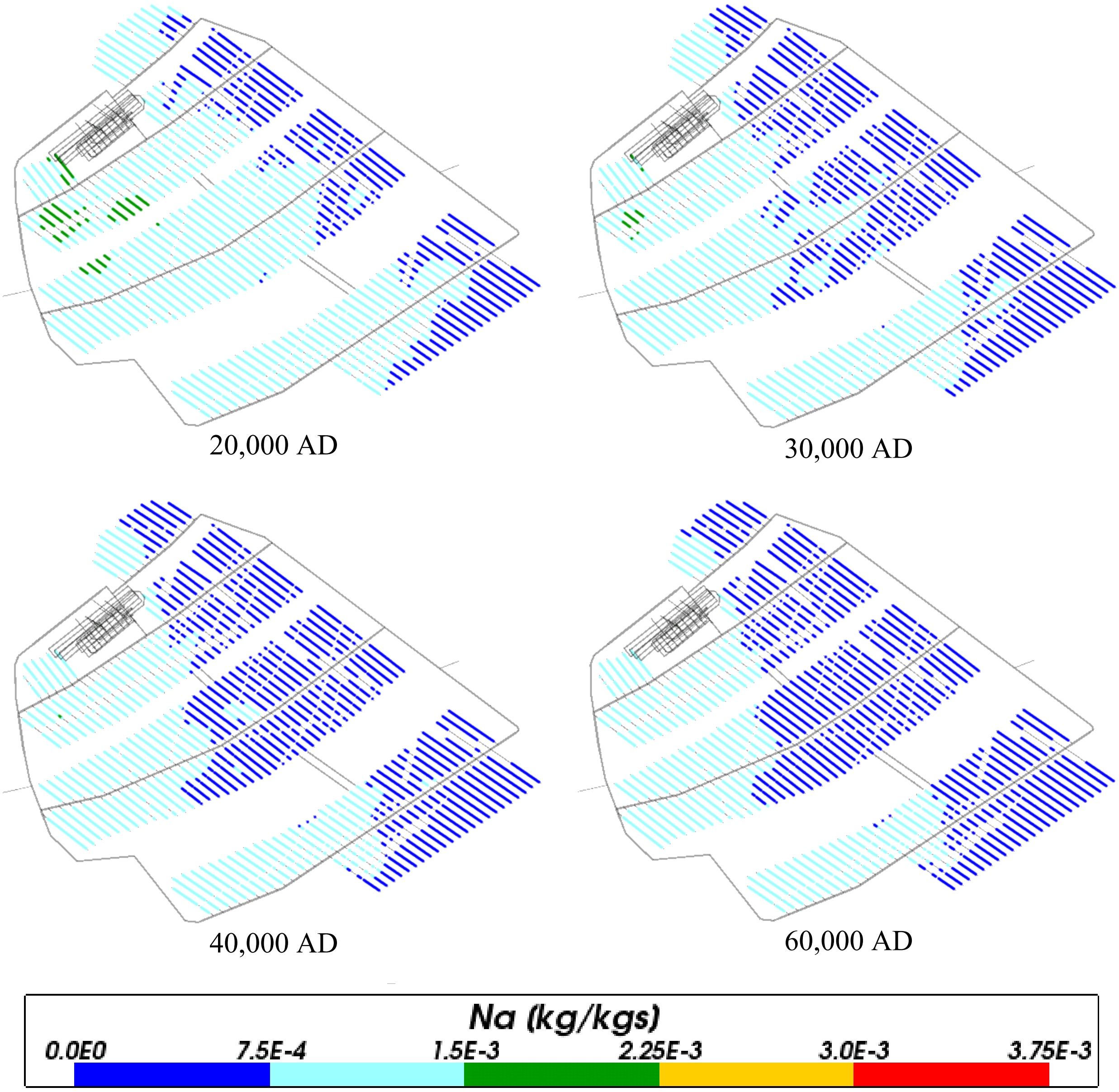

Figure 4-21. *Total sodium mass fractions for Case 1 at deposition hole locations for time periods 20,000 AD to 60,000 AD.*

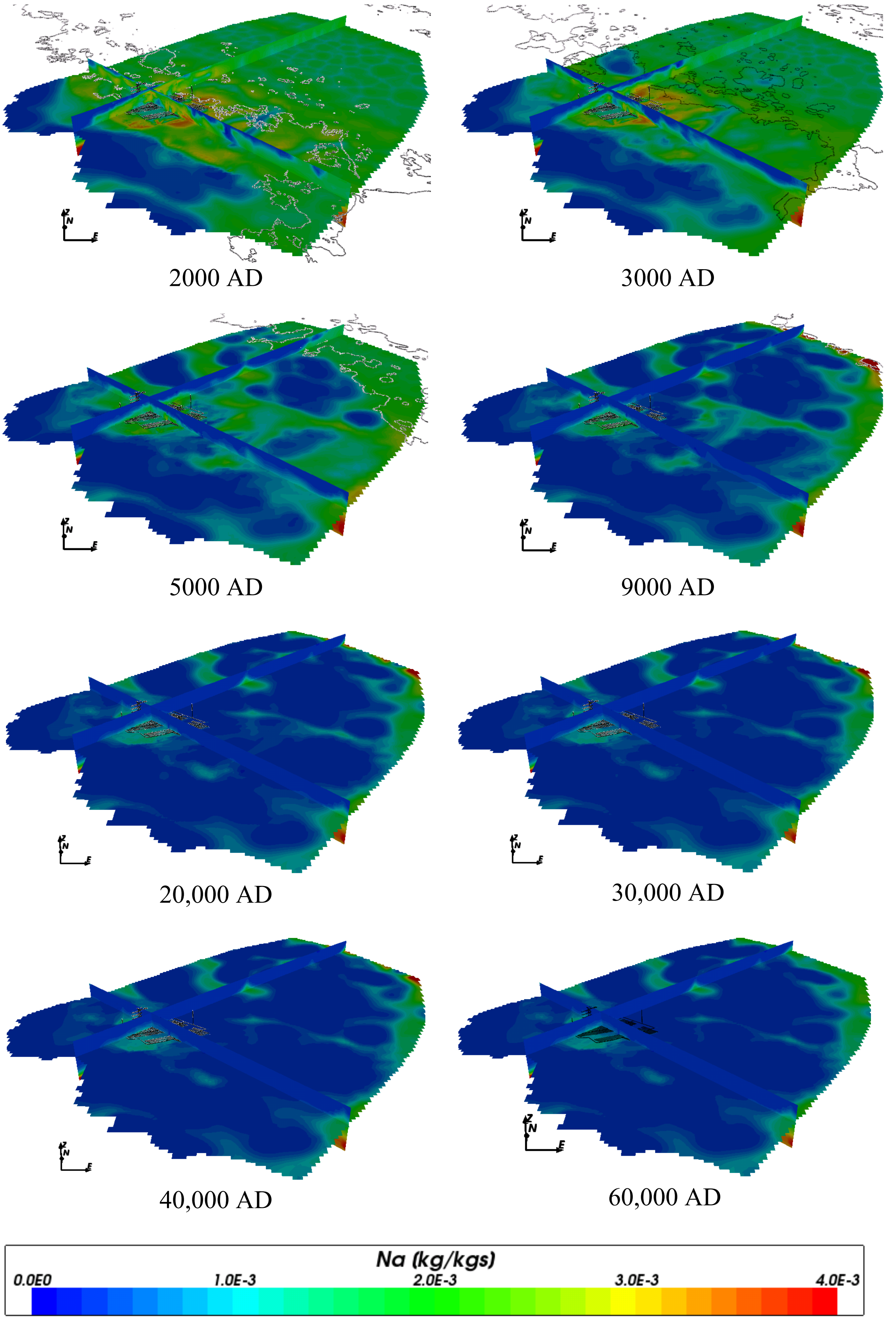

2000 AD

3000 AD

5000 AD

9000 AD

20,000 AD

30,000 AD

40,000 AD

60,000 AD

Figure 4-22. *Total sodium mass fractions on regional scale slices through the repository volume for Case 1 for time periods 2000 AD to 60,000 AD.*

4.2.7 Sulphur

The box and whisker plot for total sulphur (Figure 4-23) shows the amount of sulphur decreasing over time, with the spread of values also decreasing, as seen by the decreasing size of the whiskers. Figure 4-24 and Figure 4-25 show that the main changes in concentrations around the deposition holes are between 2000 AD and 9000 AD, with the concentration of total sulphur being low and unchanging for later times.

Figure 4-26 shows that sulphur behaves in a similar way to sodium, starting reasonably high across the model and dropping to a low value at later times. For sulphur however, the north easterly flow seen for other chemical species is less evident.

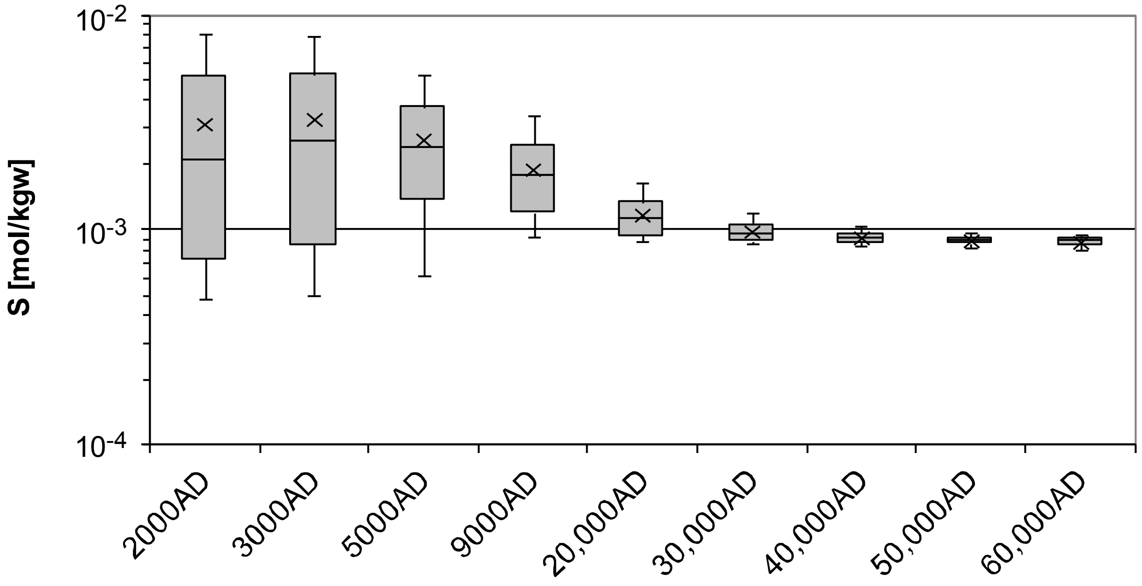

Figure 4-23. *Box and whisker plot showing the statistical distribution of total sulphur molalities for Case 1 on a regular grid of points within the repository volume between elevations -490 m and -460 m. The statistical measures are the median, the 25th and 75th percentiles (box), the mean (cross) and the 5th and 95th percentiles (whiskers).*

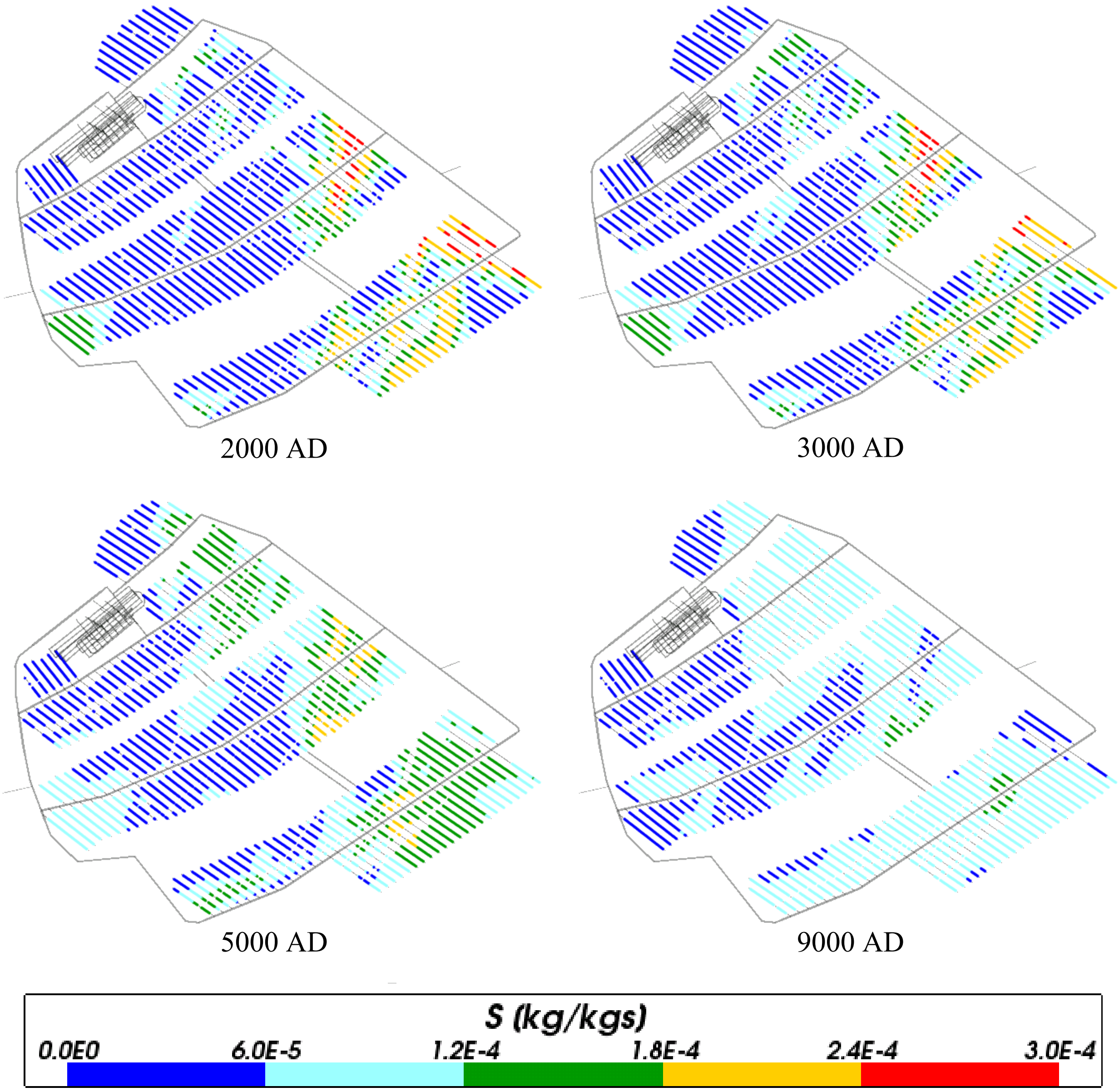

Figure 4-24. *Total sulphur mass fractions for Case 1 at deposition hole locations for time periods 2000 AD to 9000 AD.*

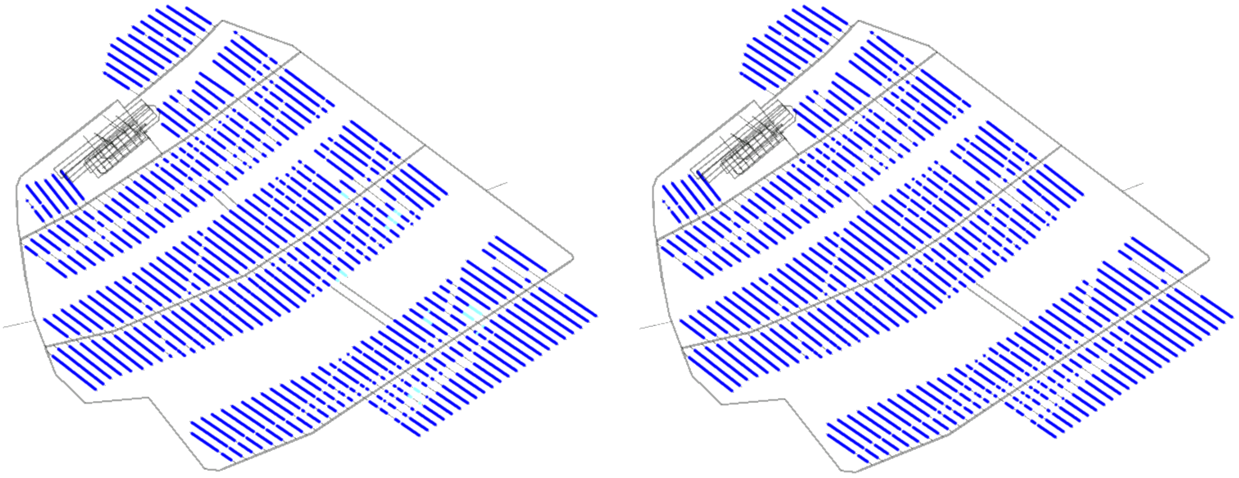

20,000 AD

30,000 AD

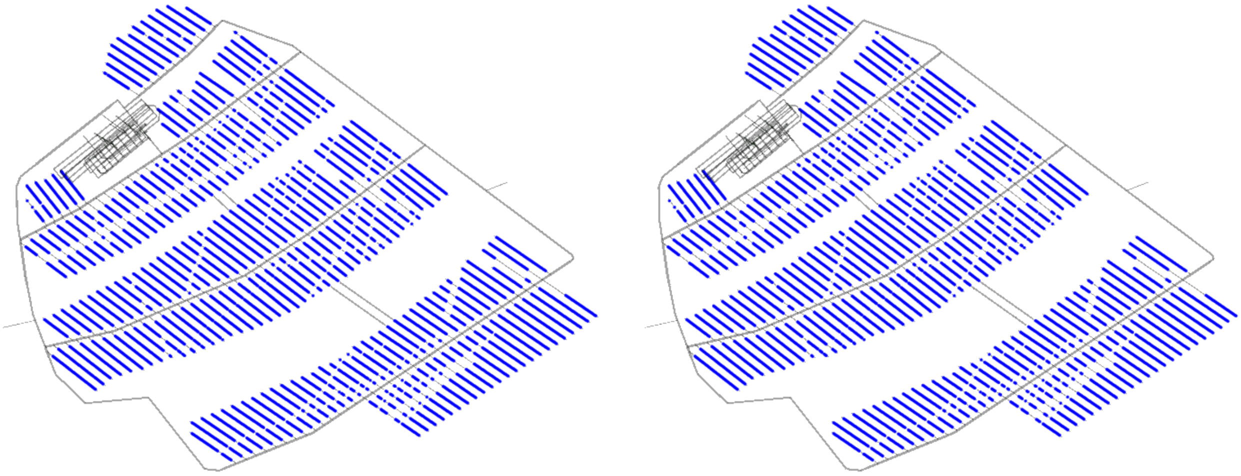

40,000 AD

60,000 AD

Figure 4-25. *Total sulphur mass fractions for Case 1 at deposition hole locations for time periods 20,000 AD to 60,000 AD.*

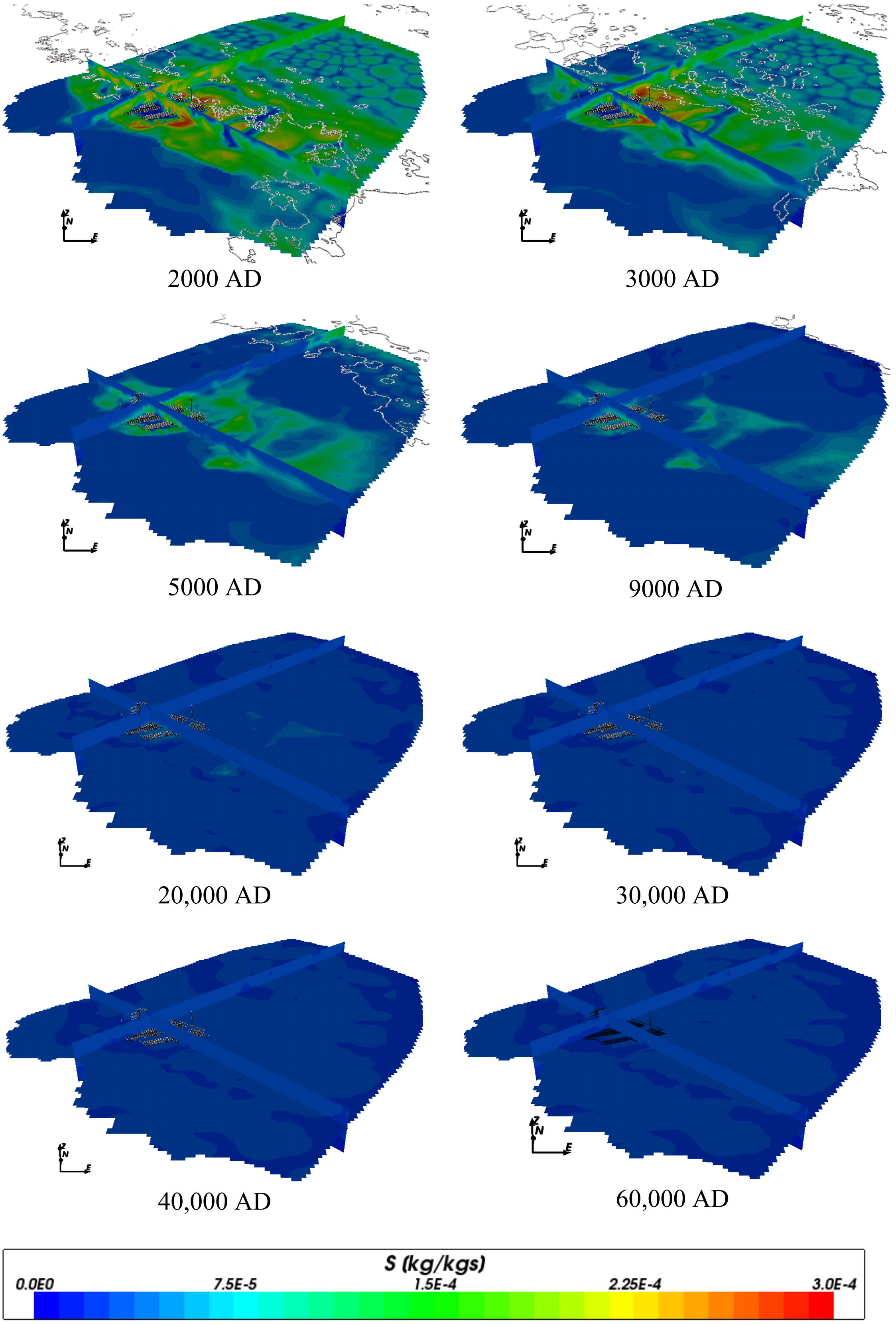

2000 AD

3000 AD

5000 AD

9000 AD

20,000 AD

30,000 AD

40,000 AD

60,000 AD

Figure 4-26. *Total sulphur mass fractions on regional scale slices through the repository volume for Case 1 for time periods 2000 AD to 60,000 AD.*

4.3 Case 2

The evolution of groundwater composition for this case will be due to the transport and mixing of components originating from different reference waters. However, the concentrations of reactive species will be modified by the chemical reactions considered for this case, which include equilibration of groundwater with calcite, quartz and amorphous iron (II) sulphide. It is expected that the reactions will have an effect on pH, Eh, and the concentrations of total inorganic carbon, calcium, sulphur and iron.

4.3.1 pH

Figure 4-27, Figure 4-28 and Figure 4-29 show the values of pH around the repository for Case 2 decreasing with time, but levelling off at later times to a pH of approximately 6.75. Figure 4-30 shows values of pH over the regional area. Between 2000 AD and 9000 AD there is a slight lowering of pH in the north east of the model, but overall there is little change in pH over the time period.

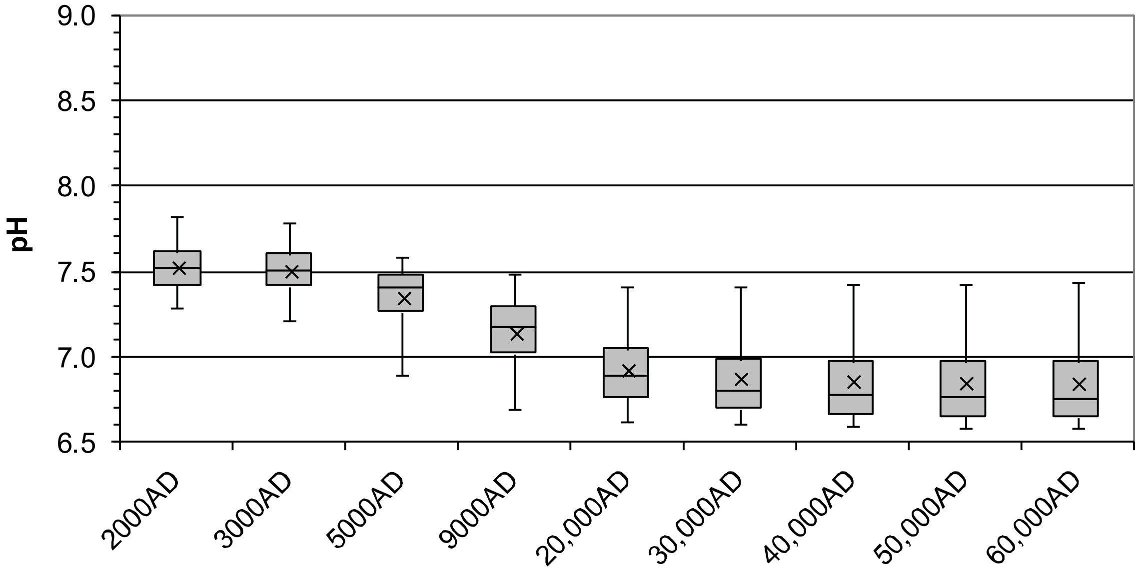

Figure 4-27. Box and whisker plot showing the statistical distribution of pH for Case 2 on a regular grid of points within the repository volume between elevations -490 m and -460 m. The statistical measures are the median, the 25th and 75th percentiles (box), the mean (cross) and the 5th and 95th percentiles (whiskers).

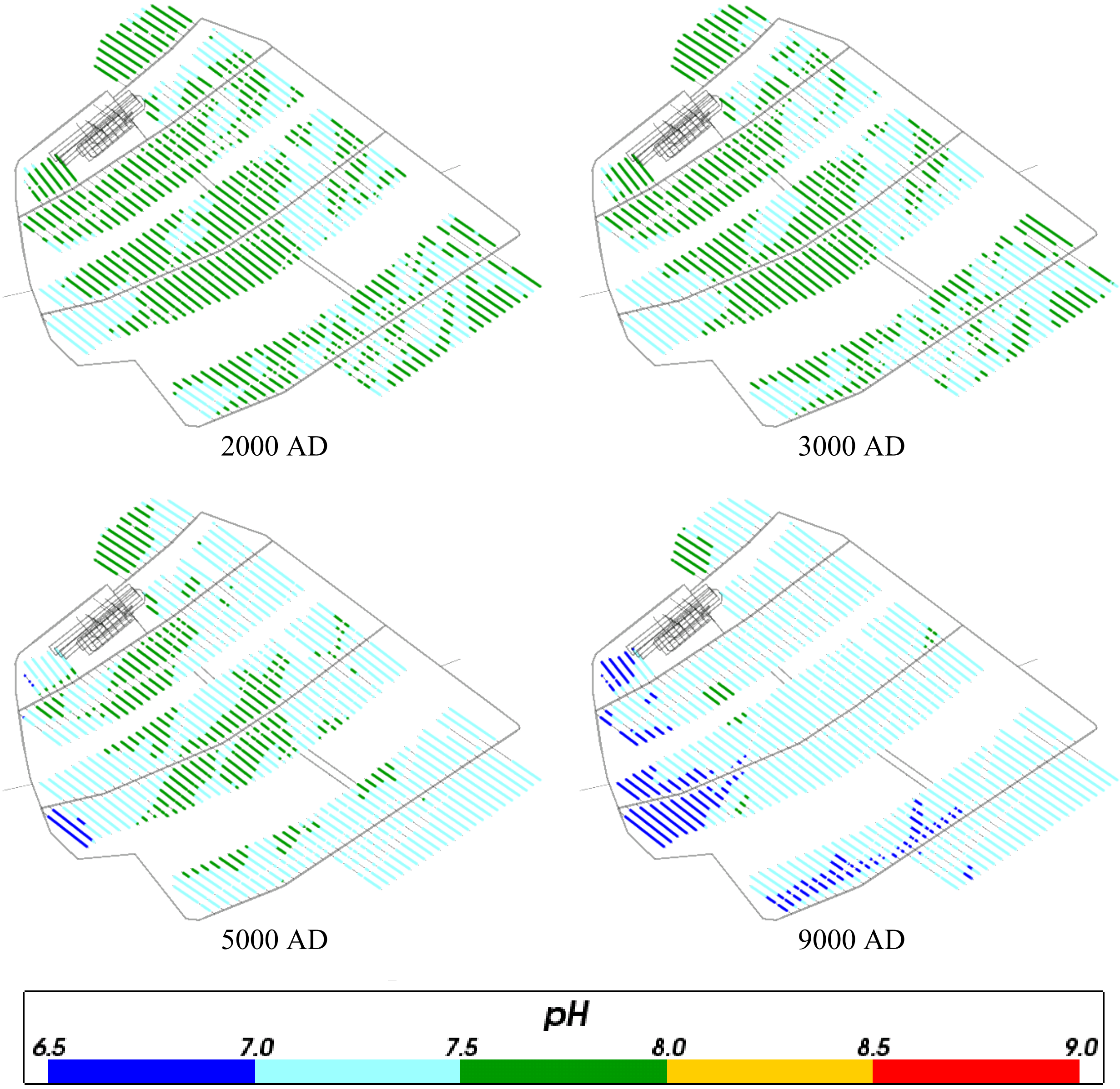

Figure 4-28. *Values of pH for Case 2 at deposition hole locations for time periods 2000 AD to 9000 AD.*

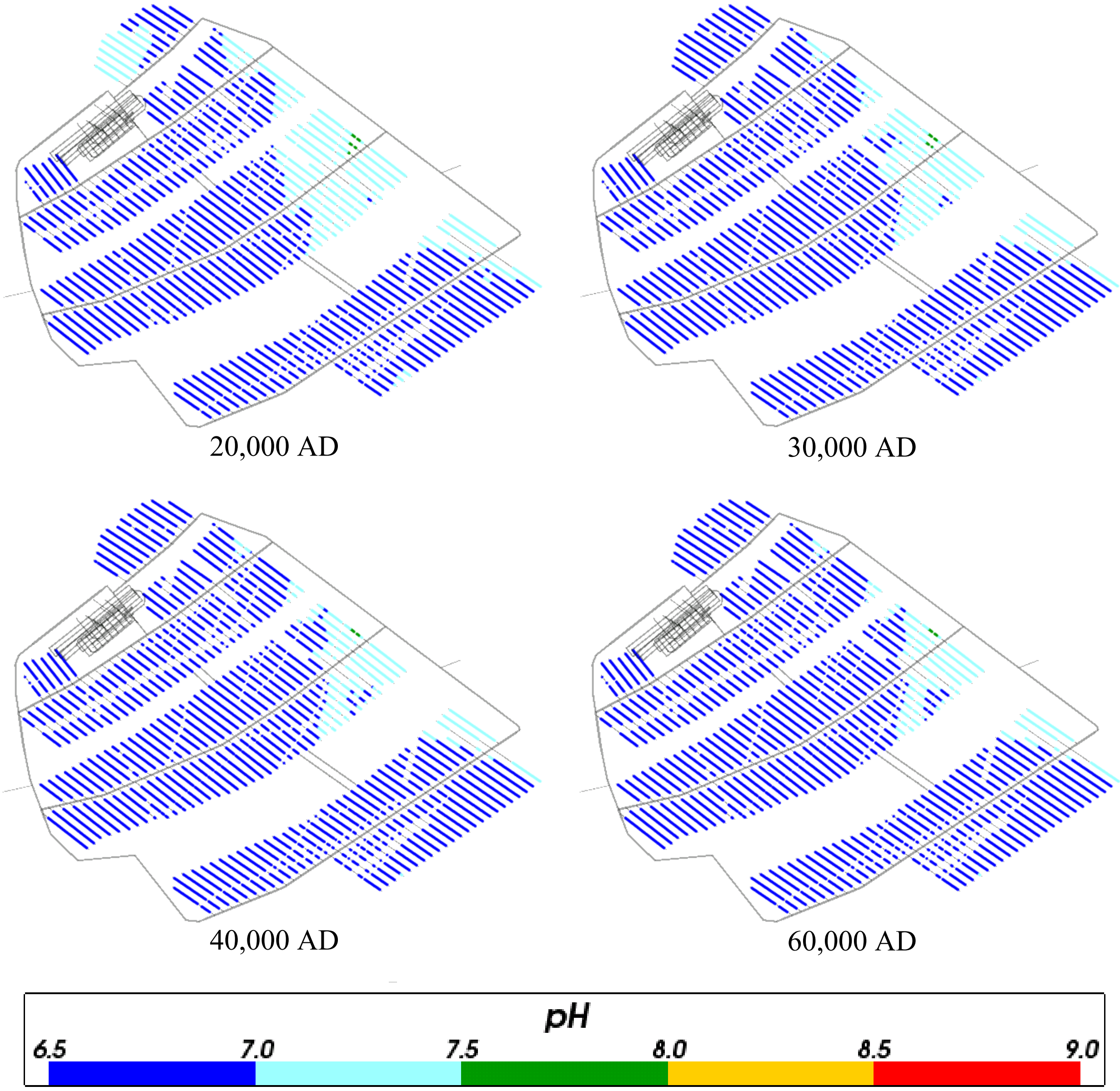

20,000 AD

30,000 AD

40,000 AD

60,000 AD

Figure 4-29. *Values of pH for Case 2 at deposition hole locations for time periods 20,000 AD to 60,000 AD.*

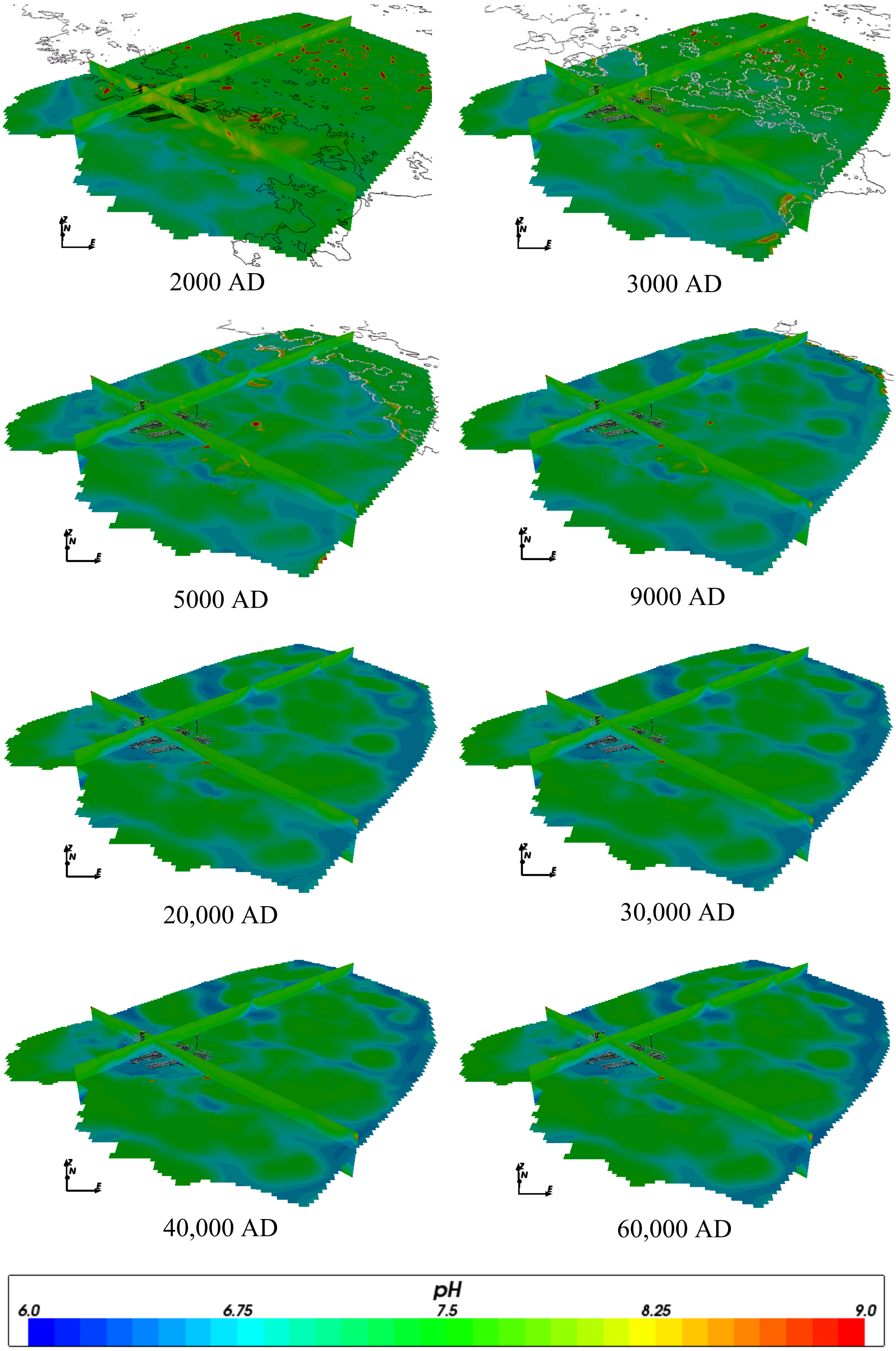

2000 AD

3000 AD

5000 AD

9000 AD

20,000 AD

30,000 AD

40,000 AD

60,000 AD

Figure 4-30. *Values of pH on regional scale slices through the repository volume for Case 2 for time periods 2000 AD to 60,000 AD.*

4.3.2 Eh (or pe)

Figure 4-31 shows the value of Eh in the repository region and Figure 4-32 and Figure 4-33 show the value of pe at the deposition hole locations for Case 2. Figure 4-31 shows that the value of Eh rises over time due to infiltration of Altered Meteoric water with a higher Eh, but flattens off after 30,000 AD. A similar pattern is seen for pe at the deposition hole locations in Figure 4-32 and Figure 4-33.

Figure 4-34 shows regional slice plots of pe over time. In Case 2, pe is increasing at early times, with larger values being swept in a north easterly direction. At later times (20,000 AD onwards) there is little change in pe.

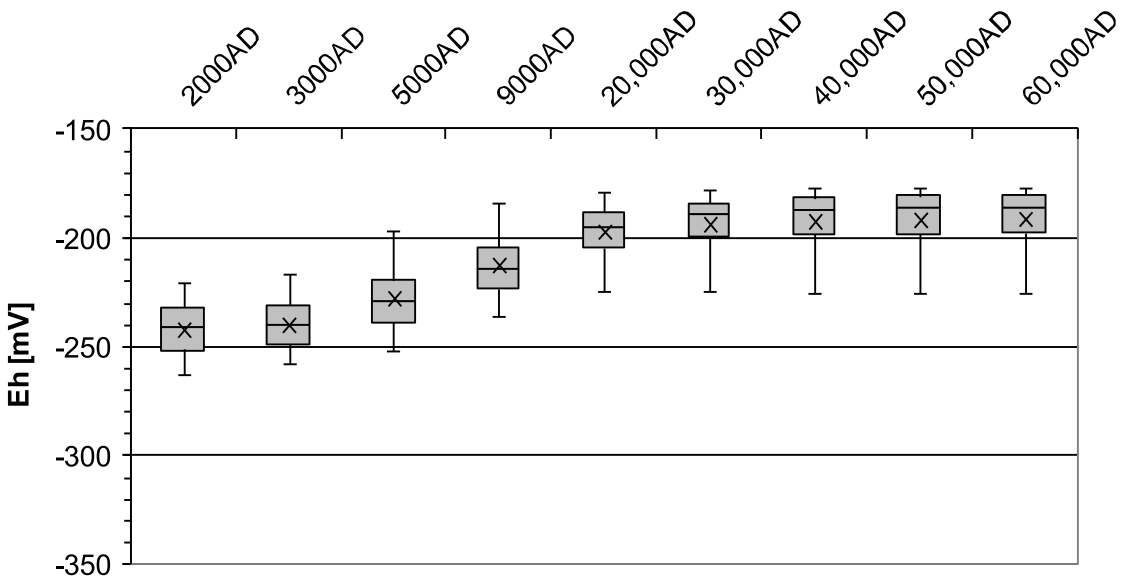

Figure 4-31. Box and whisker plot showing the statistical distribution of Eh for Case 2 on a regular grid of points within the repository volume between elevations -490 m and -460 m. The statistical measures are the median, the 25th and 75th percentiles (box), the mean (cross) and the 5th and 95th percentiles (whiskers).

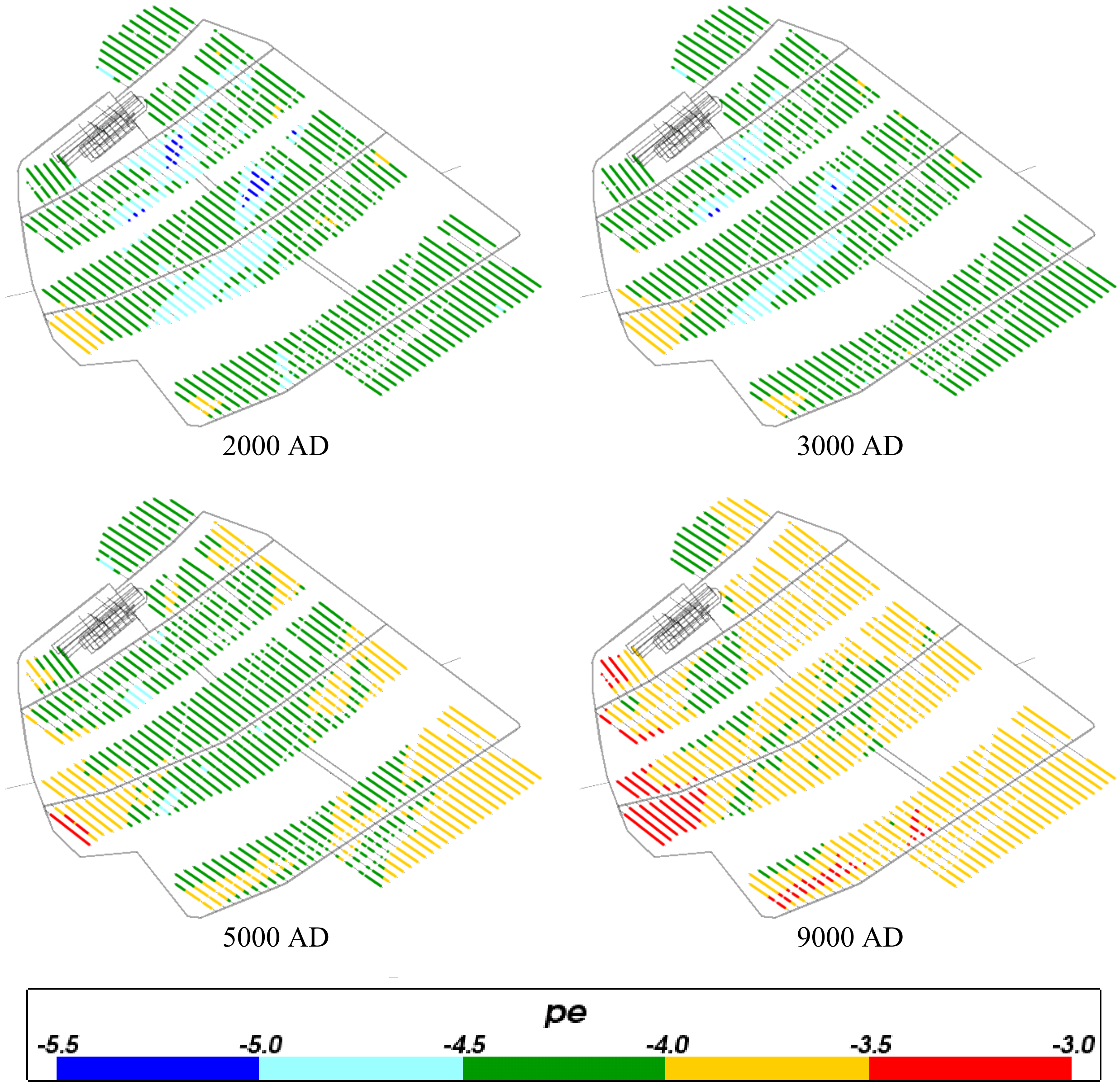

Figure 4-32. *Values of pe for Case 2 at deposition hole locations for time periods 2000 AD to 9000 AD.*

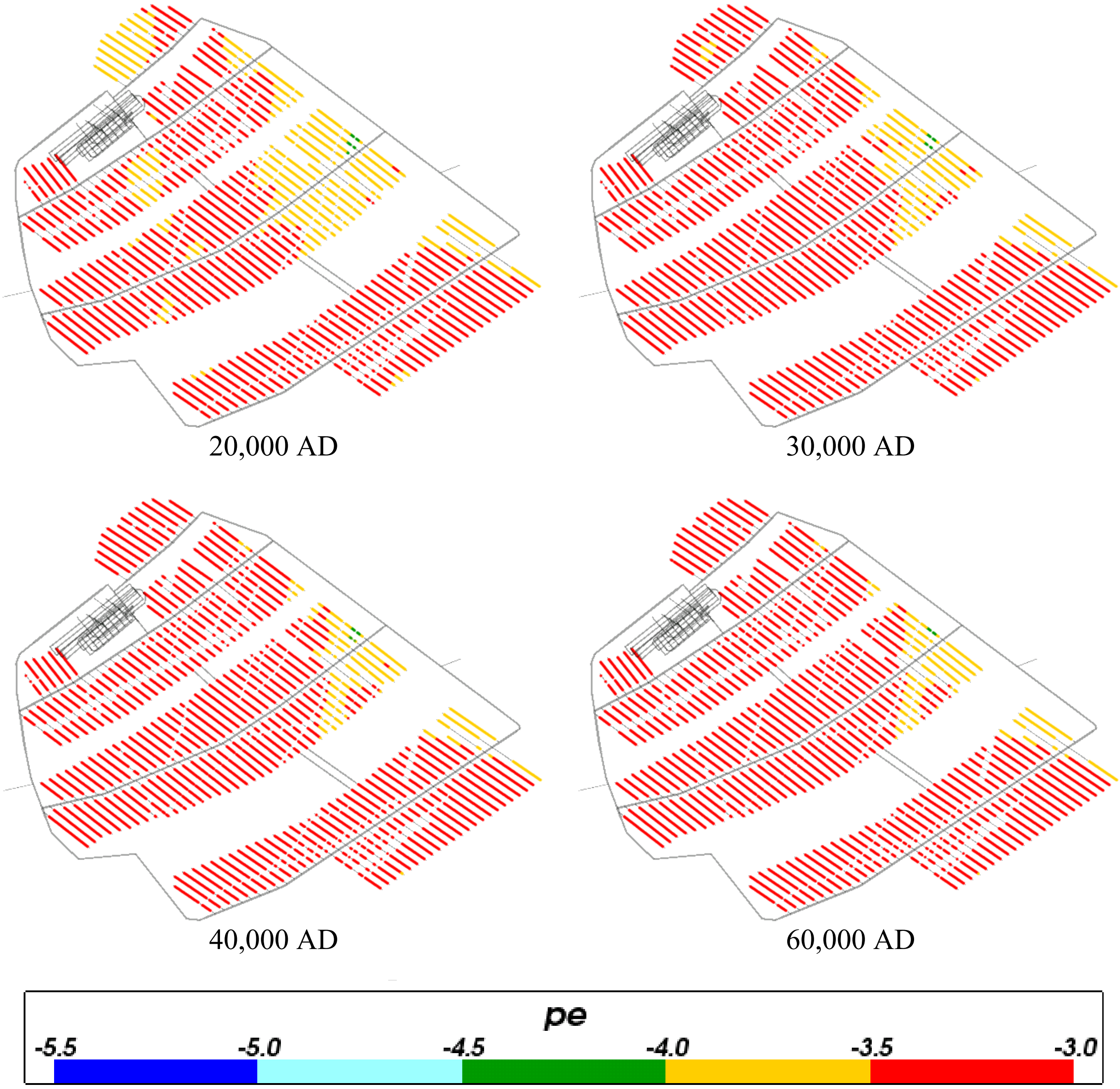

20,000 AD

30,000 AD

40,000 AD

60,000 AD

Figure 4-33. *Values of pe for Case 2 at deposition hole locations for time periods 20,000 AD to 60,000 AD.*

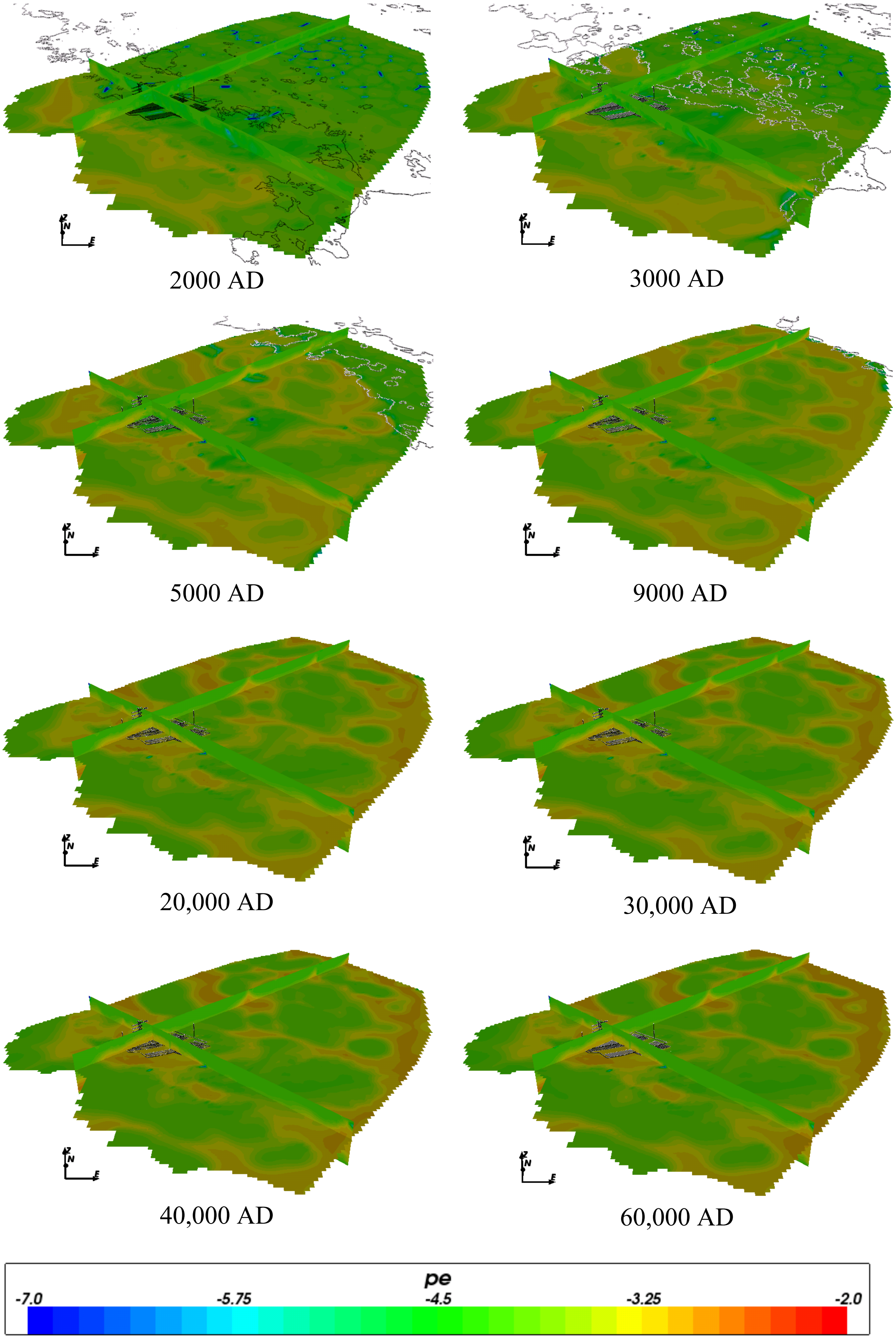

Figure 4-34. *Values of pe on regional scale slices through the repository volume for Case 2 for time periods 2000 AD to 60,000 AD.*

4.3.3 TDS and sum of cations

Figure 4-1 and Figure 4-2 show the statistical distribution of TDS and the sum of cation charge molalities for Case 2. As with Case 1, the two plots are closely related, with the sum of cation charges plot mirroring the TDS plot. Both figures show similar trends to that seen in Case 1, decreasing gradually over time and levelling out at later times.

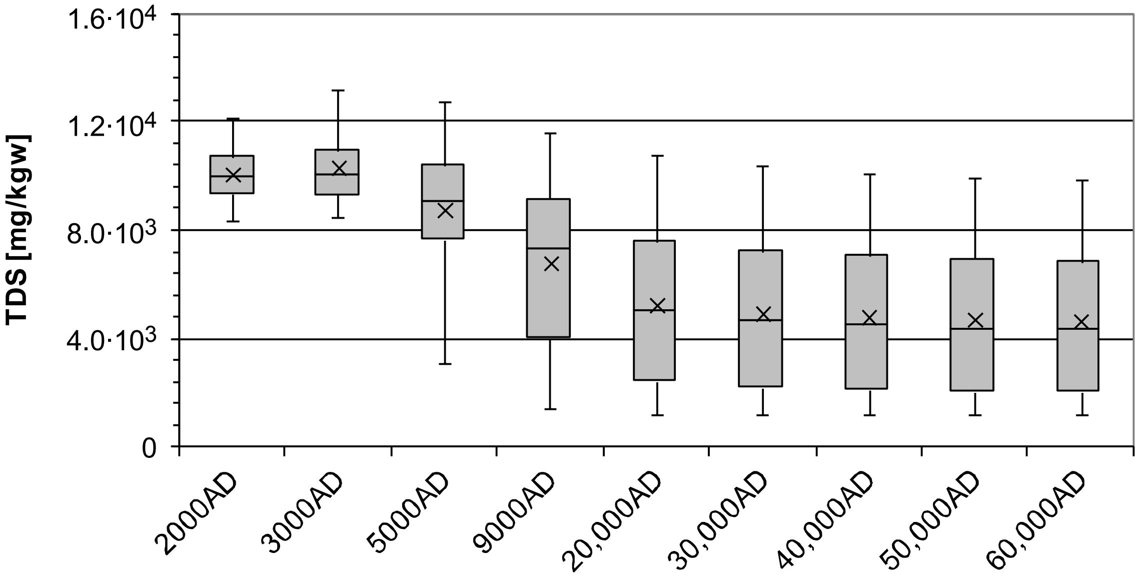

Figure 4-35. Box and whisker plot showing the statistical distribution of TDS for Case 2 on a regular grid of points within the repository volume between elevations -490 m and -460 m. The statistical measures are the median, the 25th and 75th percentiles (box), the mean (cross) and the 5th and 95th percentiles (whiskers).

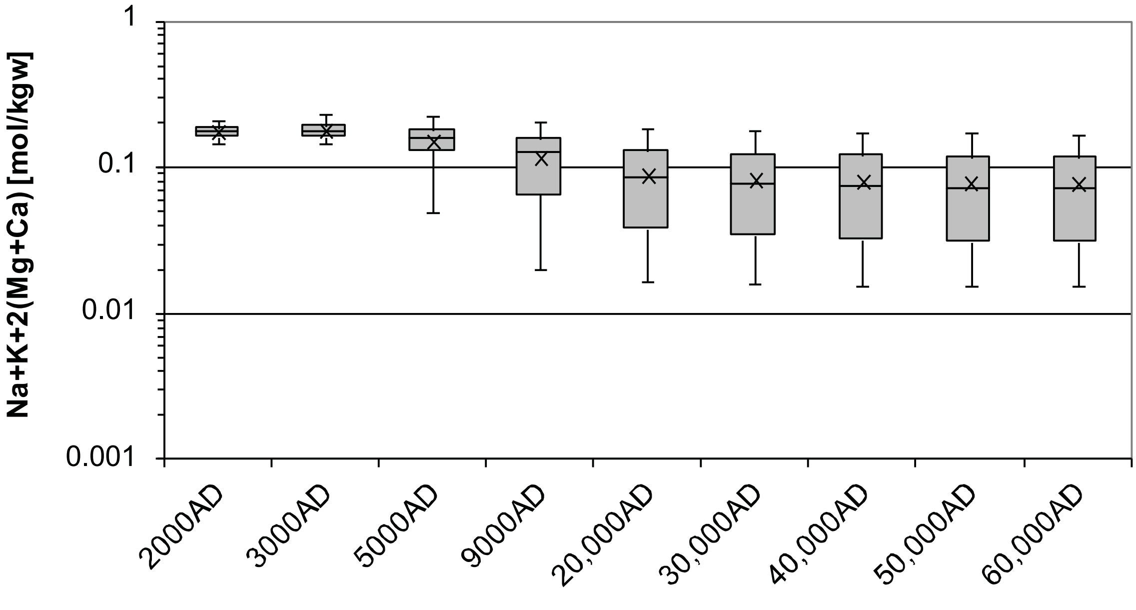

Figure 4-36. Box and whisker plot showing the statistical distribution of sum of cation charges (Na+K+2(Mg+Ca)) molalities for Case 2 on a regular grid of points within the repository volume between elevations -490 m and -460 m. The statistical measures are

the median, the 25th and 75th percentiles (box), the mean (cross) and the 5th and 95th percentiles (whiskers).

4.3.4 Carbon

Figure 4-37, Figure 4-38, Figure 4-39 and Figure 4-40 show plots of total inorganic carbon for Case 2. The first three figures show very similar trends to those seen in the no chemistry case (Case 1, results shown in Figure 4-3 to Figure 4-6), except for slightly lower values of total inorganic carbon at times over 20,000 AD. This implies that the effect of the chemical reactions on total inorganic carbon is minimal for this case. Figure 4-40, which shows total inorganic carbon over the regional scale, is very similar to Figure 4-6, except for at later times where Figure 4-40 shows slightly increased concentrations of total inorganic carbon (as seen by the larger proportion of orange coloured areas on the plots). This implies that there is some dissolution of calcite.

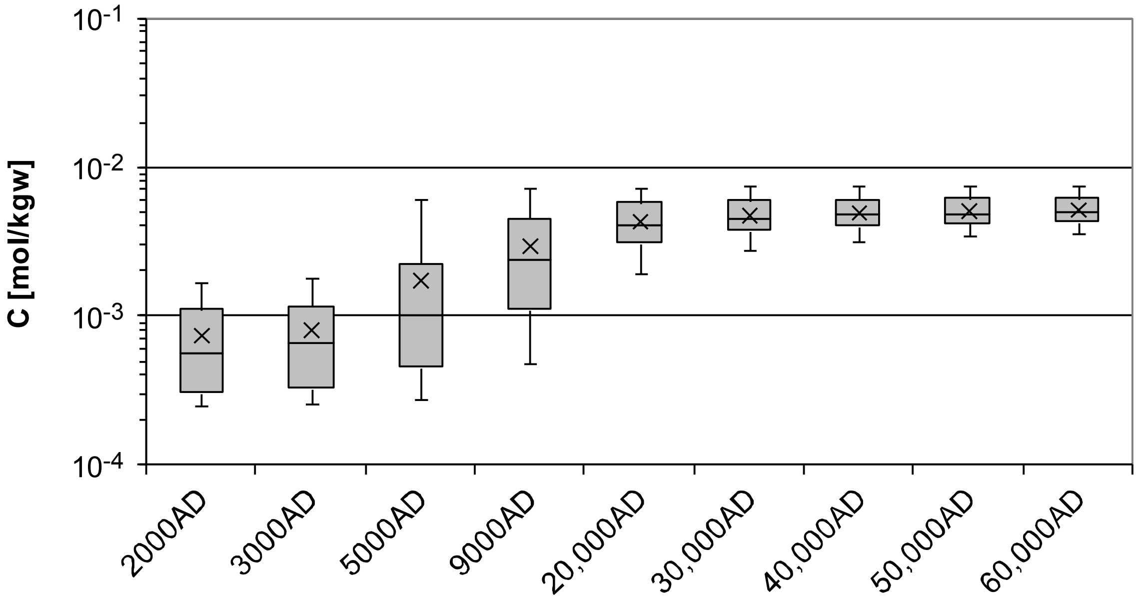

Figure 4-37. *Box and whisker plot showing the statistical distribution of total inorganic carbon molalities for Case 2 on a regular grid of points within the repository volume between elevations -490 m and -460 m. The statistical measures are the median, the 25th and 75th percentiles (box), the mean (cross) and the 5th and 95th percentiles (whiskers).*

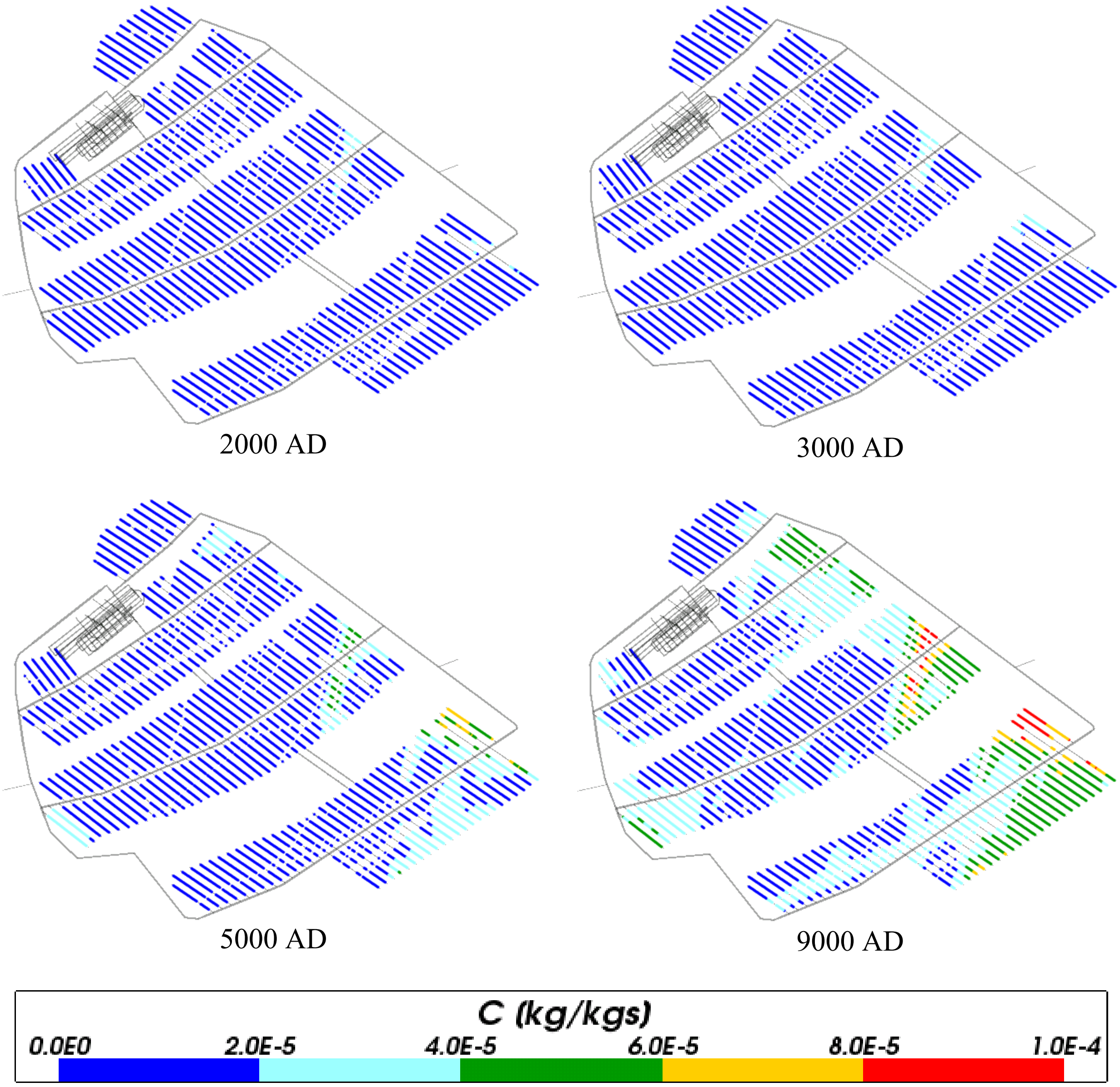

Figure 4-38. *Total inorganic carbon mass fractions for Case 2 at deposition hole locations for time periods 2000 AD to 9000 AD.*

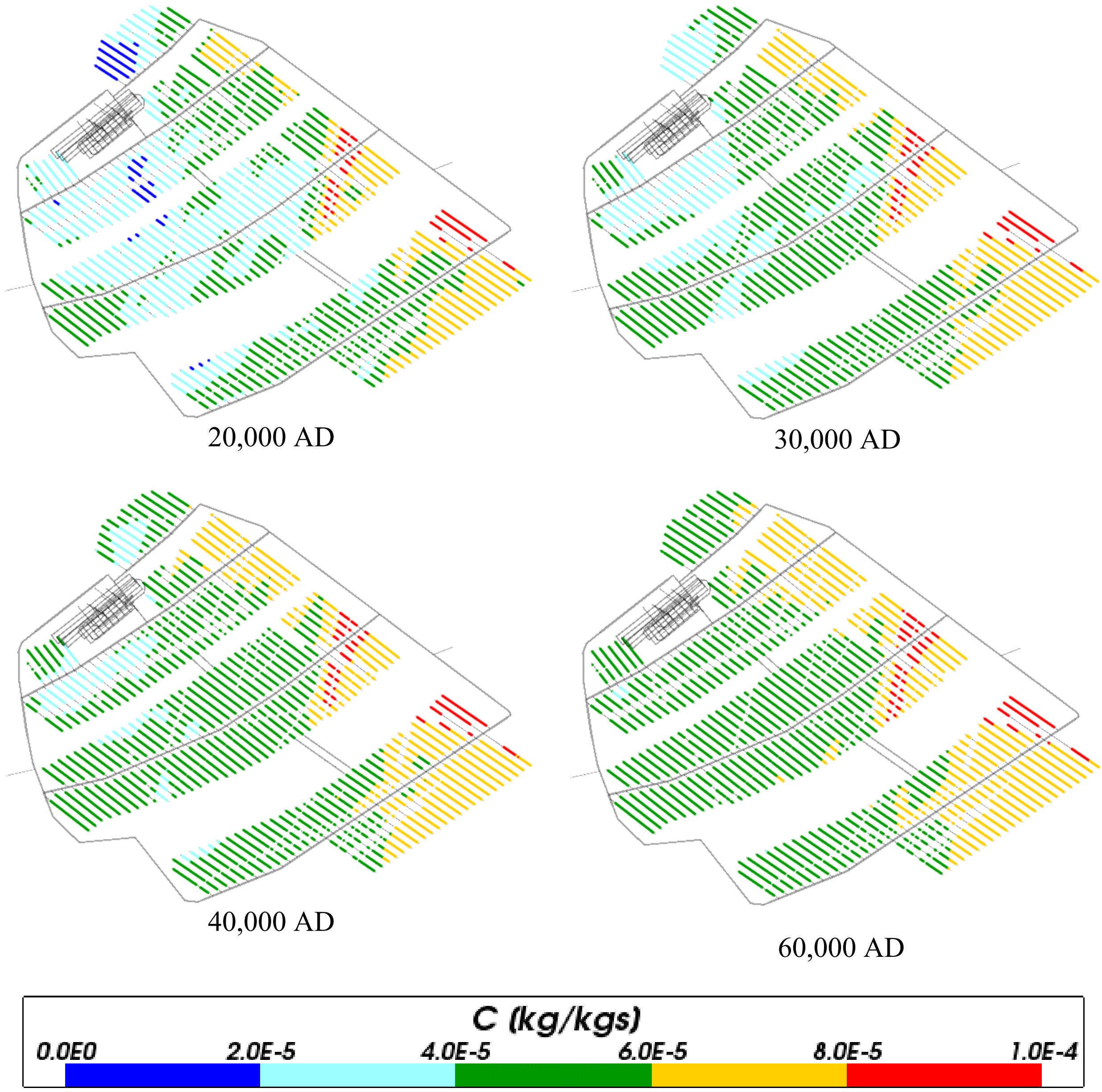

Figure 4-39. *Total inorganic carbon mass fractions for Case 2 at deposition hole locations for time periods 20,000 AD to 60,000 AD.*

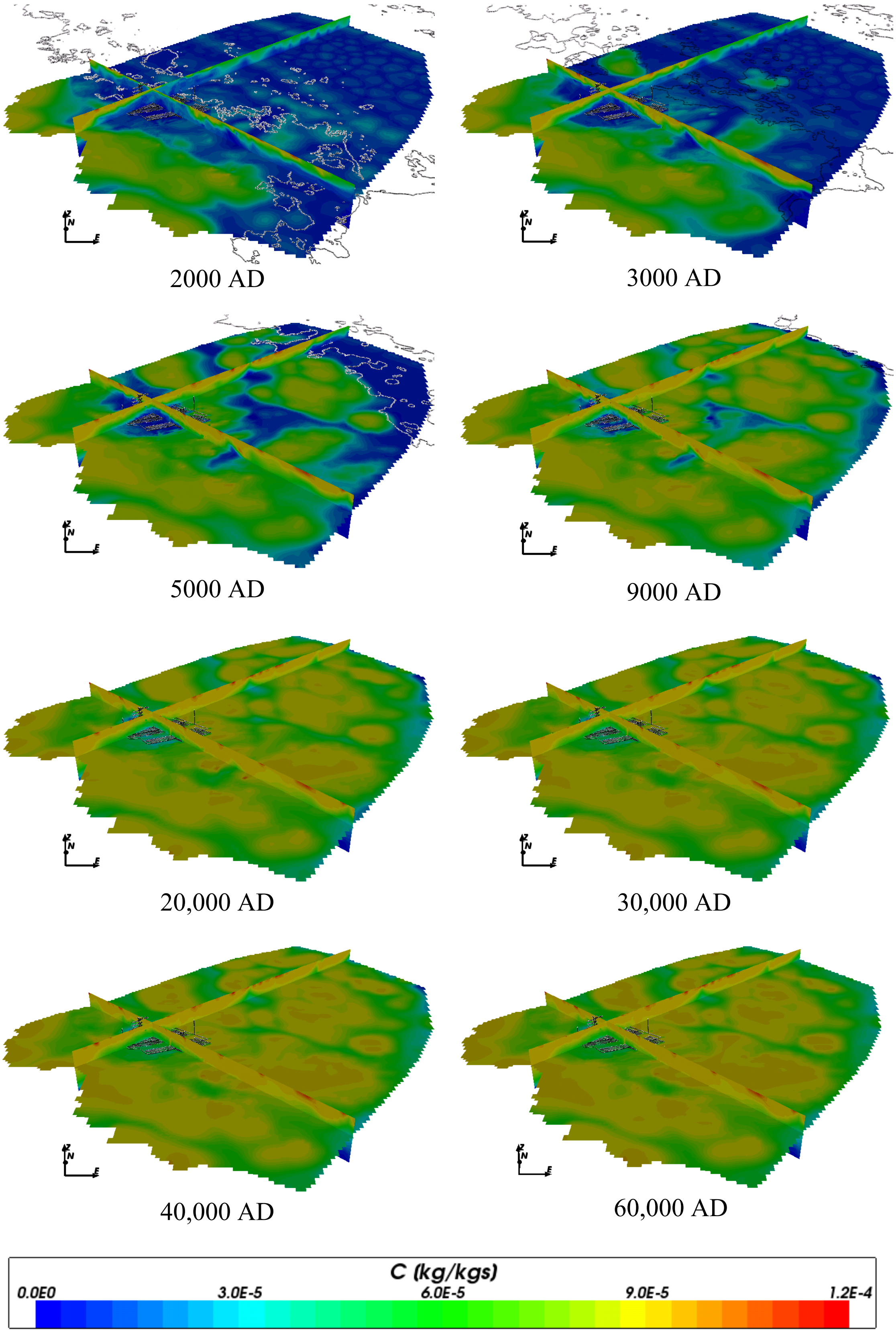

2000 AD

3000 AD

5000 AD

9000 AD

20,000 AD

30,000 AD

40,000 AD

60,000 AD

Figure 4-40. *Total inorganic carbon mass fractions on regional scale slices through the repository volume for Case 2 for time periods 2000 AD to 60,000 AD*

4.3.5 Calcium

The concentration of total calcium both in the repository area and on the regional scale (shown in Figure 4-41 to Figure 4-44) is very similar to that seen in Case 1, even for later times, implying that the chemical reactions have little effect on the calcium concentration.

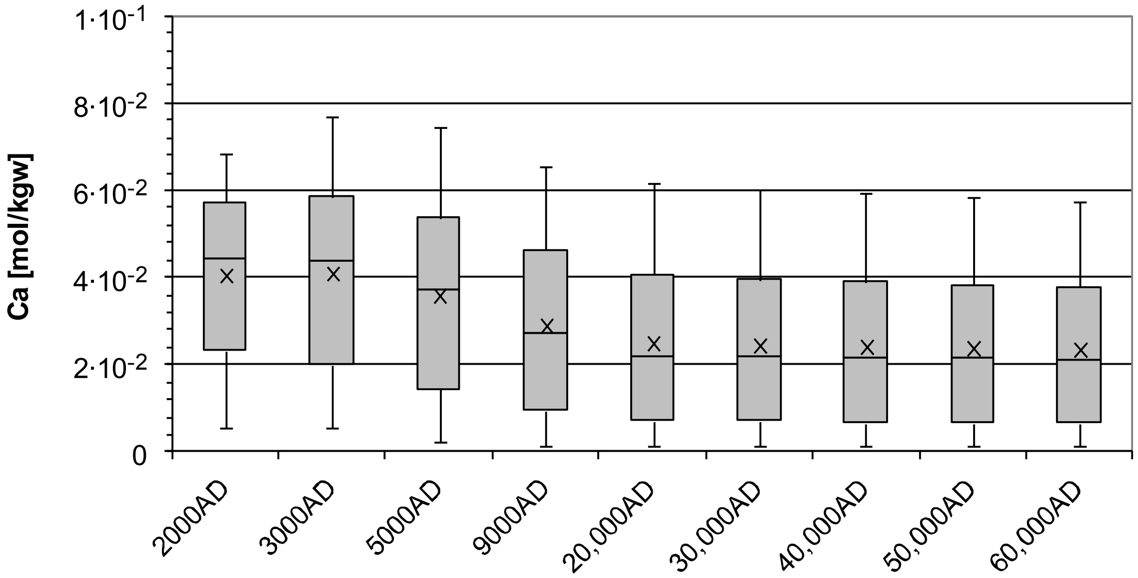

Figure 4-41. *Box and whisker plot showing the statistical distribution of total calcium molalities for Case 2 on a regular grid of points within the repository volume between elevations -490 m and -460 m. The statistical measures are the median, the 25th and 75th percentiles (box), the mean (cross) and the 5th and 95th percentiles (whiskers).*

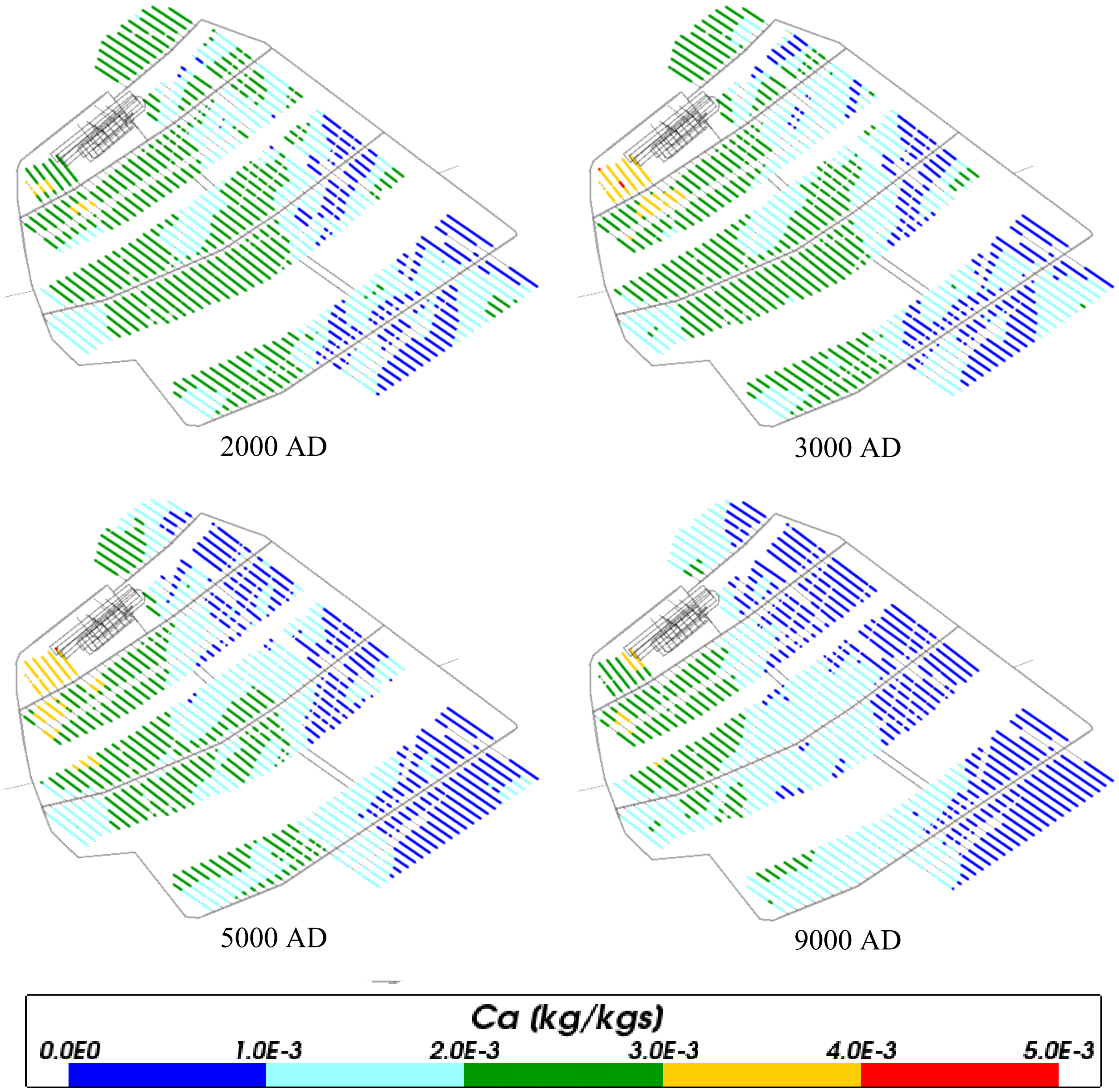

2000 AD

3000 AD

5000 AD

9000 AD

Figure 4-42. *Total calcium mass fractions for Case 2 at deposition hole locations for time periods 2000 AD to 9000 AD.*

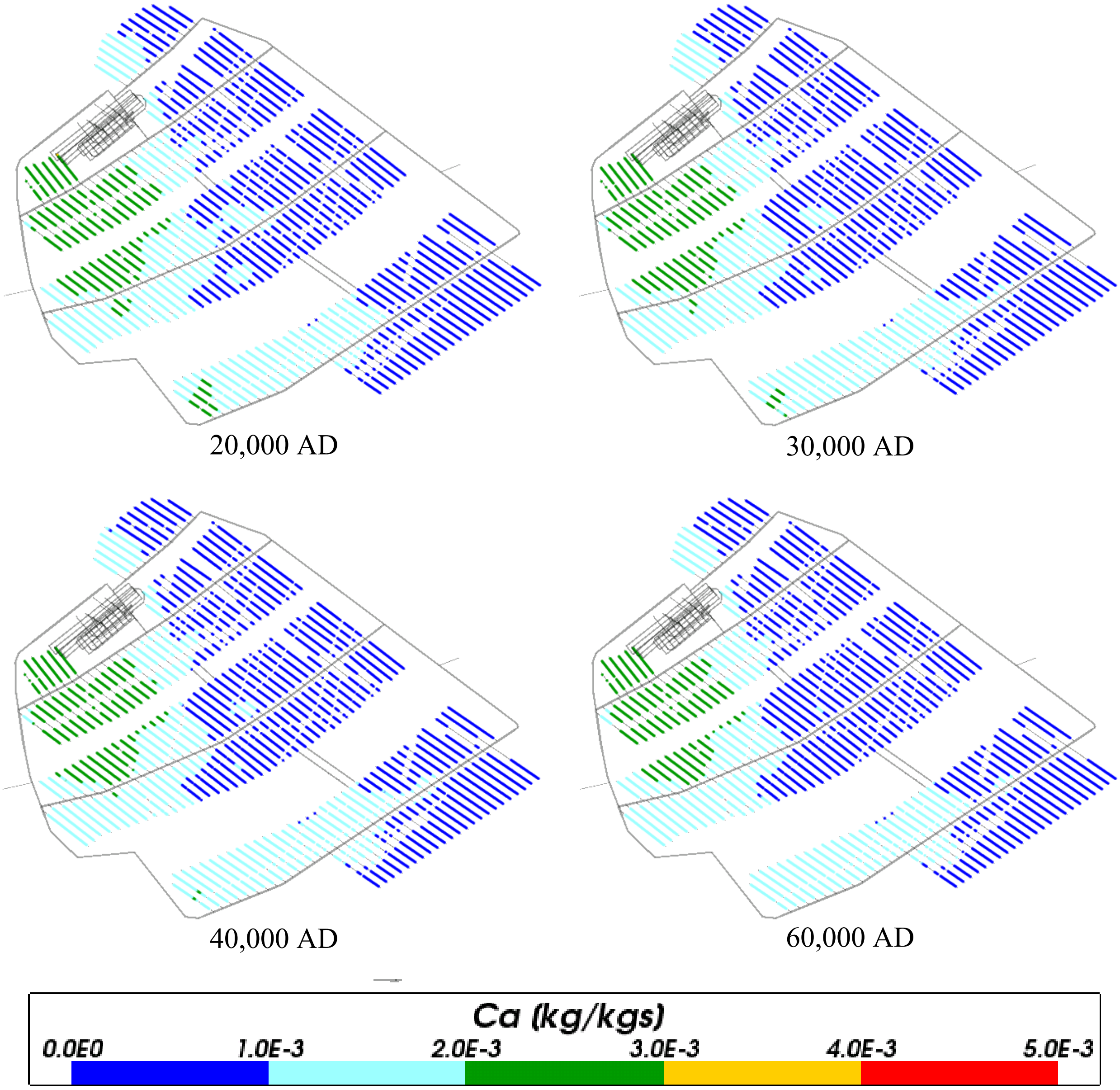

Figure 4-43. *Total calcium mass fractions for Case 2 at deposition hole locations for time periods 20,000 AD to 60,000 AD.*

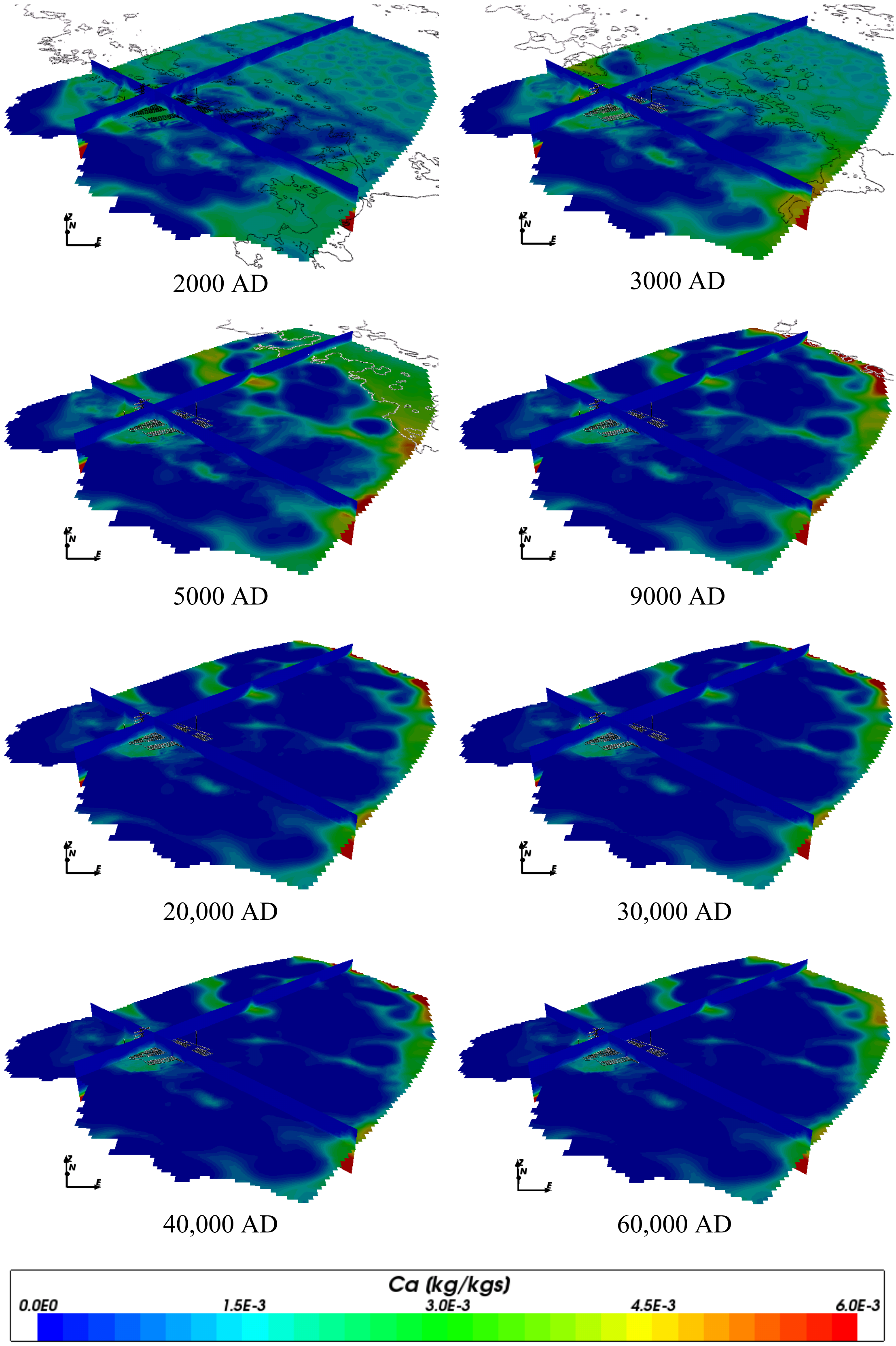

__Figure 4-44.__ Total calcium mass fractions on regional scale slices through the repository volume for Case 2 for time periods 2000 AD to 60,000 AD

4.3.6 Chloride

Figure 4-45, Figure 4-46 and Figure 4-47 show the chloride concentrations for Case 2. Since chloride is a non-reactive component, the results are very similar to Case 1 (no chemistry). Similarly, the concentrations of chloride across the model (Figure 4-48) are very similar to Case 1.

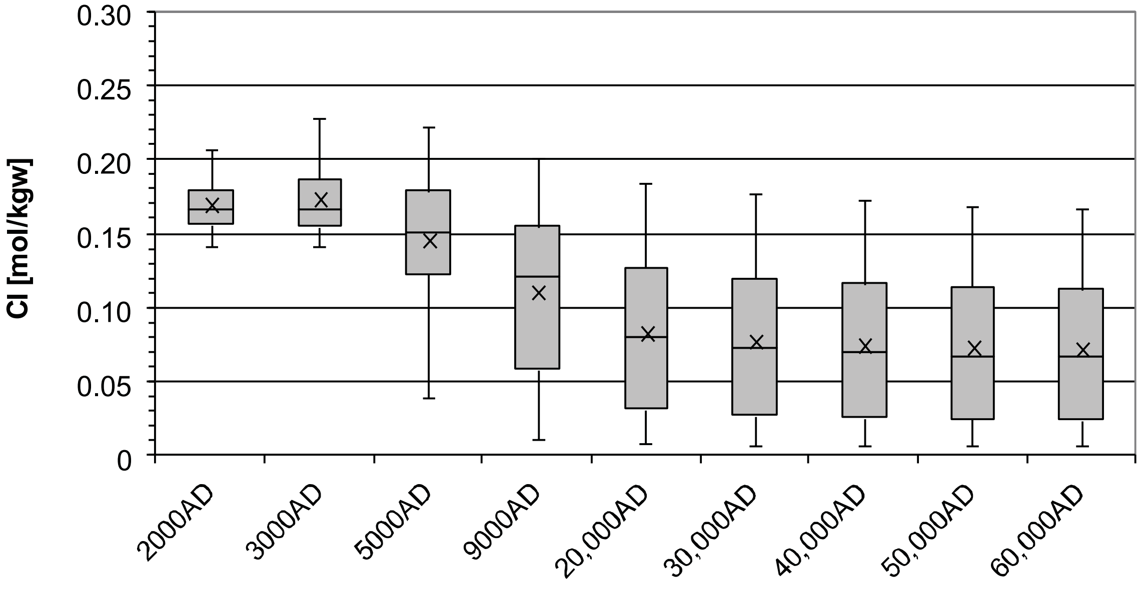

Figure 4-45. *Box and whisker plot showing the statistical distribution of total chloride molalities for Case 2 on a regular grid of points within the repository volume between elevations -490 m and -460 m. The statistical measures are the median, the 25th and 75th percentiles (box), the mean (cross) and the 5th and 95th percentiles (whiskers).*

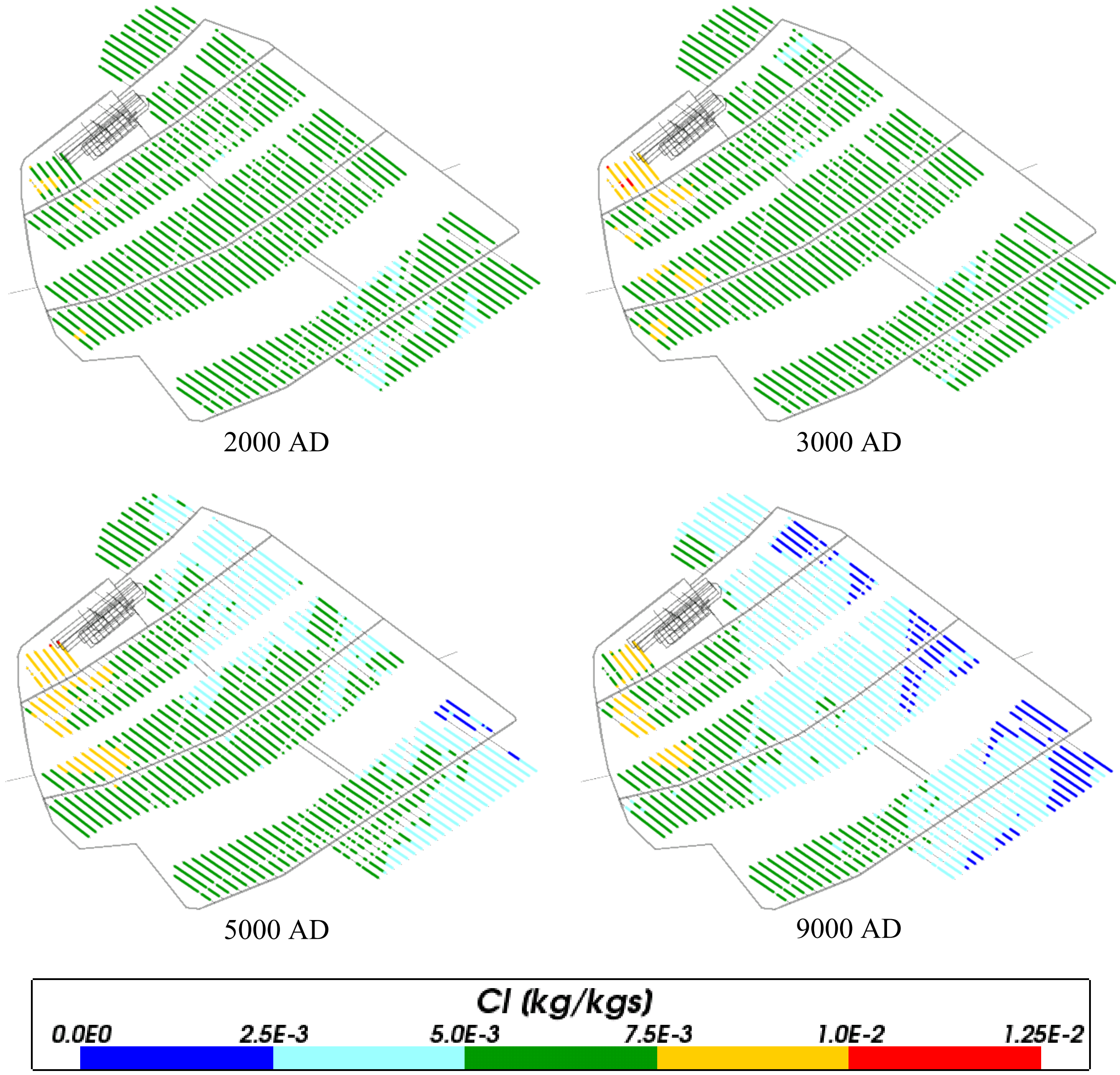

Figure 4-46. *Total chloride mass fractions for Case 2 at deposition hole locations for time periods 2000 AD to 9000 AD.*

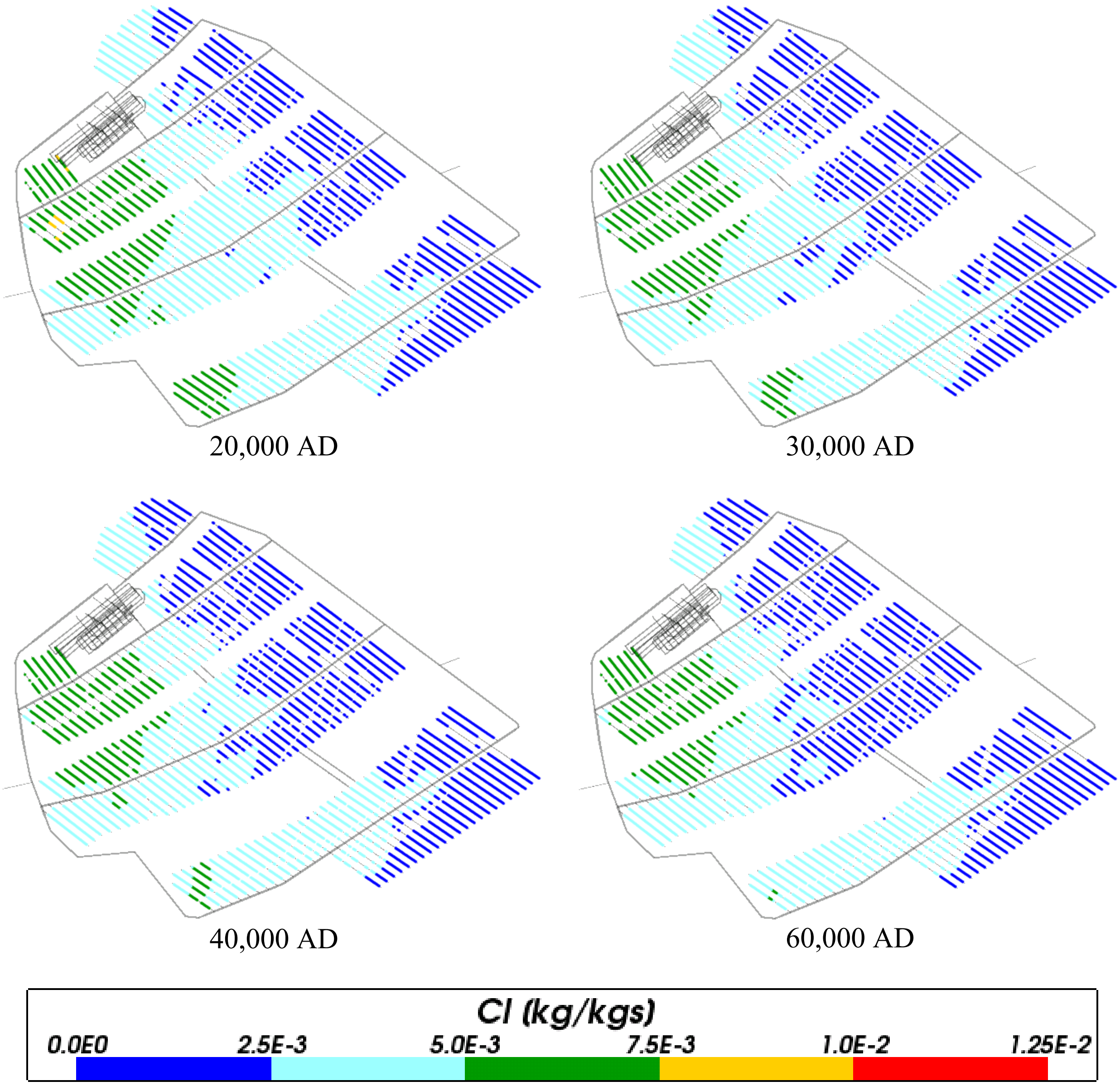

Figure 4-47. *Total chloride mass fractions for Case 2 at deposition hole locations for time periods 20,000 AD to 60,000 AD.*

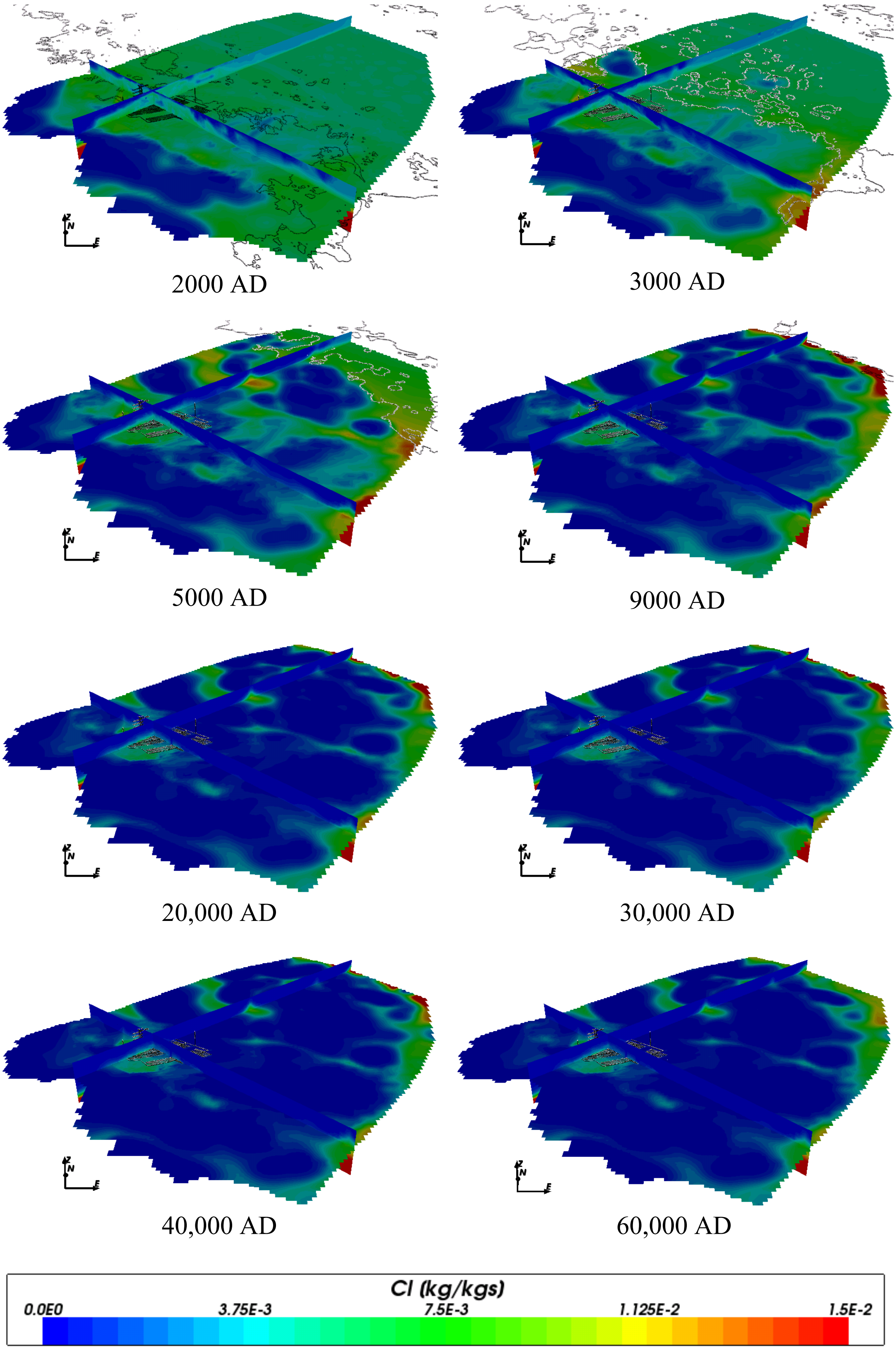

Figure 4-48. *Total chloride mass fractions on regional scale slices through the repository volume for Case 2 for time periods 2000 AD to 60,000 AD.*

4.3.7 Iron

Unlike the previously discussed chemical species, the chemical reactions included in Case 2 appear to have a marked effect on the concentration of total iron around the repository (Figure 4-49, Figure 4-50 and Figure 4-51). In Case 1 the concentration of iron remained low around the repository and little change could be seen over time. For Case 2 however, the concentration of iron increases over time, levelling off after 40,000 AD (see Figure 4-49). As this effect was not seen in Case 1, it can be assumed that it is directly related to the chemical reactions included in Case 2.

This difference is also apparent at the regional scale, as shown in Figure 4-52. The total iron concentration can clearly be seen increasing with time over the model from the south west to the north east.

The iron concentrations up to 9000 AD are about half to one order of magnitude lower than those reported in Figure 6-20 of Salas et al. (2010). However, the iron concentrations are low and sensitive to minor changes in groundwater composition, which could arise due to the coupled nature of the flow, transport and geochemistry used for this study compared to SR-Site.

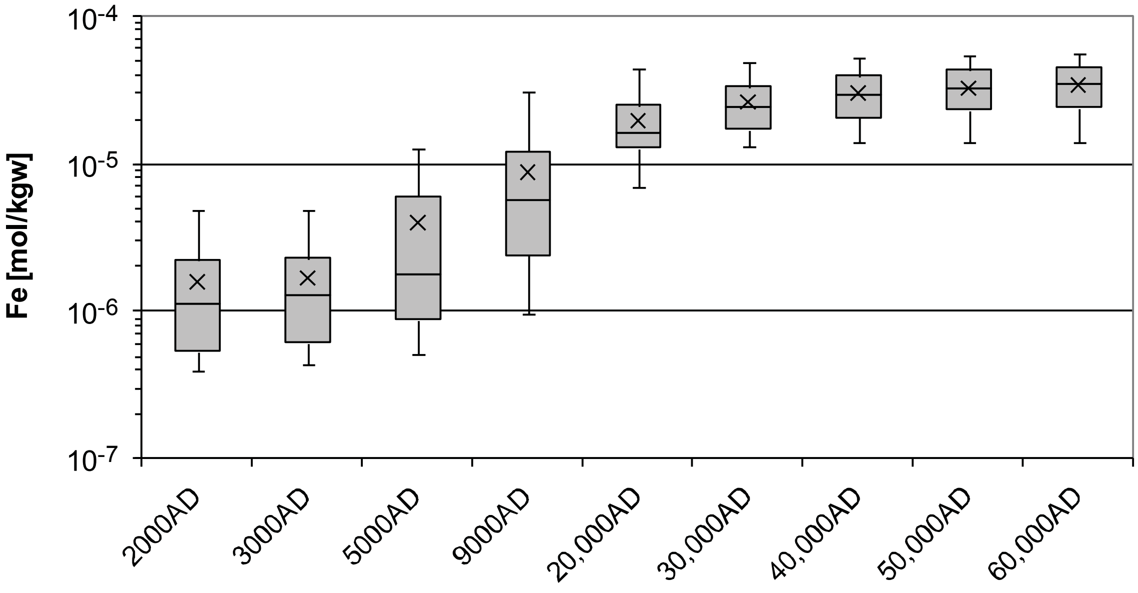

Figure 4-49. *Box and whisker plot showing the statistical distribution of total iron molalities for Case 2 on a regular grid of points within the repository volume between elevations -490 m and -460 m. The statistical measures are the median, the 25th and 75th percentiles (box), the mean (cross) and the 5th and 95th percentiles (whiskers).*

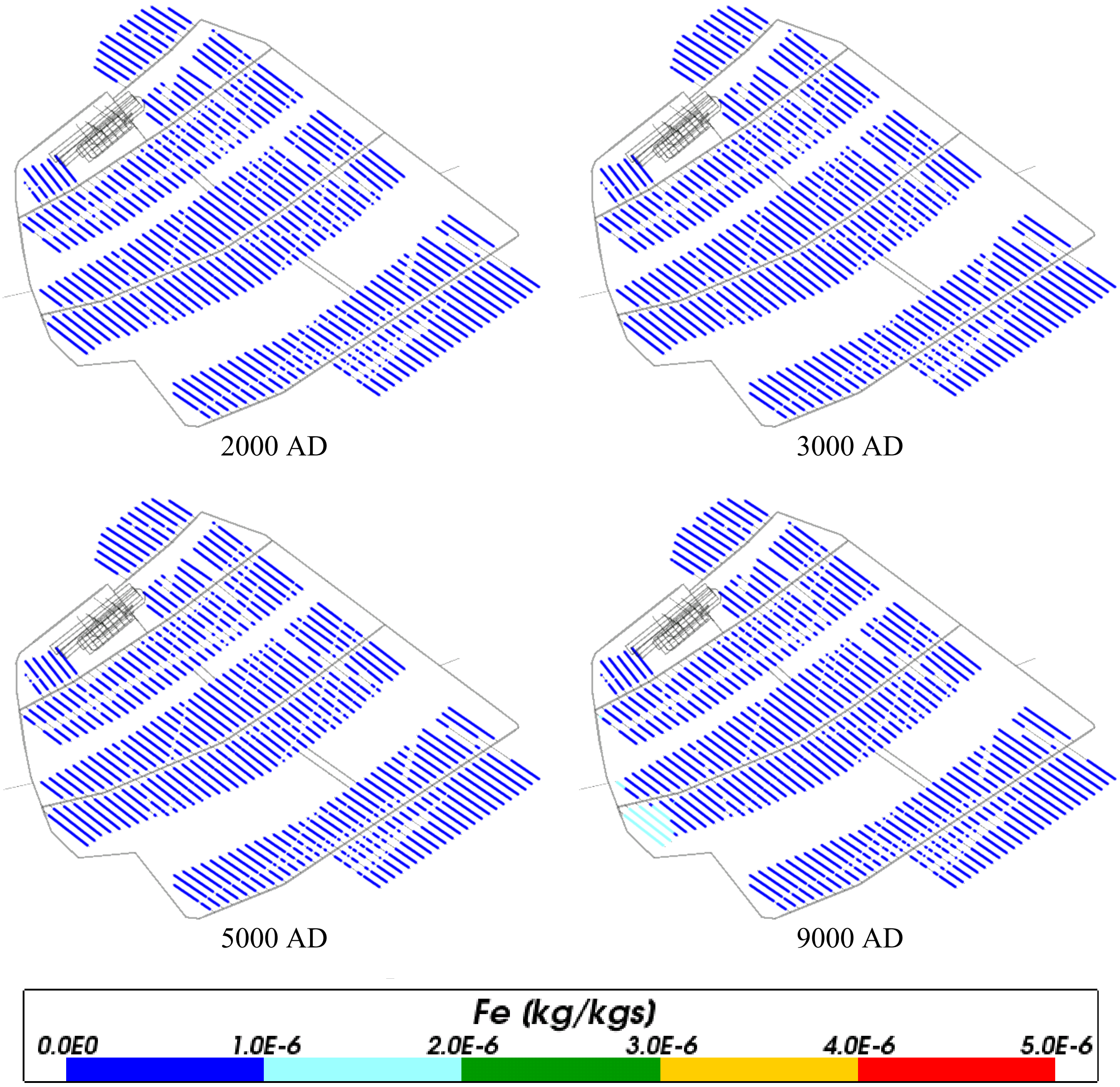

2000 AD

3000 AD

5000 AD

9000 AD

Figure 4-50. *Total iron mass fractions for Case 2 at deposition hole locations for time periods 2000 AD to 9000 AD.*

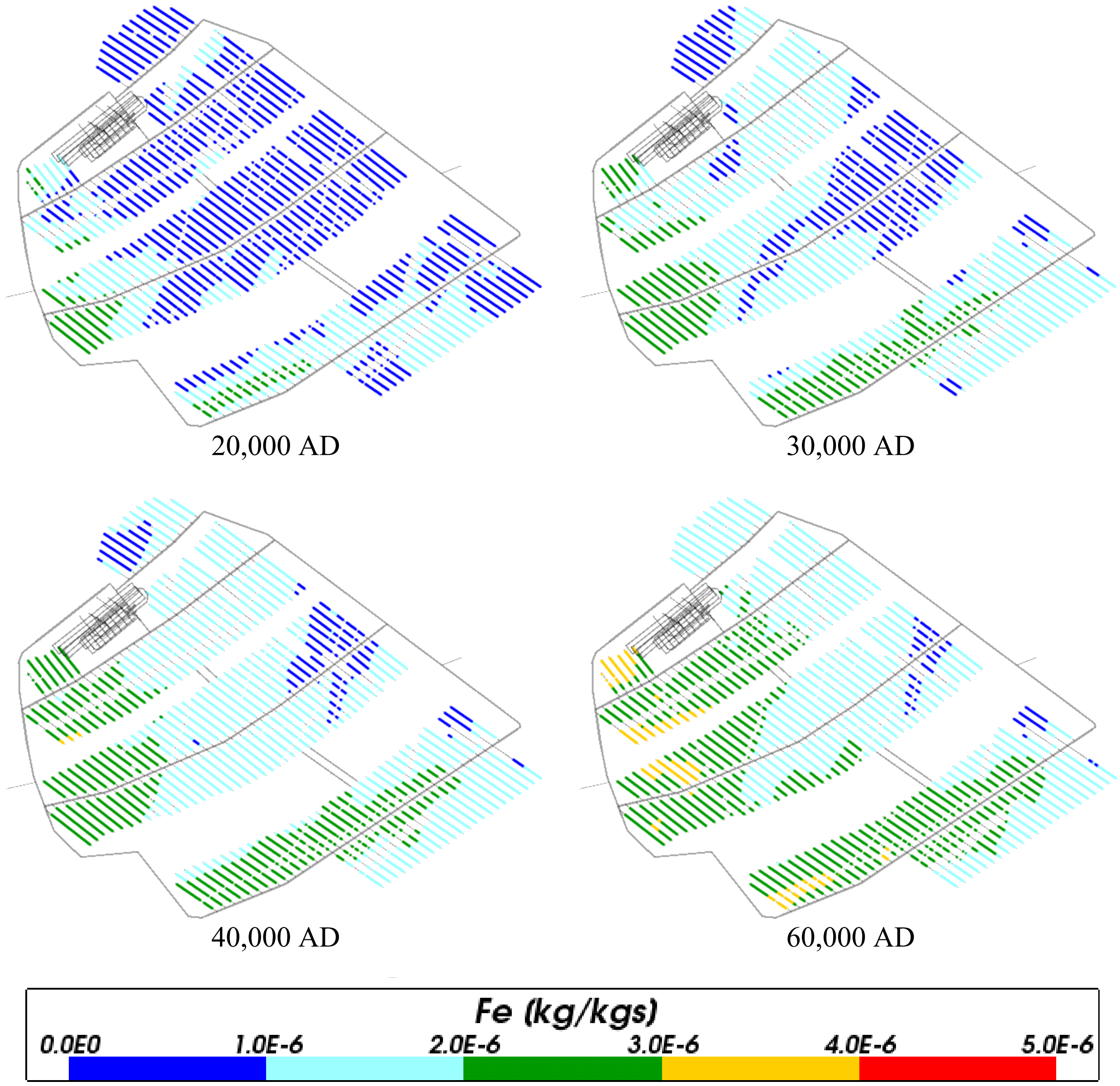
20,000 AD

30,000 AD

40,000 AD

60,000 AD

Figure 4-51. *Total iron mass fractions for Case 2 at deposition hole locations for time periods 20,000 AD to 60,000 AD.*

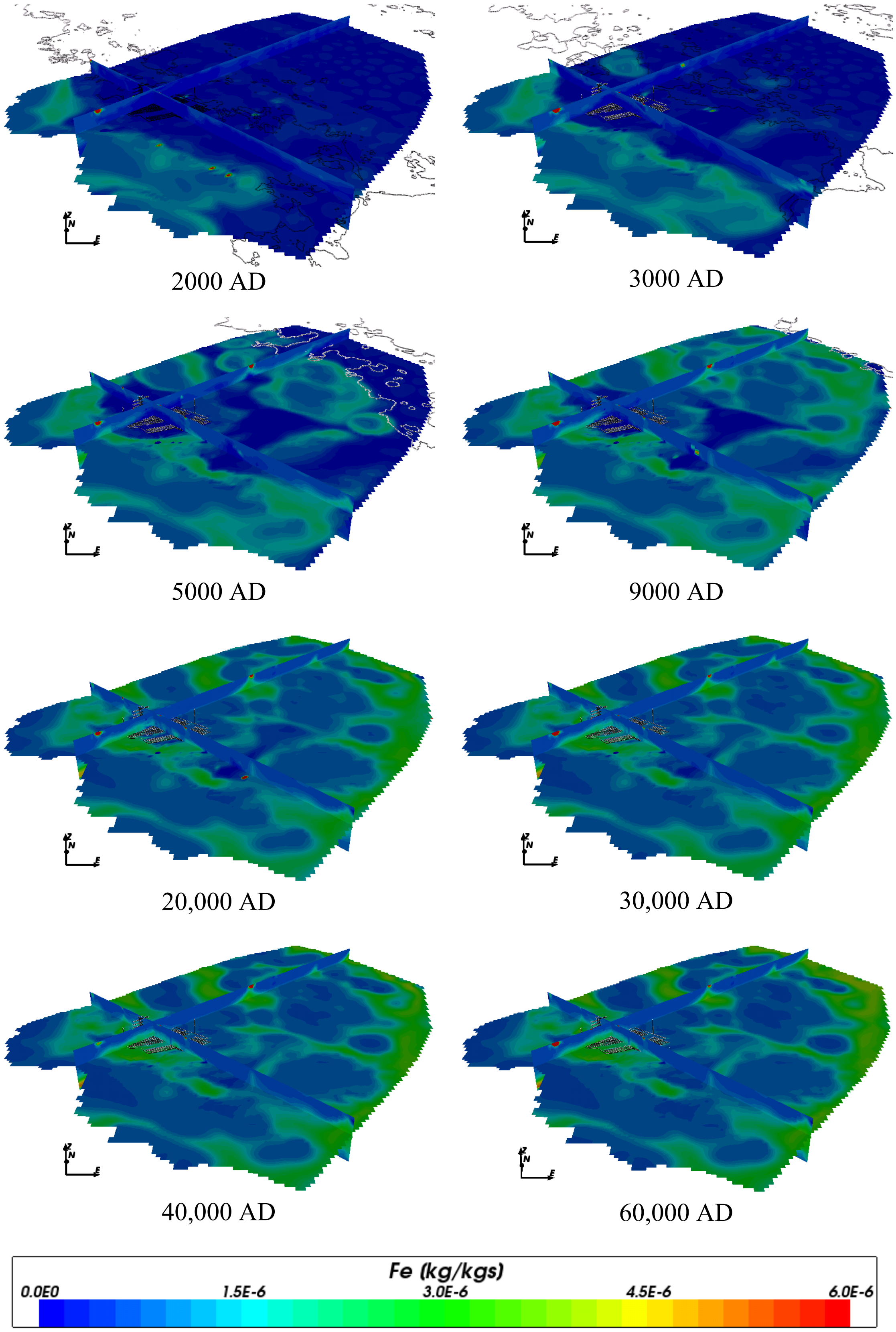

Figure 4-52. *Total iron mass fractions on regional scale slices through the repository volume for Case 2 for time periods 2000 AD to 60,000 AD.*

4.3.8 Sodium

The concentration of sodium (Figure 4-53, Figure 4-54, Figure 4-55 and Figure 4-56) is again very similar to Case 1 as this is a non-reactive species.

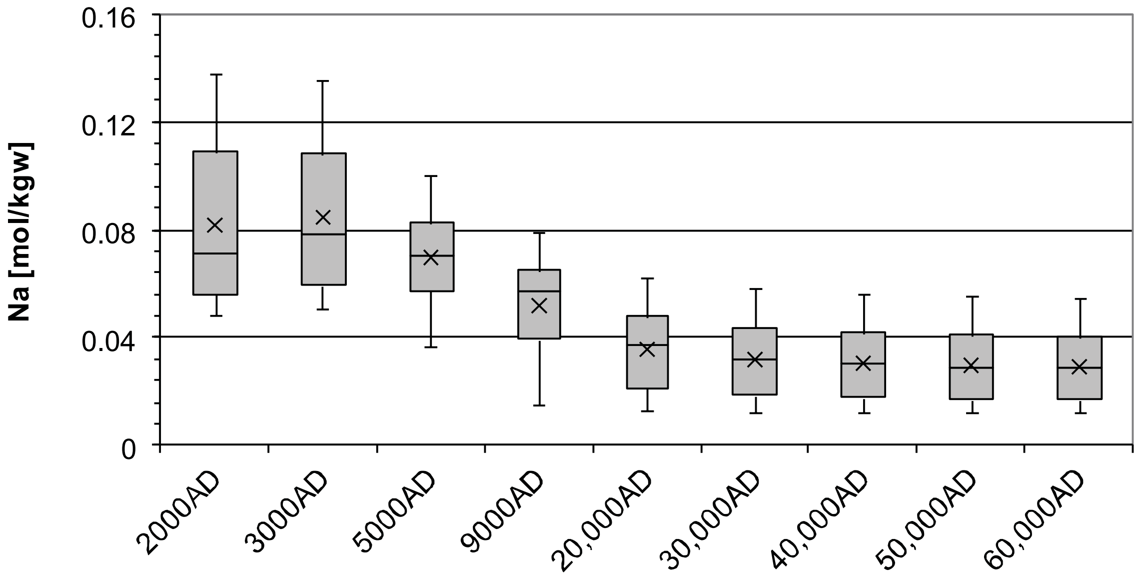

Figure 4-53. *Box and whisker plot showing the statistical distribution of total sodium molalities for Case 2 on a regular grid of points within the repository volume between elevations -490 m and -460 m. The statistical measures are the median, the 25th and 75th percentiles (box), the mean (cross) and the 5th and 95th percentiles (whiskers).*

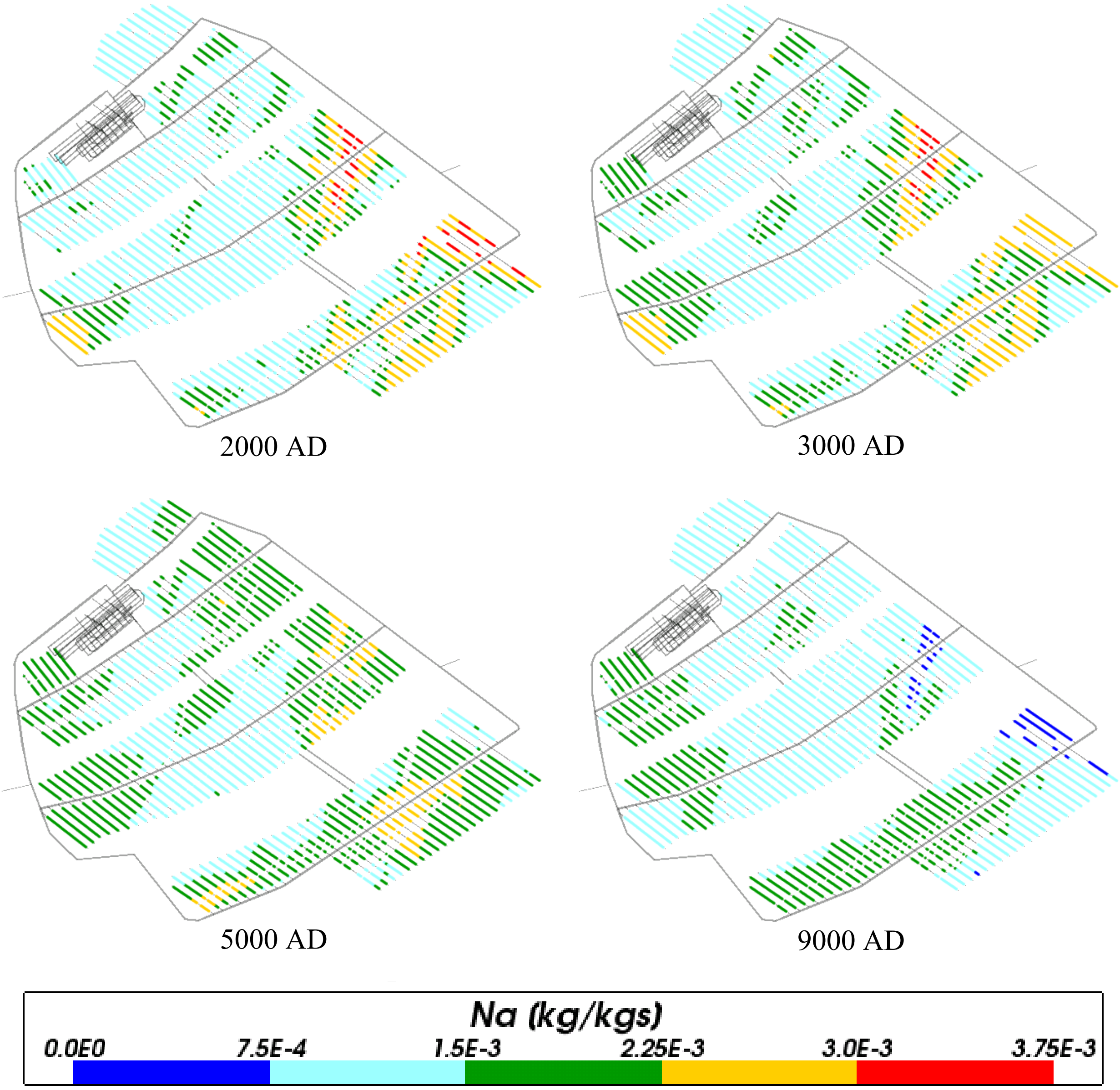

2000 AD

3000 AD

5000 AD

9000 AD

Figure 4-54. *Total sodium mass fractions for Case 2 at deposition hole locations for time periods 2000 AD to 9000 AD.*

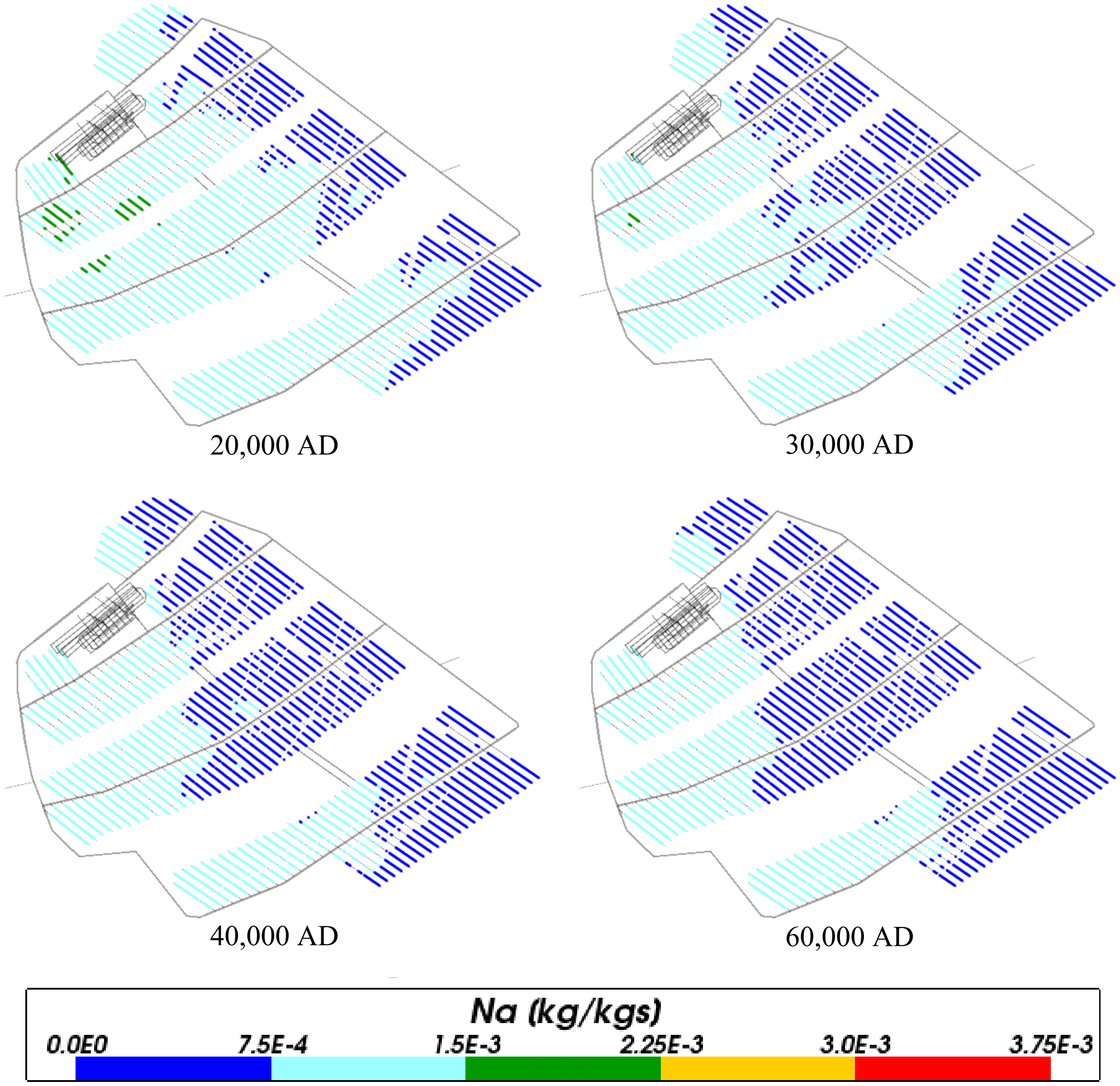

20,000 AD

30,000 AD

40,000 AD

60,000 AD

Figure 4-55. *Total sodium mass fractions for Case 2 at deposition hole locations for time periods 20,000 AD to 60,000 AD.*

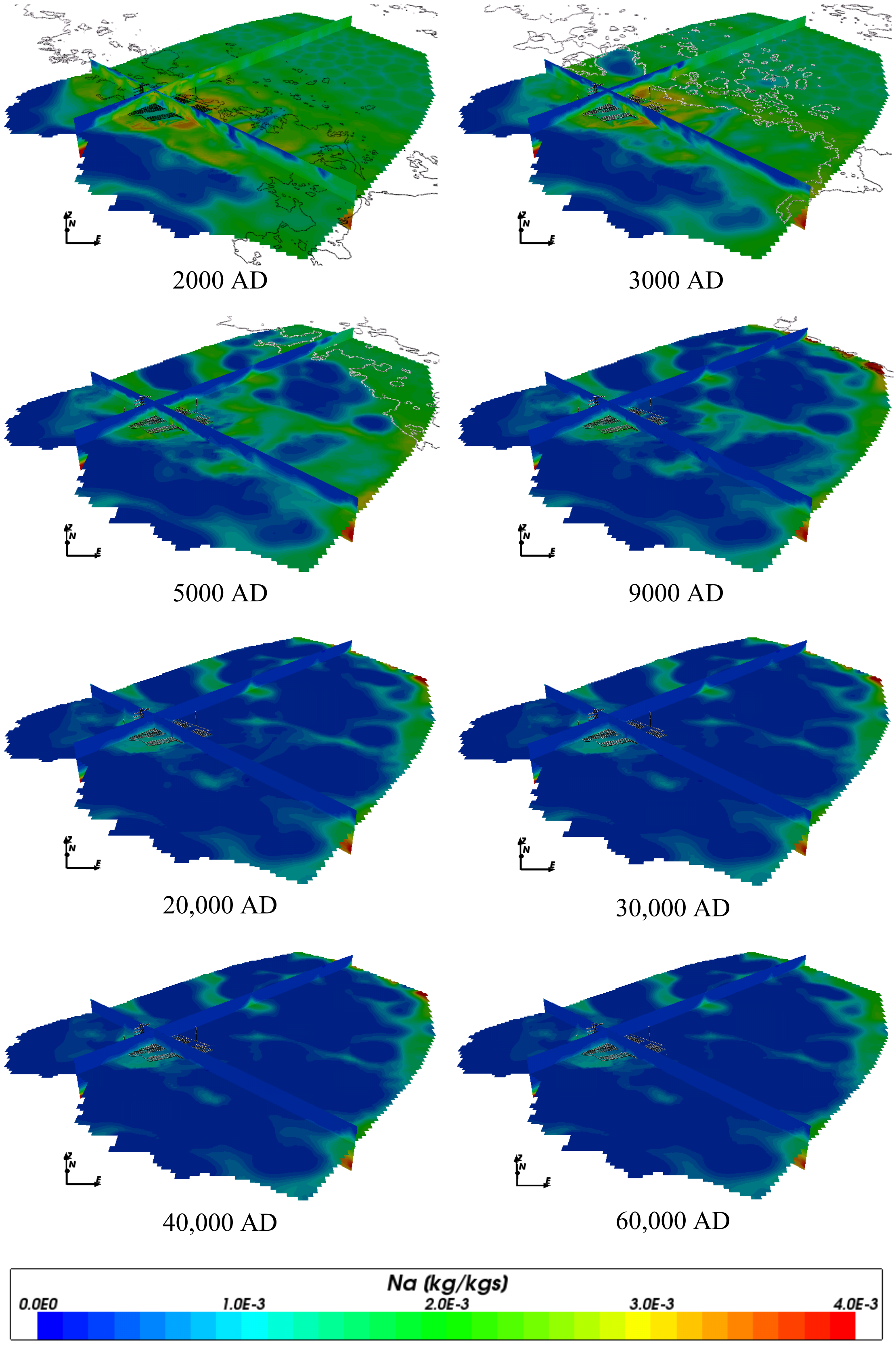

Figure 4-56. *Total sodium mass fractions on regional scale slices through the repository volume for Case 2 for time periods 2000 AD to 60,000 AD.*

4.3.9 Sulphate

Figure 4-57, Figure 4-58 and Figure 4-59 show the sulphate concentrations around the repository for Case 2. The mean concentrations and the spatial variability decrease over time and remain low for times after 20,000 AD.

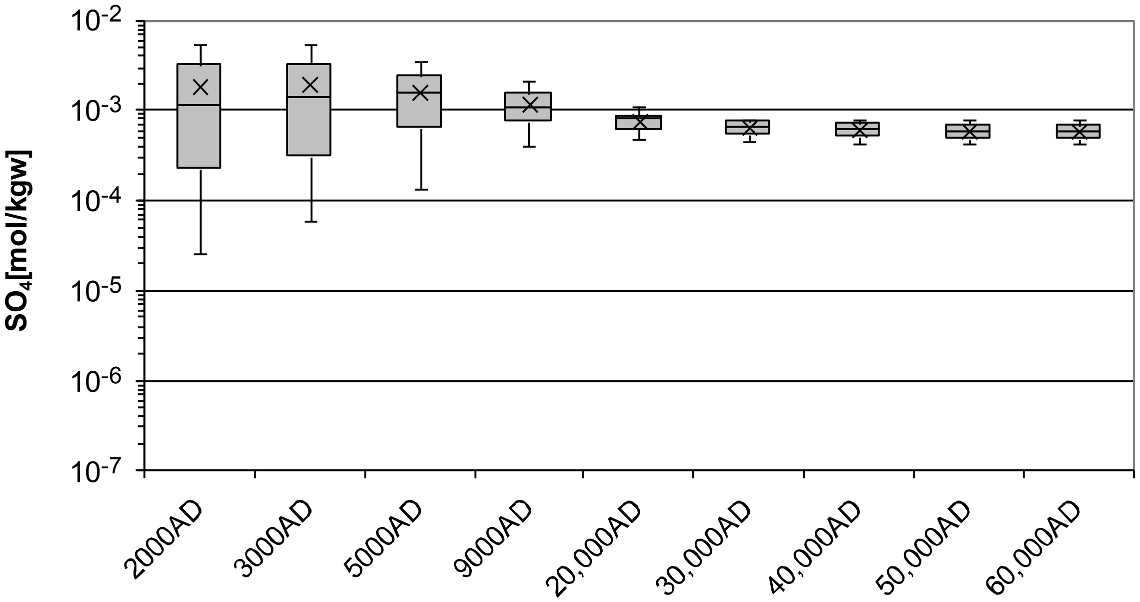

Figure 4-57. *Box and whisker plot showing the statistical distribution of sulphate molalities for Case 2 on a regular grid of points within the repository volume between elevations -490 m and -460 m. The statistical measures are the median, the 25th and 75th percentiles (box), the mean (cross) and the 5th and 95th percentiles (whiskers).*

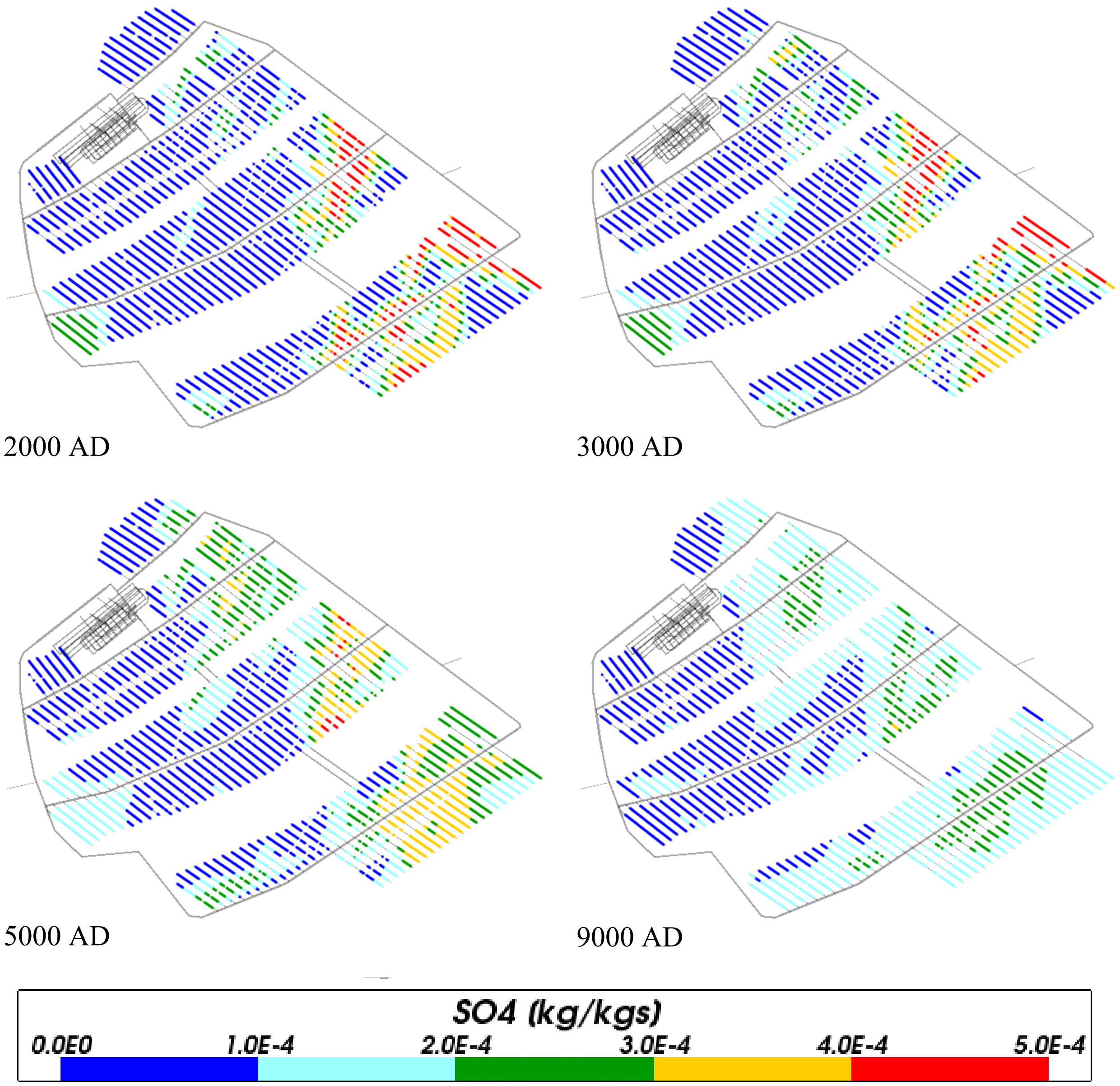

2000 AD

3000 AD

5000 AD

9000 AD

Figure 4-58. *Total sulphate mass fractions for Case 2 at deposition hole locations for time periods 2000 AD to 9000 AD.*

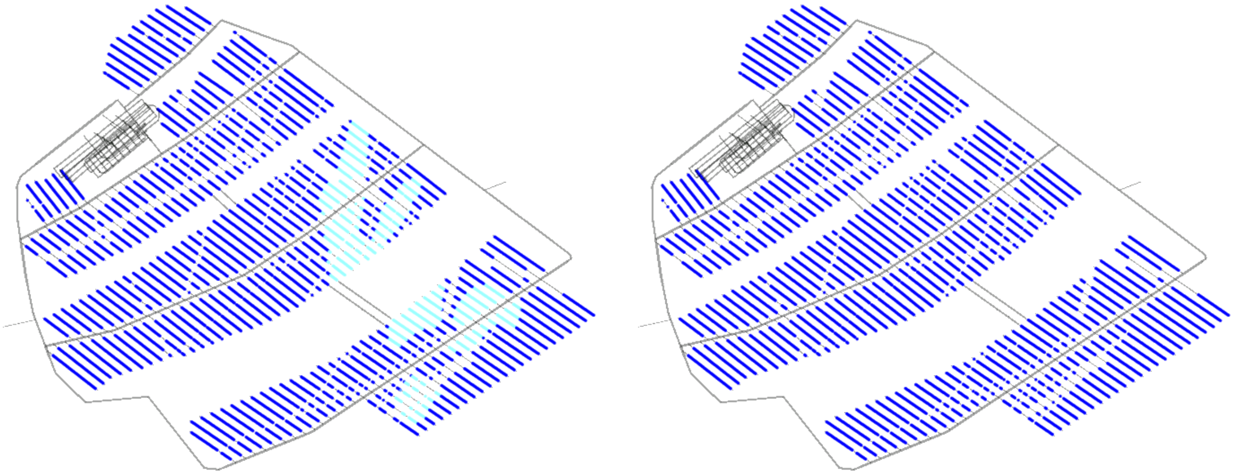

20,000 AD

30,000 AD

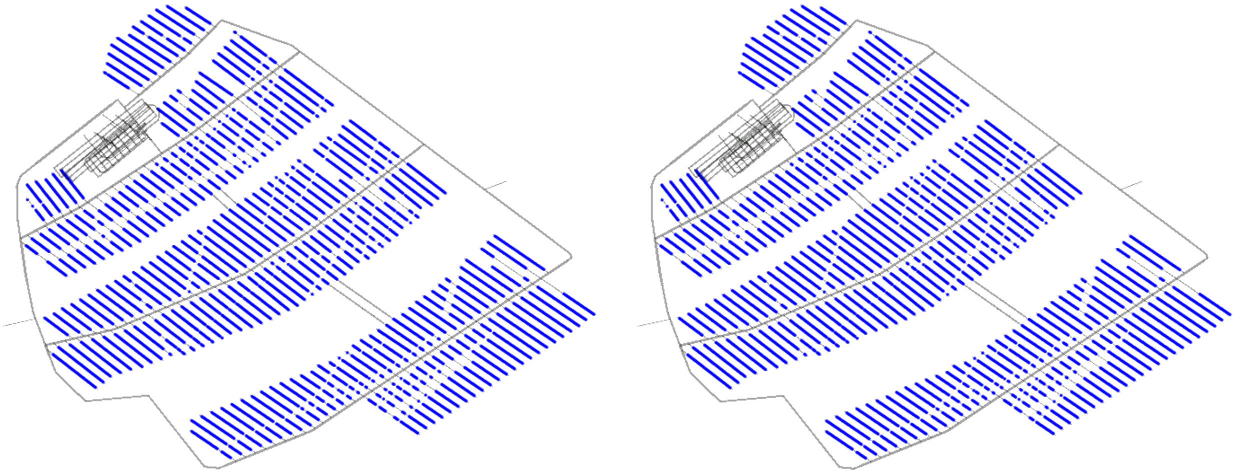

40,000 AD

60,000 AD

Figure 4-59. *Total sulphate mass fractions for Case 2 at deposition hole locations for time periods 20,000 AD to 60,000 AD.*

4.4 Case 3

The evolution of groundwater composition for this case will also be due to the transport and mixing of components originating from different reference waters. However, a different set of chemical reactions are considered for this case, which includes equilibration of groundwater with calcite, quartz and iron (III) oxyhydroxide. It is expected that the reactions will have an effect on pH, Eh, and the concentrations of total inorganic carbon, calcium, sulphur and iron.

The results for this case showed less penetration of meteoric water to repository depth compared to the other cases. These results are therefore more favourable from a safety assessment perspective. However, the simulations for this case had some numerical difficulties when carrying out the geochemical calculations at some locations within the model. Since this could potentially have an impact on groundwater transport and the evolution of the groundwater composition, these optimistic results will not be reported until further investigations have been carried out.

4.5 Case 4

The evolution of groundwater composition for this case will be due to the transport and mixing of components originating from different reference waters. The concentrations of reactive species will be modified by equilibrium reactions with the mineral phases considered. This case differs from previous cases in the number and types of mineral phases considered (see Section 3.2). Equilibration of groundwater with calcite, quartz, amorphous iron (II) sulphide, kaolinite, albite, and K-feldspar is considered. It is expected that the equilibrium reactions will have an effect on pH, Eh, and the concentrations of total inorganic carbon, sulphur, sodium, calcium and iron.

4.5.1 pH

Figure 4-60, Figure 4-61 and Figure 4-62 show a slight increase in pH over time around the repository for Case 4. This is the opposite trend as compared to previous cases, and is due to the different set of mineral equilibrium reactions considered. Figure 4-63 shows the evolution of pH on a regional scale for Case 4.

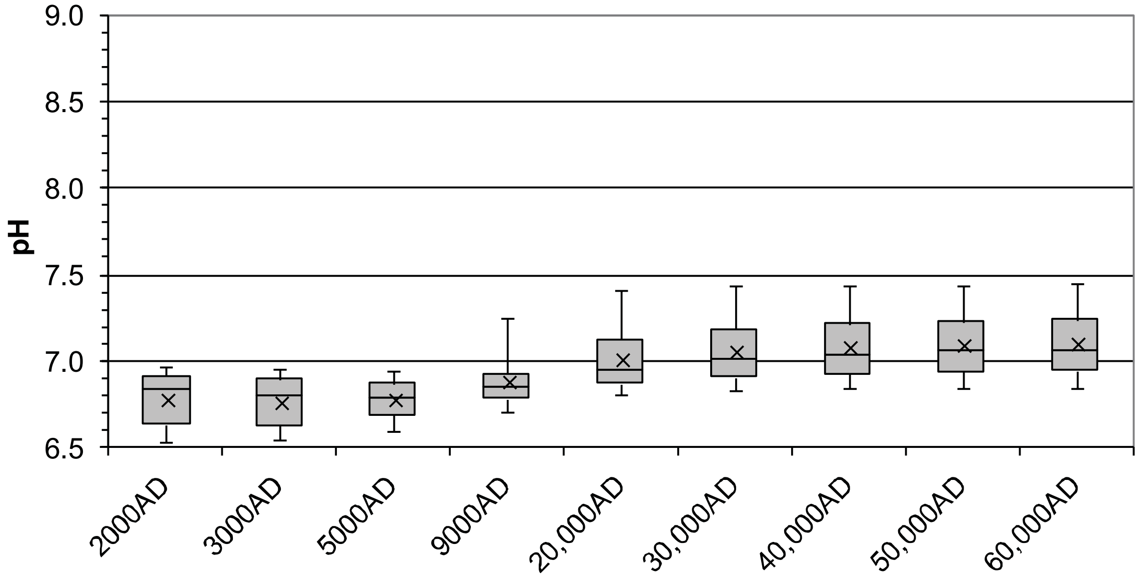

Figure 4-60. *Box and whisker plot showing the statistical distribution of pH for Case 4 on a regular grid of points within the repository volume between elevations -490 m and -460 m. The statistical measures are the median, the 25th and 75th percentiles (box), the mean (cross) and the 5th and 95th percentiles (whiskers).*

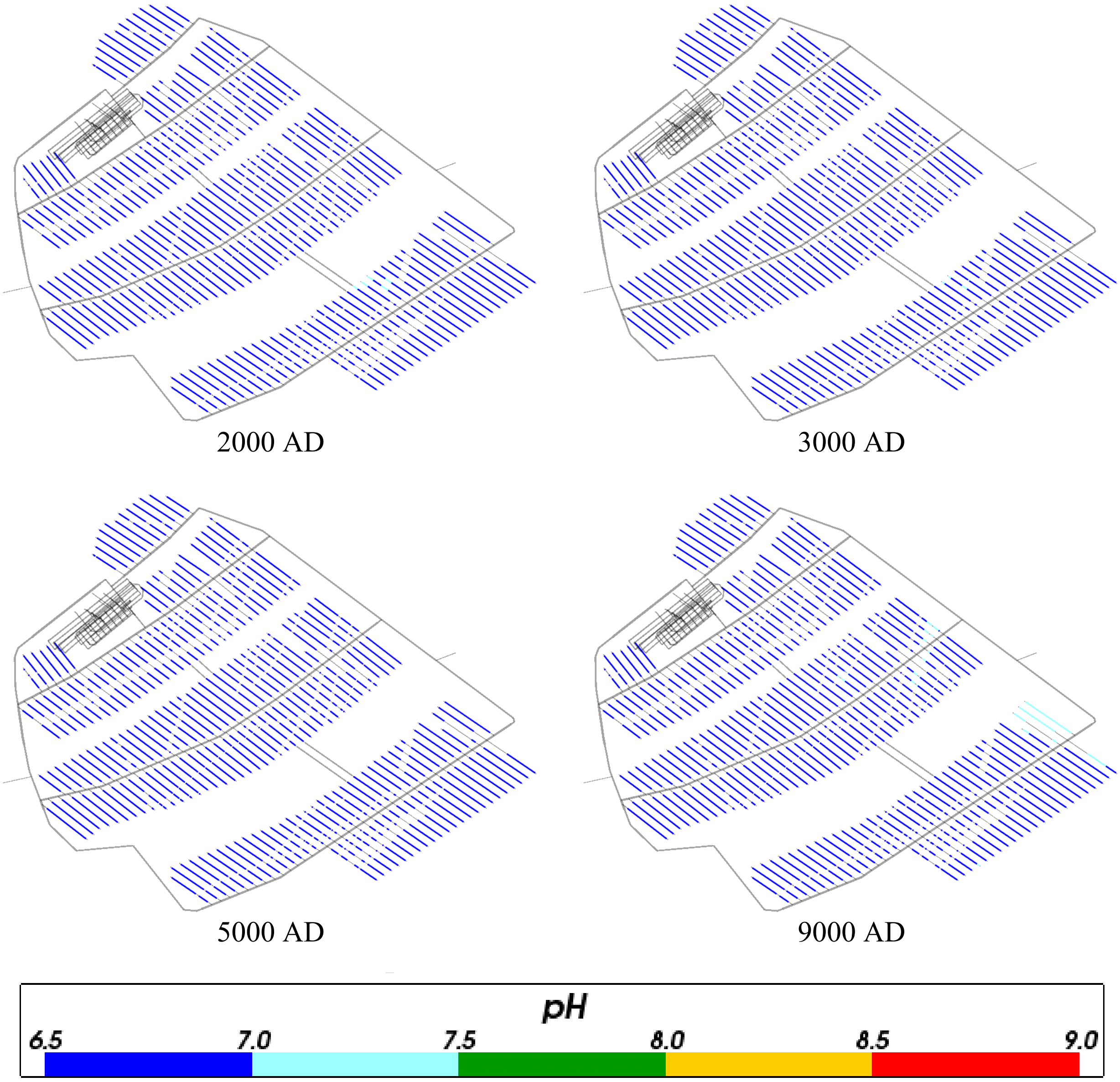

2000 AD

3000 AD

5000 AD

9000 AD

Figure 4-61. *Values of pH for Case 4 at deposition hole locations for time periods 2000 AD to 9000 AD.*

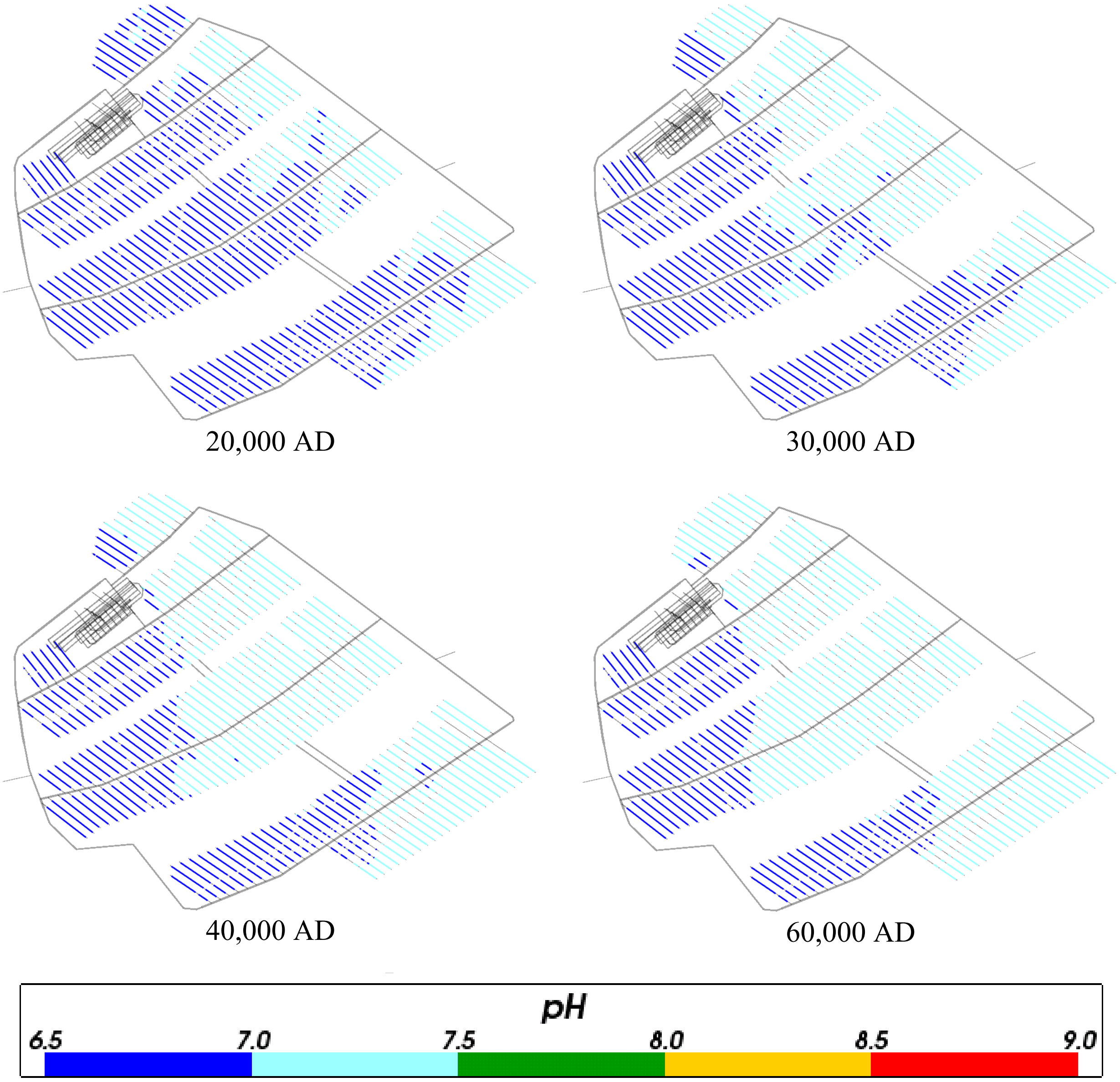

Figure 4-62. *Values of pH for Case 4 at deposition hole locations for time periods 20,000 AD to 60,000 AD.*

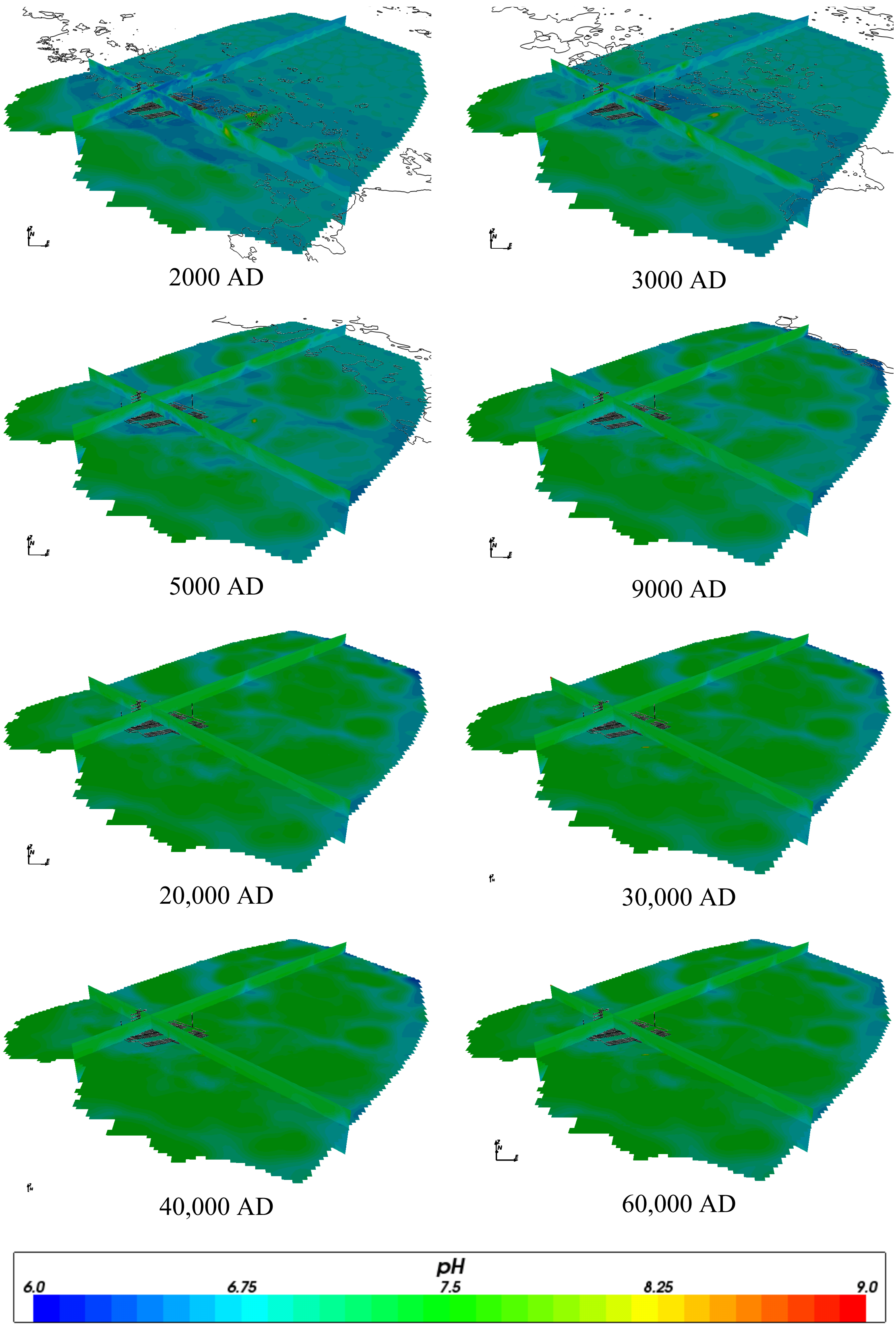

Figure 4-63. *Values of pH on regional scale slices through the repository volume for Case 4 for time periods 2000 AD to 60,000 AD.*

4.5.2 Eh (or pe)

Figure 4-64 shows the statistical distribution of Eh around the repository and Figure 4-65 and Figure 4-66 show the value of pe in the deposition hole locations. The mean value of pe increases slightly up to 5000 AD after which the spatial variability decreases and the mean value drops slightly over time.

The trend of decreasing spatial variability after 5000 AD is also evident from Figure 4-67 which shows the value of pe on the slices covering the model area.

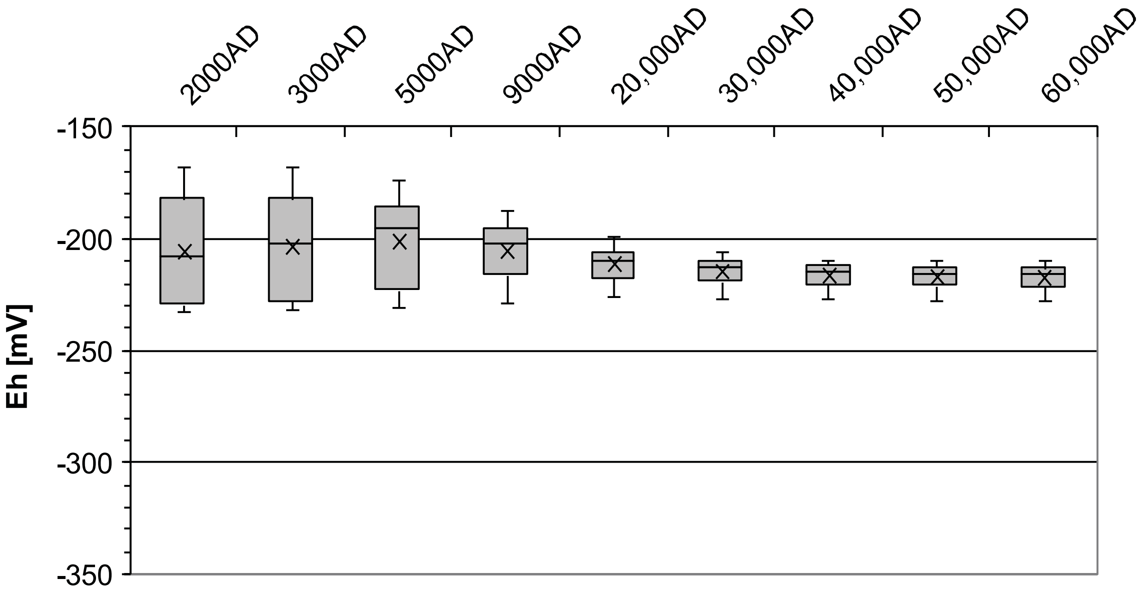

Figure 4-64. *Box and whisker plot showing the statistical distribution of Eh for Case 4 on a regular grid of points within the repository volume between elevations -490 m and -460 m. The statistical measures are the median, the 25th and 75th percentiles (box), the mean (cross) and the 5th and 95th percentiles (whiskers).*

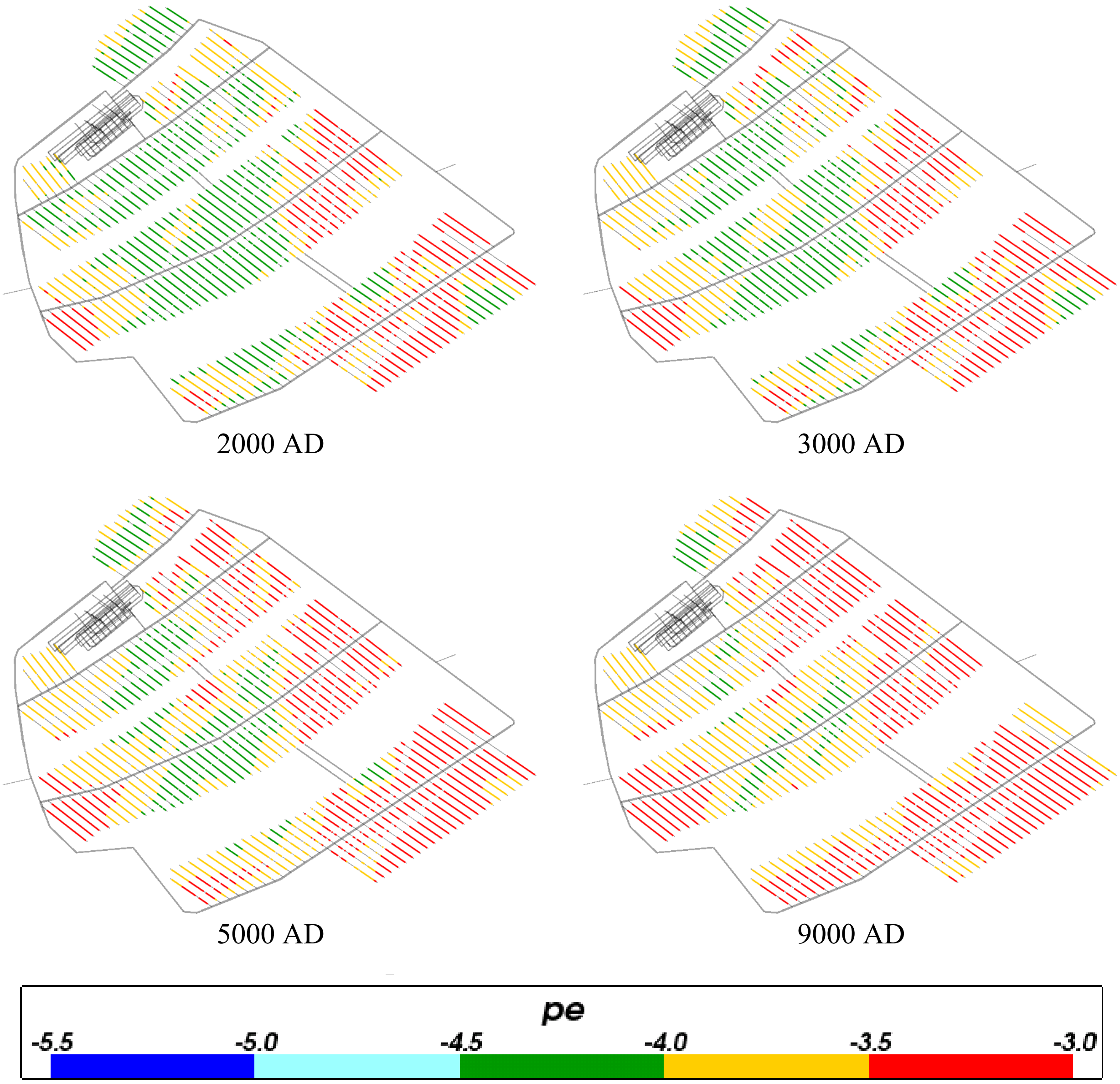

Figure 4-65. *Values of pe for Case 4 at deposition hole locations for time periods 2000 AD to 9000 AD.*

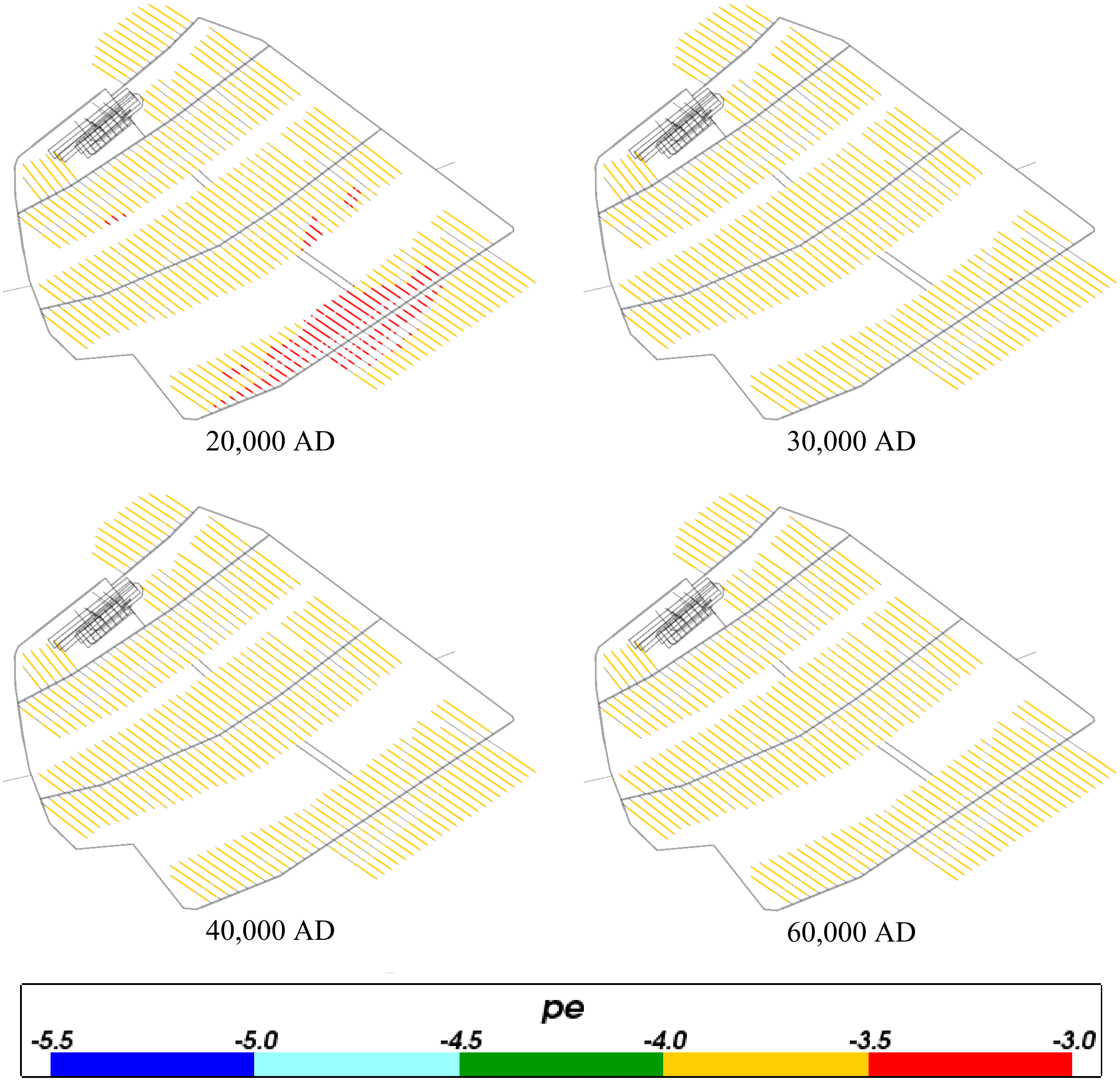

20,000 AD

30,000 AD

40,000 AD

60,000 AD

Figure 4-66. *Values of pe for Case 4 at deposition hole locations for time periods 20,000 AD to 60,000 AD.*

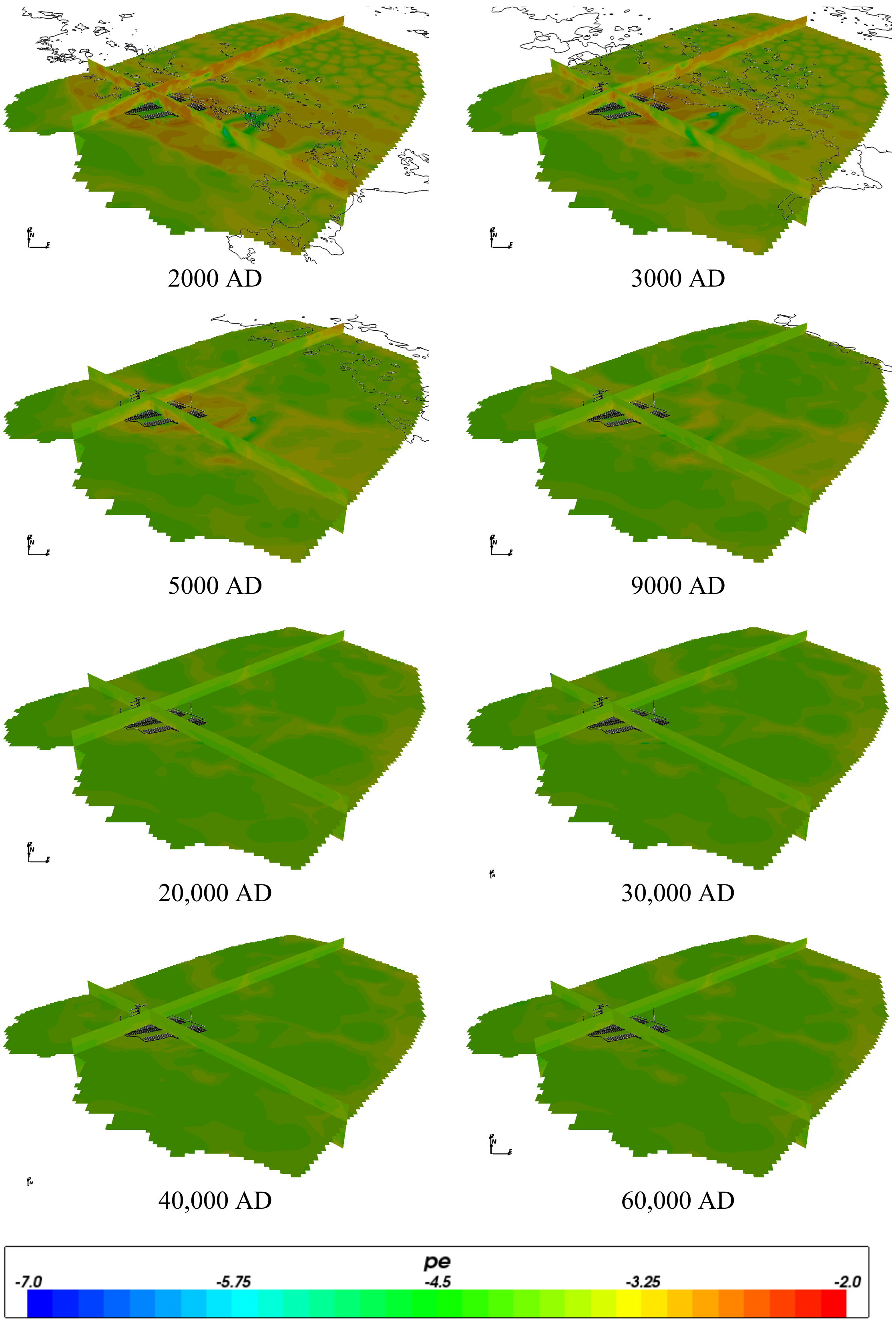

2000 AD

3000 AD

5000 AD

9000 AD

20,000 AD

30,000 AD

40,000 AD

60,000 AD

Figure 4-67. *Values of pe on regional scale slices through the repository volume for Case 4 for time periods 2000 AD to 60,000 AD.*

4.5.3 TDS and sum of cations

Figure 4-68 and Figure 4-69 show the statistical distribution of TDS and the sum of cation molalities around the repository for Case 4. As for the previous cases, the plots are closely related, with the sum of cations plot mirroring the TDS plot. The TDS and sum of cations do reduce significantly over time as for Cases 1 and 2, and tend to level out after 30,000 AD.

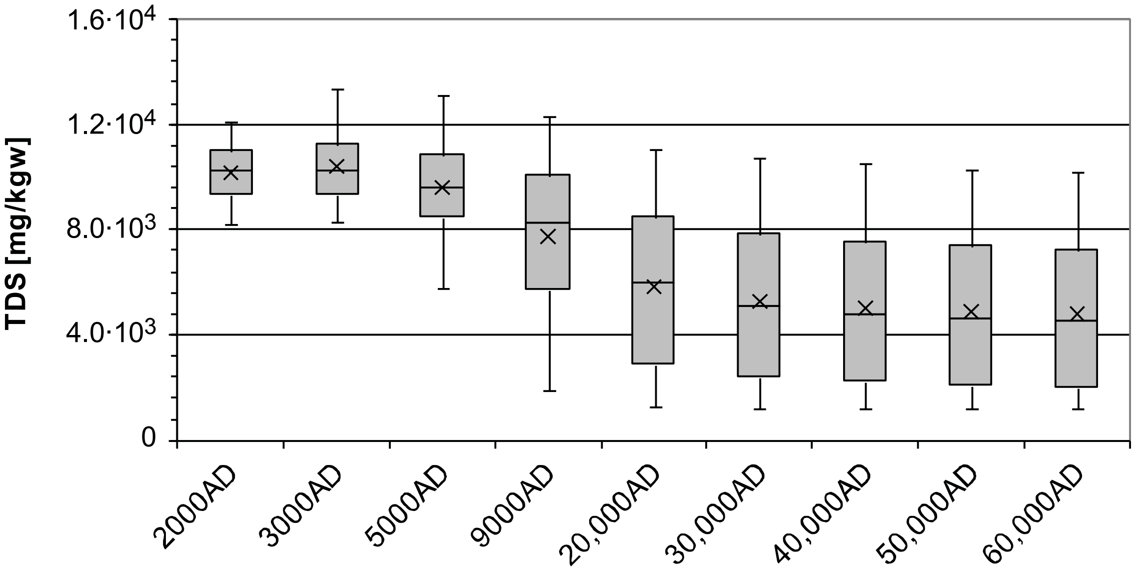

Figure 4-68. *Box and whisker plot showing the statistical distribution of TDS for Case 4 on a regular grid of points within the repository volume between elevations -490 m and -460 m. The statistical measures are the median, the 25th and 75th percentiles (box), the mean (cross) and the 5th and 95th percentiles (whiskers).*

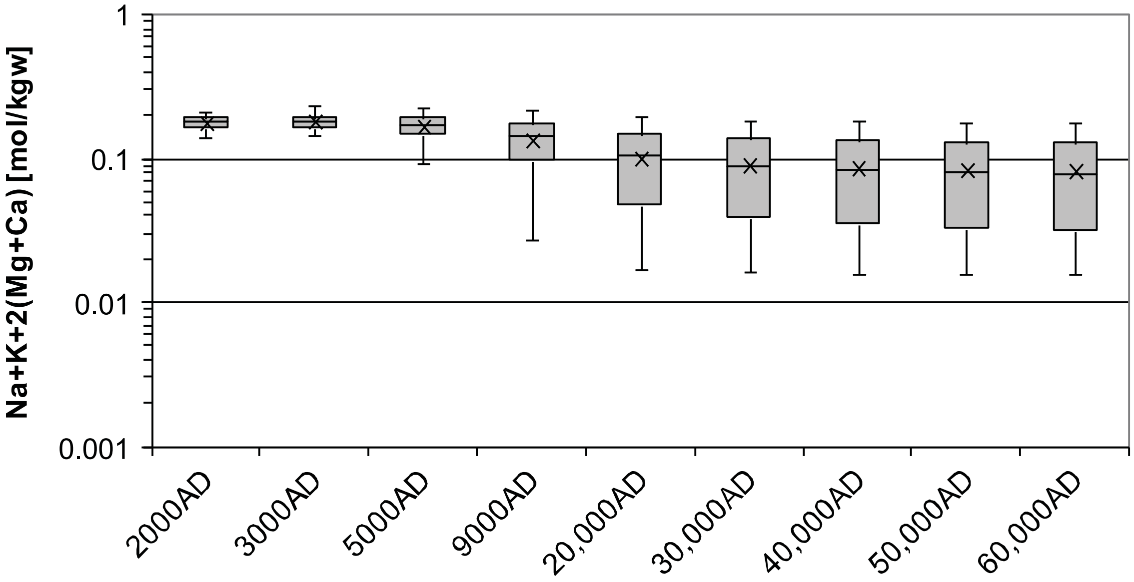

Figure 4-69. *Box and whisker plot showing the statistical distribution of sum of cation charges (Na+K+2(Mg+Ca)) molalities for Case 4 on a regular grid of points within the repository volume between elevations -490 m and -460 m. The statistical measures are*

the median, the 25th and 75th percentiles (box), the mean (cross) and the 5th and 95th percentiles (whiskers).

4.5.4 Carbon

Figure 4-70, Figure 4-71 and Figure 4-72 show the concentrations of total inorganic carbon around the repository for Case 4. Unlike the previous cases the mean value of total inorganic carbon molalities decreases over time, and show a larger spatial variability at the early times up to 9000 AD. The spatial distribution is similar to previous cases with predominance of higher values at the north to north-east part of the repository, but the concentration span and mean value up to 9000 AD is significantly larger in Case 4. At later times, Case 4 show lower total inorganic carbon concentrations in the deposition holes than Cases 1 and 2.

Figure 4-73 shows the evolution of carbon over time on a regional scale. A much higher spatial variability is evident in total inorganic carbon concentrations at the early times as compared to the previous cases. Strong depth dependence is apparent from the figure, in particular during early times, with high total inorganic carbon concentrations at the surface and decreasing with depth.

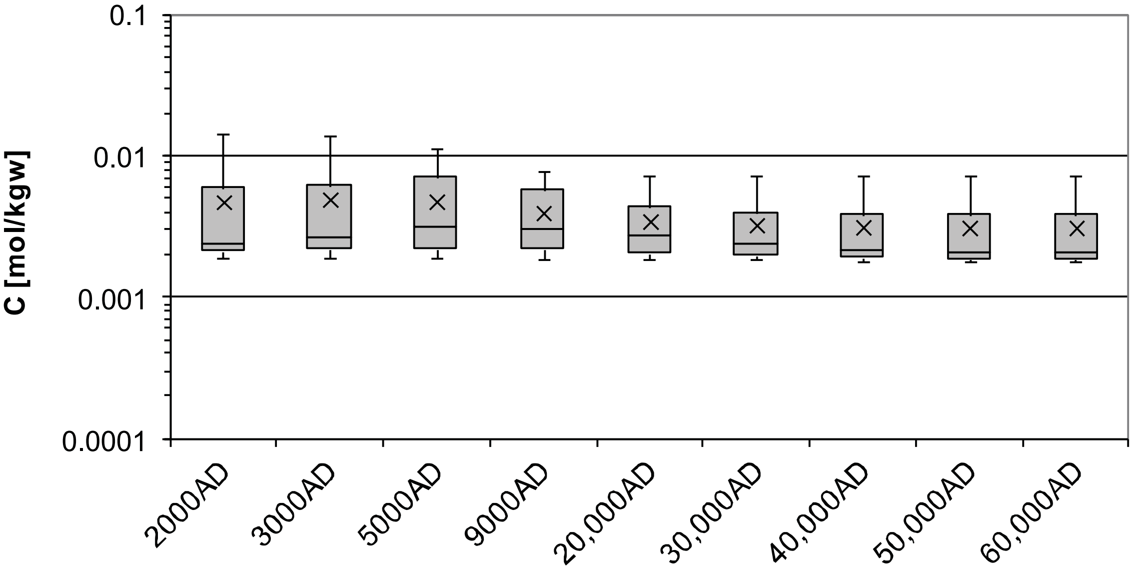

Figure 4-70. *Box and whisker plot showing the statistical distribution of total inorganic carbon molalities for Case 4 on a regular grid of points within the repository volume between elevations -490 m and -460 m. The statistical measures are the median, the 25th and 75th percentiles (box), the mean (cross) and the 5th and 95th percentiles (whiskers).*

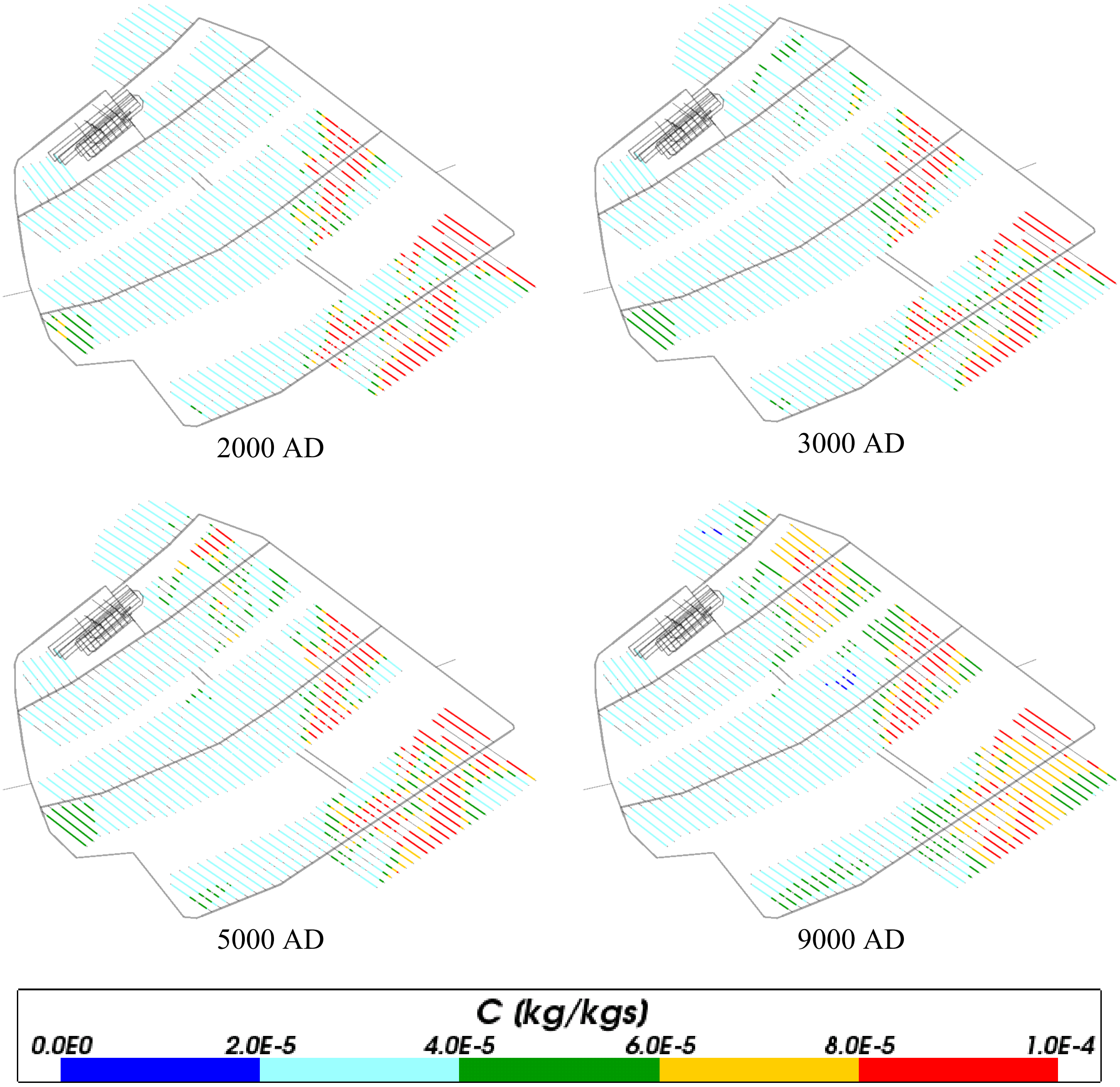

Figure 4-71. *Total inorganic carbon mass fractions for Case 4 at deposition hole locations for time periods 2000 AD to 9000 AD.*

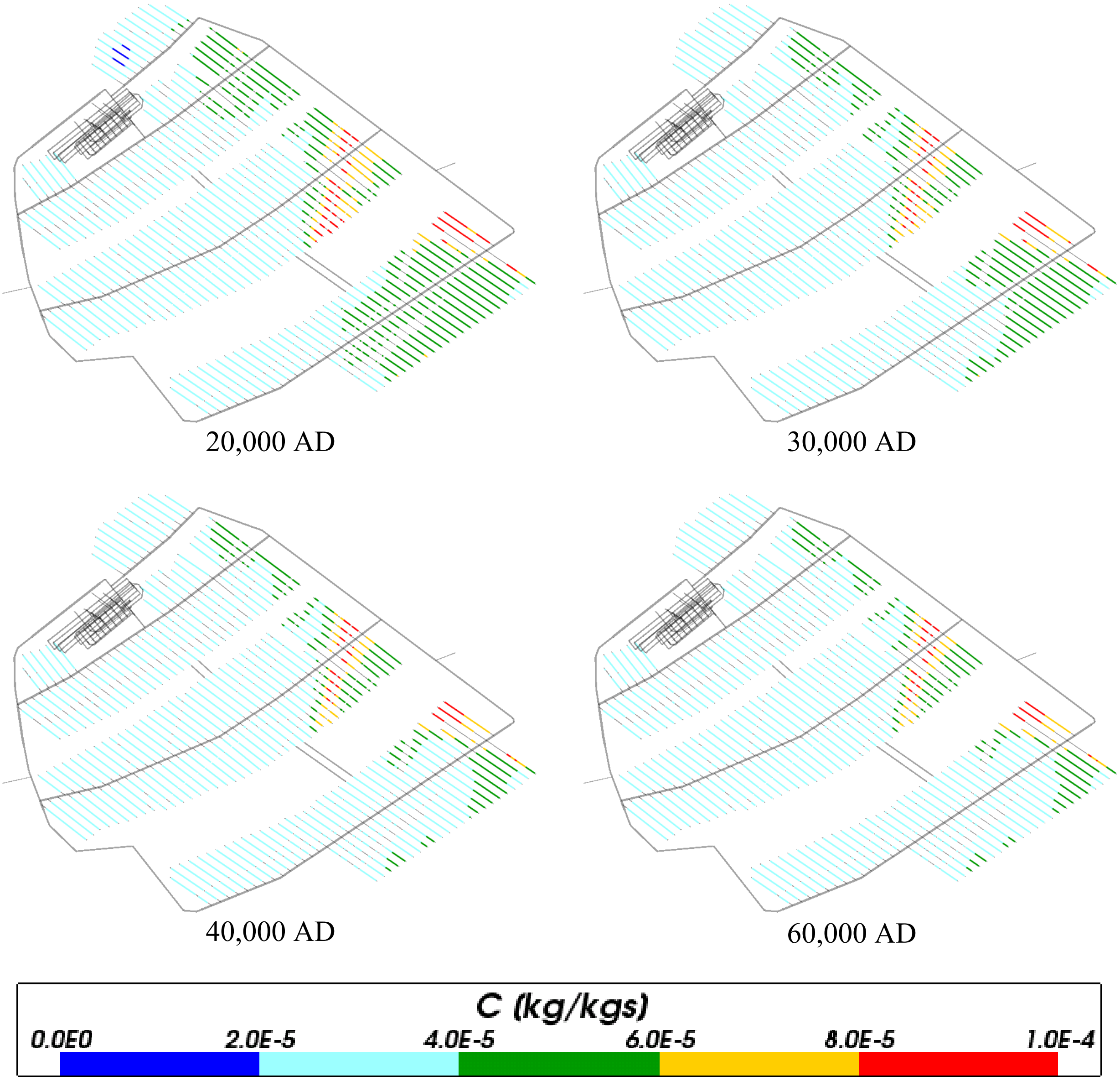

Figure 4-72. *Total inorganic carbon mass fractions for Case 4 at deposition hole locations for time periods 20,000 AD to 60,000 AD.*

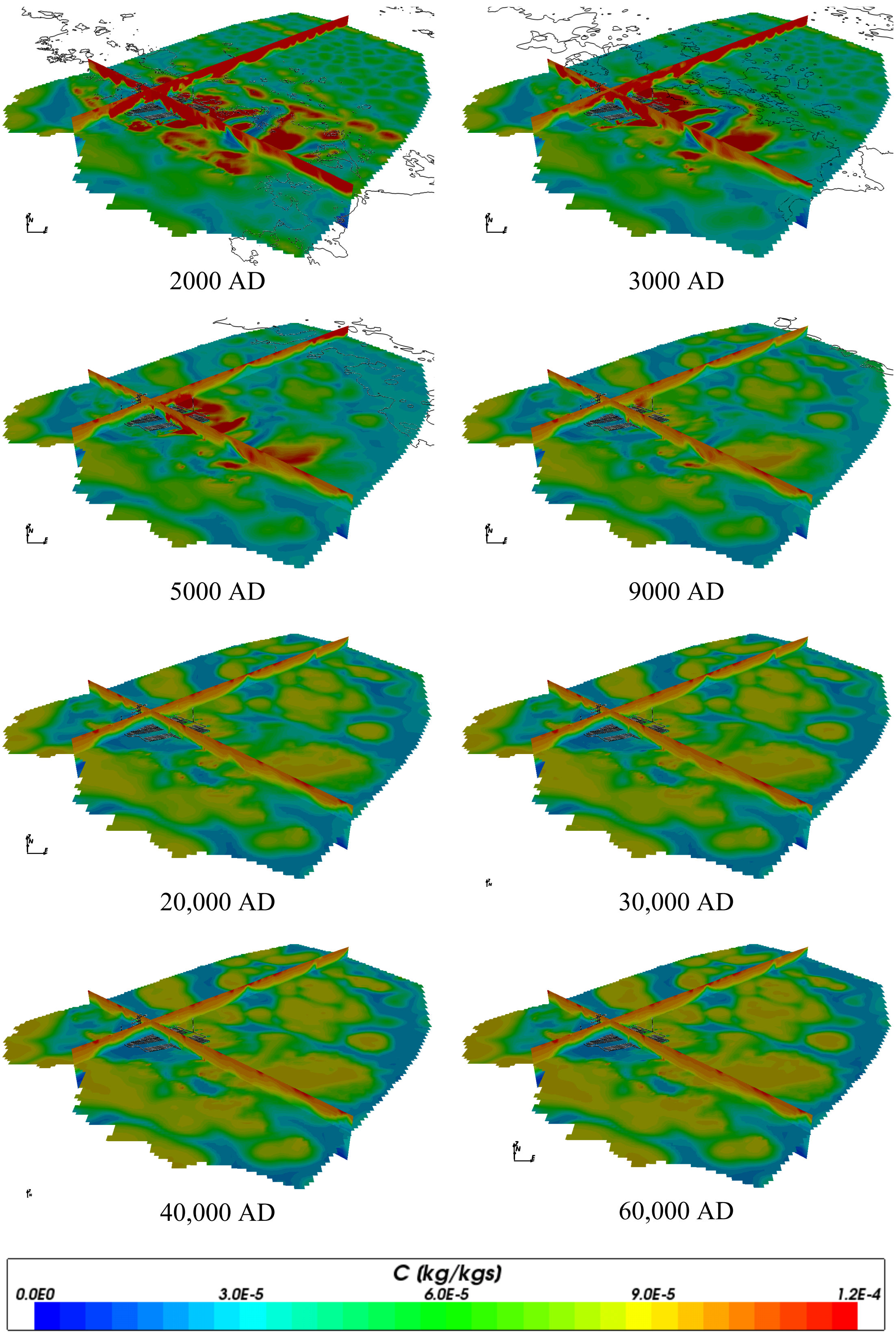
2000 AD

3000 AD

5000 AD

9000 AD

20,000 AD

30,000 AD

40,000 AD

60,000 AD

Figure 4-73. *Total inorganic carbon mass fractions on regional scale slices through the repository volume for Case 4 for time periods 2000 AD to 60,000 AD.*

4.5.5 Calcium

The values for calcium concentrations around the repository (Figure 4-74, Figure 4-75 and Figure 4-76) for Case 4 is very similar to that of Cases 1 and 2 with a trend of calcium decreasing with time. The ranges of values at each time are also similar to Cases 1 and 2.

Figure 4-77 shows the evolution of calcium over time on the regional scale. These results are also very similar to those of Cases 1 and 2. The close similarity with Case 1 indicates that the chemical reactions considered in Case 4 have only minor influence on the calcium concentrations.

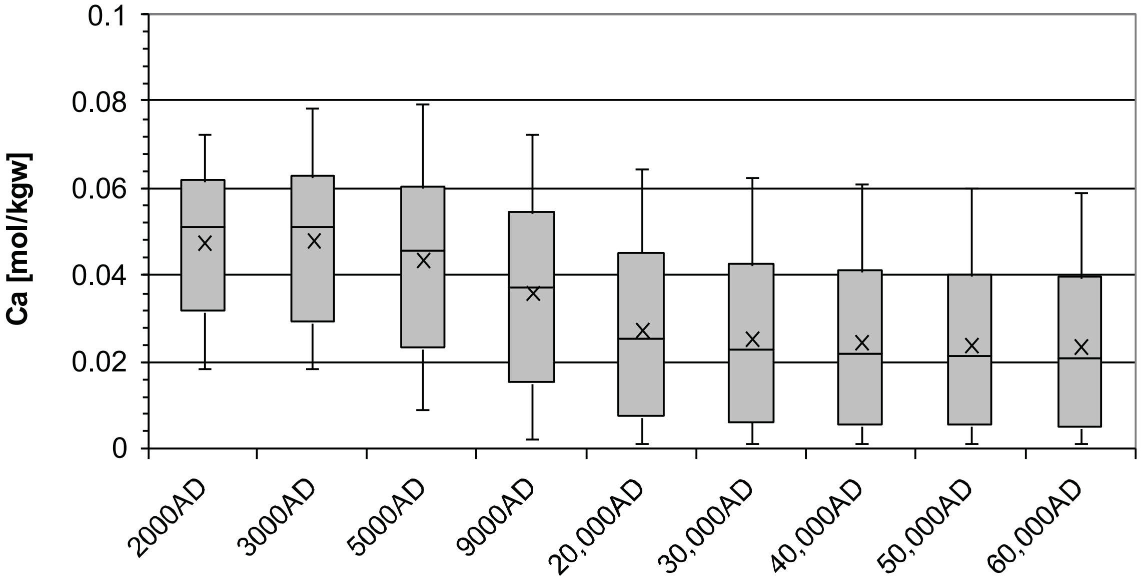

Figure 4-74. *Box and whisker plot showing the statistical distribution of total calcium molalities for Case 4 on a regular grid of points within the repository volume between elevations -490 m and -460 m. The statistical measures are the median, the 25th and 75th percentiles (box), the mean (cross) and the 5th and 95th percentiles (whiskers).*

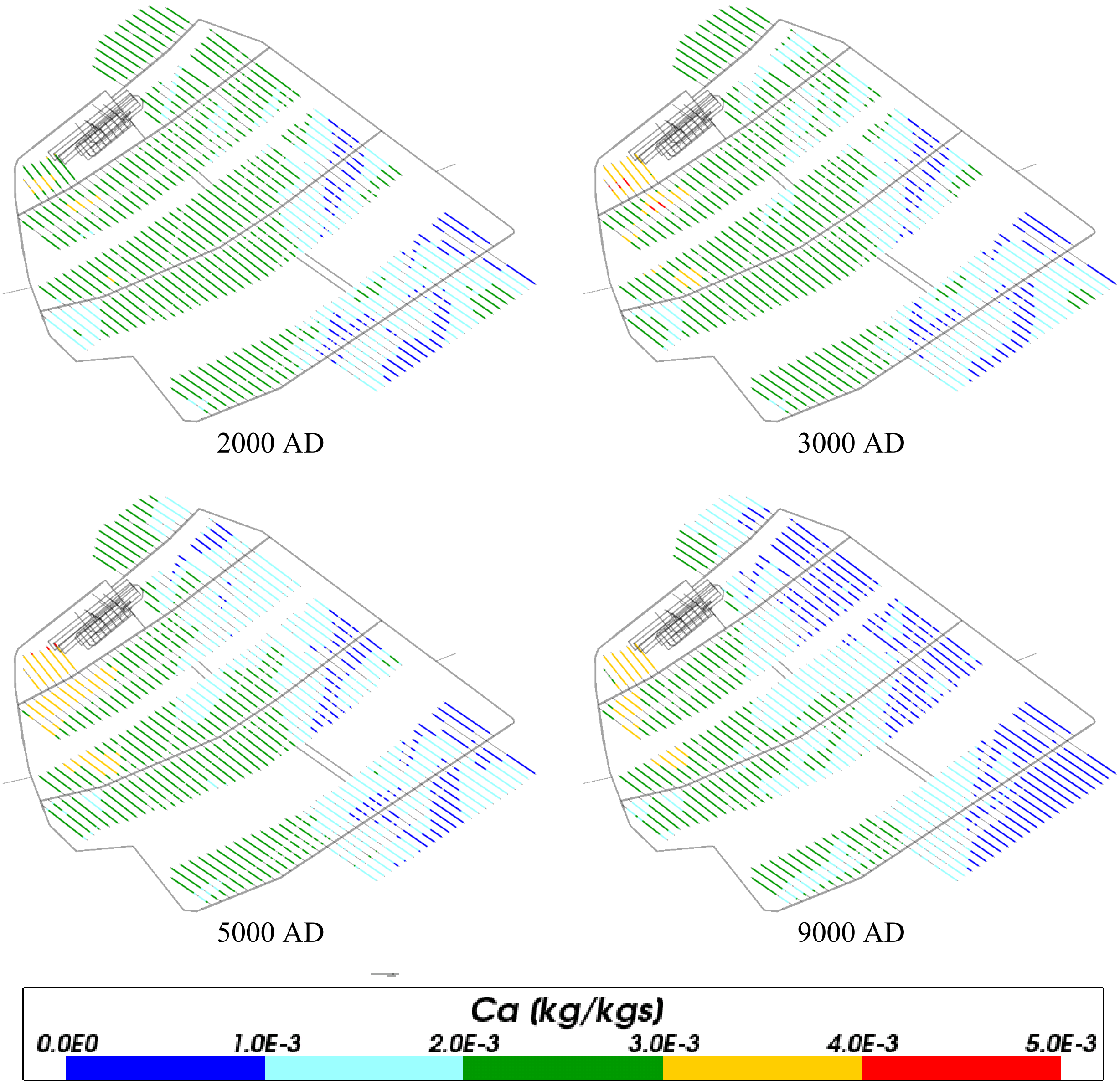
2000 AD

3000 AD

5000 AD

9000 AD

Figure 4-75. *Total calcium mass fractions for Case 4 at deposition hole locations for time periods 2000 AD to 9000 AD.*

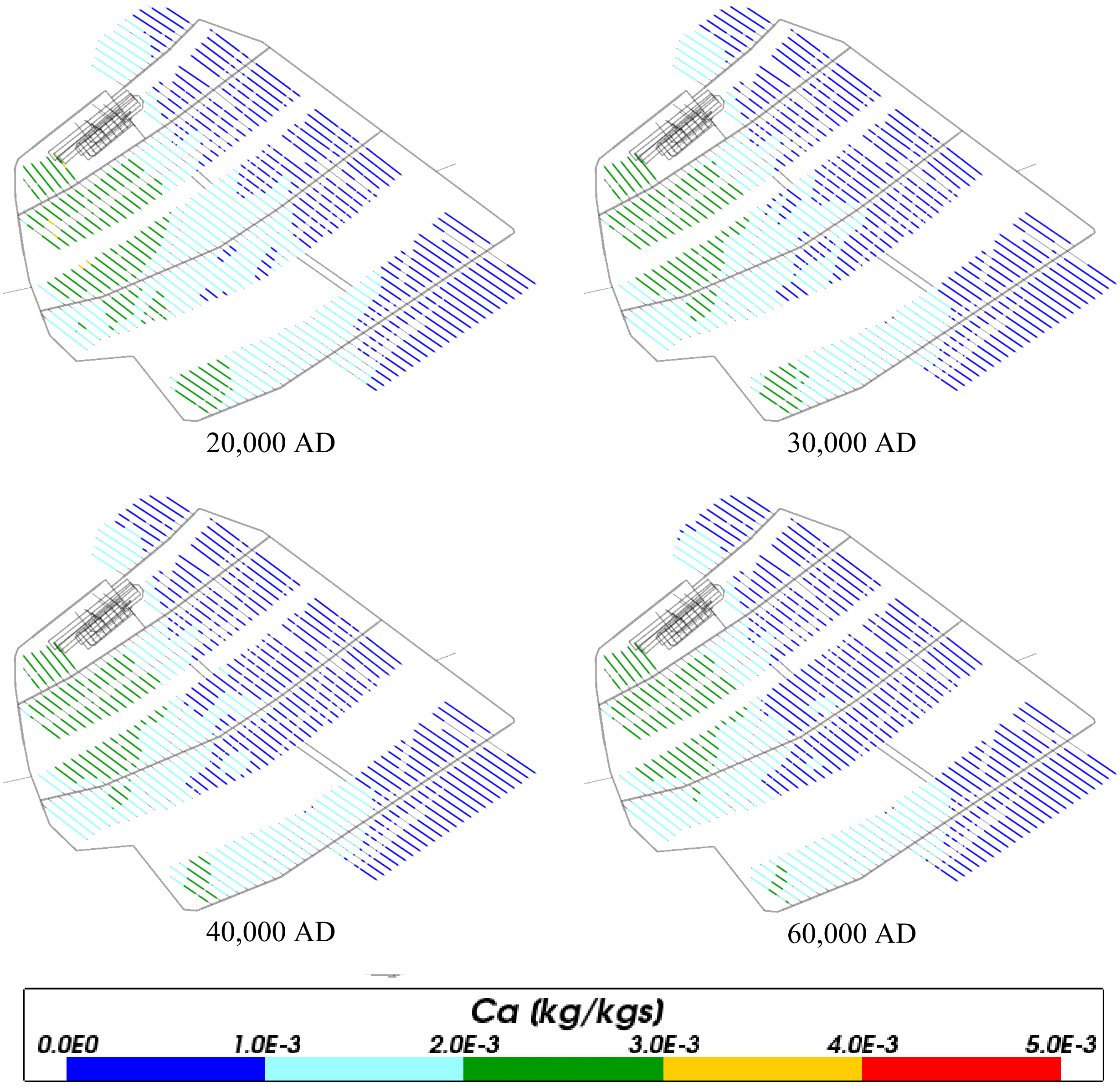

Figure 4-76. *Total calcium mass fractions for Case 4 at deposition hole locations for time periods 20,000 AD to 60,000 AD.*

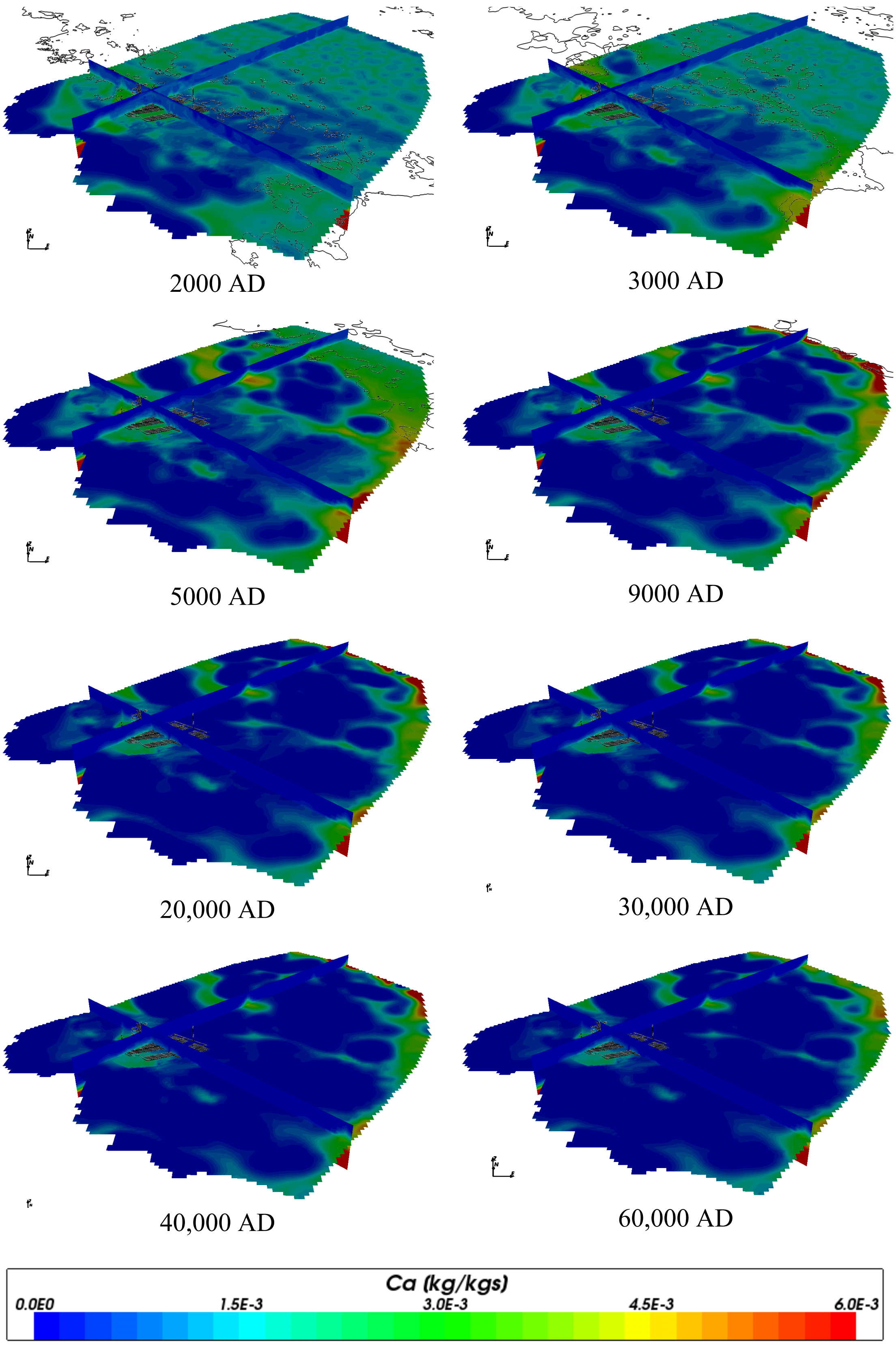
2000 AD

3000 AD

5000 AD

9000 AD

20,000 AD

30,000 AD

40,000 AD

60,000 AD

Figure 4-77. *Total calcium mass fractions on regional scale slices through the repository volume for Case 4 for time periods 2000 AD to 60,000 AD.*

4.5.6 Chloride

Figure 4-78, Figure 4-79 and Figure 4-80 show the chloride concentrations around the repository. Mean and median values of chloride concentrations decrease over time and the result are very similar to those seen for Cases 1 and 2. Also the spatial variability in the repository volume in Figure 4-79 and Figure 4-80 and in the model volume in Figure 4-81 is very similar to Cases 1 and 2. This similarity indicates that chemical reactions considered in Case 4 have no significant influence on the chloride concentrations.

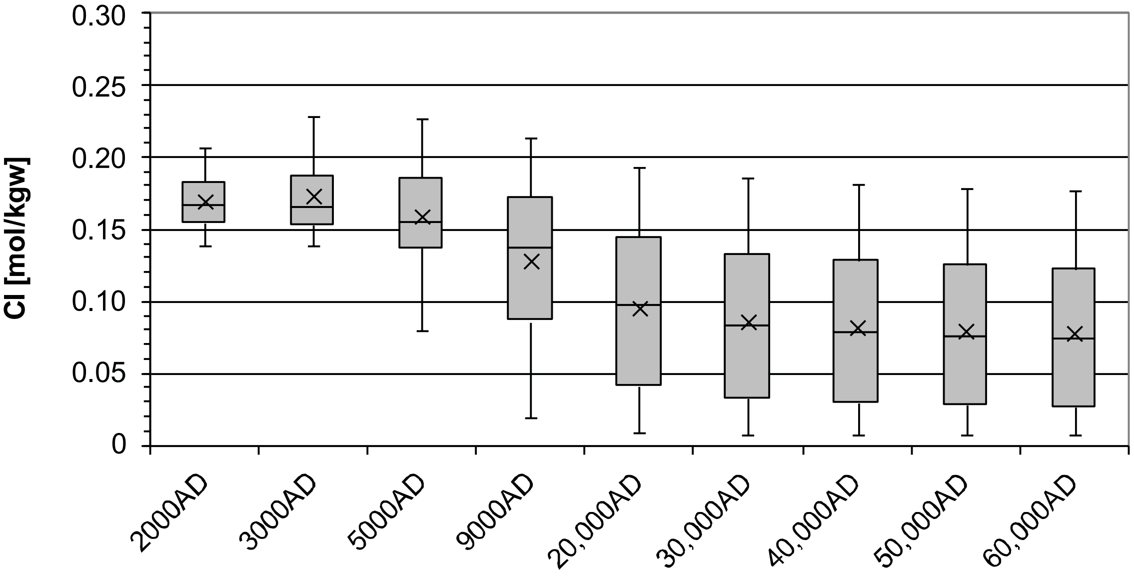

Figure 4-78. *Box and whisker plot showing the statistical distribution of total chloride molalities for Case 4 on a regular grid of points within the repository volume between elevations -490 m and -460 m. The statistical measures are the median, the 25th and 75th percentiles (box), the mean (cross) and the 5th and 95th percentiles (whiskers).*

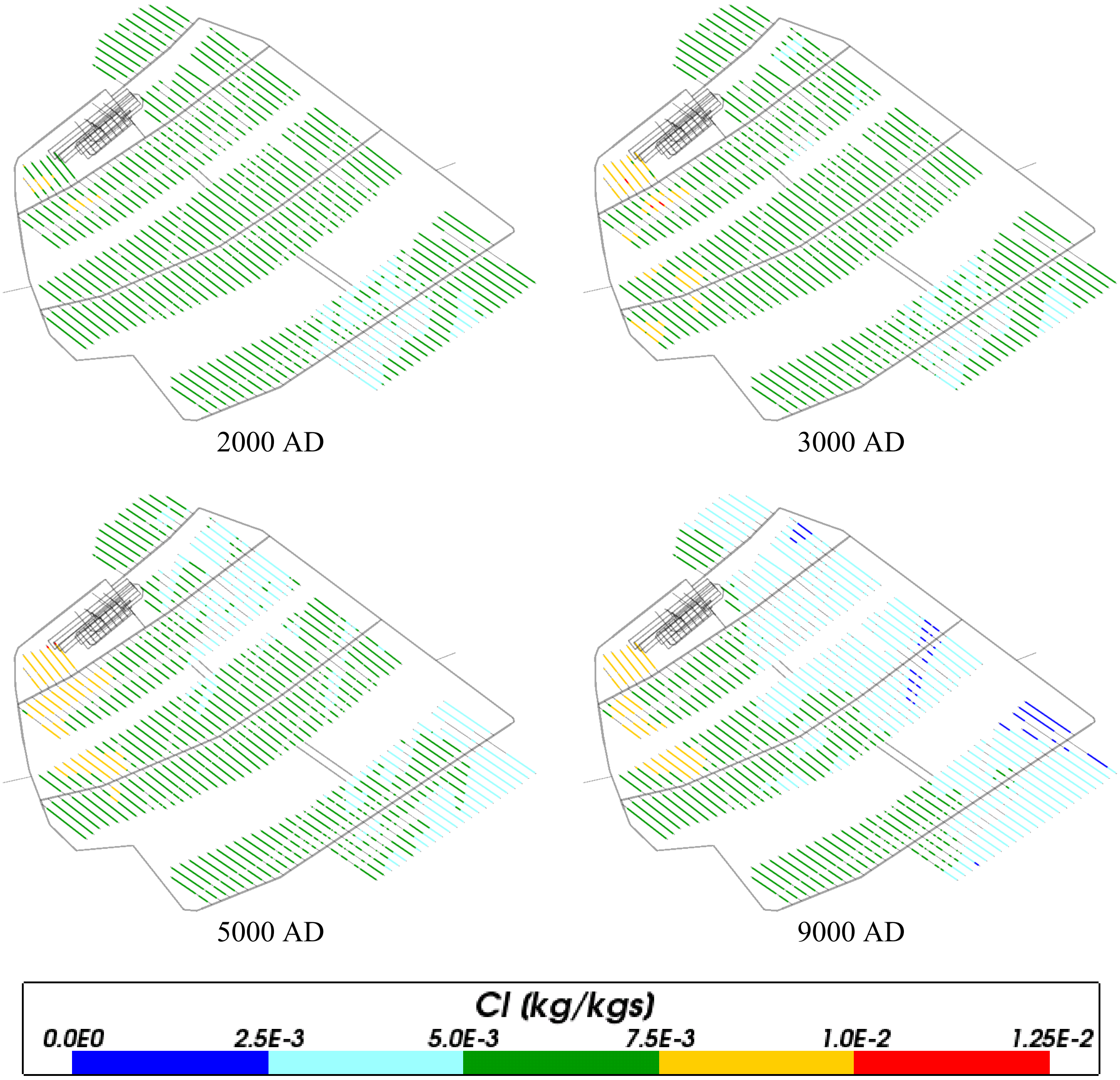

2000 AD

3000 AD

5000 AD

9000 AD

Figure 4-79. *Total chloride mass fractions for Case 4 at deposition hole locations for time periods 2000 AD to 9000 AD.*

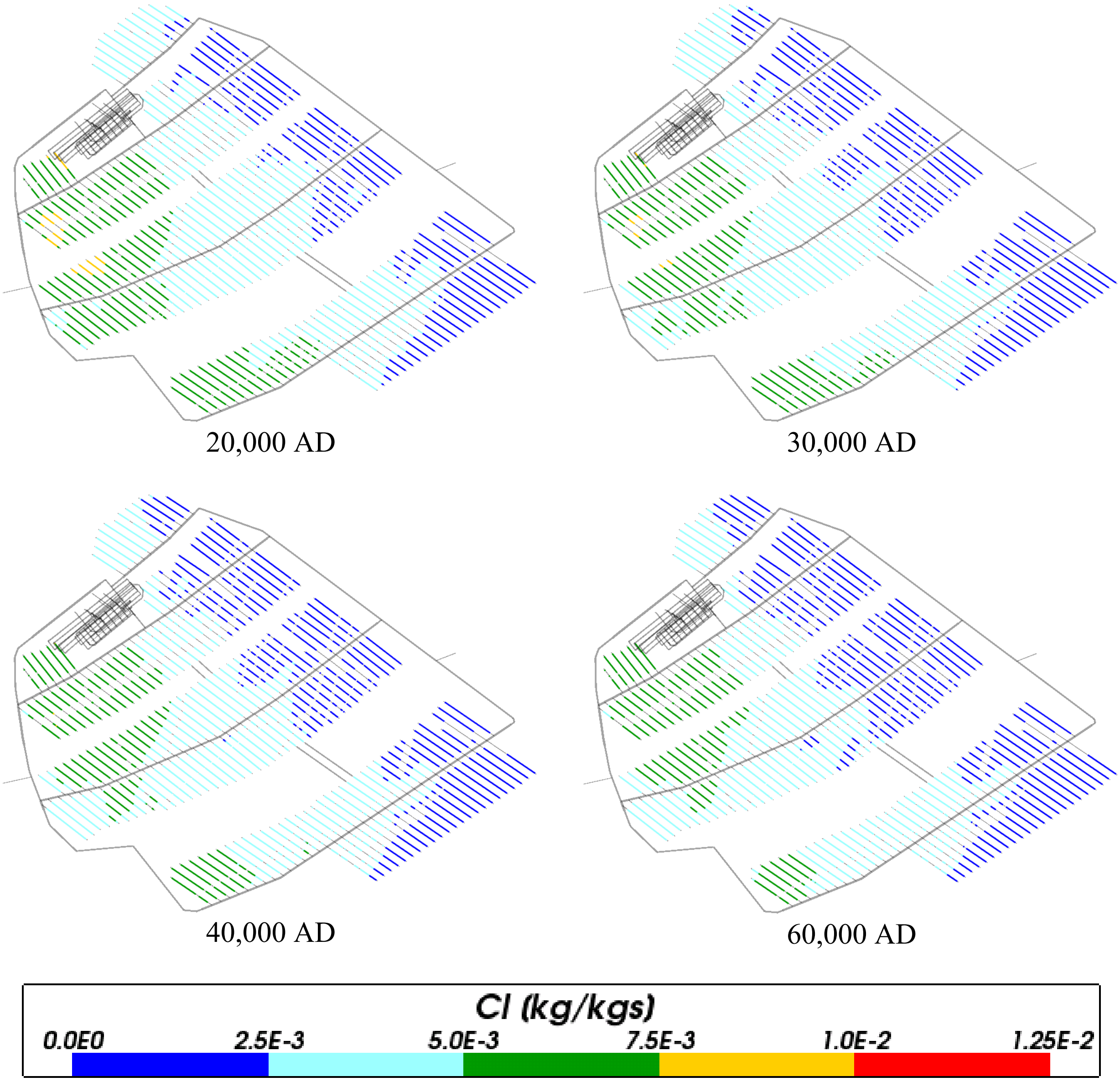

20,000 AD

30,000 AD

40,000 AD

60,000 AD

Figure 4-80. *Total chloride mass fractions for Case 4 at deposition hole locations for time periods 20,000 AD to 60,000 AD.*

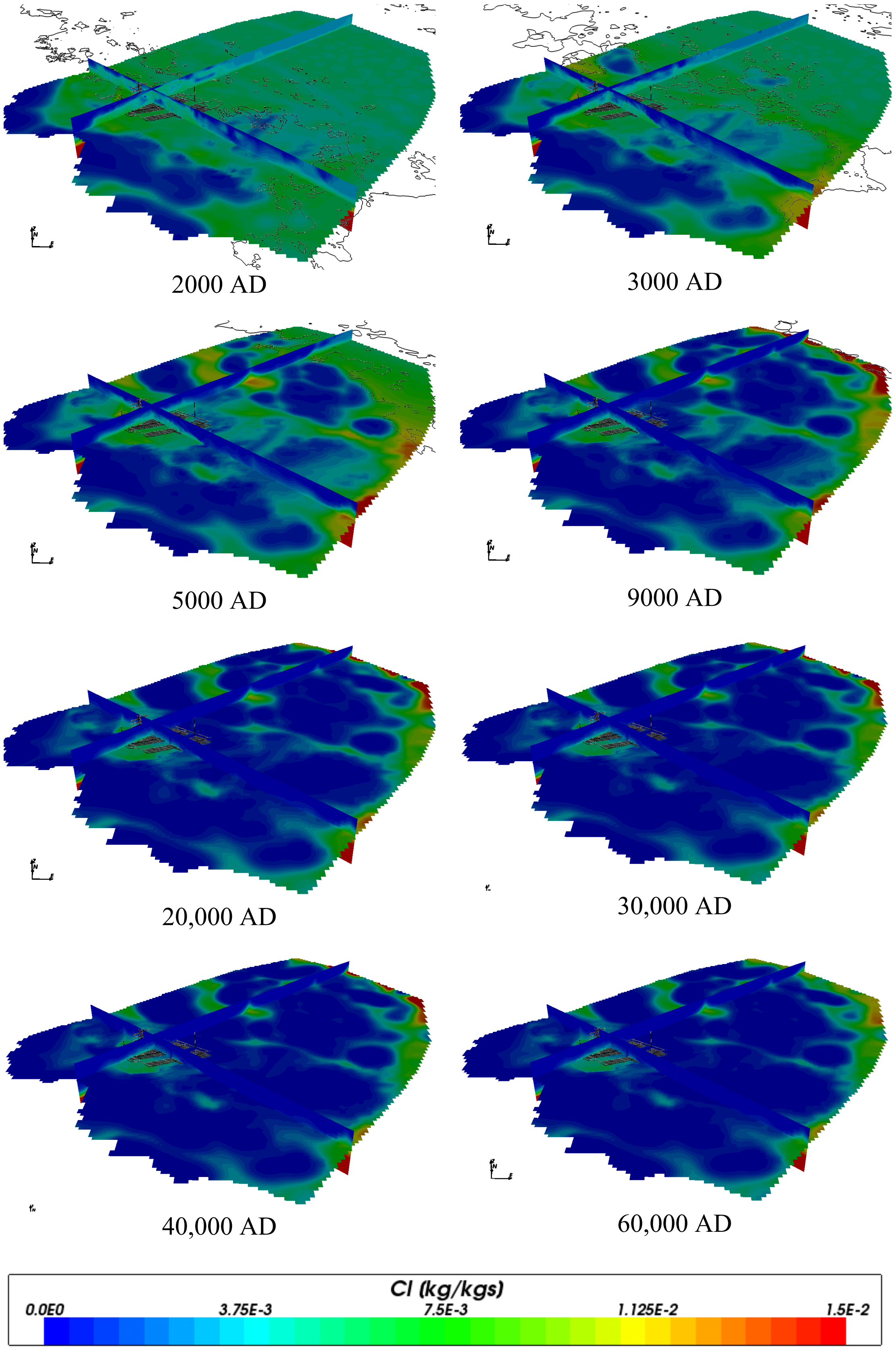

2000 AD

3000 AD

5000 AD

9000 AD

20,000 AD

30,000 AD

40,000 AD

60,000 AD

Figure 4-81. *Total chloride mass fractions on regional scale slices through the repository volume for Case 4 for time periods 2000 AD to 60,000 AD.*

4.5.7 Iron

The evolution of total iron concentrations in the repository region for Case 4 is shown in Figure 4-82, Figure 4-83 and Figure 4-84 and on the regional scale in Figure 4-85. The change in iron concentration with time in Case 4 is relatively small, with a similar trend as in Case 1 with a decreasing spatial variability. On the regional scale a larger spatial variability is evident, particularly at the early times up to 5,000 AD, as compared to Case 1, where no chemical reactions are included.

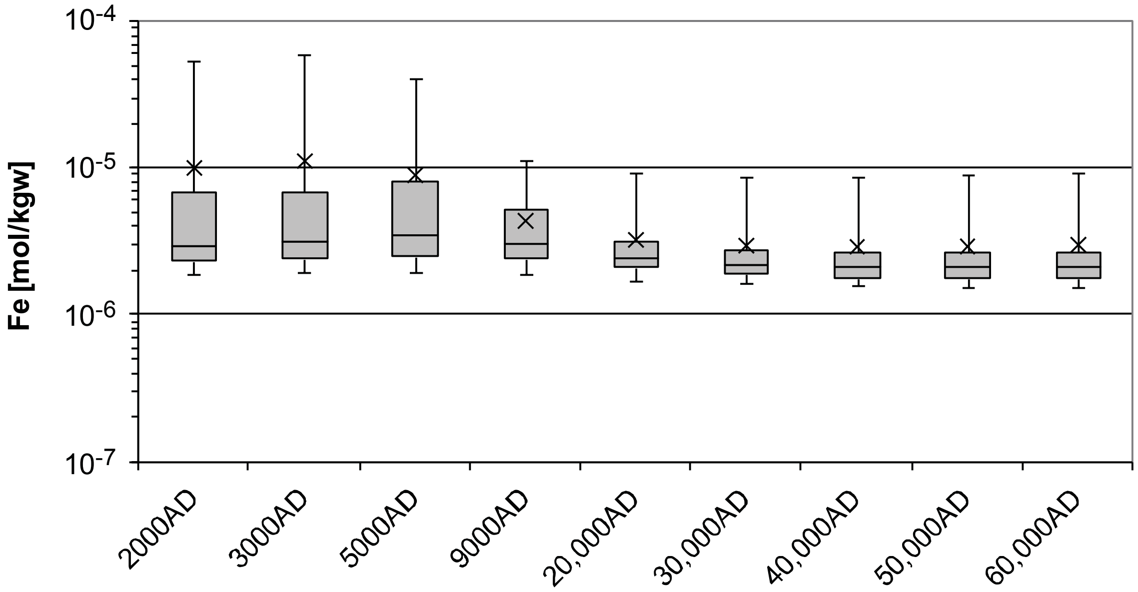

Figure 4-82. *Box and whisker plot showing the statistical distribution of total iron molalities for Case 4 on a regular grid of points within the repository volume between elevations -490 m and -460 m. The statistical measures are the median, the 25th and 75th percentiles (box), the mean (cross) and the 5th and 95th percentiles (whiskers).*

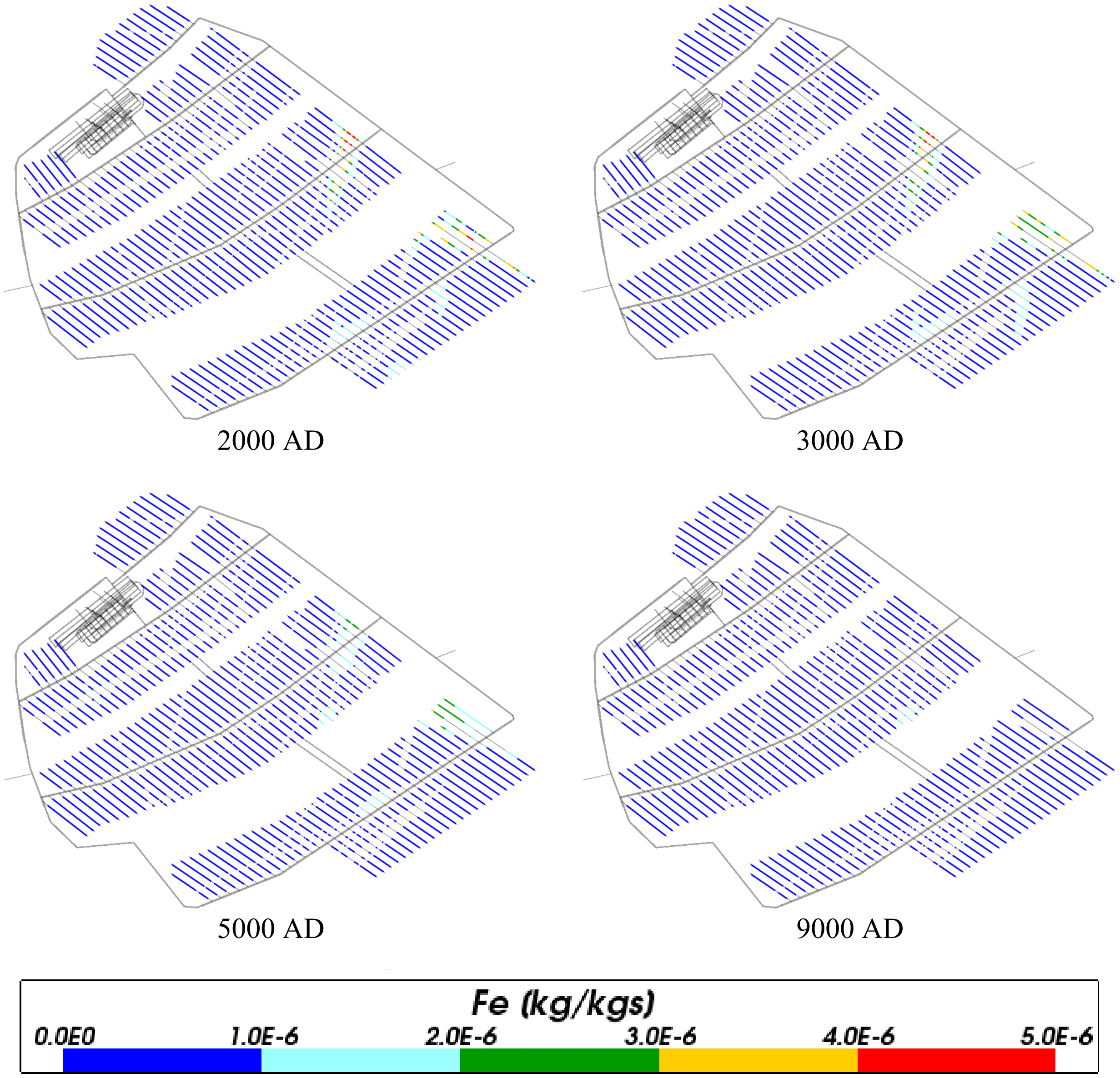

Figure 4-83. *Total iron mass fractions for Case 4 at deposition hole locations for time periods 2000 AD to 9000 AD.*

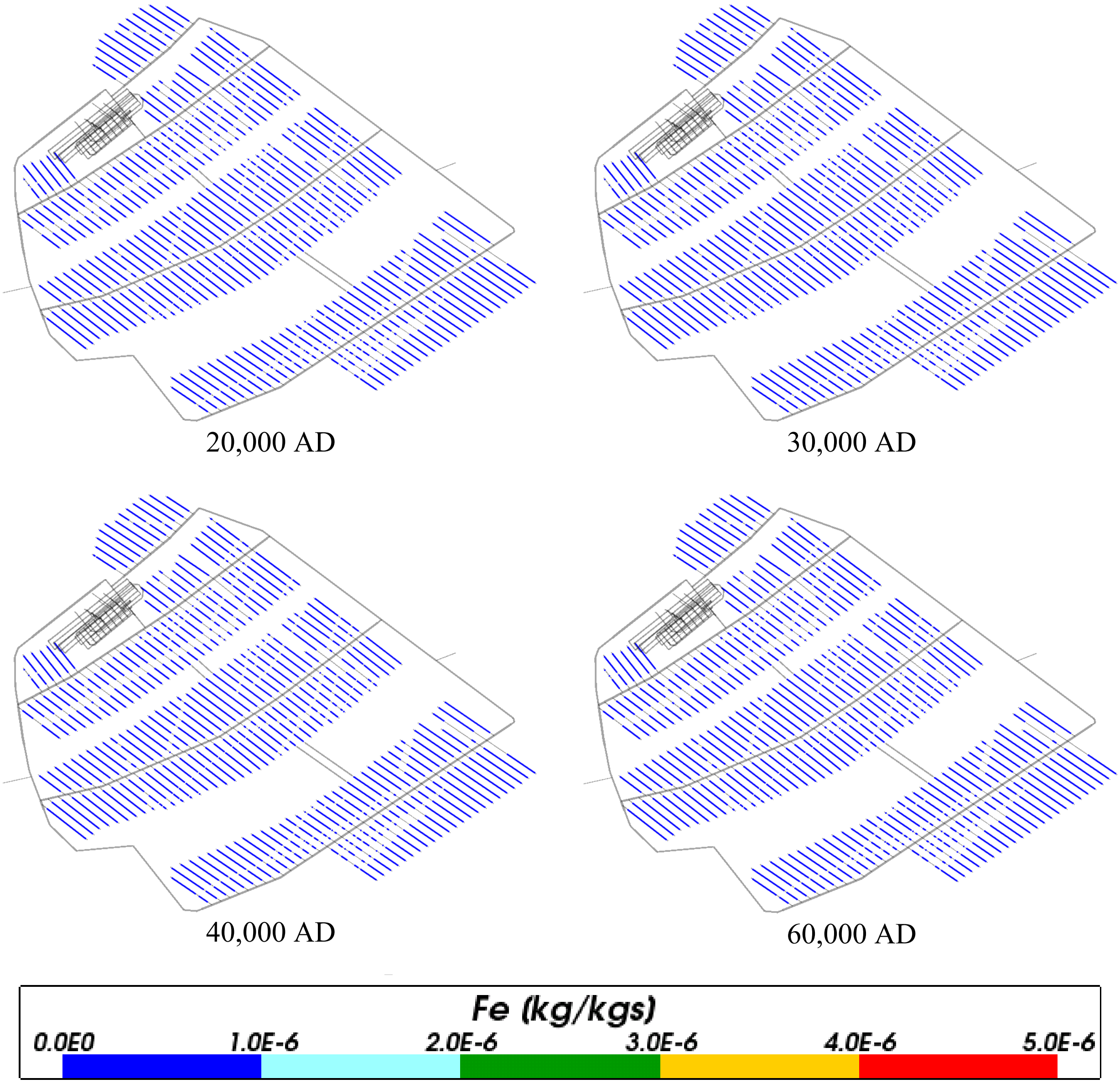
20,000 AD

30,000 AD

40,000 AD

60,000 AD

Figure 4-84. *Total iron mass fractions for Case 4 at deposition hole locations for time periods 20,000 AD to 60,000 AD.*

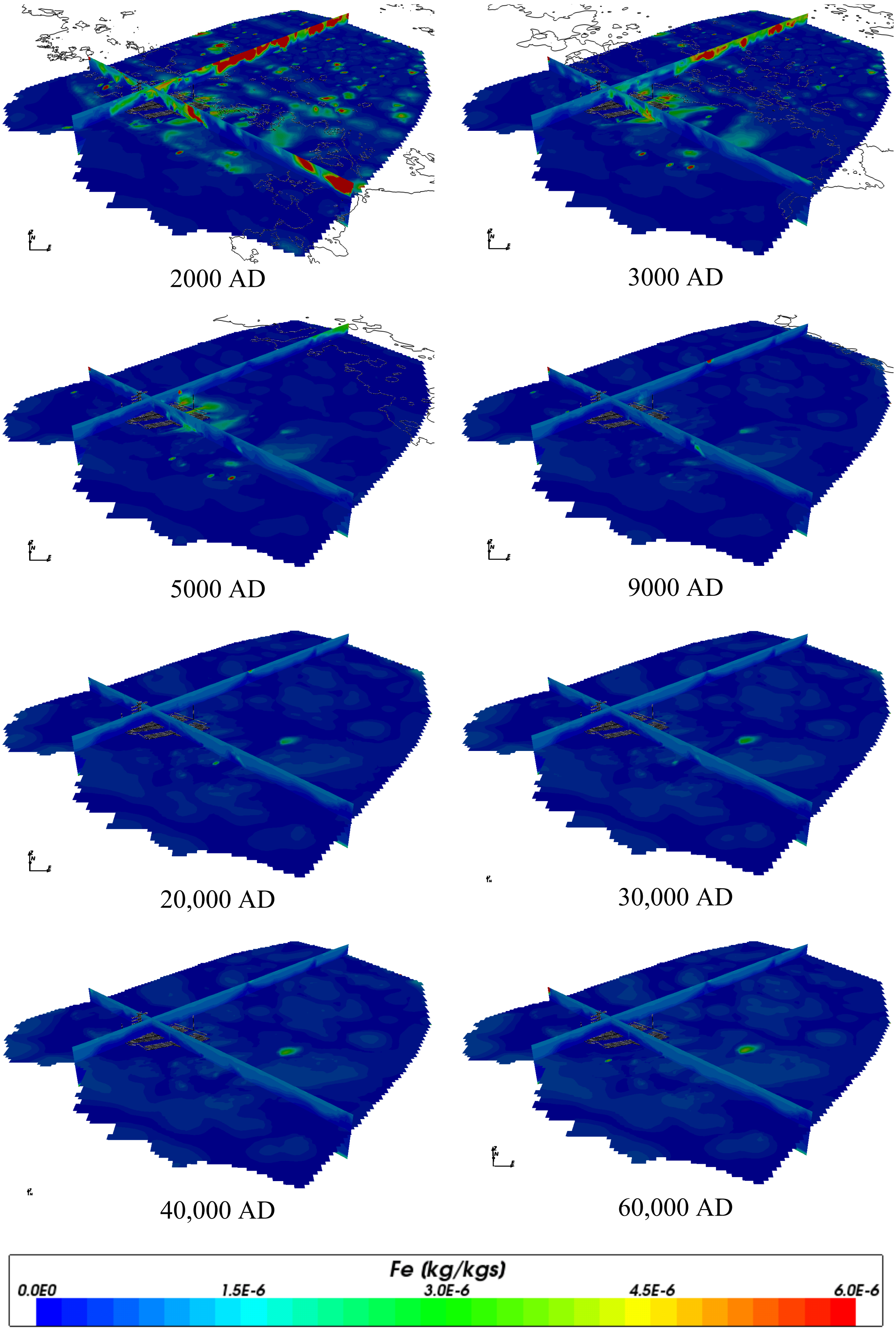

2000 AD

3000 AD

5000 AD

9000 AD

20,000 AD

30,000 AD

40,000 AD

60,000 AD

Figure 4-85. *Total iron mass fractions on regional scale slices through the repository volume for Case 4 for time periods 2000 AD to 60,000 AD.*

4.5.8 Sodium

The mean value of sodium concentrations around the repository (Figure 4-86, Figure 4-87 and Figure 4-88) decreases with time similarly as for Case 1 and 2, although the temporal variation is slightly less in Case 4. Also the spatial evolution in sodium concentrations in the repository volume (Figure 4-87 and Figure 4-88) and in the model volume (Figure 4-89) is relatively similar as for Cases 1 and 2. This indicates that the chemical equilibrium reactions considered in Case 4 have only minor influence on the sodium concentrations.

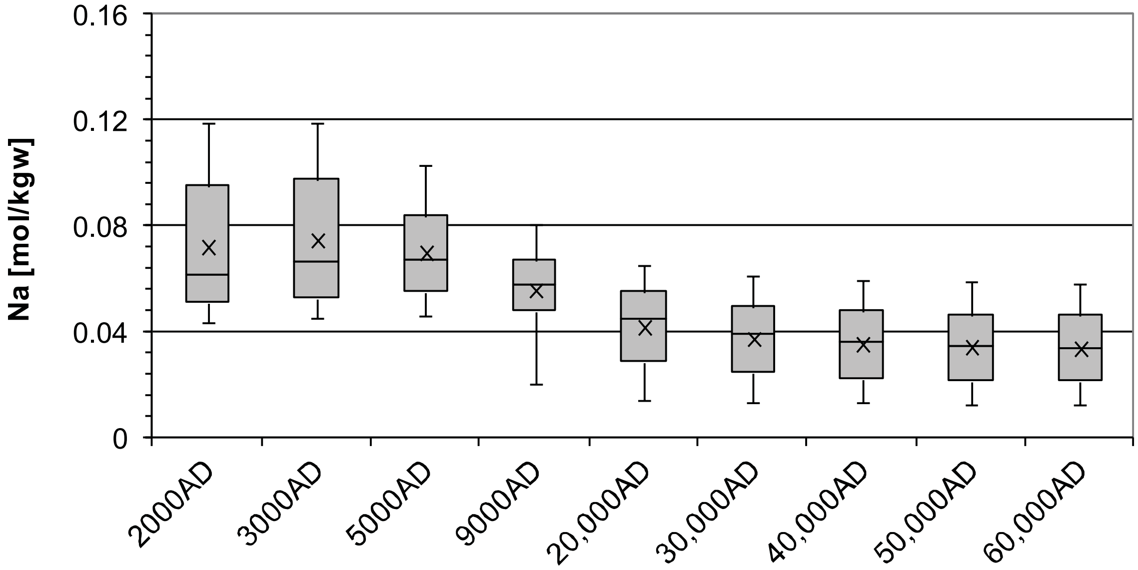

Figure 4-86. Box and whisker plot showing the statistical distribution of total sodium molalities for Case 4 on a regular grid of points within the repository volume between elevations -490 m and -460 m. The statistical measures are the median, the 25th and 75th percentiles (box), the mean (cross) and the 5th and 95th percentiles (whiskers).

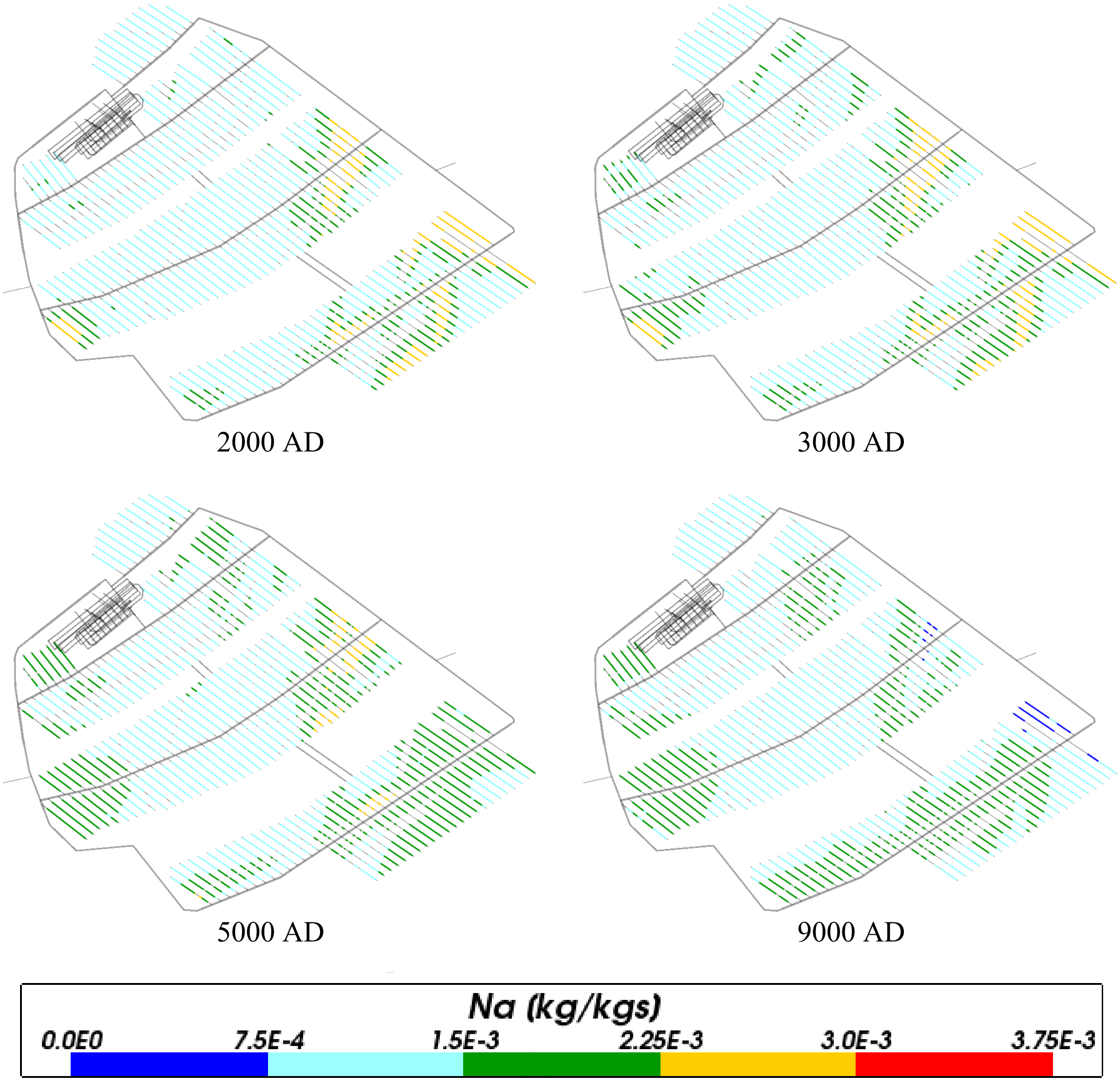

2000 AD

3000 AD

5000 AD

9000 AD

Figure 4-87. *Total sodium mass fractions for Case 4 at deposition hole locations for time periods 2000 AD to 9000 AD.*

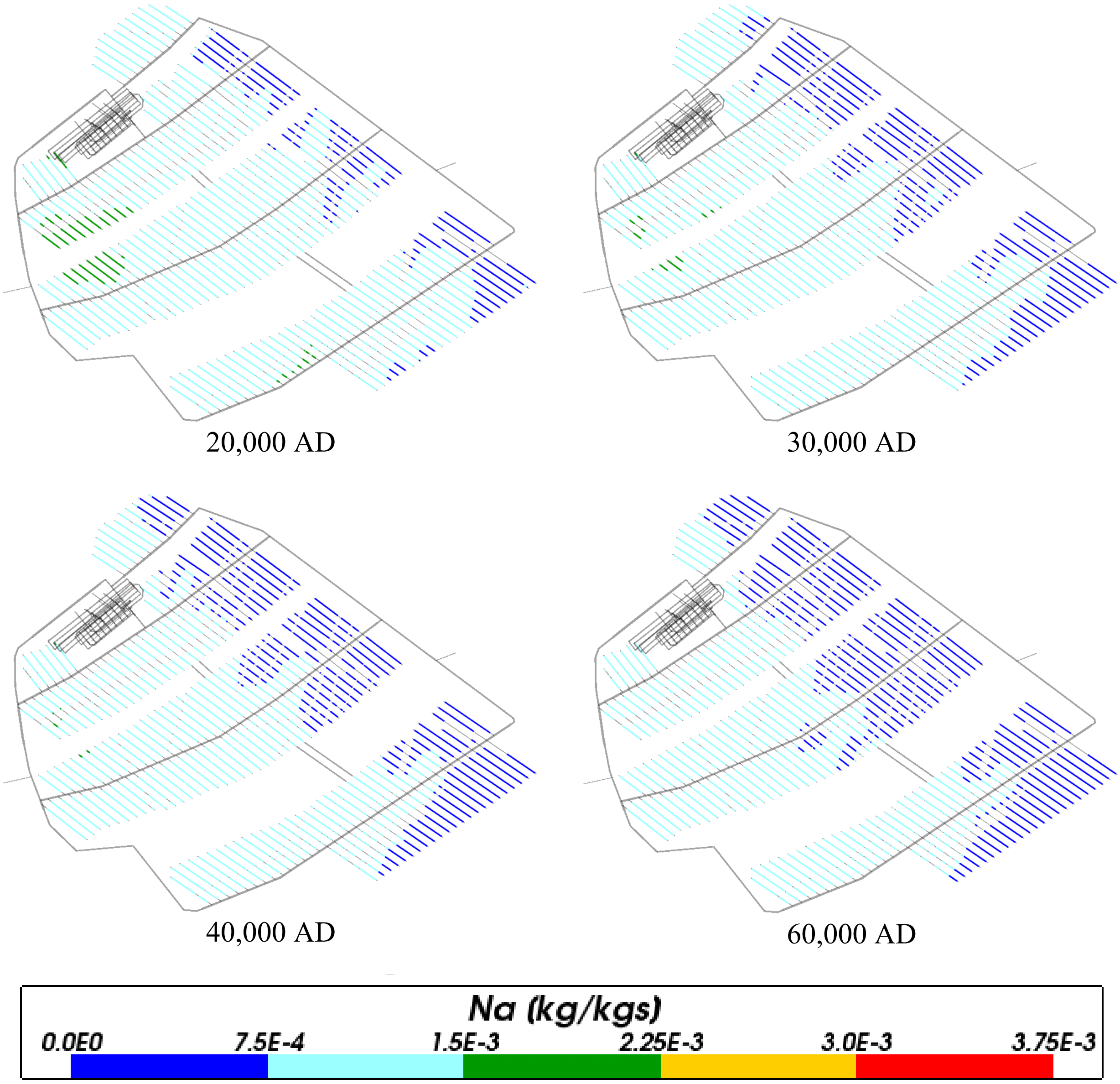

Figure 4-88. *Total sodium mass fractions for Case 4 at deposition hole locations for time periods 20,000 AD to 60,000 AD.*

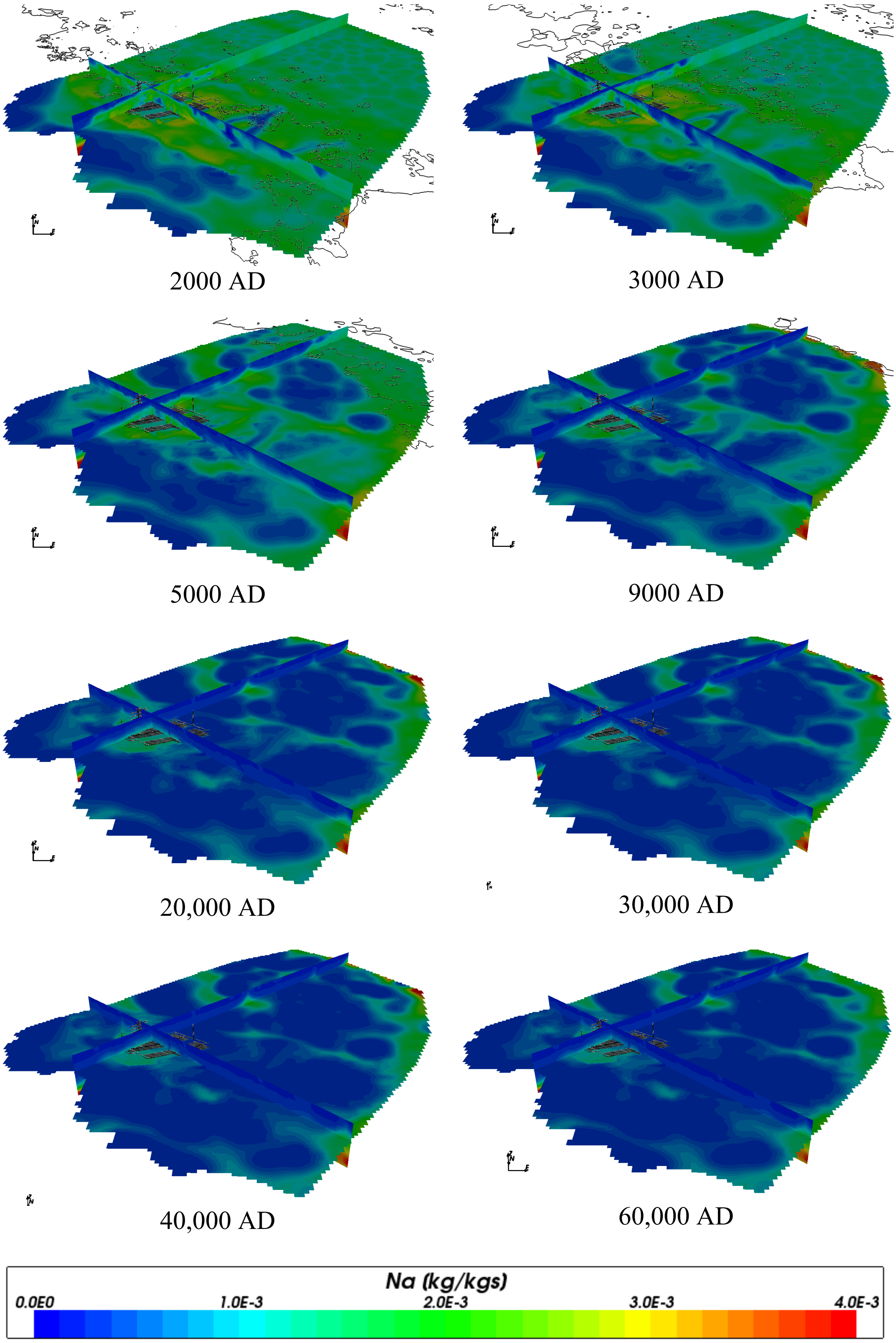

Figure 4-89. *Total sodium mass fractions on regional scale slices through the repository volume for Case 4 for time periods 2000 AD to 60,000 AD.*

4.5.9 Sulphate

Figure 4-90 shows the evolution in sulphate concentrations around the repository. The mean values are similar to those in Case 2, but with a greater spatial variability at the early times up to 5,000 AD in Case 4. The spatial variability within the repository volume is shown in Figure 4-91 and Figure 4-92.

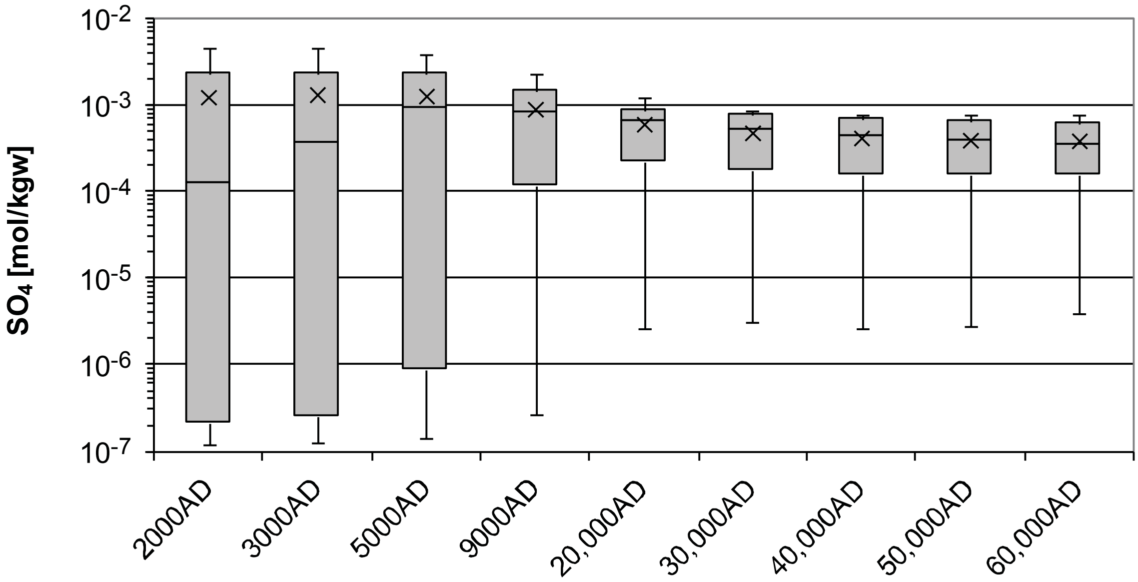

Figure 4-90. *Box and whisker plot showing the statistical distribution of sulphate molalities for Case 4 on a regular grid of points within the repository volume between elevations -490 m and -460 m. The statistical measures are the median, the 25th and 75th percentiles (box), the mean (cross) and the 5th and 95th percentiles (whiskers).*

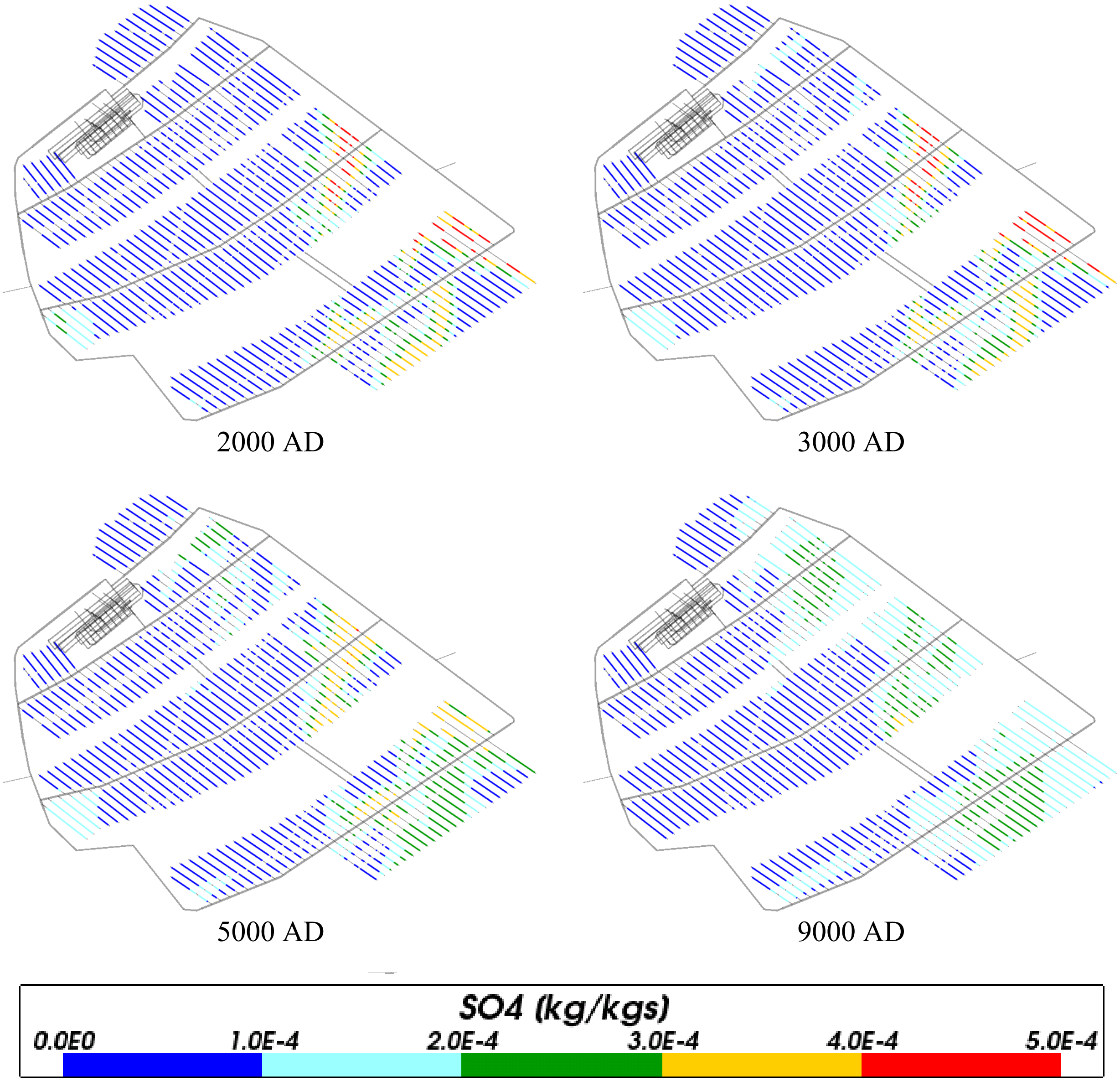

Figure 4-91. *Total sulphate mass fractions for Case 4 at deposition hole locations for time periods 2000 AD to 9000 AD.*

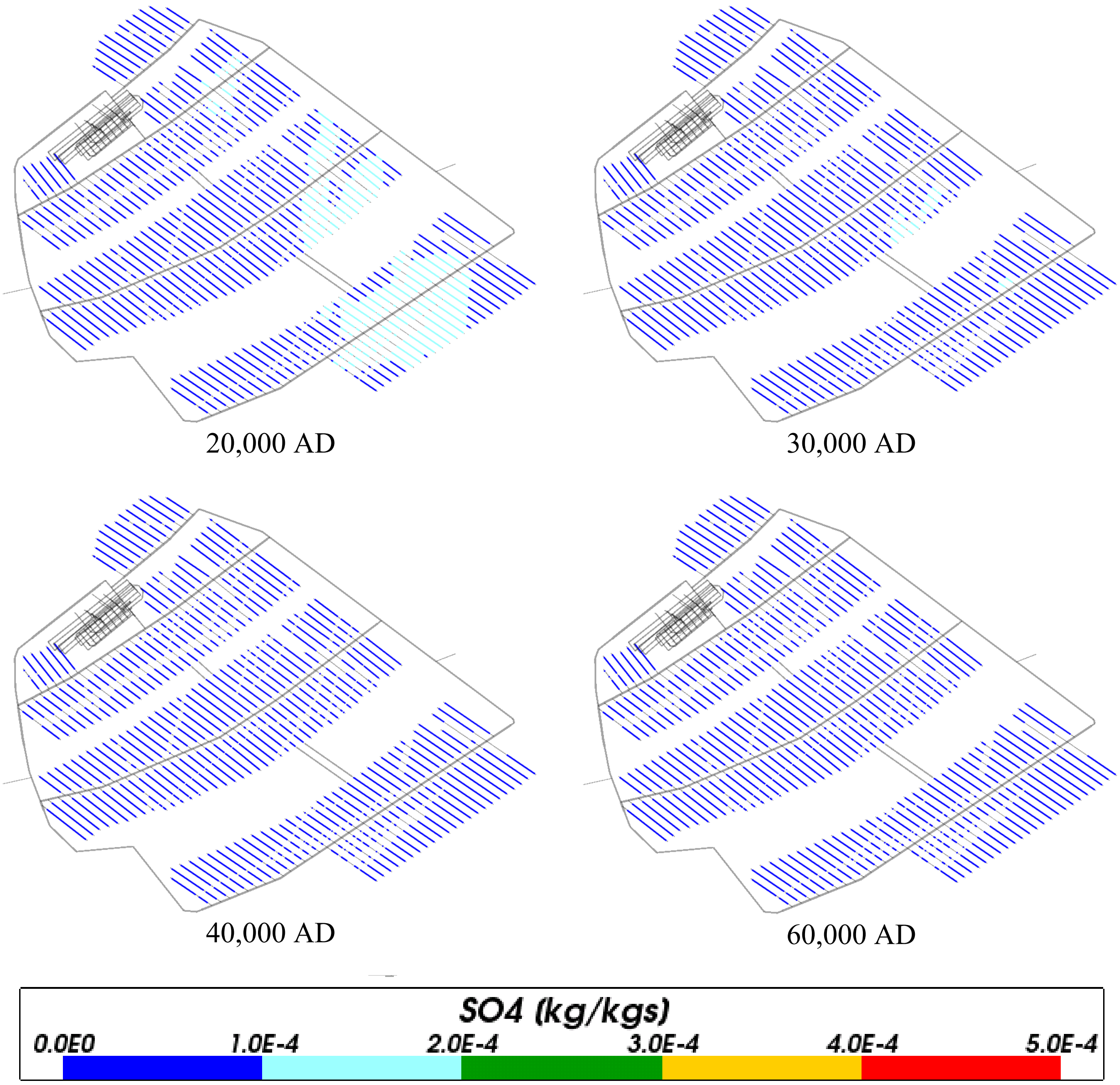
20,000 AD

30,000 AD

40,000 AD

60,000 AD

Figure 4-92. *Total sulphate mass fractions for Case 4 at deposition hole locations for time periods 20,000 AD to 60,000 AD.*

4.6 Case 5

The evolution of groundwater composition for this case will be due to the transport and mixing of components originating from different reference waters. The concentrations of reactive species will be modified by equilibrium reactions with the mineral phases considered. The number and types of mineral phases considered (see Section 3.2) is the same as for Case 2, where equilibration of the groundwater with calcite, quartz and amorphous iron (II) sulphide was included. Case 5 differs in that it includes a more dilute meteoric water (Dilute Meteoric water in *Table 3-1*) as compared to the other cases, infiltrating at the top boundary for land areas above sea level. It is expected that the equilibrium reactions will have an effect on pH, Eh, and the concentrations of total inorganic carbon, calcium, sulphur, and iron.

4.6.1 pH

Figure 4-93, Figure 4-94, Figure 4-95 show a decreasing pH with time for Case 5 around the repository, similar to that in Case 2 but with slightly higher mean pH values and less spatial variability in the repository volume after 30,000 AD. These differences are due to the more dilute meteoric water infiltrating land areas above sea level in Case 5. Figure 4-96 shows values of pH over the regional area.

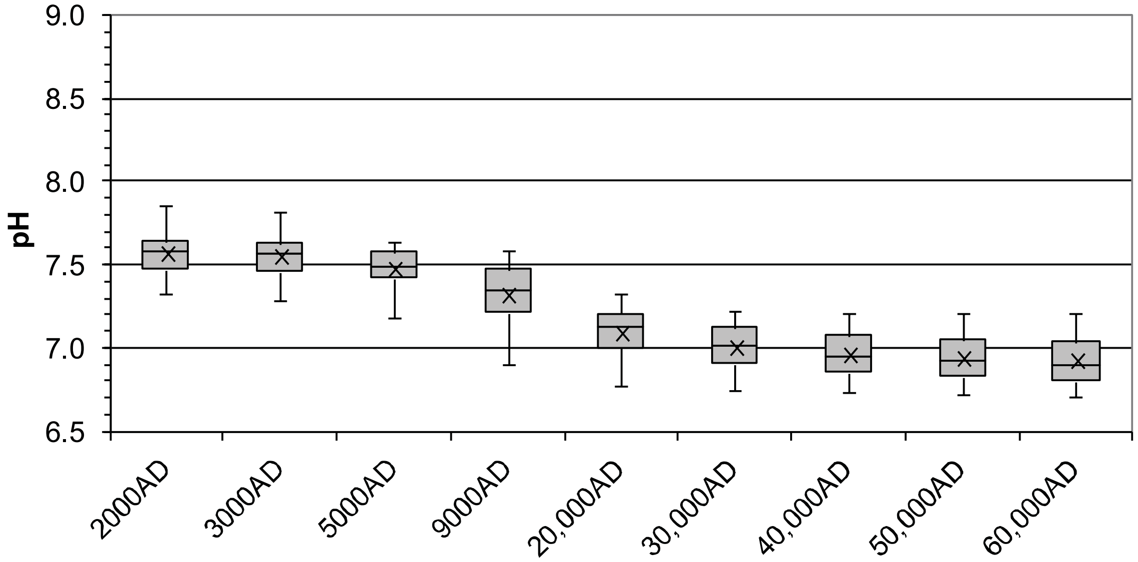

Figure 4-93. *Box and whisker plot showing the statistical distribution of pH for Case 5 on a regular grid of points within the repository volume between elevations -490 m and -460 m. The statistical measures are the median, the 25th and 75th percentiles (box), the mean (cross) and the 5th and 95th percentiles (whiskers).*

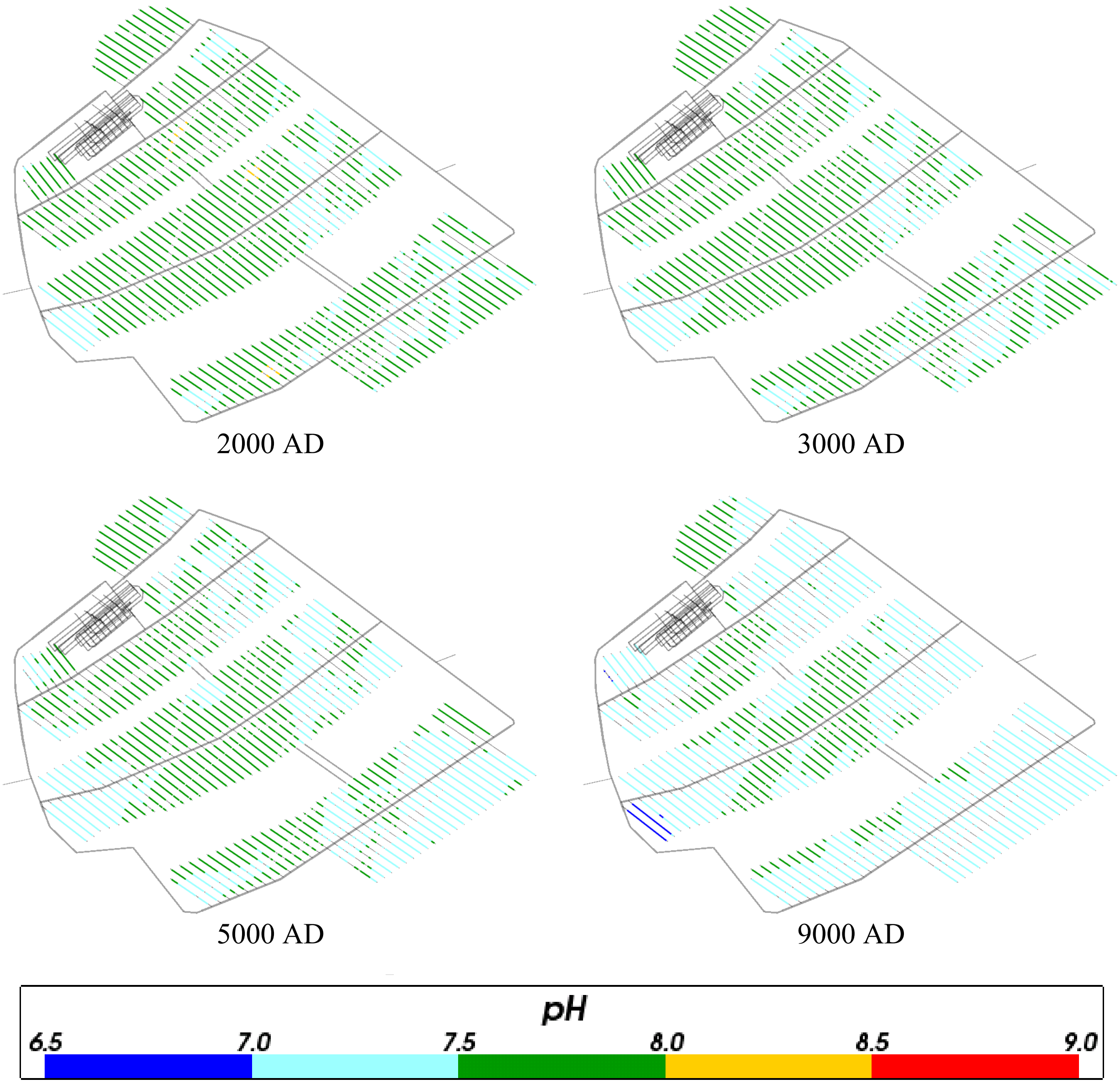
2000 AD 3000 AD
5000 AD 9000 AD

Figure 4-94. *Values of pH for Case 5 at deposition hole locations for time periods 2000 AD to 9000 AD.*

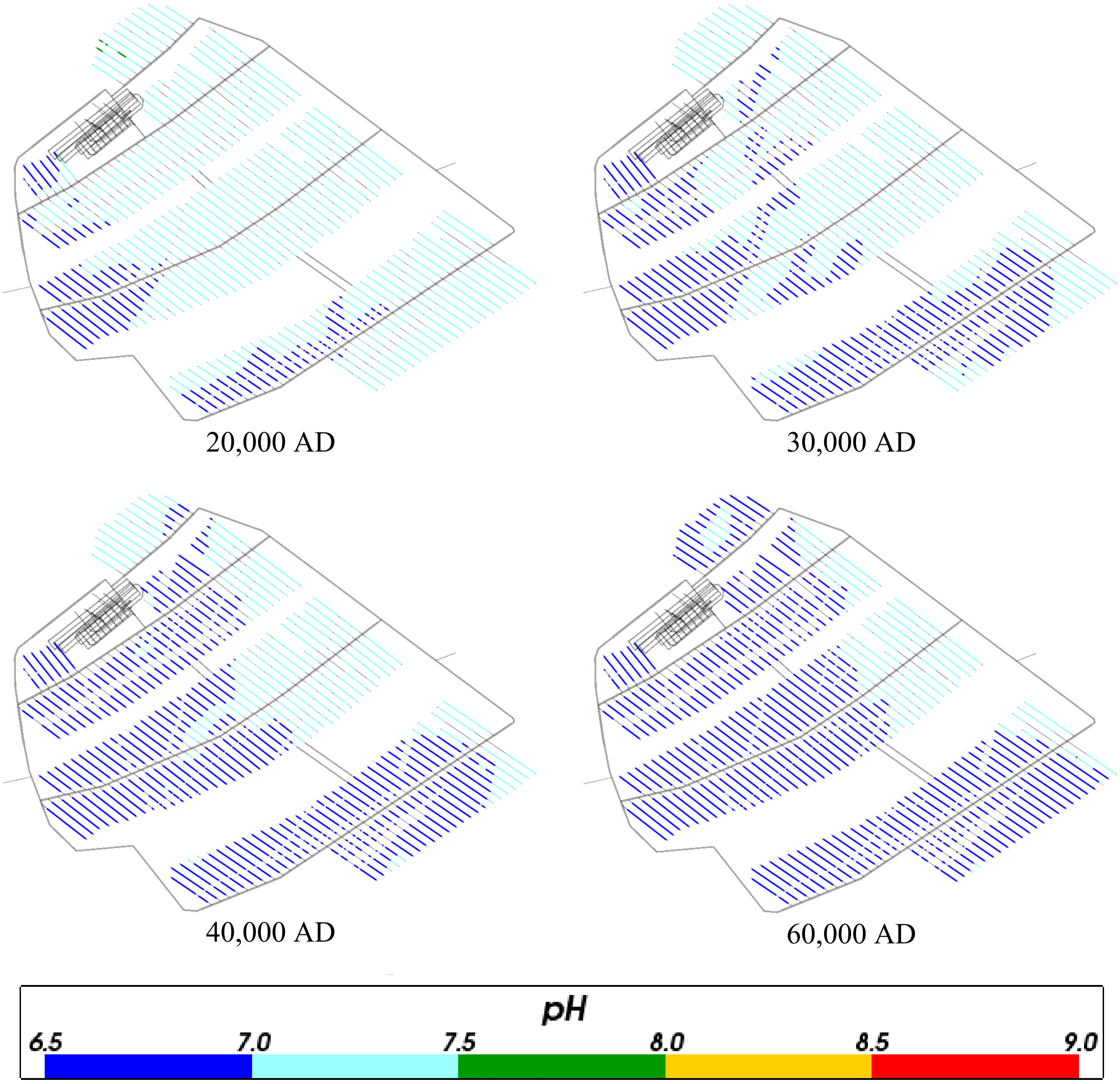

20,000 AD

30,000 AD

40,000 AD

60,000 AD

Figure 4-95. *Values of pH for Case 5 at deposition hole locations for time periods 20,000 AD to 60,000 AD.*

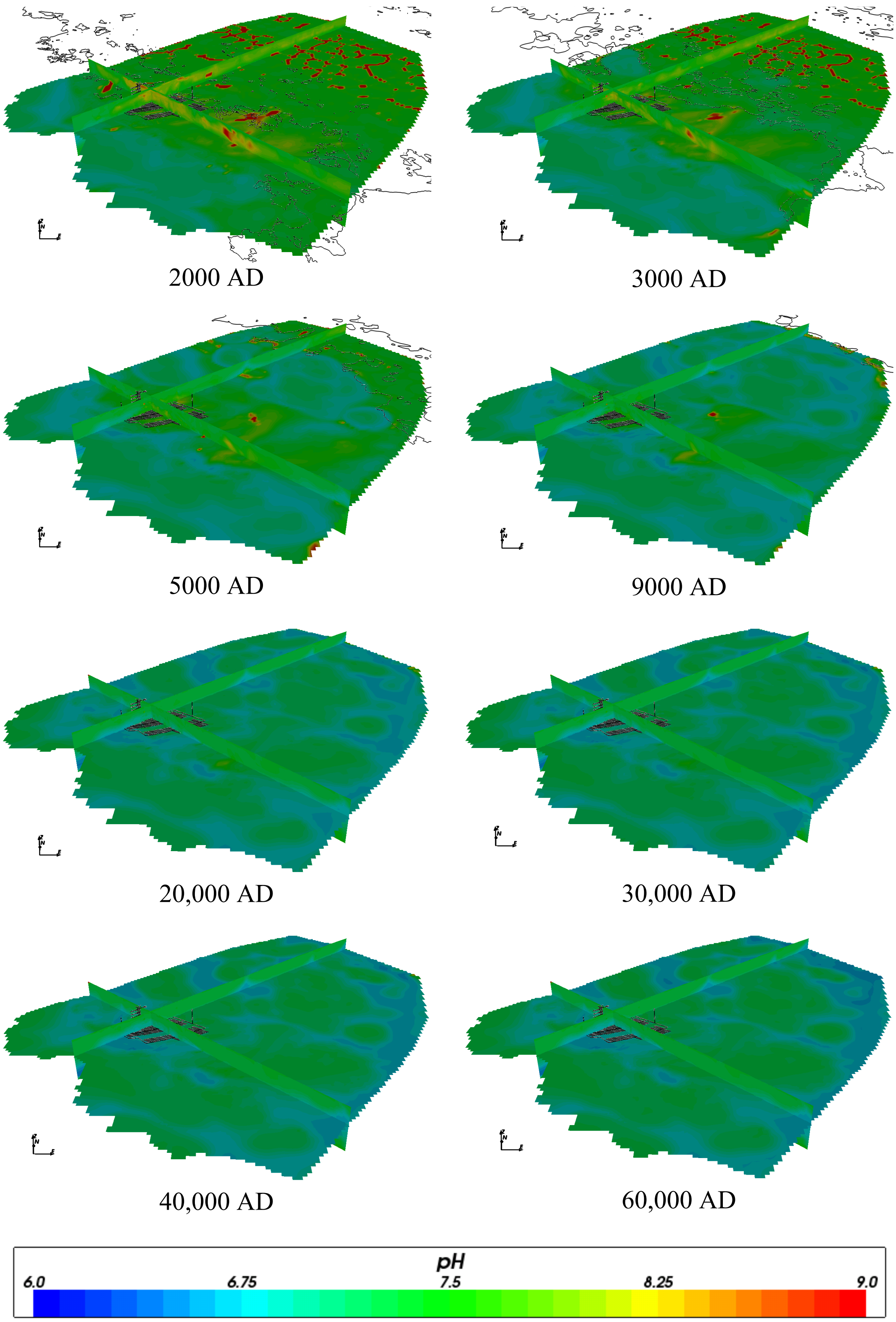
2000 AD

3000 AD

5000 AD

9000 AD

20,000 AD

30,000 AD

40,000 AD

60,000 AD

Figure 4-96. *Values of pH on regional scale slices through the repository volume for Case 5 for time periods 2000 AD to 60,000 AD.*

4.6.2 Eh (or pe)

Figure 4-97 shows the value of Eh in the repository region and Figure 4-98 and Figure 4-99 show the value of pe at the deposition hole locations for Case 5. These results are very similar to those for Case 2 with only slightly lower mean values and somewhat less spatial variability after 20,000 AD for Case 5.

Figure 4-100 shows the regional slice plots of pe over time for Case 5. As for Case 2, pe is increasing at early times, with larger values being swept in a north easterly direction, and little changes after 20,000 AD.

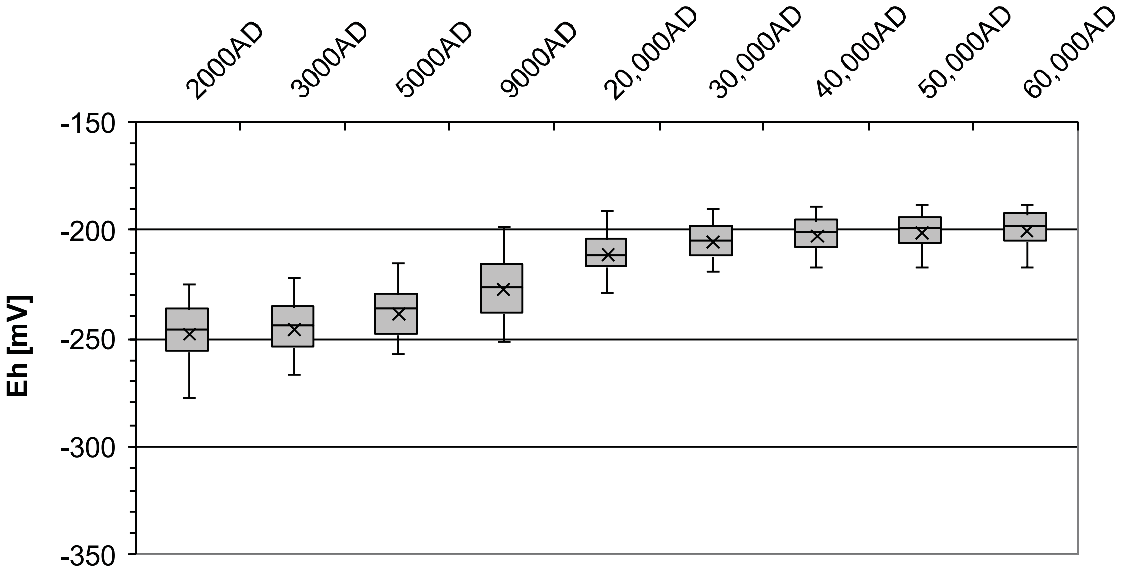

__Figure 4-97.__ Box and whisker plot showing the statistical distribution of Eh for Case 5 on a regular grid of points within the repository volume between elevations -490 m and -460 m. The statistical measures are the median, the 25th and 75th percentiles (box), the mean (cross) and the 5th and 95th percentiles (whiskers).

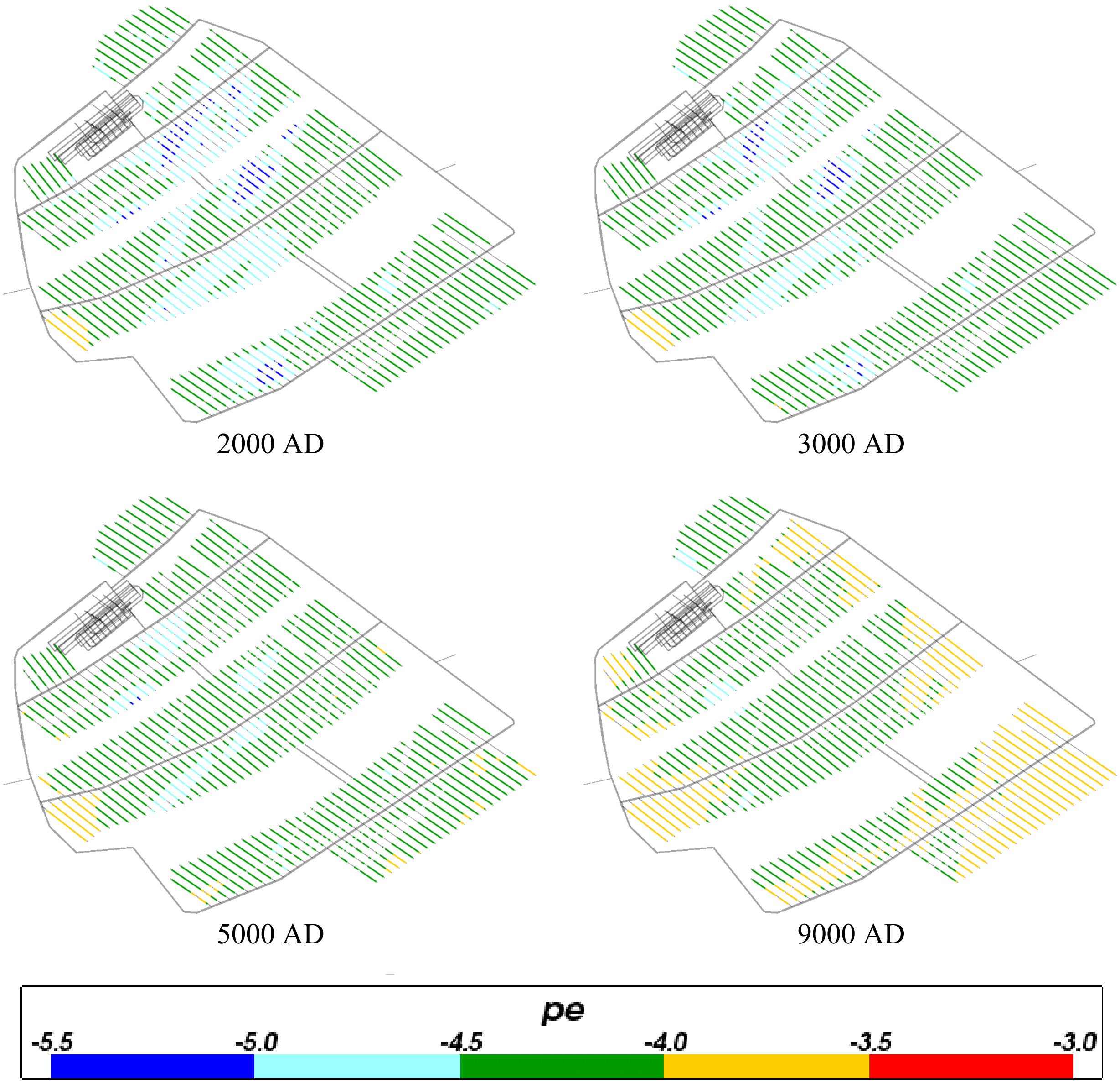

2000 AD

3000 AD

5000 AD

9000 AD

Figure 4-98. *Values of pe for Case 5 at deposition hole locations for time periods 2000 AD to 9000 AD.*

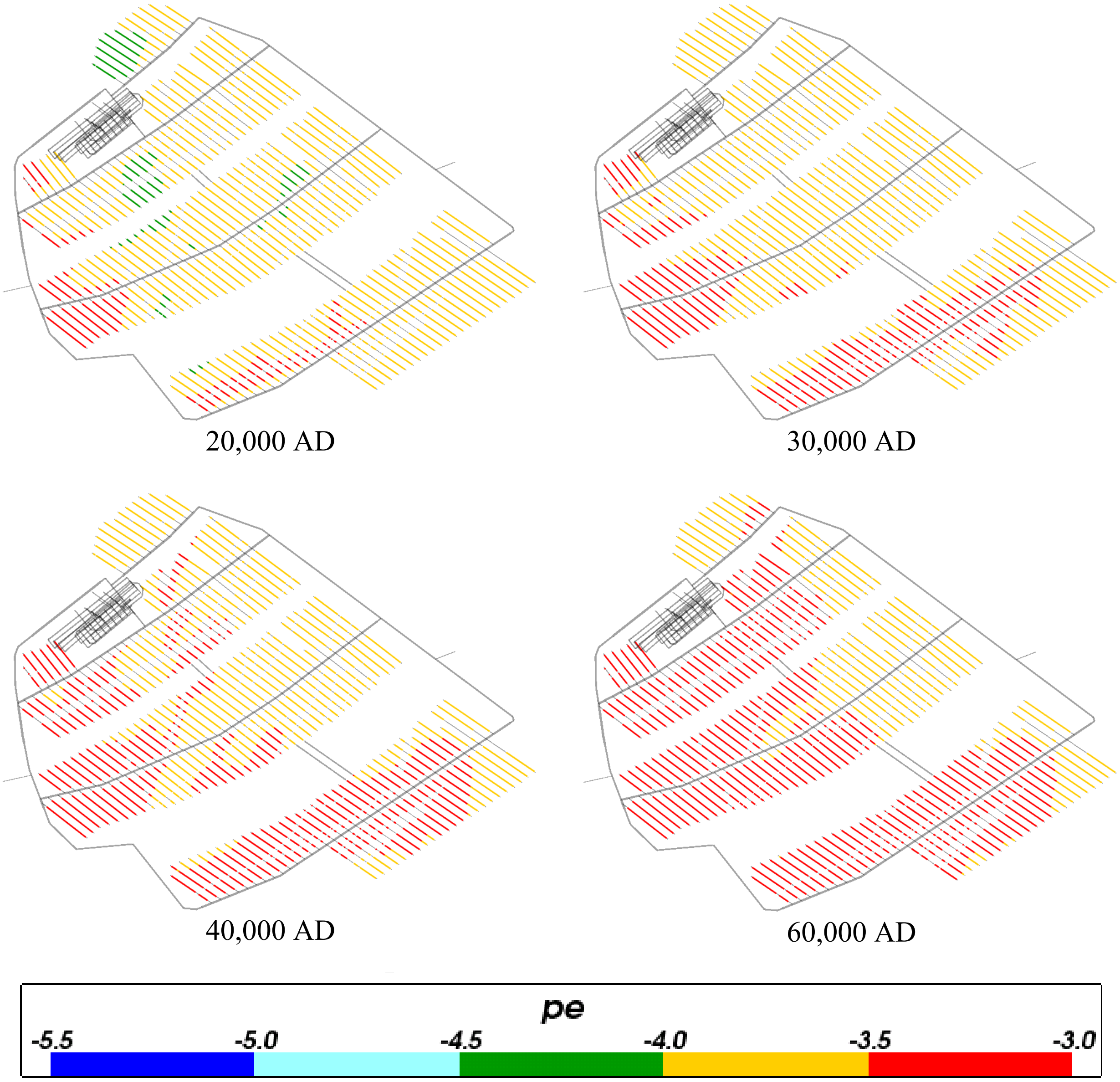
20,000 AD

30,000 AD

40,000 AD

60,000 AD

Figure 4-99. *Values of pe for Case 5 at deposition hole locations for time periods 20,000 AD to 60,000 AD.*

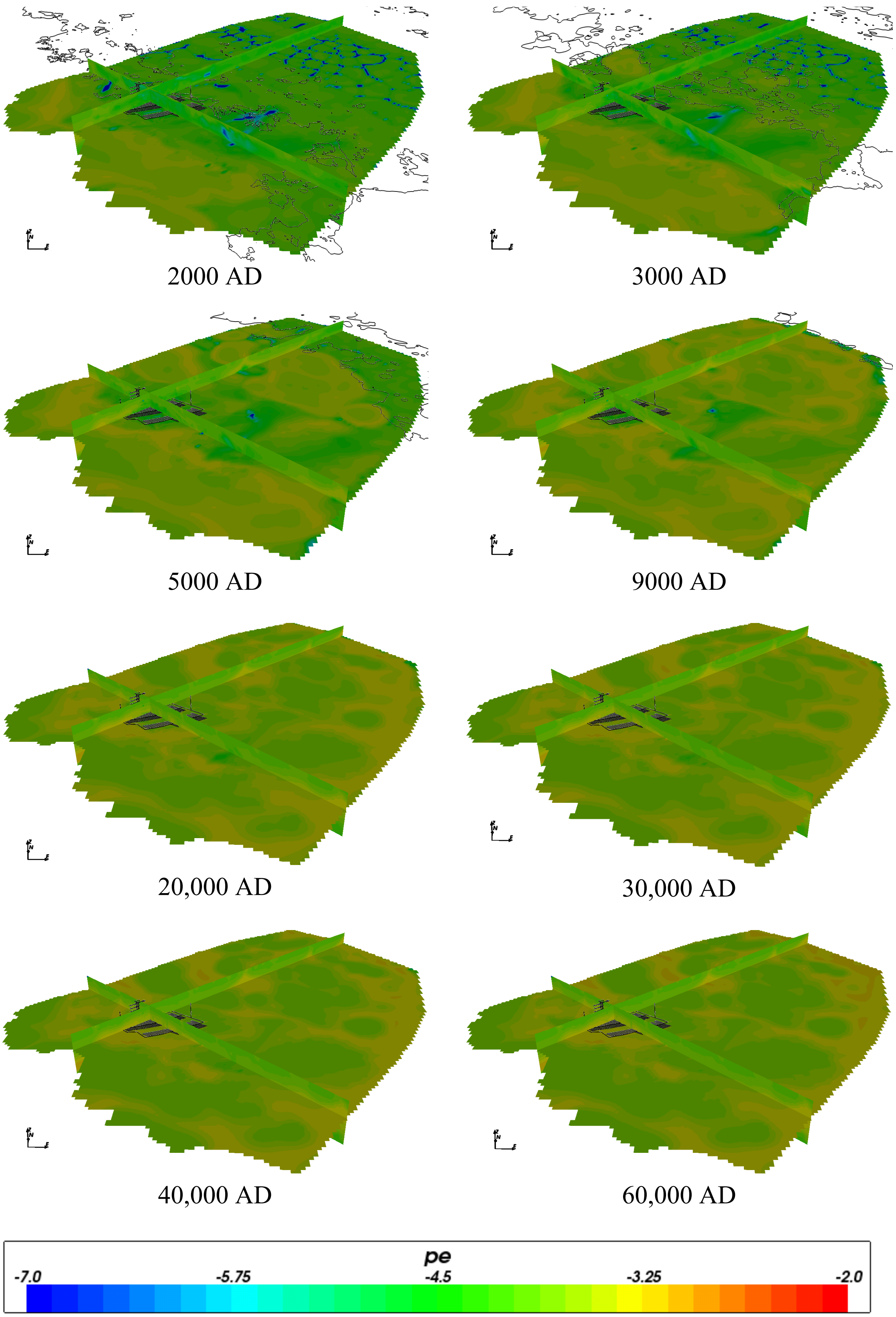

Figure 4-100. *Values of pe on regional scale slices through the repository volume for Case 5 for time periods 2000 AD to 60,000 AD.*

4.6.3 TDS and sum of cations

Figure 4-101 and Figure 4-102 show the statistical distribution of TDS and the sum of cation charge molalities in the repository region for Case 5. The evolution with time is very similar to the corresponding results for Cases 1 and 2 with only slightly lower mean values of TDS for Case 5, a difference that may be due to the more dilute meteoric water infiltrating land areas below sea level in Case 5.

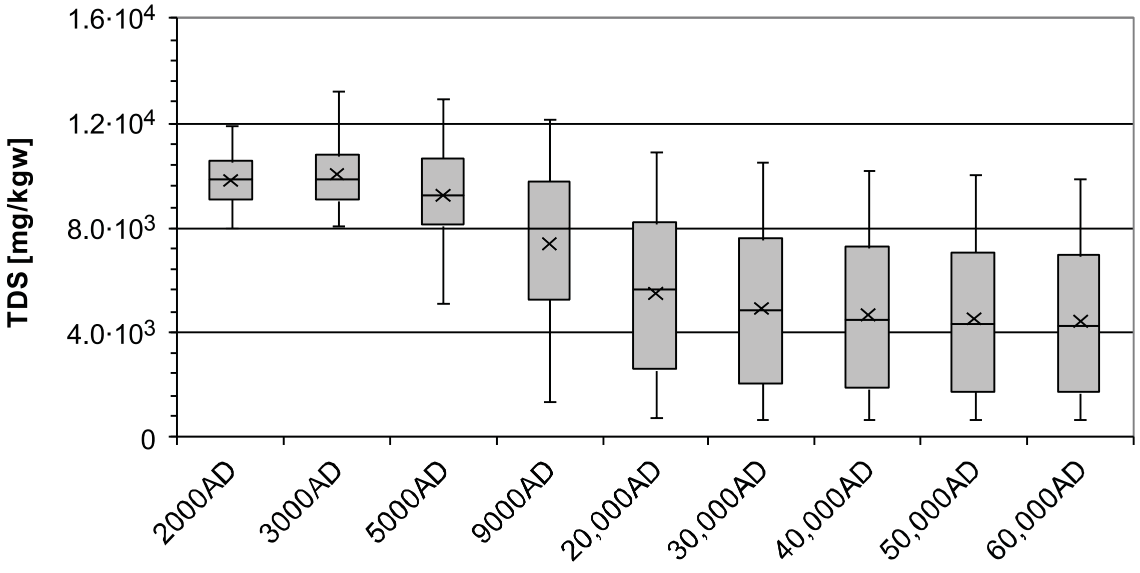

Figure 4-101. *Box and whisker plot showing the statistical distribution of TDS for Case 5 on a regular grid of points within the repository volume between elevations -490 m and -460 m. The statistical measures are the median, the 25th and 75th percentiles (box), the mean (cross) and the 5th and 95th percentiles (whiskers).*

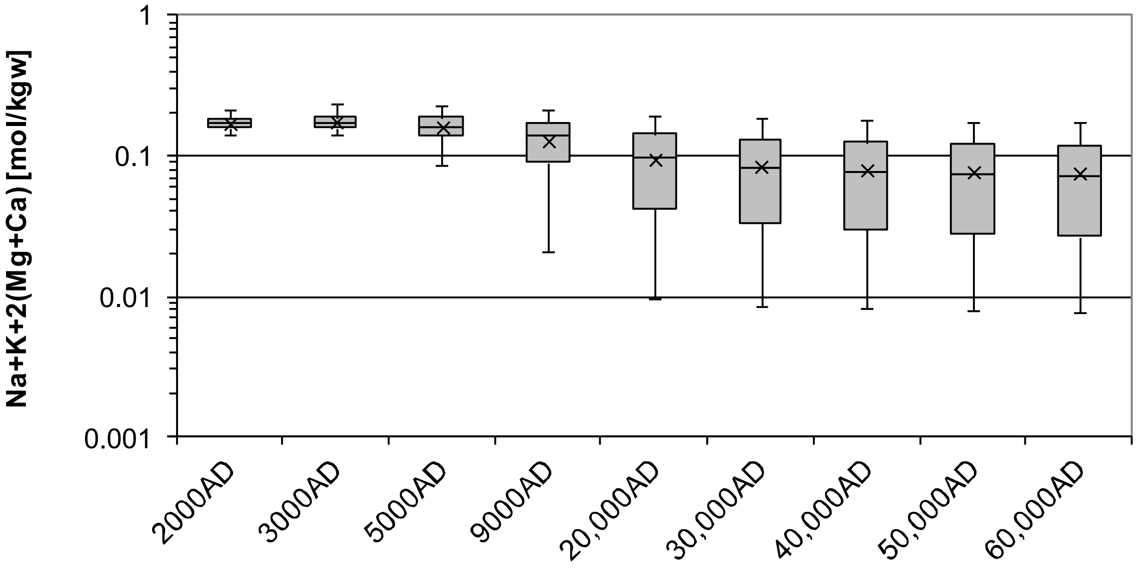

Figure 4-102. *Box and whisker plot showing the statistical distribution of sum of cation charges (Na+K+2(Mg+Ca)) molalities for Case 5 on a regular grid of points within the repository volume between elevations -490 m and -460 m. The statistical measures are the median, the 25th and 75th percentiles (box), the mean (cross) and the 5th and 95th percentiles (whiskers).*

4.6.4 Carbon

Figure 4-103, Figure 4-104, Figure 4-105 and Figure 4-106 show plots of total inorganic carbon for Case 5. At early times up to 3,000 AD the total inorganic carbon concentrations in the repository region, shown in the first three figures, are very similar to that in Case 2. At later times the concentrations are lower in Case 5, as a consequence of the more dilute meteoric water infiltrating in that case. A similar trend, with generally lower concentrations of inorganic carbon on the regional scale in Case 5, can be seen when comparing Figure 4-106 with the corresponding figure for Case 2.

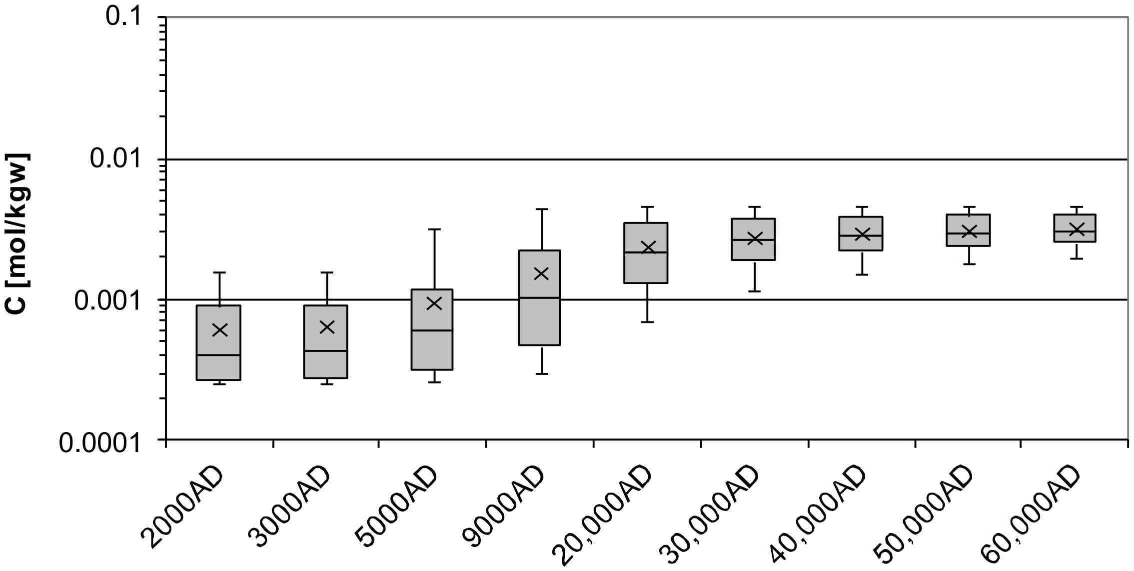

Figure 4-103. *Box and whisker plot showing the statistical distribution of total inorganic carbon molalities for Case 5 on a regular grid of points within the repository volume between elevations -490 m and -460 m. The statistical measures are the median, the 25th and 75th percentiles (box), the mean (cross) and the 5th and 95th percentiles (whiskers).*

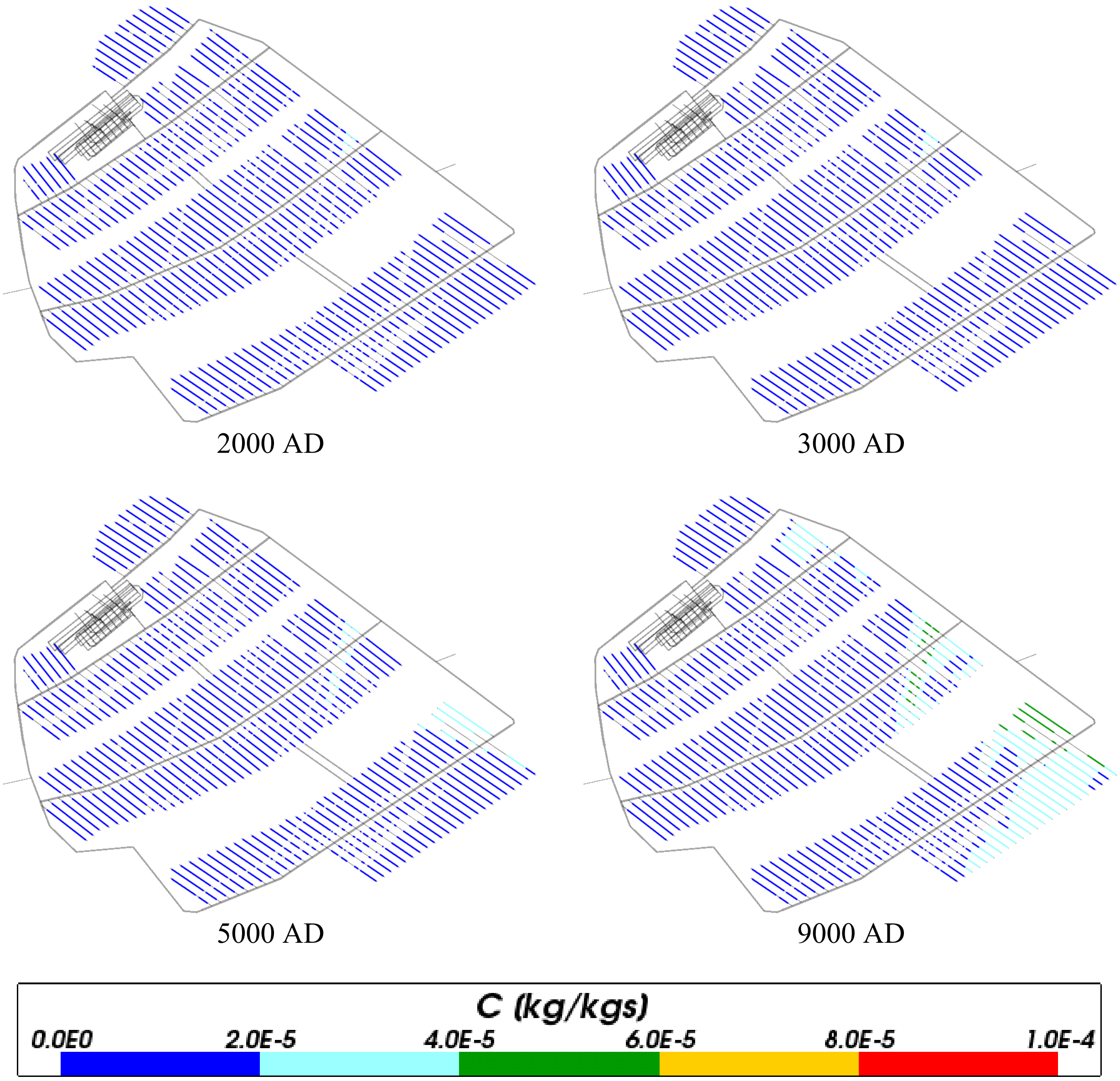

2000 AD

3000 AD

5000 AD

9000 AD

Figure 4-104. *Total inorganic carbon mass fractions for Case 5 at deposition hole locations for time periods 2000 AD to 9000 AD.*

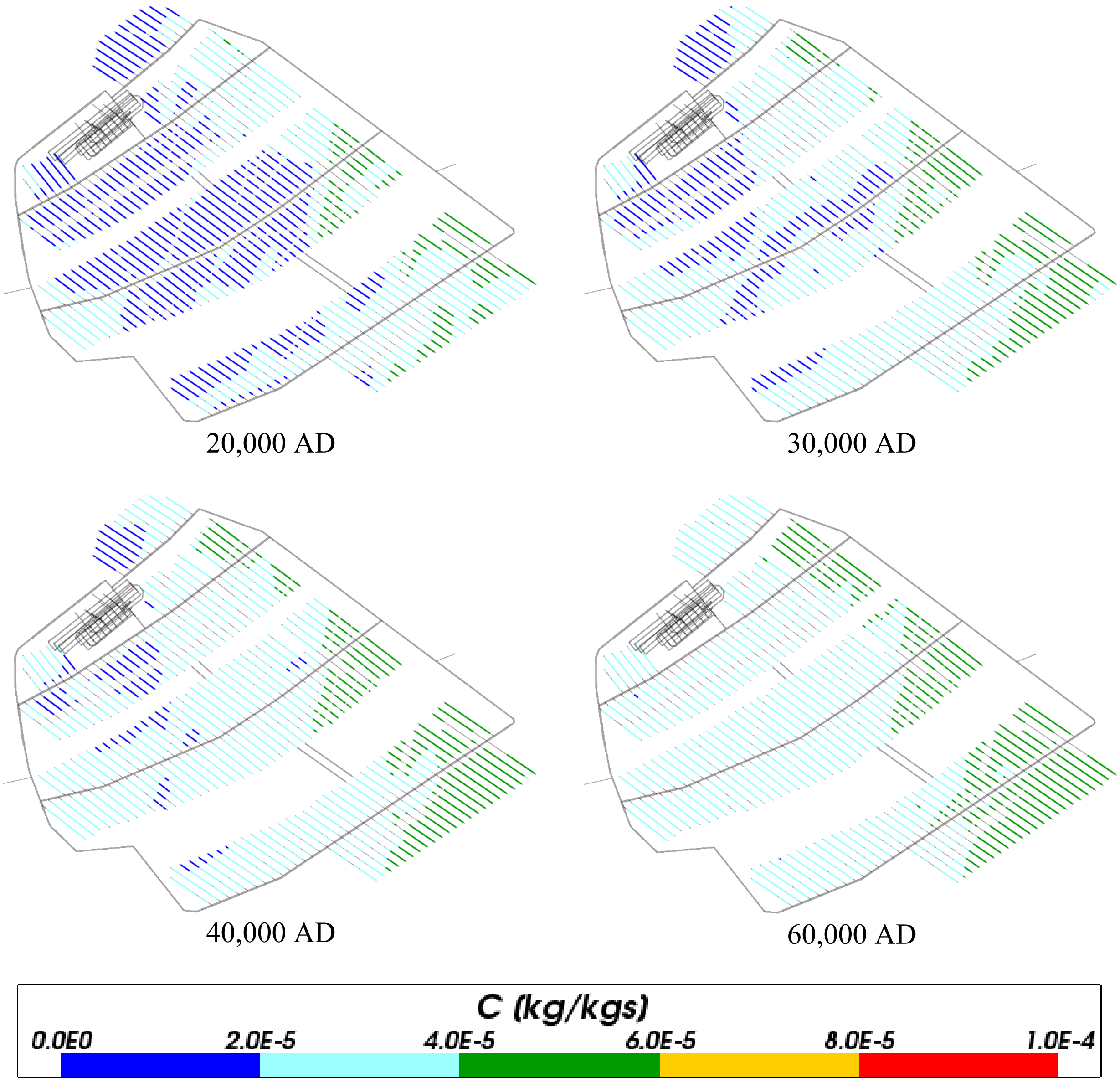

20,000 AD

30,000 AD

40,000 AD

60,000 AD

Figure 4-105. *Total inorganic carbon mass fractions for Case 5 at deposition hole locations for time periods 20,000 AD to 60,000 AD.*

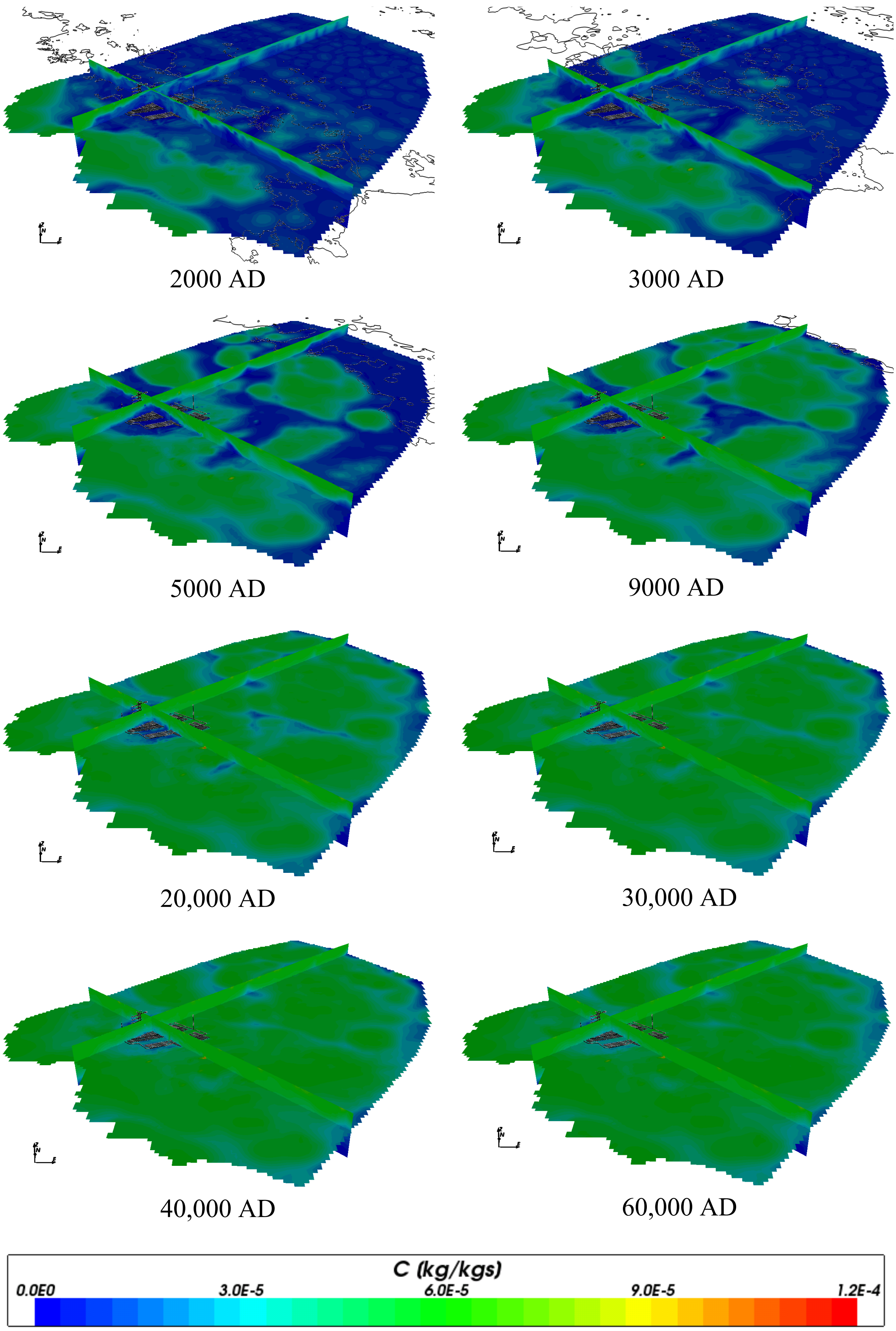

Figure 4-106. *Total inorganic carbon mass fractions on regional scale slices through the repository volume for Case 5 for time periods 2000 AD to 60,000 AD.*

4.6.5 Calcium

The concentration of total calcium is similar to that seen in Cases 1 and 2, around the repository (shown in Figure 4-107, Figure 4-108 and Figure 4-109) as well as on the regional scale (shown in Figure 4-110). The calcium concentrations are only slightly higher in Case 5 as compared to Cases 1 and 2. This implies that the chemical reactions have little influence on the calcium concentrations also when more dilute meteoric water is infiltrating land areas above sea level as in Case 5.

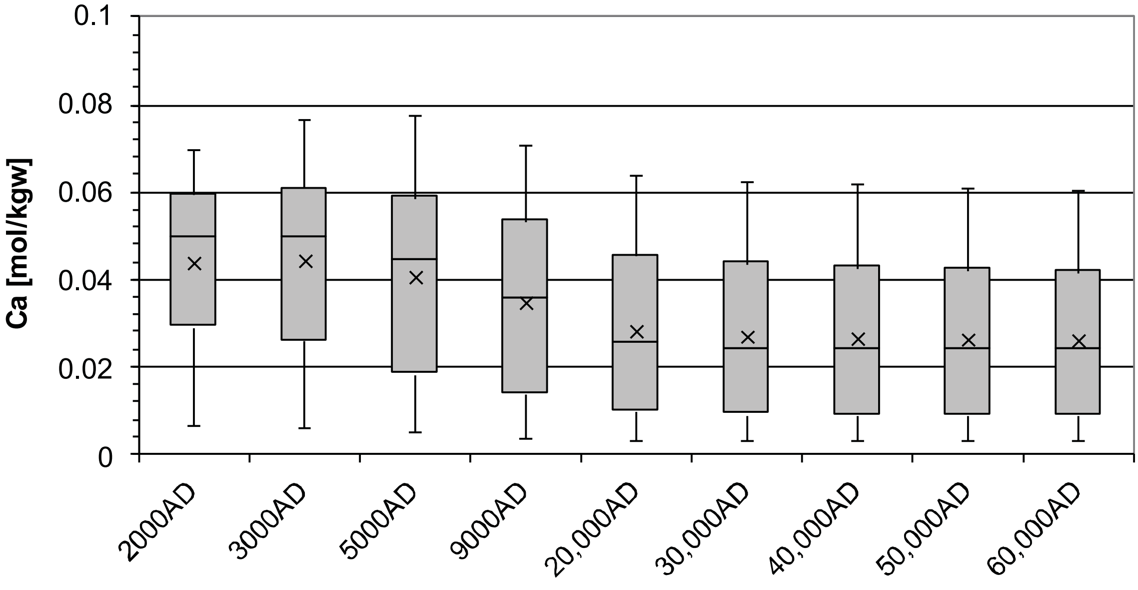

Figure 4-107. *Box and whisker plot showing the statistical distribution of total calcium molalities for Case 5 on a regular grid of points within the repository volume between elevations -490 m and -460 m. The statistical measures are the median, the 25th and 75th percentiles (box), the mean (cross) and the 5th and 95th percentiles (whiskers).*

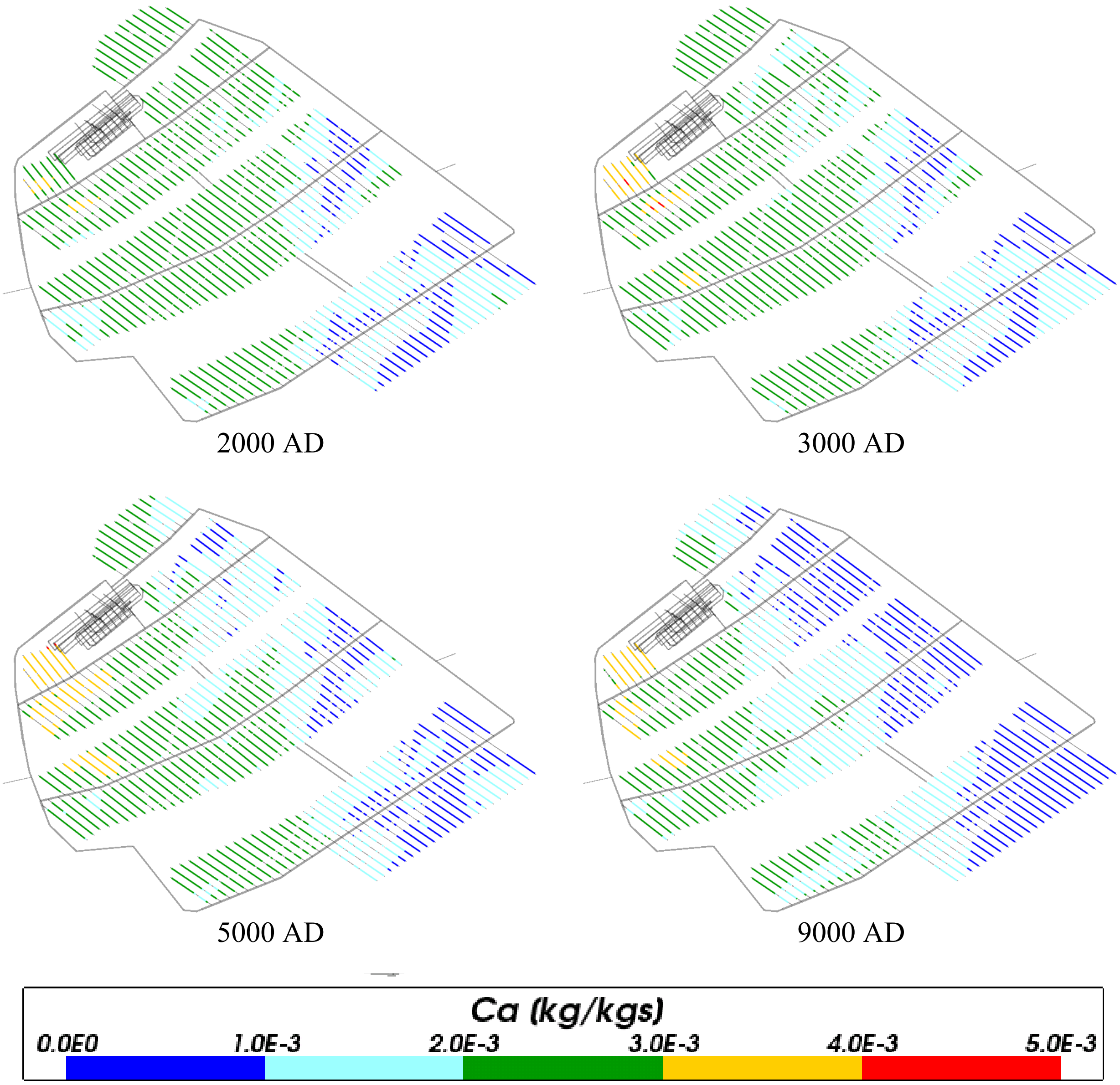

Figure 4-108. *Total calcium mass fractions for Case 5 at deposition hole locations for time periods 2000 AD to 9000 AD.*

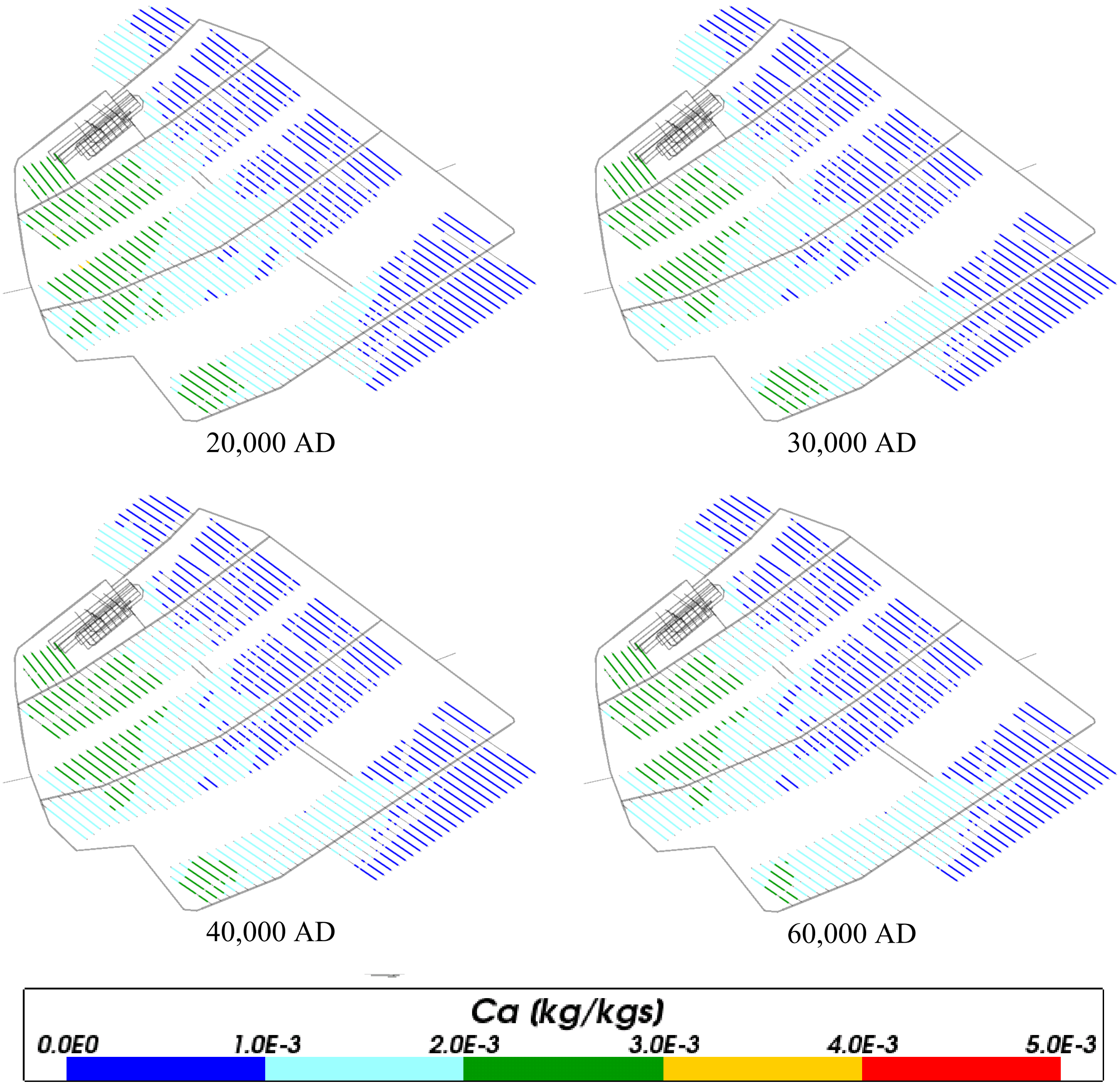

20,000 AD

30,000 AD

40,000 AD

60,000 AD

Figure 4-109. *Total calcium mass fractions for Case 5 at deposition hole locations for time periods 20,000 AD to 60,000 AD.*

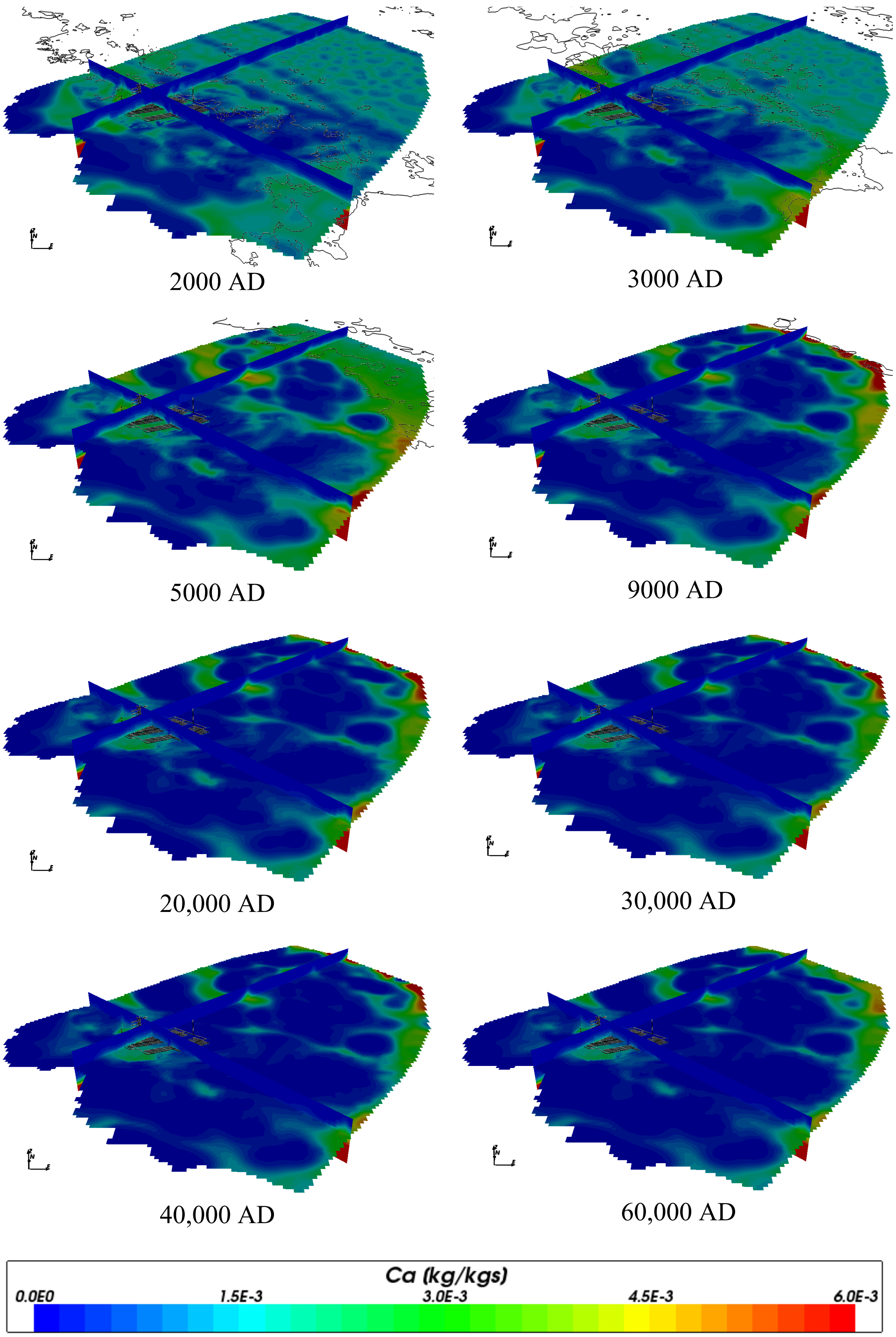

***Figure 4-110.** Total calcium mass fractions on regional scale slices through the repository volume for Case 5 for time periods 2000 AD to 60,000 AD.*

4.6.6 Chloride

Being a non-reactive component in this case, chloride concentrations in the repository area (shown in Figure 4-111, Figure 4-112 and Figure 4-113) and on the regional scale (shown in Figure 4-114) are expected to be similar to that in Case 1 where no chemical reactions are included. The similarities are also apparent when comparing the statistics for the cases, although some minor differences can be seen (e.g. for 5,000 and 9,000 AD) where the mean concentrations are slightly lower in Case 5. This may partly be due to a slightly affected flow field as a result of chemical reactions and their small influence on water densities and partly due to the more dilute meteoric water infiltrating land areas above sea level in Case 5.

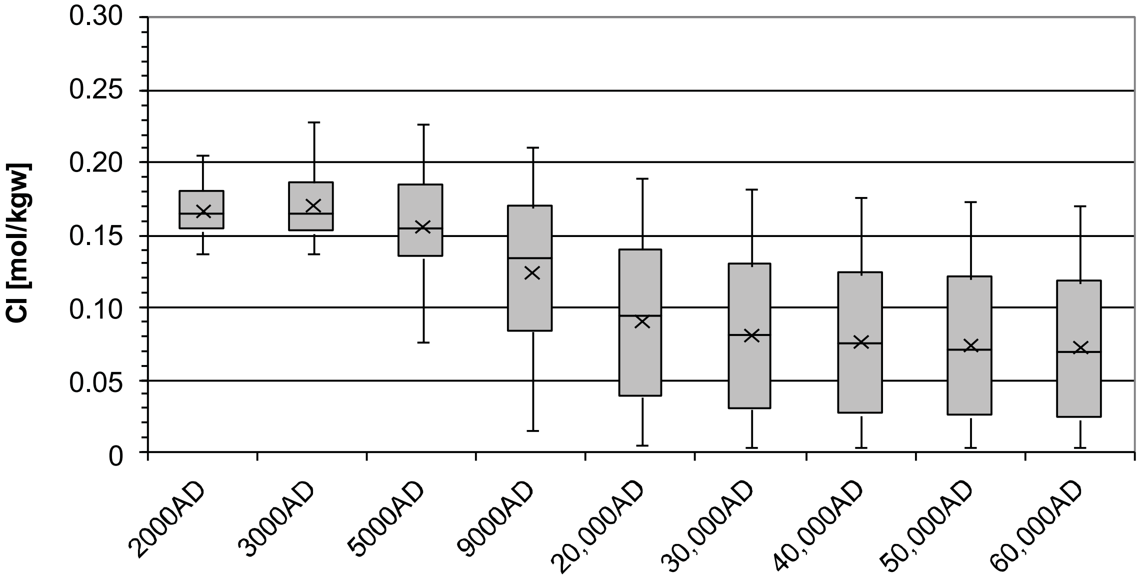

Figure 4-111. Box and whisker plot showing the statistical distribution of total chloride molalities for Case 5 on a regular grid of points within the repository volume between elevations -490 m and -460 m. The statistical measures are the median, the 25th and 75th percentiles (box), the mean (cross) and the 5th and 95th percentiles (whiskers).

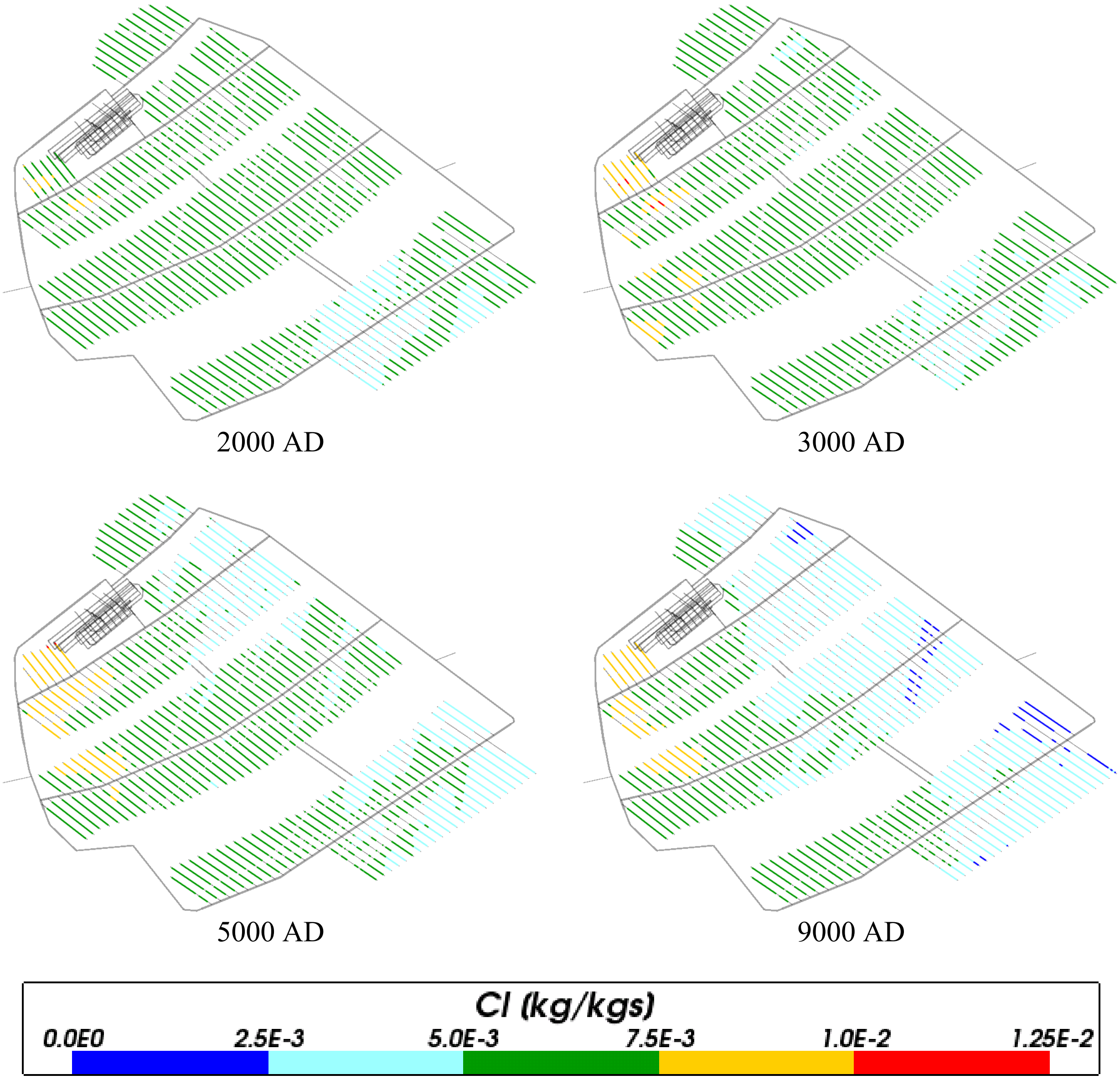

2000 AD

3000 AD

5000 AD

9000 AD

Figure 4-112. *Total chloride mass fractions for Case 5 at deposition hole locations for time periods s 2000 AD to 9000 AD.*

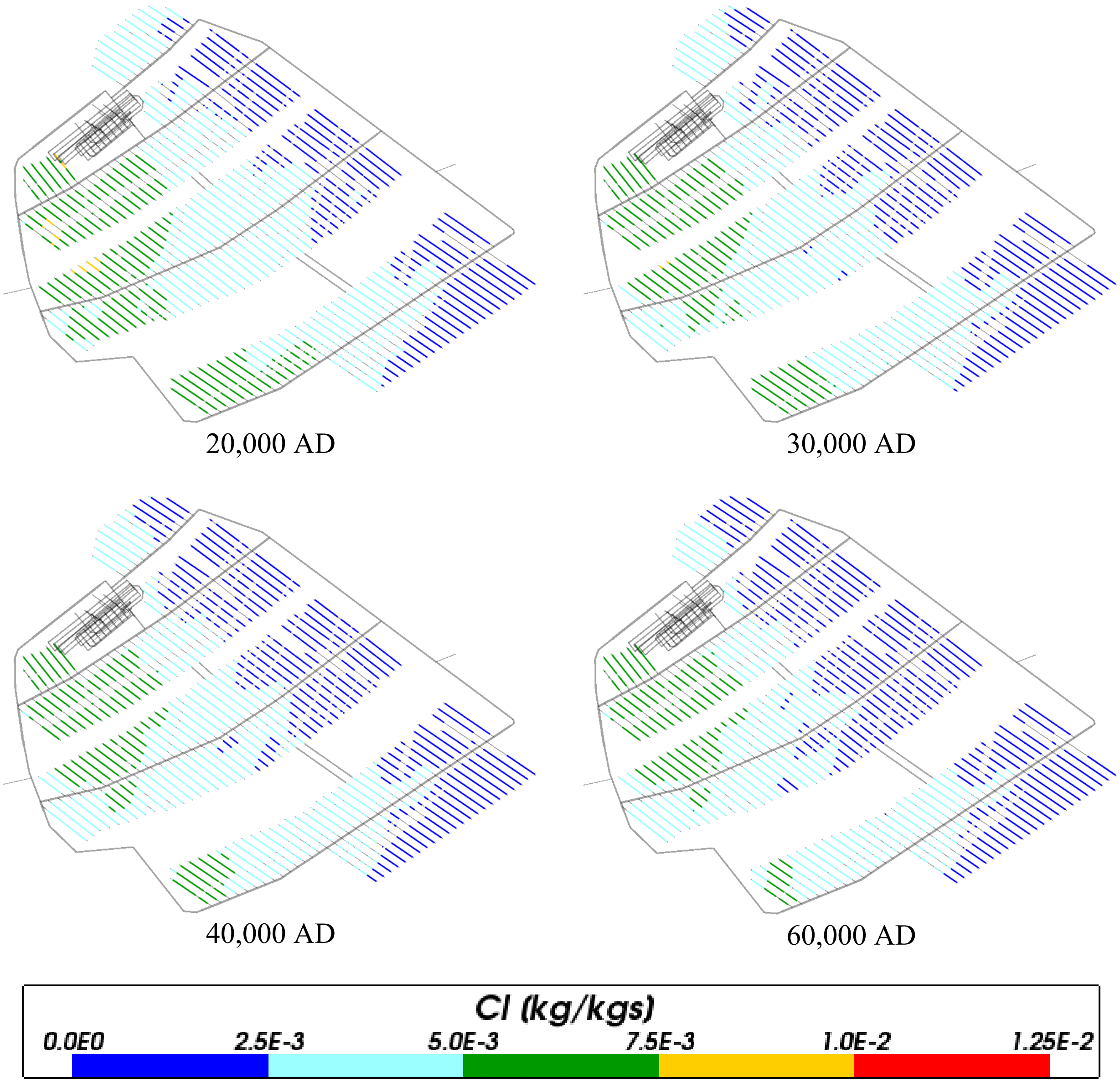

20,000 AD

30,000 AD

40,000 AD

60,000 AD

Figure 4-113. *Total chloride mass fractions for Case 5 at deposition hole locations for time periods 20,000 AD to 60,000 AD.*

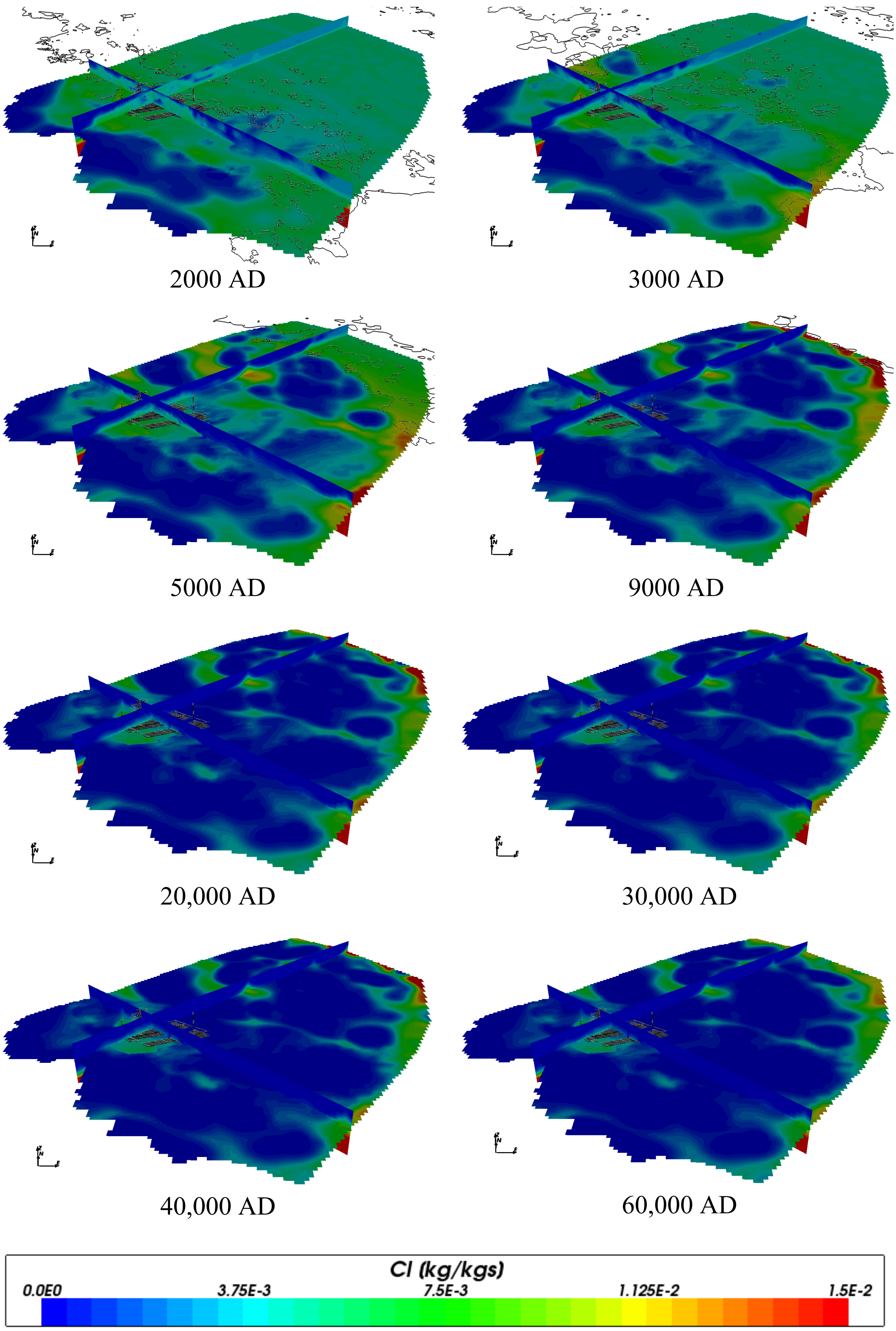

Figure 4-114. *Total chloride mass fractions on regional scale slices through the repository volume for Case 5 for time periods 2000 AD to 60,000 AD.*

4.6.7 Iron

The evolution of total iron concentrations in the repository region for Case 5 is shown in Figure 4-115, Figure 4-116 and Figure 4-117 and on the regional scale in Figure 4-118. The results are very similar to Case 2, differing in slightly lower mean concentrations in Case 5. This may be due to the more dilute meteoric water infiltrating land areas above sea level in Case 5.

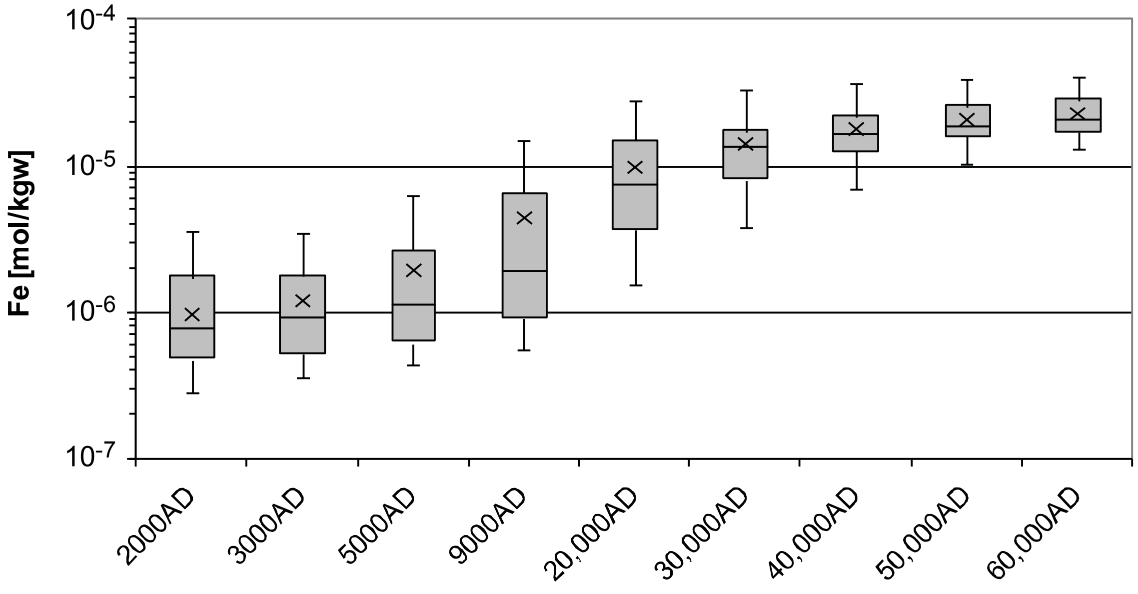

Figure 4-115. *Box and whisker plot showing the statistical distribution of total iron molalities for Case 5 on a regular grid of points within the repository volume between elevations -490 m and -460 m. The statistical measures are the median, the 25th and 75th percentiles (box), the mean (cross) and the 5th and 95th percentiles (whiskers).*

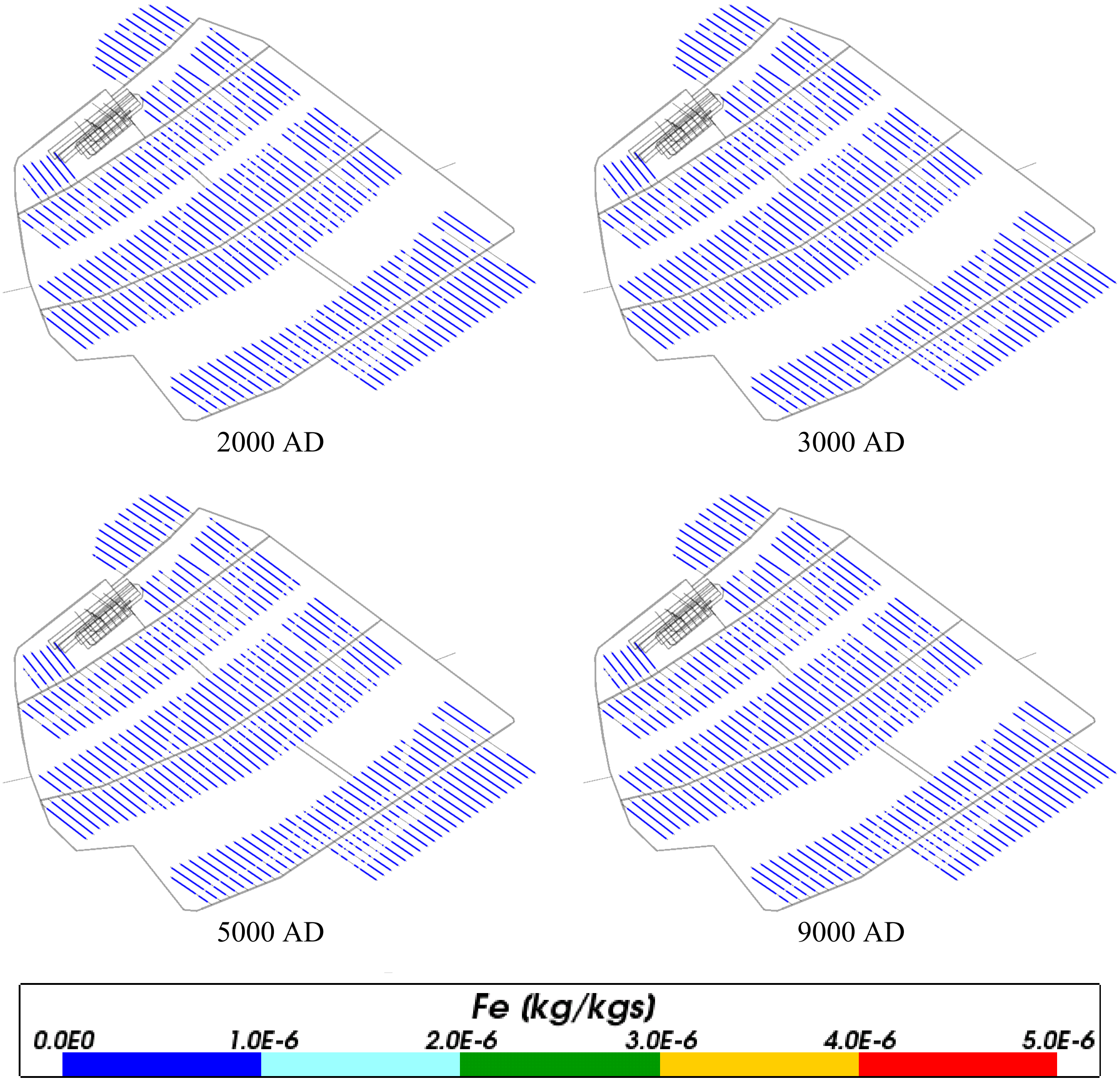

Figure 4-116. *Total iron mass fractions for Case 5 at deposition hole locations for time periods 2000 AD to 9000 AD.*

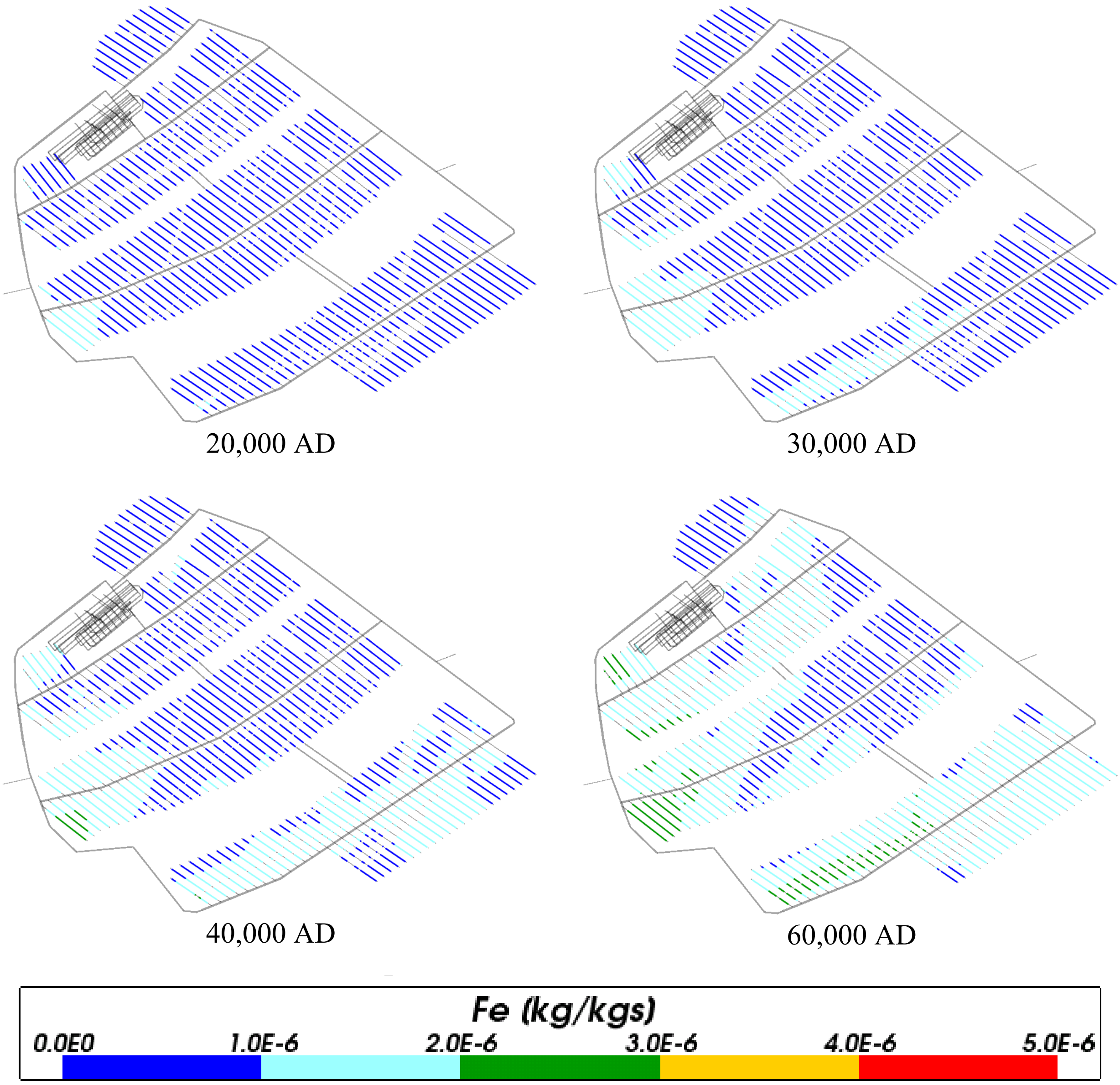

20,000 AD

30,000 AD

40,000 AD

60,000 AD

Figure 4-117. *Total iron mass fractions for Case 5 at deposition hole locations for time periods 20,000 AD to 60,000 AD.*

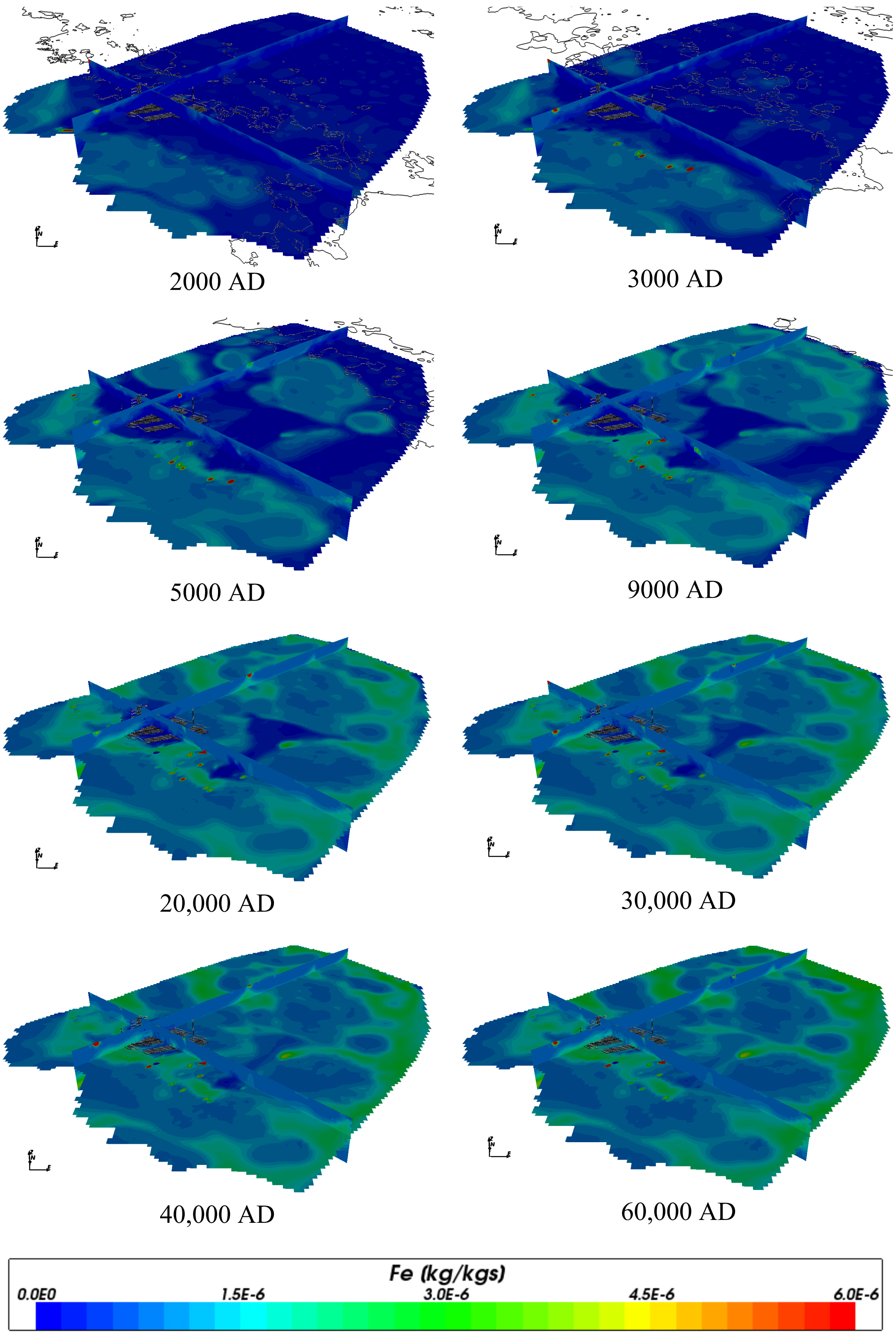

2000 AD

3000 AD

5000 AD

9000 AD

20,000 AD

30,000 AD

40,000 AD

60,000 AD

Figure 4-118. *Total iron mass fractions on regional scale slices through the repository volume for Case 5 for time periods 2000 AD to 60,000 AD.*

4.6.8 Sodium

The concentration of sodium both in the repository area (shown in Figure 4-119, Figure 4-120 and Figure 4-121) and on the regional scale (shown in Figure 4-122) are similar to Case 1. This is expected as sodium is not included in any reactions considered in Case 5. However, some small difference are apparent when comparing the results for these cases, in general the sodium concentrations are slightly lower in Case 5 than in Case 1. As for chloride, this may partly be due to minor changes in the flow field as a result of chemical reactions affecting water densities and partly due to the more dilute meteoric water infiltrating land areas above sea level in Case 5.

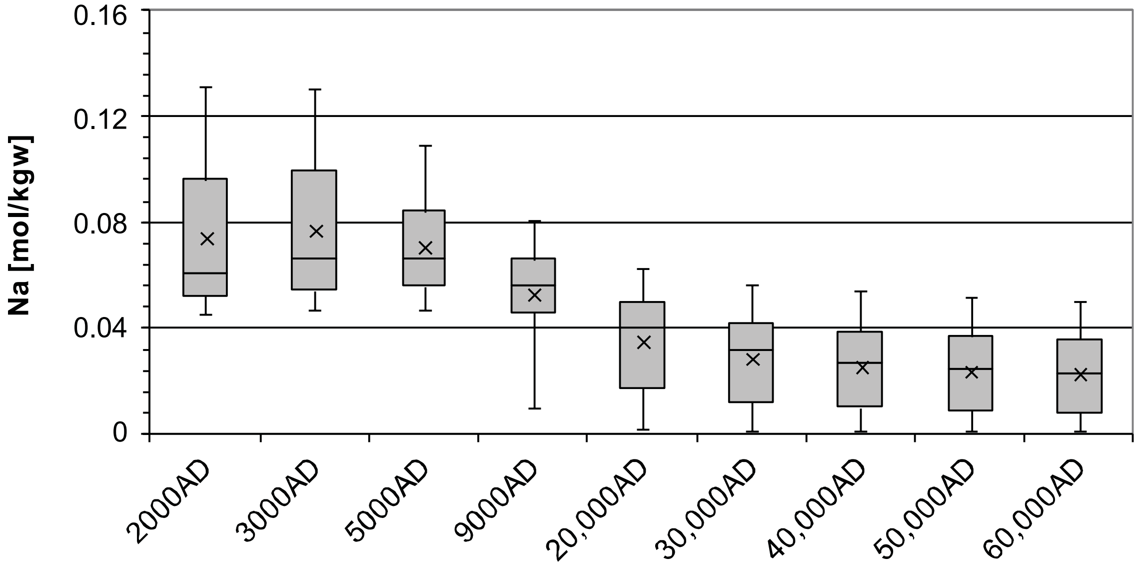

Figure 4-119. *Box and whisker plot showing the statistical distribution of total sodium molalities for Case 5 on a regular grid of points within the repository volume between elevations -490 m and -460 m. The statistical measures are the median, the 25th and 75th percentiles (box), the mean (cross) and the 5th and 95th percentiles (whiskers).*

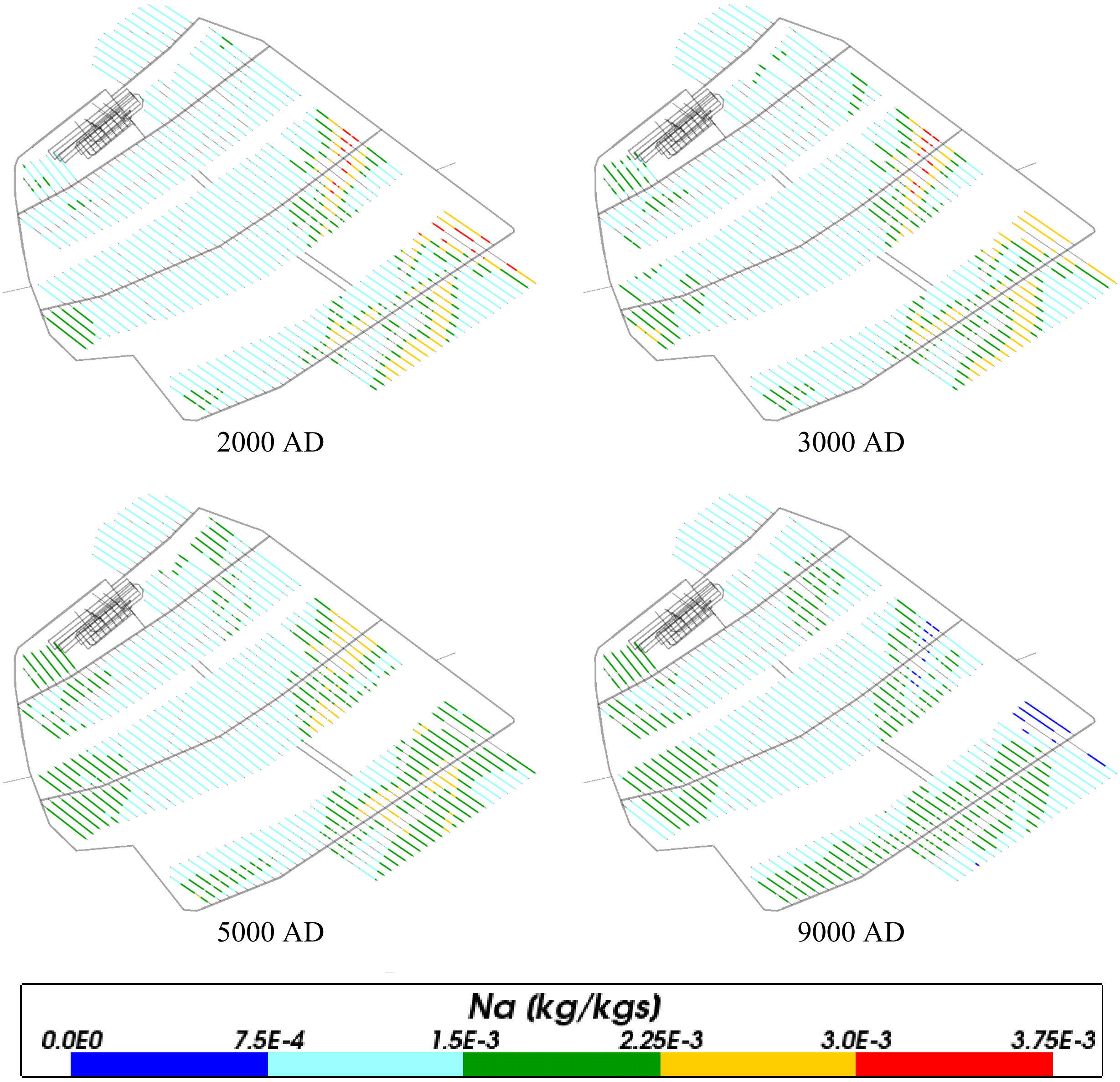

2000 AD

3000 AD

5000 AD

9000 AD

Figure 4-120. *Total sodium mass fractions for Case 5 at deposition hole locations for time periods 2000 AD to 9000 AD.*

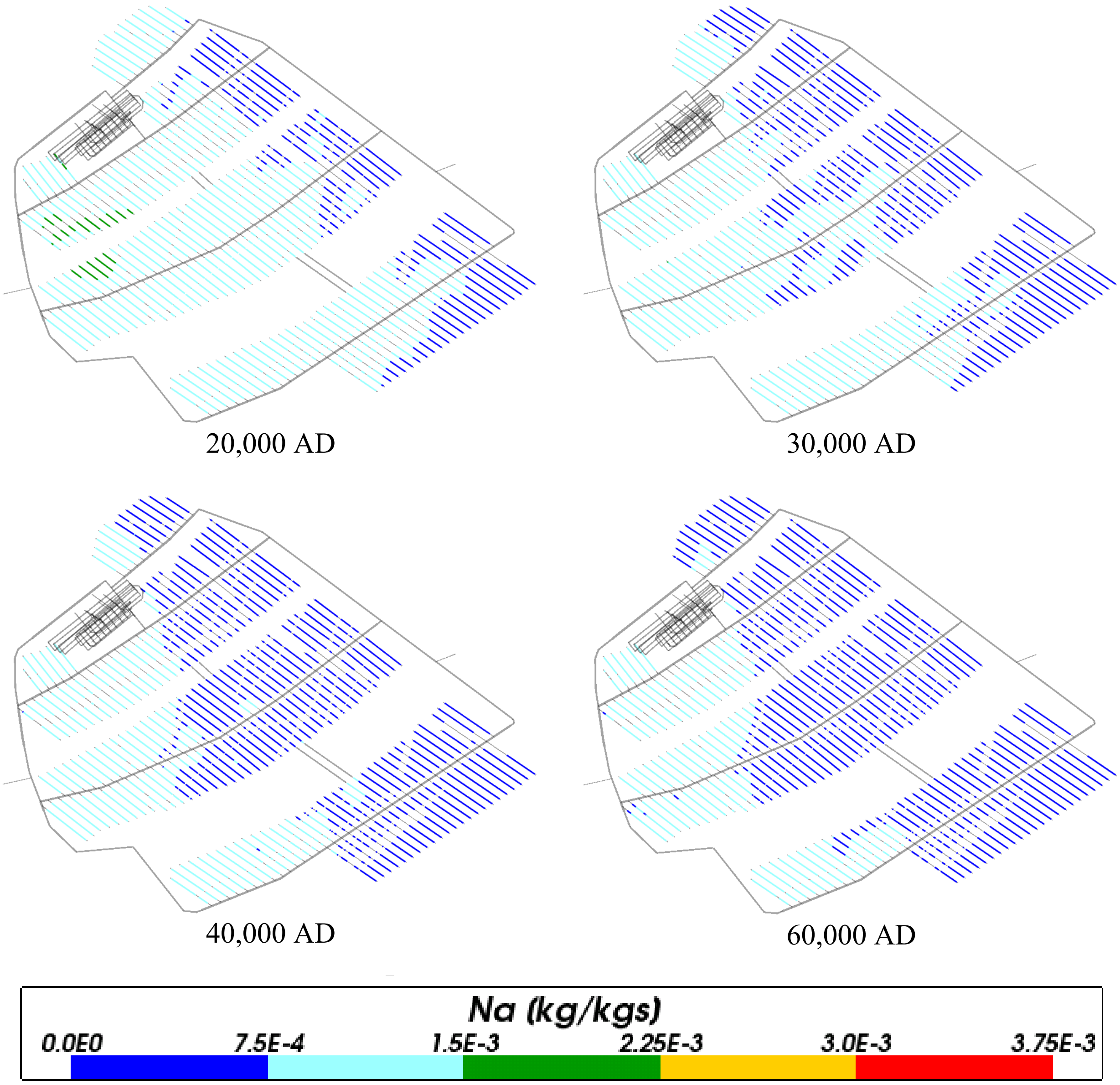

20,000 AD

30,000 AD

40,000 AD

60,000 AD

Figure 4-121. *Total sodium mass fractions for Case 5 at deposition hole locations for time periods 20,000 AD to 60,000 AD.*

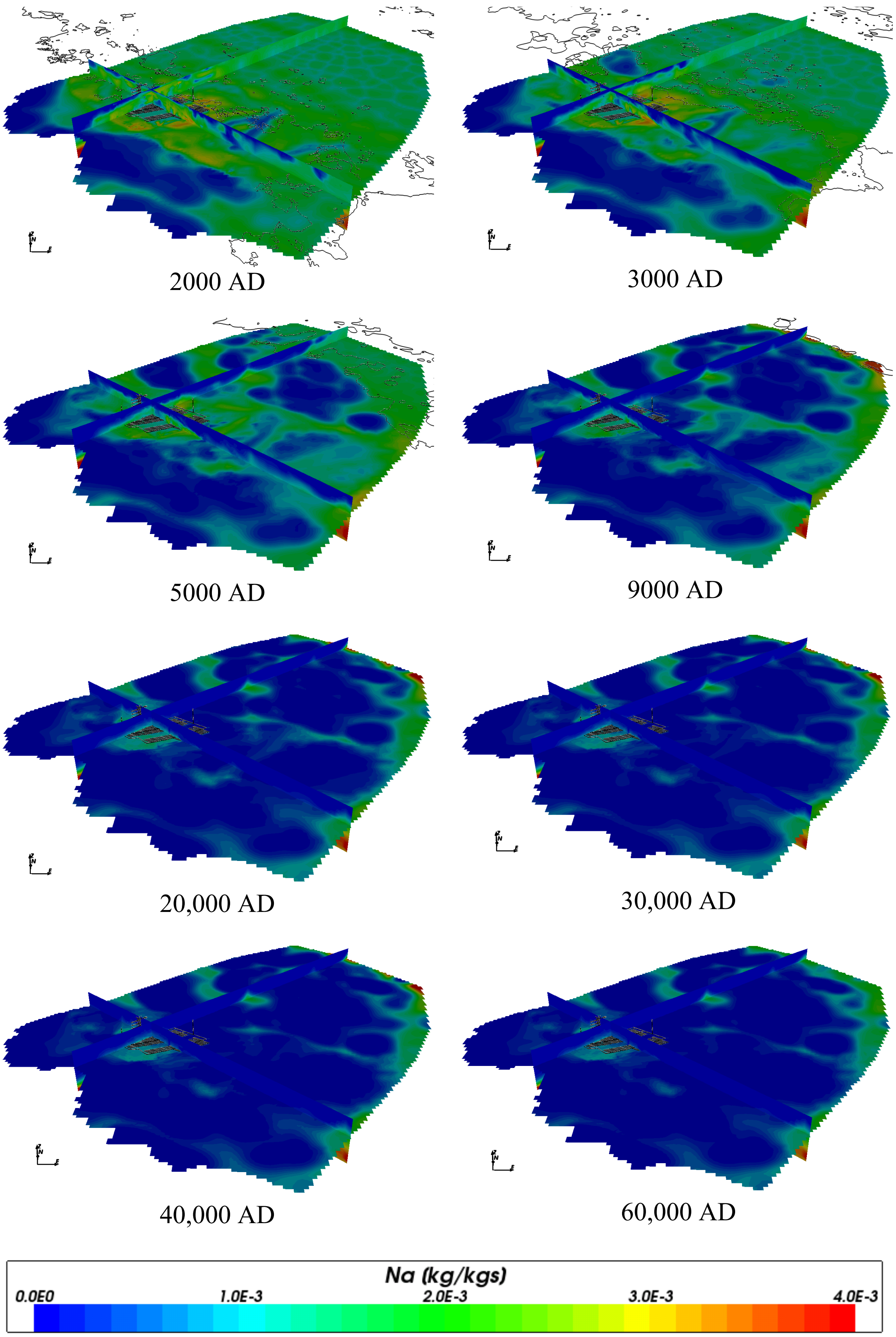

Figure 4-122. *Total sodium mass fractions on regional scale slices through the repository volume for Case 5 for time periods 2000 AD to 60,000 AD.*

4.6.9 Sulphate

Figure 4-123, Figure 4-124 and Figure 4-125 show the evolution in sulphate concentrations around the repository in Case 5. The mean values are similar to those in Case 2, but a greater spatial variability is evident at early times in Case 5. This trend is also seen in Case 4.

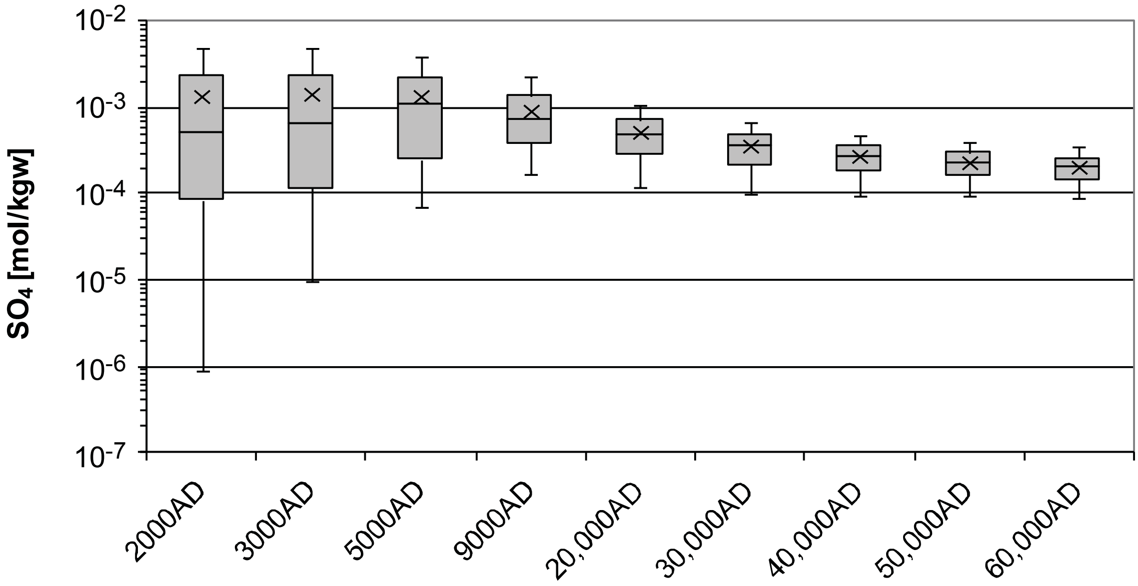

Figure 4-123. *Box and whisker plot showing the statistical distribution of sulphate molalities for Case 5 on a regular grid of points within the repository volume between elevations -490 m and -460 m. The statistical measures are the median, the 25th and 75th percentiles (box), the mean (cross) and the 5th and 95th percentiles (whiskers).*

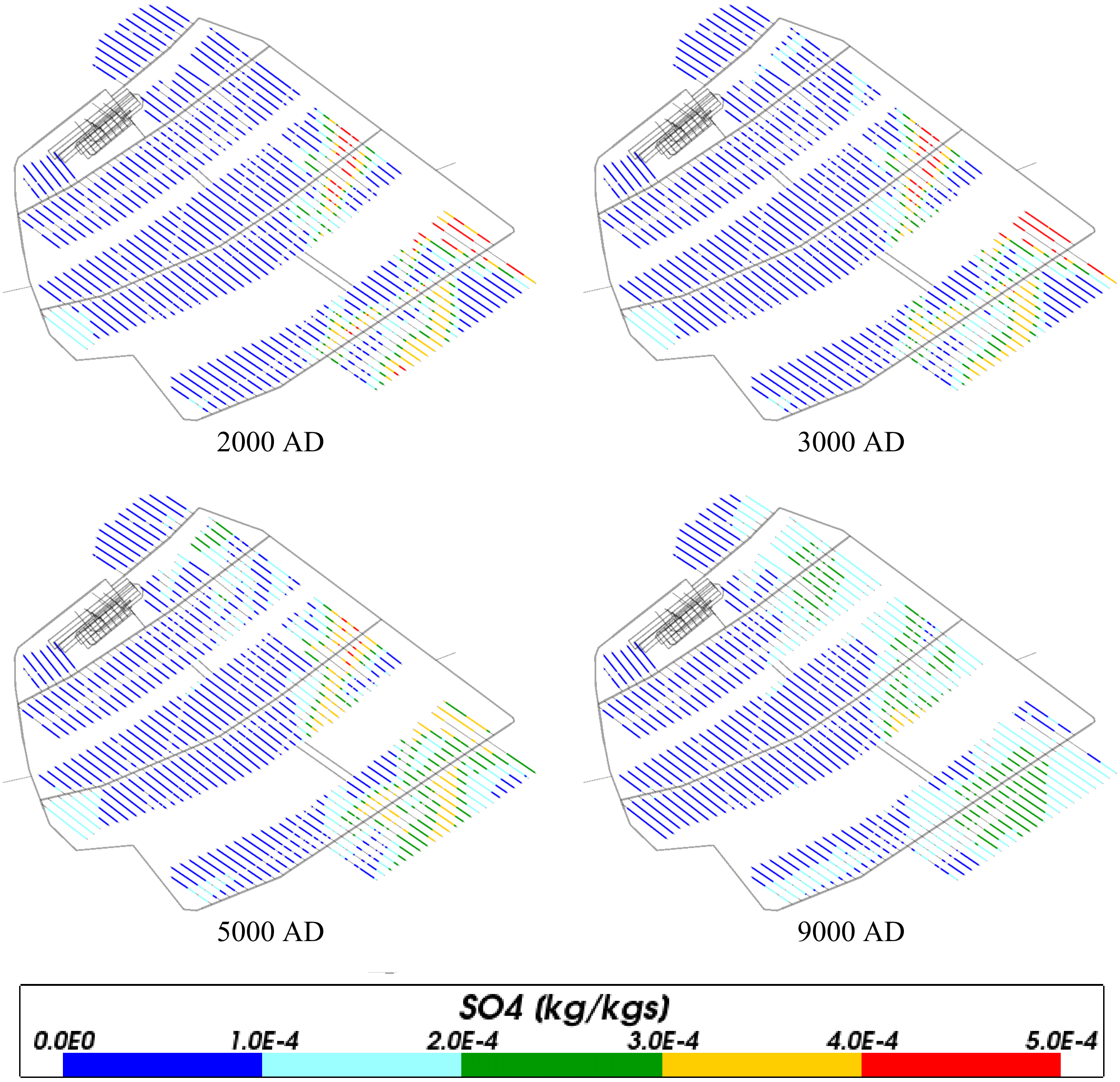
2000 AD
3000 AD
5000 AD
9000 AD

***Figure 4-124.** Sulphate mass fractions for Case 5 at deposition hole locations for time periods 2000 AD to 9000 AD.*

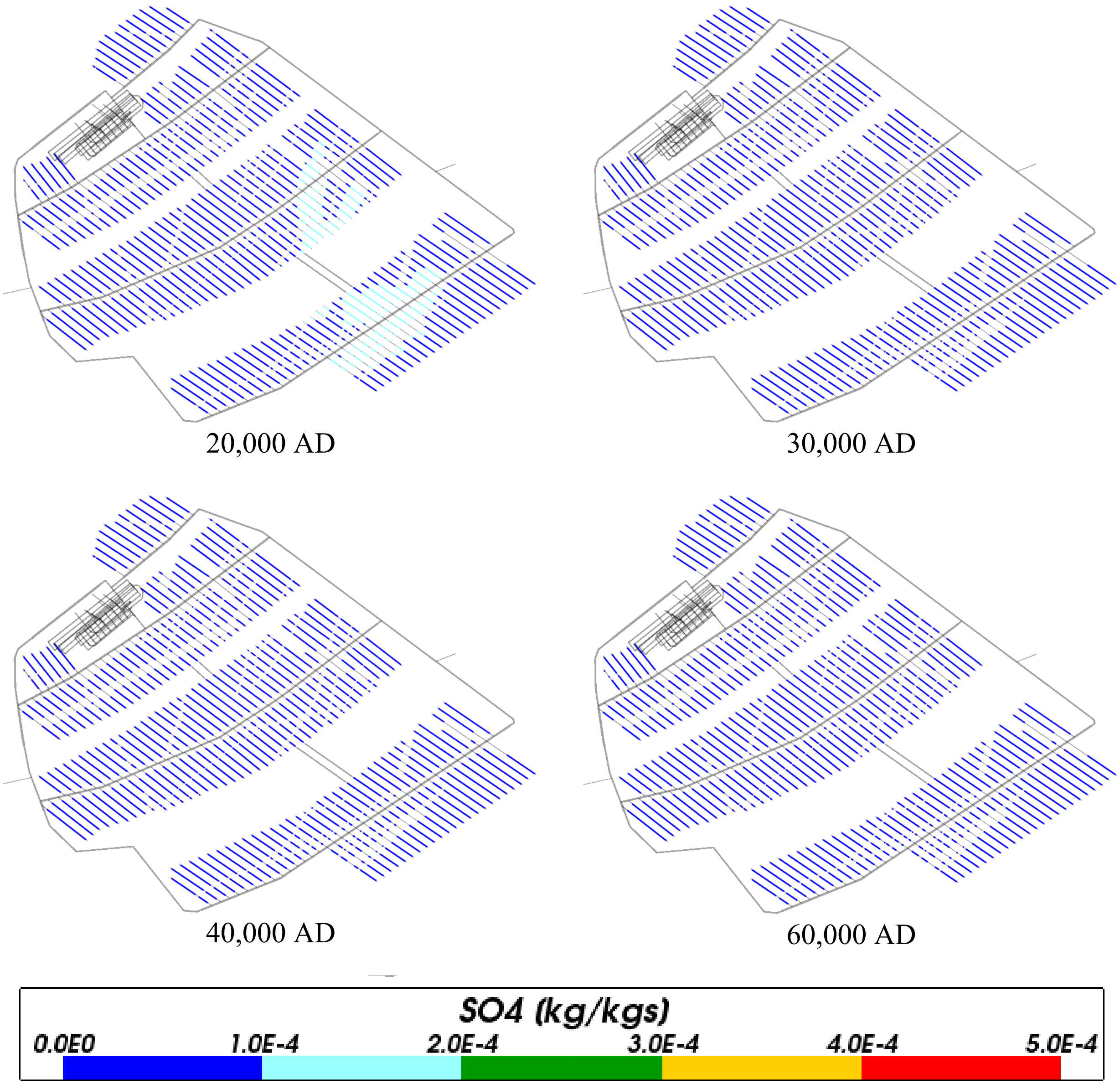

Figure 4-125. *Sulphate mass fractions for Case 5 at deposition hole locations for time periods 20,000 AD to 60,000 AD.*

5 Conclusions

This report describes calculations of the groundwater composition and geochemical conditions in the host rock for a proposed spent nuclear fuel repository at Forsmark for an extended temperate climate period from 8,000 BC to 60,000 AD. During this period the site would be exposed to an increased duration of infiltrating meteoric water compared to the SR-Site base case, which could have an impact on safety functions related to geochemical conditions. A number of cases were modelled based on different chemical reactions or a different composition for the infiltrating meteoric water.

Case 1 included no chemical reactions and only modelled transient, variable density groundwater flow and transport. This case showed that over time meteoric water could penetrate to repository depth, leading to a reduction in salinity and an increase in the concentration of total inorganic carbon. The results are consistent with those obtained for SR-Site up to 9,000 AD in Joyce et al. (2010) and with those at 10,000 AD and 60,000 AD for dilute water penetration calculations in Section 10.3.6 of SKB (2011).

Case 2 included equilibration of groundwater with calcite, quartz and amorphous iron (II) sulphide. This case showed similar results to Case 1, but allowed the calculation of pH and Eh. The median pH in the repository volume fell from around 7.5 to around 6.8, whilst the median Eh rose from about -240 mV to around -190 mV.

Case 3 included equilibration of groundwater with calcite, quartz and iron (III) oxyhydroxide. Conclusions related to this case will be reported after further investigations have been carried out.

Case 4 included equilibration with a few more mineral phases than in previous cases, calcite, quartz, amorphous iron (II) sulphide, kaolinite, albite, and K-feldspar. The difference in mineral phases considered resulted in a lower pH around the repository (less than one pH unit) at early times up to 9,000 AD as compared to Case 2, but increased at later times and levelled off at a slightly higher pH (median around 7.1) than in Case 2. Eh around the repository in Case 4 was fairly constant with a median ranging from -220 to -200 throughout the time span modelled. The total inorganic carbon concentrations around the repository showed a greater spatial variability and also higher mean values at early times up to 3,000 AD as compared with Case 2. This is due to a sharp vertical concentration gradient with a transition from high to low concentrations that occurred at repository depth as can be seen in Figure 4-73. This is particularly evident for early times up to 3,000 AD. At later times the variability decreased and the mean concentration levelled off at a slightly lower level than in Case 2. As with total inorganic carbon, the iron concentrations showed a greater spatial variability and higher mean values around the repository in Case 4 as compared with Case 2, particularly at early times. The median concentration however, does not change significantly throughout the simulated time span in Case 4. Also the sulphate concentrations around the repository showed a greater spatial variability as compared with Case 2, but with similar mean values. Other components showed only minor differences as compared to Case 2.

The model in Case 5 was identical to Case 2 except that the meteoric water, infiltrating at the top boundary in land areas located above the sea level, was more dilute in Case 5.

This resulted in very similar pH, Eh and solution species concentrations as in Case 2, but in general with slightly lower concentration values.

In terms of the rock safety functions for chemically favourable conditions considered for SR-Site in Section 10.3.16 of SKB (2011), the following conclusions can be drawn from the present study:

a) Reducing conditions; Eh limited.
As for SR-Site, reducing conditions were maintained within the repository volume for all cases.

b) Salinity; TDS limited.
The 95th percentile of TDS for all cases was less than $1.3 \cdot 10^4$ mg/kg$_w$ at all times, which is consistent with the value of 12 g/L reported in SKB (2011) and is well below the limit of 35 g/L for the repository backfill.

c) Ionic strength; $\sum q[M^{q+}] > 4$ mM charge equivalent.
The 5th percentile of the cation charge concentration remained higher than $4.0 \cdot 10^{-3}$ mol/kg$_w$ for all cases at all times. For all but case 5 it remained higher than $1.0 \cdot 10^{-2}$ mol/kg$_w$.

d) Concentrations of potassium and iron; limited.
The 95th percentile for potassium concentration did not rise above $3.0 \cdot 10^{-3}$ mol/kg$_w$ for any case at any time within the repository volume. This is consistent with the maximum value of $4.0 \cdot 10^{-3}$ mol/L reported in SKB (2011). The 95th percentile for iron concentration did not rise above $6.0 \cdot 10^{-5}$ mol/kg$_w$ for any case at any time within the repository volume. This is consistent with the maximum value of $1.0 \cdot 10^{-4}$ mol/L reported in SKB (2011).

e) pH; pH < 11.
The 95th percentile for pH did not rise above 8.0 within the repository volume for any of the cases at any time.

f) Avoid chloride assisted corrosion; pH > 4 and $[CL^-] < 2$ M.
The 5th percentile for pH did not fall below 6.5 for any of the cases at any time and the 95th percentile for chloride concentration did not rise above $2.3 \cdot 10^{-1}$ mol/kg$_w$.

The results of this work show that the geochemical environment of the site changes little beyond the climate period considered for SR-Site and hardly at all beyond 20,000 AD. The groundwater composition is primarily determined by flow and transport, with only minor changes resulting from the geochemical reactions considered. Additionally, the geochemical safety functions used for SR-Site are met for all of the cases throughout the time period studied.

References

AMEC, 2013a. CONNECTFLOW Release 10.5 Technical summary document. AMEC/ENV/CONNECTFLOW/15, AMEC, UK.

AMEC, 2013b. NAMMU Release 10.5 Technical summary document. AMEC/ENV/CONNECTFLOW/8, AMEC, UK.

AMEC, 2013c. NAPSAC Release 10.5 Technical summary document. AMEC/ENV/CONNECTFLOW/12, AMEC, UK.

Bosson E, Gustafsson L-G, Sassner M, 2008. Numerical modelling of surface hydrology and near-surface hydrogeology at Forsmark. Site descriptive modelling, SDM-Site Forsmark. SKB R-08-09, Svensk Kärnbränslehantering AB.

Charlton S R, Parkhurst D L, 2011. Modules based on the geochemical model PHREEQC for use in scripting and programming languages. Computers and Geosciences 37, 1653–1663.

Follin S, 2008. Bedrock hydrogeology Forsmark. Site descriptive modelling, SDM-Site Forsmark. SKB R-08-95, Svensk Kärnbränslehantering AB.

Follin S, Levén J, Hartley L, Jackson P, Joyce S, Roberts D, Swift B, 2007a. Hydrogeological characterisation and modelling of deformation zones and fracture domains, Forsmark modelling stage 2.2. SKB R-07-48, Svensk Kärnbränslehantering AB.

Follin S, Johansson P-O, Hartley L, Jackson P, Roberts D, Marsic N, 2007b. Hydrological conceptual model development and numerical modelling using CONNECTFLOW, Forsmark modelling stage 2.2. SKB R-07-49, Svensk Kärnbränslehantering AB.

Hartley L, Joyce S, 2013. Approaches and algorithms for groundwater flow modeling in support of site investigations and safety assessment of the Forsmark site, Sweden. Journal of Hydrology 500, 200–216.

Hedenström A, Sohlenius G, Strömgren M, Brydsten L, Nyman H, 2008. Depth and stratigraphy of regolith at Forsmark. Site descriptive modelling, SDM-Site Forsmark. SKB R-08-07, Svensk Kärnbränslehantering AB.

Jackson C P, Hoch A R, Todman S, 2000. Self-consistency of a heterogeneous continuum porous medium representation of a fractured medium. Water Resources Research 36, 189–202.

Joyce S, Simpson T, Hartley L, Applegate D, Hoek J, Jackson P, Swan D, Marsic N and Follin S, 2010. Groundwater flow modelling of periods with temperate climate conditions – Forsmark. SKB R-09-20, Svensk Kärnbränslehantering AB.

Olofsson I, Simeonov A, Stephens M, Follin S, Nilsson A-C, Röshoff K, Lindberg U, Lanaro F, Fredriksson A, Persson L, 2007. Site descriptive modelling Forsmark, stage 2.2. A fracture domain concept as a basis for the statistical modelling of fractures and minor deformation zones, and interdisciplinary coordination. SKB R-07-15, Svensk Kärnbränslehantering AB.

Parkhurst D L, Appelo C A J, 1999. User's guide to PHREEQC (version 2): a computer program for speciation, batch-reaction, one-dimensional transport, and inverse geochemical calculations. Water-Resources Investigations Report 99-4259, U.S. Geological Survey, Denver, Colorado.

Rhén I, Follin S, Hermanson J, 2003. Hydrological Site Descriptive Model – a strategy for its development during Site Investigations. SKB R-03-08, Svensk Kärnbränslehantering AB.

Salas J, Gimeno M J, Auqué L, Molinero J, Gómez J, Juárez I, 2010. SR-Site – hydrogeochemical evolution of the Forsmark site. SKB TR-10-58, Svensk Kärnbränslehantering AB.

SKB, 2008. Site description of Forsmark at completion of the site investigation phase SDM-Site Forsmark. SKB TR-08-05, Svensk Kärnbränslehantering AB.

SKB, 2010. Climate and climate-related issues for the safety assessment SR-Site. SKB TR-10-49, Svensk Kärnbränslehantering AB.

SKB, 2011. Long-term safety for the final repository for spent nuclear fuel at Forsmark. Main report of the SR-Site project. SKB TR-11-01, Svensk Kärnbränslehantering AB.

Svensson U, Follin S, 2010. Groundwater flow modelling of the excavation and operational phases – Forsmark. SKB R-09-19, Svensk Kärnbränslehantering AB.

Vidstrand P, Follin S, Zugec N, 2010. Groundwater flow modelling of periods with periglacial and glacial climate conditions – Forsmark. SKB R-09-21, Svensk Kärnbränslehantering AB.